



**HAL**  
open science

# Study of photoreceivers under proton, electron, and gamma-ray irradiation for the LISA mission

Paul Colcombet

► **To cite this version:**

Paul Colcombet. Study of photoreceivers under proton, electron, and gamma-ray irradiation for the LISA mission. Astrophysics [astro-ph]. Université Côte d'Azur, 2024. English. NNT: 2024COAZ5022 . tel-04719465

**HAL Id: tel-04719465**

**<https://theses.hal.science/tel-04719465v1>**

Submitted on 3 Oct 2024

**HAL** is a multi-disciplinary open access archive for the deposit and dissemination of scientific research documents, whether they are published or not. The documents may come from teaching and research institutions in France or abroad, or from public or private research centers.

L'archive ouverte pluridisciplinaire **HAL**, est destinée au dépôt et à la diffusion de documents scientifiques de niveau recherche, publiés ou non, émanant des établissements d'enseignement et de recherche français ou étrangers, des laboratoires publics ou privés.

# THÈSE DE DOCTORAT

Étude de photorécepteurs sous irradiation de  
protons, électrons et rayons gamma pour la  
mission LISA

**Paul COLCOMBET**

ARTEMIS - Laboratoire d'Astrophysique Relativiste, Théories, Expériences, Métrologie,  
Instrumentation, Signaux

**Présentée en vue de l'obtention  
du grade de docteur en sciences de la  
planète et de l'univers d'Université Côte  
d'Azur**

**Dirigée par :** Nicoleta Dinu-Jaeger,  
Christophe Inguibert

**Soutenue le :** 29 mai 2024

**Devant le jury, composé de :**

Olivier Gravrand, Directeur de Recherche,  
CEA-LETI

Vincent Goiffon, Professeur, ISAE-  
SUPAERO

Martin Hewitson, Research Group Leader,  
AEI

Gilles Metris, Astronome, CNRS-GEOAZUR



# Étude de photorécepteurs sous irradiation de protons, électrons et rayons gamma pour la mission LISA

Jury :

Rapporteurs

Vincent Goiffon, Professeur, École Nationale Supérieure de l'Aéronautique et de l'Aspace (ISAE-SUPAERO) Toulouse France

Olivier Gravrand, Directeur de Recherche, Laboratoire d'Électronique des Technologies de l'Information (CEA-Leti) Grenoble France

Éxamineurs

Martin Hewitson, Research Group Leader, Max Planck Institute for Gravitational Physics (AEI) Hannover Allemagne

Gilles Metris, Astronome, Laboratoire Géoazur (CNRS-GEOAZUR) Valbonne France

Directeurs

Nicoleta Dinu-Jaeger, Ingénieur de recherche, Laboratoire Artemis (CNRS-ARTEMIS) Nice, France

Christophe Inguibert, Directeur de recherche, Office national d'études et de recherches aérospatiales (ONERA), Toulouse France

# Abstract

Scheduled for 2035, the Laser Interferometer Space Antenna (LISA), led by the European Space Agency (ESA), represents a pioneering effort as the first space-based Gravitational Waves (GWs) detector. Operating within the 0.1 mHz to 1 Hz range, LISA extends the capabilities of terrestrial detectors. This advancement will open a new window to our universe and a new era in cosmological studies. The mission's design features three spacecraft, arranged in an equilateral triangle with each side spanning 2.5 million km, trailing the Earth in its orbit around the Sun. Central to LISA's function are its high-precision laser interferometers, which detect distance fluctuations between test masses in free fall within each spacecraft, with sensitivity to changes as subtle as a dozen picometers. The detection technology of LISA lies in its Quadrant Photoreceivers (QPRs), critical for recording interferometric signals. These QPRs incorporate large areas and low capacitance  $\text{In}_{0.53}\text{Ga}_{0.47}\text{As}$  Quadrant Photodiodes (QPDs) connected to low noise Transimpedance Amplifier (TIA), all enclosed within a mechanical enclosure. Over its projected 12.5-year lifespan, LISA will encounter diverse radiation types, predominantly from solar emissions. Such radiation can degrade the QPDs by inducing crystal defects that alter the semiconductor properties, impairing the device's performance. The objective of this thesis was to study the impact of the space radiation environment on the  $\text{InGaAs}$  QPDs' main electro-optical parameters. This investigation was further extended to assess the consequential implications of such degradations on the QPR performances and, by extension, the LISA interferometric measurements. The devices have been provided by the member countries of the LISA Consortium QPR Working Group, namely Netherlands (NL) and Japan (JP) for the QPDs, and Germany (DE) for the Front End Electronics (FEEs).

In this context, I have developed and calibrated five experimental set-ups, allowing me to evaluate the main QPDs' parameters such as dark current, capacitance, and Quantum Efficiency (QE) but also the overall QPR parameters like Equivalent Input Current Noise (EICN) and phase and amplitude responses to interferometric LISA-like signals. I have also developed Python routines, allowing an automatic analysis of the experimental data. I have used these experimental and software to evaluate the QPD and the QPR parameters, before and after three irradiation types, using respectively protons (20 and 60 MeV,  $1 \times 10^9$  up to  $1 \times 10^{12}$  p/cm<sup>2</sup>), gamma rays (1 to 237 krad), and electrons (0.5 and 1 MeV,  $0.5 \times 10^{12}$  up to  $5 \times 10^{12}$  e/cm<sup>2</sup>). The maximum irradiation conditions exceeded approximately times the LISA requirements fixed by ESA. I have directly participated in the irradiation campaigns, collaborating closely with technical teams from Centre Antoine Lacasagne (CAL) in Nice for protons irradiation and ONERA in Toulouse for gamma rays and electron irradiations.

The findings demonstrated the device's robust radiation tolerance, with no critical failures observed and almost all QPDs meeting LISA's requirements even post-irradiation. I compared our measured experimental damage factor to those of the literature and explored how the intrinsic characteristics of QPDs, such as doping level and bias voltage, influence the Non-Ionising Energy Loss (NIEL) scaling approach. Finally, I established a clear connection between the overall system's degradation, manifested through increased noise levels and reduced amplitude response, and the modification of the QPDs' parameters. This shows the ability to predict the impact of radiation damaged QPDs on the functionality of the QPRs and, by extension, on the accuracy of LISA's GWs measurements.

**Key words:** LISA, Space Environment,  $\text{InGaAs}$  photodiodes, Photoreceptors, Non-ionizing displacement dose.

# Résumé

Programmée pour 2035, la mission Laser Interferometer Space Antenna (LISA), pilotée par l'Agence Spatiale Européenne (ESA), marquera une première en devenant le premier détecteur spatial d'Ondes Gravitationnelles (GWs). Opérant dans la gamme des basses fréquences de 0,1 mHz à 1 Hz inaccessibles aux détecteurs terrestres, LISA ouvrira une nouvelle fenêtre sur notre univers et une nouvelle ère dans l'étude de la cosmologie. Le design présente trois vaisseaux formant un triangle équilatéral de 2,5 millions de km de côté, suivant la Terre dans son orbite autour du Soleil. Au cœur du fonctionnement de LISA se trouvent trois interféromètres laser de haute précision, pouvant détecter des fluctuations de distance de l'ordre d'une dizaine de picomètres entre deux tests masses en chute libre positionnées dans chaque vaisseau. La technologie de détection de LISA repose sur des Photorécepteurs à Quadrants (QPR), essentiels pour enregistrer les signaux interférométriques. Chaque QPR se compose d'une Photodiode à Quadrants (QPD) en  $\text{In}_{0.53}\text{Ga}_{0.47}\text{As}$  à large surface et à faible capacité couplée à un Amplificateur à Transimpédance (TIA) à faible bruit, le tout assemblé dans un boîtier mécanique. Au cours de sa durée de vie de 12,5 ans, LISA sera confrontée à divers types de rayonnements, principalement en provenance du soleil. Un tel rayonnement peut dégrader les QPDs en induisant des défauts cristallins modifiant les propriétés électroniques du semi-conducteur et donc en altérant les performances des QPDs.

L'objectif de cette thèse était d'étudier l'impact de l'environnement radiatif spatial sur les principaux paramètres électro-optiques des QPDs InGaAs ainsi que leurs répercussions sur les performances des QPRs et, par extension, sur les mesures interférométriques de LISA. Les dispositifs ont été fournis par les pays membres du groupe de travail QPR du LISA consortium, à savoir les Pays-Bas (NL) et le Japon (JP) pour les QPDs, et l'Allemagne (DE) pour les FEEs.

Dans ce contexte, j'ai développé et calibré cinq montages expérimentaux, permettant d'évaluer les principaux paramètres électro-optiques des QPDs tel que le courant d'obscurité, la capacité et l'efficacité quantique, ainsi que les paramètres du QPR comme le bruit de courant équivalent d'entrée et sa réponse en phase et en amplitude face à des signaux interférométriques équivalents à ceux utilisés dans LISA. J'ai également développé des routines Python, permettant une procédure d'analyse automatique des données expérimentales. Ces développements expérimentaux et programmes ont permis d'évaluer ces paramètres des QPDs et QPRs, avant et après trois campagnes d'irradiation, utilisant des protons (20 et 60 MeV,  $1 \times 10^9$  à  $1 \times 10^{12}$  p/cm<sup>2</sup>), des rayons gamma (1 à 237 krad) et des électrons (0,5 et 1 MeV,  $0,5 \times 10^{12}$  à  $5 \times 10^{12}$  e/cm<sup>2</sup>). Les conditions d'irradiation maximales dépassaient environ 5 fois les exigences pour LISA formulées par l'ESA. J'ai directement participé aux campagnes d'irradiation, en collaboration étroite avec les équipes techniques du Centre de Protonthérapie Antoine Lacassagne (CAL) de Nice pour l'irradiation des protons et de l'ONERA de Toulouse pour les irradiations des rayons gamma et des électrons).

Les résultats ont démontré la robustesse de ces nouveaux dispositifs face aux radiations, sans aucune défaillance critique observée et avec presque toutes les QPDs répondant aux exigences de LISA. J'ai comparé le facteur expérimental de dommage aux résultats existants dans la littérature et exploré comment les caractéristiques intrinsèques des QPDs, telles que le niveau de dopage et la tension de polarisation influencent leur vulnérabilité face aux radiations. Un lien fut établi entre la dégradation globale du système, manifestée par une augmentation des niveaux de bruit du QPR et une réduction de la réponse en amplitude, avec la détérioration des paramètres des QPDs. Cela permet de prédire l'impact des QPDs irradiées sur le fonctionnement du QPR et, par extension, sur la précision des mesures de LISA.

**Mots-clés:** LISA, Environnement Spatial, InGaAs photodiodes, Photorecepteurs, Dommages de déplacement.

# Remerciements

Je tiens à exprimer ma profonde gratitude à mes deux directeurs de thèse, Nicoleta Dinu-Jaeger et Christophe Inguibert, pour m'avoir donné l'opportunité de réaliser ce doctorat à l'Observatoire de la Côte d'Azur et à l'ONERA. Cette collaboration a été particulièrement enrichissante, l'Observatoire, avec la mission LISA et son expertise en optique, et l'ONERA, avec son expertise en dommages radiatifs et en environnement spatial, se complétant parfaitement. Tous deux ont été pour moi une source inestimable d'apprentissage et de croissance.

Je tiens également à remercier les équipes respectives de l'ONERA et de l'OCA, notamment Michel Lintz, Thierry Nuns, Marco Nardello, Sara Bruhier, Angélique Guitard, et Nathalie Reboulet, pour leur soutien technique et administratif.

Je remercie aussi le consortium QPR LISA pour avoir fourni les QPD et FEE, ainsi que pour leurs conseils et discussions. Un grand merci aux équipes du Centre Antoine Lacassagne, en particulier à Petter Hofverberg, pour leur soutien et la campagne d'irradiation sous protons.

Je souhaite exprimer ma gratitude aux équipes de l'Observatoire et de l'ONERA pour leur accueil chaleureux et les bons moments partagés. Un merci tout particulier à Amaël Roubeau Tissot, mon voisin de bureau, à Fabiola Gerosa, Marjorie Galinier, et Jochen Stadler.

Je n'oublie pas non plus les rencontres à l'ONERA : Agnès Lecadre Scotto, François Villamizar, Bastien Delacroix, Lucas Nicolas, Quentin Peysson, Adrian Beyler, Laurianne Martinet, Maria Tahtouh, Rabia Kiraz, et Gwendoline Marc.

En dehors de l'OCA et de l'ONERA, j'aimerais remercier mon ancienne colocataire Lisa Ballanger, ainsi que Yoann Le Blévennec, Julien Pincemaille, Mehdi Nafkka, et Concetta Pizzonia pour toutes les soirées, randonnées et autres moments agréables qui m'ont permis de me détendre pendant la thèse.

Enfin, je tiens à exprimer ma reconnaissance éternelle à ma famille. Leur soutien constant, leur amour, et leur confiance en moi ont rendu cette thèse possible dès le départ. Je leur en suis infiniment reconnaissant.

# Contents

<b>Acronyms</b>	<b>xiii</b>
<b>Notation</b>	<b>xvi</b>
<b>1 Introduction</b>	<b>1</b>
1.1 Fascination with gravitational waves . . . . .	1
1.2 Evolution of gravitational wave detectors from Earth to space . . . . .	1
1.3 LISA Mission: a new window into our universe . . . . .	2
1.4 LISA detection principle . . . . .	3
1.5 Radiation effects on LISA photoreceivers . . . . .	3
1.6 Research goals and thesis structure . . . . .	4
<b>2 Theoretical and technical background on GWs detectors</b>	<b>6</b>
2.1 Detection of Gravitational Waves . . . . .	6
2.1.1 Introduction to Gravitational Waves . . . . .	6
2.1.2 Introduction to interferometry . . . . .	7
Young’s double-slit experiment . . . . .	8
Michelson Interferometer . . . . .	8
2.1.3 Gravitational Waves detectors . . . . .	9
Ground based detectors . . . . .	9
Space-based detectors . . . . .	10
2.2 LISA mission . . . . .	11
2.2.1 Spacecraft Constellation . . . . .	11
2.2.2 Instrument description . . . . .	12
Drag-Free Attitude Control System (MOSA) . . . . .	12
Phase Measurement System . . . . .	13
Lasers System . . . . .	14
2.2.3 Measurement Principle . . . . .	14
Optical Signals . . . . .	15
2.3 Photoreceivers . . . . .	17
2.3.1 General introduction . . . . .	17
2.3.2 Photodiodes technologies . . . . .	18
The PN junction in photodiode mode . . . . .	18
PIN Photodiodes . . . . .	20
DDR Photodiodes . . . . .	20
2.3.3 Photodiodes optoelectronic characteristic . . . . .	22
Electrical Equivalent Circuit . . . . .	22
Dark current . . . . .	23
Quantum efficiency . . . . .	23
2.3.4 Photoreceivers noise model . . . . .	23
The shot noise . . . . .	24
The thermal noise . . . . .	24
Operational amplifier noise . . . . .	25

Global noise model . . . . .	25
<b>3 Space Environment and Radiation Effects</b>	<b>26</b>
3.1 LISA Space Environment . . . . .	26
3.1.1 Orbit . . . . .	26
3.1.2 Solar Radiation and Cosmic Radiation . . . . .	26
3.1.3 Cosmic Rays . . . . .	27
3.1.4 Others . . . . .	28
3.2 Radiation-Matter Interactions . . . . .	28
3.2.1 Interactions with the Electronic Cloud . . . . .	28
3.2.2 Interactions with the Atomic Nucleus . . . . .	29
3.2.3 Bremsstrahlung Radiation . . . . .	30
3.3 Displacement Defects . . . . .	31
3.3.1 Crystal Defects . . . . .	31
3.3.2 Formation of defect . . . . .	33
3.4 Effects of displacement damage in semi-conductors . . . . .	34
3.5 Modeling Radiation Damage in Semiconductors . . . . .	36
3.5.1 Stopping power and cross section . . . . .	36
3.5.2 Linear Energy Transfer and Non-Ionizing Energy Loss . . . . .	37
3.5.3 Displacement damage threshold . . . . .	38
3.5.4 Radiation Dose . . . . .	38
3.6 From experimental damage factor to the NIEL . . . . .	39
3.6.1 Experimental damage factor . . . . .	39
3.6.2 NIEL scaling approach . . . . .	40
3.6.3 NIEL limitation . . . . .	40
3.7 Radiation resilience requirements for LISA . . . . .	41
3.7.1 Non-ionizing Dose . . . . .	41
3.7.2 Ionizing Dose . . . . .	42
3.7.3 LISA requirements using OMERE Software . . . . .	42
<b>4 Irradiation Campaigns and LISA QPD and QPR tests</b>	<b>44</b>
4.1 Overview of LISA Photoreceivers . . . . .	44
4.1.1 InGaAs Quadrant Photodiode (QPD) . . . . .	44
JP QPDs . . . . .	45
NL QPDs . . . . .	45
4.1.2 Front Ends Electronics . . . . .	46
4.2 Irradiation Campaigns . . . . .	47
4.2.1 Irradiation Facilities . . . . .	47
Protons irradiation facility: Centre Antoine Lacassagne (CAL) . . . . .	47
Electrons Irradiation Facility: ONERA . . . . .	48
Gamma rays Irradiation Facility: ONERA . . . . .	50
4.2.2 Irradiation conditions . . . . .	50
4.3 QPD Dark current and capacitance measurement . . . . .	52
4.3.1 Experimental bench and instruments description . . . . .	52
4.3.2 Measurement protocols . . . . .	54
4.3.3 Evaluation setup performances . . . . .	54
4.4 QPD Quantum efficiency measurement . . . . .	56
4.4.1 Experimental bench and instruments description . . . . .	56
4.4.2 Measurement principle . . . . .	58
4.4.3 Instruments and calibration methods . . . . .	58
Measurement of the optical power ratio $R_{out4,3}$ . . . . .	58
Beam profile calibration . . . . .	59
Beam alignment with the QPD . . . . .	60
4.4.4 Measurement Protocol . . . . .	61

4.4.5	Evaluation of Setup Performance . . . . .	61
	Evaluation of the measurement error . . . . .	61
4.5	QPR Input equivalent current noise measurement . . . . .	62
4.5.1	Principle behind the ‘White Light’ method . . . . .	62
4.5.2	Experimental setup and instrument description . . . . .	62
4.5.3	Experimental protocol description . . . . .	64
	Dark Condition Measurement . . . . .	64
	Light condition measurement . . . . .	64
	Setup floor measurement . . . . .	64
	Data Processing . . . . .	65
4.5.4	Instruments and calibration methods . . . . .	66
4.5.5	Evaluation of setup performance . . . . .	67
4.6	QPR Phase and amplitude response to LISA interferometric equivalent signal . . . .	68
4.6.1	Detailed Experimental Setup and Instrumentation . . . . .	68
	LISA interferometric signal generation . . . . .	69
	Signal monitoring and test module . . . . .	70
	Control and acquisition system . . . . .	71
4.6.2	Measurement principle . . . . .	72
	LISA Heterodyne Signal . . . . .	72
	Modulator Output Signal . . . . .	72
	Matching the two signals . . . . .	73
4.6.3	Instruments and calibration methods . . . . .	74
4.6.4	Measurement Protocols . . . . .	75
4.6.5	Evaluation of Setup Performance . . . . .	75
	Modulator factor . . . . .	75
	TIA Gain . . . . .	76
<b>5</b>	<b>Results and Analysis</b>	<b>78</b>
5.1	Impact of Irradiation on QPD Performance . . . . .	78
5.1.1	Pre-Irradiation test results . . . . .	78
	Dark Current . . . . .	78
	Capacitance . . . . .	80
	Quantum Efficiency . . . . .	82
5.1.2	In-situ and post-irradiation test results . . . . .	82
	Dark Current versus irradiation conditions . . . . .	83
	Capacitance versus irradiation conditions . . . . .	85
	Quantum efficiency versus irradiation conditions . . . . .	89
5.1.3	Experimental damage factors applied to dark current . . . . .	91
5.1.4	NIEL Scaling Approach applied to dark current . . . . .	94
	Refined Electron NIEL Calculations . . . . .	96
	Impact of the electric fields on the damage factor . . . . .	97
5.1.5	NIEL Scaling Approach applied to the capacitance and quantum efficiency .	102
5.2	Impact of irradiated QPD on QPR performances . . . . .	103
5.2.1	Pre-irradiation test results . . . . .	103
	Input Equivalent Current Noise . . . . .	103
	Phase and Amplitude Output Signal . . . . .	105
5.2.2	In-situ and post-irradiation test results . . . . .	107
	Input Equivalent Current Noise versus irradiation conditions . . . . .	107
	Equivalent Input Current Noise versus model . . . . .	109
	Phase and Amplitude QPR response versus irradiation conditions . . . . .	110
<b>6</b>	<b>Conclusion</b>	<b>112</b>
<b>A</b>	<b>Experimental damage factor from literature</b>	<b>126</b>

# List of Figures

1.1	Artist’s impression of two merging black holes generating GWs (Courtesy of Caltech JPL). . . . .	1
1.2	Virgo site aerial view [12]. . . . .	2
1.3	NASA illustration of LISA [18]. . . . .	3
2.1	Illustration of a GW propagating in the z-axis with a ‘+’ polarization (left), and with a ‘x’ polarization (right) [19], [20]. . . . .	7
2.2	Diagram of Young’s double-slit experiment. . . . .	8
2.3	Schematic of the Michelson Interferometer. . . . .	9
2.4	Simplified diagram of the LIGO detector [20]. . . . .	10
2.5	LISA’s equilateral triangle configuration. . . . .	12
2.6	Test Mass (TM) to TM measurement principle within a Moving Optical Sub-Assembly (MOSA) (top) and their combination to form a LISA link (bottom) [25]. . . . .	15
2.7	Interaction between LISA the incoming (Receive (RX)) laser beam with the local (Local (LO)) laser beam. . . . .	17
2.8	Schematic diagram of LISA QPR system with (1) the QPD, (2) the FEE, and (3) the mechanical enclosure. . . . .	18
2.9	Light to electrical signal conversion in Photodiode (PD): energy diagram (bottom) and PN junction dynamics under a bias voltage. . . . .	19
2.10	Output current of the PN junction in function of the $V_{\text{bias}}$ applied. In blue correspond of the current with no incoming light ( $P_{\text{opt}} = 0$ ) and in red with $P_{\text{opt}} > 0$ and increasing. . . . .	20
2.11	Cross-sectional view of a PIN PD. . . . .	20
2.12	Ultra-fast InGaAs Dual-Depletion Region (DDR) PD structure [37]. . . . .	21
2.13	The basic InGaAs/InP heterojunction dual-depletion photodiode at zero bias [34]. . . . .	21
2.14	The basic dual-depletion diode under strong reverse bias voltage. Both the electrons and the holes have a barrier to overcome in order to reach the p+ and n+ electrodes [34]. . . . .	22
2.15	Equivalent circuit model of a PD. . . . .	23
3.1	Orbital configuration of the LISA mission [14]. . . . .	26
3.2	Prominence eruption on the Sun captured on June 20, 2013, at 11:15 p.m. EDT by National Aeronautics and Space Administration (NASA) [44]. . . . .	27
3.3	A vast mosaic image by NASA’s Hubble Space Telescope of the Crab Nebula, a six-light-year-wide supernova remnant [46]. . . . .	28
3.4	Illustration of Coulomb interactions between an electron and a charged particle in either atomic excitation (a) or ionization (b). . . . .	29
3.5	Schematic representation of the Coulombic (a), elastic (b), and inelastic(c) interaction between a charged particle and an atomic nucleus. . . . .	30
3.6	Illustration of Frenkel Pair Formation: showing the generation of an interstitial atom and a corresponding vacancy in the crystal lattice. . . . .	31
3.7	Schematic representation of defect and subcascade formation as a function of Primary Knock-on Atoms (PKA) energy [56]. . . . .	32

3.8	Conceptual illustration of the damage produced in Si by a 50-keV primary recoil atom with isolated defects and amorphous defect clusters shown [59]. . . . .	32
3.9	Initial distribution of vacancies produced by 10 MeV protons (left), 24 GeV protons (middle) and 1 MeV neutrons (right). The plots are projections over 1 $\mu\text{m}$ of depth ( $z$ ) and correspond to a fluence of $1 \times 10^{14} \text{ cm}^2$ [58]. . . . .	33
3.10	GEANT4 simulation results showcasing trajectories in Aluminum for a) a proton and b) a electron. . . . .	33
3.11	Stages of stable defect formation in irradiated materials: 1. Displacement cascades, 2. Thermal spike diffusion with amorphous pockets, and 3. Stable defect accumulation over time. . . . .	34
3.12	Experimental recombination yields for various incident particles as a function of the applied field [62]. . . . .	35
3.13	The five physical mechanisms created by crystal defects in the semi-conductor. . . .	36
3.14	Mean cumulative solar proton flux spectra for the nominal LISA mission duration [41].	41
3.15	NIEL curve from NEMO for InGaAs both proton and electron . . . . .	43
3.16	The Displacement Damage Equivalent Fluence (DDEF) of 10 MeV, 20 MeV, and 60 MeV proton fluence as a function of shielding thickness for (a) nominal and (b) extended mission durations. . . . .	43
4.1	Labeling scheme of JP and NL QPDs (the QPDs are facing the LASER beam). . . .	45
4.2	JP QPDs of 1.0, 1.5, and 2.0 mm diameter and labelled 1, 2, 3, 4, and 5 from left to right. . . . .	45
4.3	NL QPDs of 1.5 mm diameter labelled 1, 2, 3, and 4 from left to right. . . . .	46
4.4	Picture of LISA's FEE card provided by DE. . . . .	47
4.5	Side view of R&D irradiation room at CAL proton facility. . . . .	48
4.6	Left) CAL Proton beamline, including the QPD mounting. Right) Zoom on QPD mounting. . . . .	48
4.7	The accelerators and beam lines at ONERA (Mirage is highlighted with broken white line). . . . .	49
4.8	Picture of the QPD copper support in the void chamber. . . . .	50
4.9	Picture of the QPD copper support in the void chamber. . . . .	50
4.10	Images of the experimental setup for QPD dark current and capacitance measurements: (1) Metallic enclosure housing the QPD, (2) KEITHLEY measurement system, and (3) LTR-1200 temperature control unit. . . . .	52
4.11	Interior view of the QPD metallic enclosure: (1) Metallic enclosure, (2) Copper support for the QPDs, (3) Cathode output, and (4) Anode outputs. . . . .	53
4.12	Diagram of the experimental setup for QPD dark current measurement. . . . .	53
4.13	Four-point capacitance measurement configuration [106]. . . . .	54
4.14	Measured stray currents for each SMU channel under JP (a) and NL (b) QPD configurations, highlighting the setup's maximum stray current of 21 pA at 30V. . . .	55
4.15	Measured stray capacitance for each channel under JP (a) and NL (b) QPD configurations, highlighting the setup's maximum stray capacitance at 2.63 pF at 6V. . . .	55
4.16	Image of the QPD QE setup, featuring: (1) 1064 nm fiber laser source, (2) variable optical fiber attenuator, (3) 50%/50% beam splitter, (4) National Institute of Standards and Technology (NIST)-calibrated InGaAs PD, (5) USB power monitor, (6) optical fiber collimator, (7) metallic enclosure housing the QPD, (8) XYZ translation stages, and (9) Keithley 2635B SMU. . . . .	57
4.17	Diagram of the QPD QE set-up. . . . .	57
4.18	Electrical schematic of the QPD connection to the Keithley 2635B Source Measure Unit (SMU). . . . .	57
4.19	Diagram of the optical power ratio measurement. . . . .	58
4.20	Evolution of the beam ratio between OUT4 and OUT3 over one year. . . . .	59
4.21	Picture on the optical beam profile calibration set-up with (1) the collimator, (2) the Thorlabs BC106N-VIS/M Camera Beam Profiler, and (3) the XYZ translation table. . . .	59

4.22	Image of beam profile. . . . .	60
4.23	Illustration of the laser beam's relative alignment across the QPD's segments, using XYZ translation tables. . . . .	61
4.24	Picture of the QPR EICN measurement set-up: 1. QPR in a mechanical enclosure, 2. White light source, 3. LECROY Oscilloscope, 4. Thorlabs EF500 DC Block, 5. Preamplifier, and Rohde and Schwartz Spectrum Analyzer. . . . .	63
4.25	Electrical diagram of the QPR noise and TF experimental bench. . . . .	64
4.26	Noise voltage spectral density of the QPR as a function of frequency under dark and light conditions, including the noise voltage floor of the setup. . . . .	65
4.27	Comparative analysis of EICN data smoothing techniques for channel A of the QPR using JP 1001 QPD. Techniques include a) Moving Average, b) Exponential Smoothing, c) Polynomial Fit (Degree 3), and d) Locally Weighted Scatterplot Smoothing (LOESS). . . . .	66
4.28	Electrical diagram of the EICN setup with QPR replaced by a wave generator. . . . .	67
4.29	Estimation of the experimental setup gain in function of the frequency. . . . .	67
4.30	Precision estimation for QPD a)EICN measurement and b)TIA gain for all channels VA, VB,VC, and VD . . . . .	68
4.31	Diagram of the interferometric setup with red: LISA interferometric signal generation block, green: Signal monitoring and test module block, and blue: Control and acquisition block. . . . .	69
4.32	Picture of the interferometric setup. . . . .	69
4.33	Fiber Intensity Modulator (FIM) principle schematics. . . . .	70
4.34	Lock-In Detection Process: (a) Lock-in measurement setup with a sinusoidal reference signal stimulating the DUT, and its response analyzed for amplitude and phase. (b) Lock-in amplification process, where the input signal is mixed with the reference signal and its 90 deg phase-shifted version, followed by low-pass filtering to isolate the signal from noise, with results presented in polar coordinates [112]. . . . .	72
4.35	Modulation depth ( $\Phi_m$ ) function average modulated signal ( $\langle S^{\text{MOD}}(t) \rangle$ ). . . . .	74
4.36	Detailed schematic of the experimental setup for measuring beam intensity ratios across OUT1, OUT3, and OUT4 outputs. . . . .	74
4.37	Experimental modulation factors for target values a) $m = [0.0007177]$ , b) $m = [0.08644]$ , and c) $m = [0.2132]$ plotted against optical power measured by Thorlabs PD. . . . .	76
4.38	TIA gain results versus frequency, using a) 1.5 mm JP reference QPD, and b) 1.5 mm NL reference QPD, for both EICN and interferometric setups. . . . .	77
5.1	Dark Current versus bias voltage ( $V_{\text{bias}}$ ) for a) 1.0 mm JP QPDs, b) 1.5 mm JP QPDs, c) 2.0 mm JP QPDs, and d) 1.5 mm NL QPDs at 25 °C before irradiation. Data points show the average dark current over the four QPD segments, and the grey-shaded area shows the standard deviation. Error bars represent the measurement precision. . . . .	79
5.2	Dark Current versus temperature for a) 1.0 mm JP QPDs, b) 1.5 mm JP QPDs, c) 2.0 mm JP QPDs, and d) 1.5 mm NL QPDs at 5 V for JP QPDs and 20 V for NL QPDs. Data points show the average dark current over the four QPD segments, and the shaded area shows the standard deviation between segments. Error bars represent the measurement precision. . . . .	80
5.3	Capacitance versus bias voltage ( $V_{\text{bias}}$ ) for a) 1.0 mm JP QPDs, b) 1.5 mm JP QPDs, c) 2.0 mm JP QPDs, and d) 1.5 mm NL QPDs at 25 °C and 1 MHz. Data points show the average dark current over the four QPD segments, and the grey-shaded area shows the standard deviation between segments. Error bars represent the measurement precision. . . . .	81
5.4	QE for a) 1.0 mm JP QPDs, b) 1.5 mm JP QPDs, c) 2.0 mm JP QPDs, and d) 1.5 mm NL QPDs. Data points show the average dark current over the four QPD segments, and the grey-shaded area shows the standard deviation between segments. Error bars represent the measurement precision. Measurements were performed in a clean room at a temperature of approximately $25 \pm 1$ °C. . . . .	82

5.5	Dark current versus applied fluence for each irradiation step at 20 °C and 5 V for JP QPDs and 20 V for NL QPDs. The subfigures show (a) JP QPDs under 20 and 60 MeV protons, (b) NL QPDs under 20 and 60 MeV protons, (c) JP QPDs under 0.5 and 1.0 MeV electrons, and (d) 1.5 mm NL and JP QPDs under gamma-rays. Data points show the average dark current over the four QPD segments, and the grey-shaded area shows the standard deviation between segments. Error bars represent the measurement precision. . . . .	84
5.6	Capacitance versus applied fluence for each irradiation step under 20 and 60 MeV protons for a) 1.0 mm JP QPDs, b) 1.5 mm JP QPDs, c) 2.0 mm JP QPDs, and d) 1.5 mm NL QPDs at 25 °C and 5 V for JP QPDs and 20 V for NL QPDs. Data points show the average dark current over the four QPD segments, and the grey-shaded area shows the standard deviation between segments. Error bars represent the measurement precision. For clarity in the graph, the data point at $1 \times 10^9$ p/cm represents the pre-irradiation results and does not correspond to an actual irradiation step. . . . .	86
5.7	Capacitance versus applied fluence for each irradiation step under 0.5 and 1.0 MeV electrons for a) 1.0 mm JP QPDs, b) 1.5 mm JP QPDs, and c) 2.0 mm JP QPDs at 25 °C and 5 V. Data points show the average dark current over the four QPD segments, and the grey-shaded area shows the standard deviation between segments. Error bars represent the measurement precision. For clarity in the graph, the data point at $1 \times 10^9$ p/cm represents the pre-irradiation results and does not correspond to an actual irradiation step. . . . .	87
5.8	Capacitance versus applied fluence for each irradiation step under gamma-rays for a) 1.5 mm JP QPD and b) 1.5 mm NL QPD at 25 °C and 5 V for JP QPD and 20 V for NL QPD. Data points show the average dark current over the four QPD segments, and the grey-shaded area shows the standard deviation between segments. Error bars represent the measurement precision. . . . .	88
5.9	QE for a) JP and NL QPDs under 20 and 60 MeV, b) JP QPDs under 0.5 and 1.0 MeV electrons, and c) 1.5 mm JP and 1.5 mm NL QPD under gamma-rays performed at room temperature and 5 V for JP QPD and 20 V for NL QPD. Data points show the average dark current over the four QPD segments, and the grey-shaded area shows the standard deviation between segments. Error bars represent the measurement precision. . . . .	90
5.10	Dark current experimental damage factors applied fluence for each irradiation step for a) JP QPDs under 20 and 60 MeV proton, b) NL QPDs under 20 and 60 MeV protons, and c) JP QPDs under 0.5 and 1.0 MeV electron. Data points show the average dark current over the four QPD segments, and the grey-shaded area shows the standard deviation between segments. Error bars represent the measurement precision. . . . .	93
5.11	Relative comparison between the NIEL of InGaAs and the dark current experimental damage factors from a) JP and NL QPDs under 20 and 60 MeV protons and b) JP QPDs under 0.5 and 1.0 MeV electron. Data points show the average dark current over the four QPD segments. . . . .	95
5.12	Relative comparison between the NIEL of InGaAs and the dark current experimental damage factors from a) JP and NL QPDs under 20 and 60 MeV protons and b) JP QPDs under 0.5 and 1.0 MeV electron. The scaling factor is specific to each QPD type and size. Data points show the average dark current over the four QPD segments. . . . .	95
5.13	Relative comparison between new NIEL values for InGaAs and the dark current experimental damage factors from JP QPDs under 0.5 and 1.0 MeV electron. Data points show the average dark current over the four QPD segments. . . . .	96
5.14	Relative comparison between NIEL values based on uniform distribution of $E_d$ for InGaAs and the dark current experimental damage factors from JP QPDs under 0.5 and 1.0 MeV electron. Data points show the average dark current over the four QPD segments. . . . .	97

5.15	Experimental damage factor from dark current at last irradiation step for a) JP QPDs under protons, b) NL QPDs under protons, and c) JP QPDs under electrons at different $V_{\text{bias}}$ . Each point is the average damage factor across the four QPD segments at each irradiation step at 25 °C. . . . .	99
5.16	NIEL scaling approach for a) 1.0 mm JP QPDs, b) 1.5 mm JP QPDs, c) 2.0 mm JP QPDs, and d) 1.5 mm NL QPDs under protons at different $V_{\text{bias}}$ . Data points show the average damage factor over the four QPD segments. . . . .	100
5.17	NIEL scaling approach for a) 1.0 mm JP QPDs and b) 2.0 mm JP QPDs under electrons at different $V_{\text{bias}}$ . Data points show the average damage factor over the four QPD segments. . . . .	101
5.18	NIEL scaling approach applied to a) QE results for JP and NL QPDs, and b) Capacitance results from JP QPDs. Data points show the average damage factor over the four QPD segments. . . . .	103
5.19	EICN versus frequency for a) 1.0 mm JP QPDs, b) 1.5 mm JP QPDs, c) 2.0 mm JP QPDs, and d) 1.5 mm NL QPDs, before irradiation performed at rooms temperature with $V_{\text{bias}} = 5$ V for JP QPDs and $V_{\text{bias}} = 30$ V for NL QPDs. Data points represent the average noise across four channels, processed via LOESS smoothing (detailed in Section 4.5). The grey-shaded area shows the standard deviation between segments. . . . .	104
5.20	QPR output amplitude voltage at frequencies of $f = 3, 18,$ and $28$ MHz and $m = 0.2132$ versus the AC signal amplitude arriving on the a) 1.5 mm JP QPD n°2, and b) 1.5 mm NL QPD n°2. Measurement performed at room temperature with $V_{\text{bias}} = 5$ V for JP QPDs and $V_{\text{bias}} = 30$ V for NL QPDs. . . . .	105
5.21	QPR gain from plotter and sweeper results versus the frequency for a) 1.5 mm JP QPD n°2 and b) 1.5 mm NL QPD n°2. Measurement performed at room temperature with $V_{\text{bias}} = 5$ V for JP QPDs and $V_{\text{bias}} = 30$ V for NL QPDs. Data points show the average QPR gain over the four QPR channels, and the error bars area shows the standard deviation between channels. . . . .	106
5.22	QPR phase response from plotter and sweeper results versus the frequency for a) 1.5 mm JP QPD n°2 and b) 1.5 mm NL QPD n°2. Measurement performed at room temperature with $V_{\text{bias}} = 5$ V for JP QPDs and $V_{\text{bias}} = 30$ V for NL QPDs. Data points show the average QPR phase response over the four QPR channels, and the error bars area shows the standard deviation between channels. . . . .	107
5.23	EICN versus applied fluence for each irradiation step at $f = 3, 15,$ and $30$ MHz and $5$ V for JP QPDs and $20$ V for NL QPDs. The subfigures show (a) 1.0 mm JP QPDs, (b) 1.5 mm JP QPDs, (c) 2.0 mm JP QPDs, and (d) 1.5 mm NL under 20 and 60 MeV protons. Data points show the average EICN over the four QPR channels, and the grey-shaded area shows the standard deviation between channels. Error bars represent the measurement precision. . . . .	108
5.24	Experimental value and EICN model versus frequency for a) 1.5 mm JP QPD and b) 1.5 mm NL QPD, before and after irradiation performed at rooms temperature with $V_{\text{bias}} = 5$ V for JP QPDs and $V_{\text{bias}} = 30$ V for NL QPDs. Data points represent the average noise across four channels, processed via LOESS smoothing (detailed in Section 4.5). . . . .	110
5.25	Pre and post 20 MeV protons irradiation results of the QPR gain versus frequency for a) JP 1.5 mm QPDs n°2 and b) JP 2.0 mm QPDs n°2, regrouping data from sweeper and plotter tests. Data points represent the average noise across four channels while error bars denotes the Standard Deviation (sdv) across four the four channels. . . . .	110
5.26	Pre and post 20 MeV protons irradiation results of the QPR phase versus frequency for a) JP 1.5 mm QPDs n°2 and b) JP 2.0 mm QPDs n°2, regrouping data from sweeper and plotter tests. Data points represent the average noise across four channels while error bars denotes the sdv across four the four channels. . . . .	111

# Acronyms

**AEI** Albert Einstein Institute

**AU** Astronomical Units

**CAL** Centre Antoine Lacassagne

**CNES** Centre national d'études spatiales

**DDD** Displacement Damage Dose

**DDEF** Displacement Damage Equivalent Fluence

**DDR** Dual-Depletion Region

**DE** Allemagne

**DE** Germany

**EICN** Equivalent Input Current Noise

**ESA** Agence Spatiale Européenne

**ESA** European Space Agency

**FEE** Front End Electronics

**FIM** Fiber Intensity Modulator

**GRS** Gravitational Reference System

**GW** Ondes Gravitationnelle

**GW** Gravitational Wave

**IFO** Interferometer

**JP** Japon

**JP** Japan

**LEM** Laser Electrical Module

**LET** Linear Energy Transfer

**LIGO** Laser Interferometer Gravitational-Wave Observatory

**LISA** Laser Interferometer Space Antenna

**LO** Local

**LOESS** Locally Weighted Scatterplot Smoothing

**LOM** Laser Optical Module

**MFS** Main Frequency Stabilization

**MOSA** Moving Optical Sub-Assembly

**mse** Mean Squared Error

**NASA** National Aeronautics and Space Administration

**NIEL** Non-Ionising Energy Loss

**NIST** National Institute of Standards and Technology

**NL** Pays-Bas

**NL** Netherlands

**OB** Optical Bench

**OCA** Observatoire de la Côte d'Azur

**op amps** Operational Amplifier

**PCB** Printed Circuit Boards

**PD** Photodiode

**PKA** Primary Knock-on Atoms

**PMAD** Power Management and Distribution System

**PMS** Phase Measurement Subsystem

**PR** Photoreceivers

**PRN** Pseudo-Random Noise

**QE** Quantum Efficiency

**QPD** Photodiode à Quadrants

**QPD** Quadrant Photodiode

**QPR** Photorécepteurs à Quadrants

**QPR** Quadrant Photoreceiver

**Ref-IFO** Reference Interferometer

**RX** Receive

**SCI-IFO** Science Interferometer

**sdv** Standard Deviation

**SKA** Secondary Knock-on Atoms

**SMA** SubMiniature version A connectors

**SMU** Source Measure Unit

**TDE** Threshold Displacement Energy noted  $E_d$

**TDI** Time Delay Interferometry

**TEC** Thermoelectric Controller

**TIA** Amplificateur à Transimpédance

**TIA** Transimpedance Amplifier

**TID** Total Ionizing Dose

**TM** Test Mass

**TM-IFO** Test Mass Interferometer

**TX** Transmit

# Notation

- $E_a$  Activation Energy in (eV).
- $E_d$  Displacement Threshold Energy (eV).
- $G_{\text{TIA}}$  TIA Gain of the Quadrant Photoreceivers in ( $\Omega$ ).
- $I_{\text{Keithley}}$  Output current measured by the Keithley 2635B Source Measure Unit in (A).
- $I_{\text{dark}}$  Dark current generated by a single segment of the Quadrant Photodiode (A).
- $I_{\text{ph}}$  Photocurrent generated by a single segment of the QPD in response to incident optical power  $P_{\text{opt}}$  in (A).
- $K_{\text{Idark}}$  Experimental Dark Current Damage Factor unit in (pA/particles).
- $K_{\text{QE}}$  Experimental Quantum Efficiency (QE) Damage Factor in (%/particles).
- $K_{\text{dark}}$  Universal Dark Current Damage Factor.
- $N_{\text{defects, Irr}}$  Number of defects introduced during irradiation in (no unit).
- $P_{\text{AC}}(t)$  Discontinuous or AC component of the optical input signal arriving on each QPD segment (V).
- $P_{\text{DC}}$  Continuous or DC component of the optical input signal arriving on each QPD segment in (V).
- $P_{\text{opt, NIST IR}}$  Optical power measured by the NIST-calibrated Infrared (IR) NIST Photodiode (PD) in (W).
- $P_{\text{opt}}$  Incident optical power on one segment of the Quadrant Photodiode in (W).
- $R_{\text{out4,3}}$  Optical power ratio between outputs 4 and 3 in the Quantum Efficiency (QE) and Quadrant Photodiode Receiver (QPR) Phase and Amplitude measurement setup (unitless).
- $S^{\text{HET}}(t)$  Optical output signal of each LISA heterodyne interferometer arriving on the QPR in (W).
- $S^{\text{MOD}}(t)$  Output signal of the Fiber Intensity Modulator (FIM) in (V)
- $V(t)$  Modulation voltage (also called RF voltage) send by the Zurich to the Fiber Intensity Modulator (FIM) in (V).
- $V_{\pi}$  Half-wave voltage of the Fiber Intensity Modulator (FIM) in (V).
- $V_{\text{QPR}}$  Output voltage of the Quadrant Photoreceiver (V).
- $V_{\text{QPR}}$  Quadrant Photoreceiver output voltage (V).
- $V_{\text{R,mod}}$  Bias voltage (also called DC voltage) send by the Rigol wave generator to the Fiber Intensity Modulator (FIM) in (V).
- $V_{\text{bias}}$  Reverse bias voltage applied to the Quadrant Photodiode (V).

$V_{\mathbf{pk}, \mathbf{z}}$  is the modulation peak amplitude at the Zurich output in (V).

$W$  Depletion region thickness of a photodiode in (m).

$\Phi_m$  Modulator factor is the ratio between the AC part and DC part of the interferometric signal (no unit).

$i_{\mathbf{en}}(f)$  Equivalent Input Current Noise of the Quadrant Photoreceiver ( $\text{A}/\sqrt{\text{Hz}}$ ).

$i_{\mathbf{in}}$  Operational amplifier current noise ( $\text{A}/\sqrt{\text{Hz}}$ ).

$i_{\mathbf{jn}}$  Johnson noise ( $\text{A}/\sqrt{\text{Hz}}$ ).

$i_{\mathbf{sn}}$  Shot noise ( $\text{A}/\sqrt{\text{Hz}}$ ).

$i_{\mathbf{vn}}$  Operational amplifier voltage noise ( $\text{A}/\sqrt{\text{Hz}}$ ).

$k$  Material response to radiation damage in (number of defects/m).

$m$  Modulator factor is the ratio between the AC part and DC part of the interferometric signal (no unit).

$v_{\mathbf{dark}}(f)$  Quadrant Photoreceiver output density voltage in dark in ( $\text{A}/\sqrt{\text{Hz}}$ ).

$v_{\mathbf{floor}}(f)$  Density voltage noise of the setup in open circuit in ( $\text{A}/\sqrt{\text{Hz}}$ ).

$v_{\mathbf{light}}(f)$  Quadrant Photoreceiver output density voltage in light in ( $\text{A}/\sqrt{\text{Hz}}$ ).

# Chapter 1

## Introduction

### 1.1 Fascination with gravitational waves

In 1916, Albert Einstein predicted GW as ripples in spacetime emanating from the universe's most extreme events through his theory of General Relativity [1]. GWs are produced when massive objects, such as black holes or neutron stars, collide or merge (see Figure 1.1). Analogous to how accelerated electrical charges produce electromagnetic waves, the movement of these massive bodies distorts space and time and creates GWs. These waves propagate at the speed of light, carrying information about the events that generated them. Unlike electromagnetic waves, which can be blocked or absorbed by various materials, GWs pass through matter almost unblocked, offering a unique probe to explore cosmic events, such as black holes and neutron star mergers. GWs also allow us to improve our understanding of the universe from its early moments to the present. They enable precise cosmological measurements, contribute to multi-messenger astronomy [2]–[4], and test theories of fundamental physics, including General Relativity and the nature of dark matter [4].

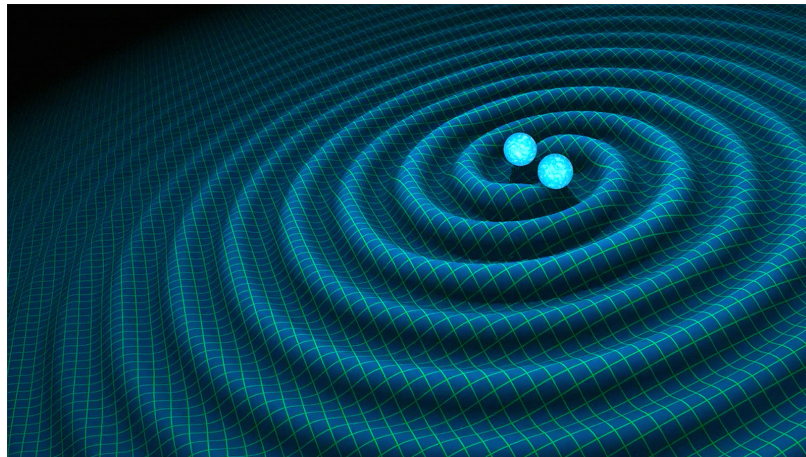


Figure 1.1: Artist's impression of two merging black holes generating GWs (Courtesy of Caltech JPL).

### 1.2 Evolution of gravitational wave detectors from Earth to space

Detecting GWs poses a significant challenge due to their extremely small amplitudes. The first detection attempts, based on Weber's 1966 suggestion, involved the resonance of a metal bar to detect

changes in its vibrational modes [5]. However, this method is limited in sensitivity and bandwidth, and conclusive detection using this technique remains elusive even to this day. Interest in developing GW detectors was reignited after Hulse and Taylor’s 1993 observation of orbital decay in a binary pulsar system, providing indirect evidence for GWs [6]. A significant advancement occurred with the suggestion to use a Michelson interferometer for detection which promised a broader frequency range, a solution validated by Gertsensshtein and Pustovoit in 1963 [7]. This approach led to the 1994 construction of the Laser Interferometer Gravitational-Wave Observatory (LIGO) in the United States, which includes two 4-kilometer-long Michelson interferometers in Washington and Louisiana. LIGO marked a historic achievement by detecting GWs for the first time on February 11, 2016, and once more on June 15, 2016 [8]. In 2003, Italy completed the Virgo detector enhancing the global network for GWs detection. On August 14, 2017, a joint effort between Virgo and the two LIGO detectors successfully captured GWs from the merger of stellar-mass black holes [9], [10]. Since this landmark event, many GW events have been and continue to be detected with Virgo and LIGO. Despite these achievements, the low-frequency GWs detection remains inaccessible due to noise from Earth’s gravitational gradient. To address this, the LISA project aims to detect GW from space, offering a solution to the limitations faced by Earth-bound detectors [11].



Figure 1.2: Virgo site aerial view [12].

### 1.3 LISA Mission: a new window into our universe

LISA is a large-scale mission led by ESA in collaboration with NASA and ESA member states, planned for launch in 2035. Following the highly successful LISA Pathfinder mission from 2015 to 2017 and the deployment of the Laser Ranging Instrument aboard the US/German Gravity Recovery and Climate Explorer Follow-on mission in 2018, the LISA mission was adopted at the beginning of 2024. As the first space-based GW detector, LISA will operate for a maximum mission duration of 12.5 years, detecting GWs in the low-frequency range of 0.1 mHz to 1 Hz, with a GW strain spectral density ranging from  $10^{-21}$  to  $10^{-23}$ . By employing high-precision laser interferometry, LISA will achieve unparalleled accuracy in GW detection, opening a new window into our universe [13]–[15].

Accessing a new frequency range, the LISA mission promises groundbreaking discoveries in cosmology and physics. Indeed, LISA aims to delve into the cosmos by studying the formation, evolution, and structure of the Milky Way and compact binary stars. It seeks to trace the merger histories of massive black holes, examine their properties and environments, and explore stellar-mass black holes and the fundamental aspects of gravity. Additionally, LISA will probe the universe’s expansion rate, investigate stochastic GWs backgrounds to understand the early universe, and search for bursts of GWs and unexpected sources [13]–[17].

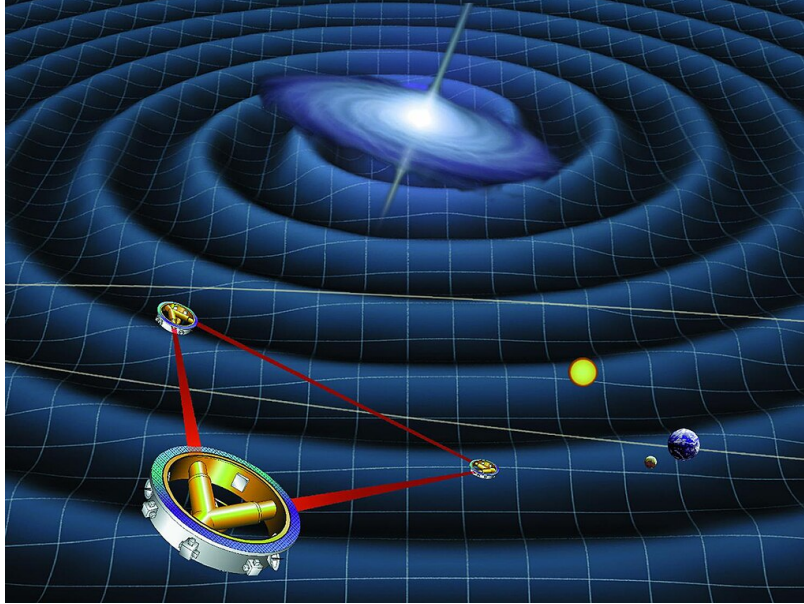


Figure 1.3: NASA illustration of LISA [18].

## 1.4 LISA detection principle

The mission shares similarities with the LIGO and Virgo detectors, which track distance variations between two suspended mirrors using laser interferometry. However, in LISA, these mirrors are substituted with free-falling masses known as 'test masses' and adopt a distinct interferometer from the Michelson type known as optical heterodyne interferometry. This method effectively manages Doppler-induced frequency shifts resulting from spacecraft velocity changes, a challenge unique to space-based detectors.

Based on this fundamental technique, LISA will consist of three spacecraft arranged in an equilateral triangle with 2.5 million km arms. While a single arm can detect GW in theory, two arms are essential for reducing frequency noise. The third arm allows for measuring the two polarization components of GW, allowing accurate determination of distances to sources. It also facilitates the creation of null streams for investigating unmodeled signals and improving the observatory's sensitivity. From an engineering standpoint, the three-arm architecture ensures operational resilience, allowing the observatory to maintain substantial scientific output even if one arm fails. Should a significant malfunction affect one arm, LISA's design allows for a reduction in sensitivity by roughly a factor of  $\sqrt{2}$  but the majority of its scientific functionality is preserved [15, p.72].

## 1.5 Radiation effects on LISA photoreceivers

An inter-satellite interferometer is a complex setup comprised of several subsystems. One of these subsystems is the read-out chain, responsible for detecting and processing optical signals. In LISA, the initial element of this chain is the QPR, charged with converting the interferometric signal into an electrical one and sending it to the rest of the read-out chain. These devices are composed of two elements. The first element is an InGaAs QPD, a semiconductor that transforms photons into electrons, generating a current referred to as the photocurrent. The QPD is segmented into four segments to facilitate its precise spatial alignment on LISA's laser beam and tilt correction. Each QPD is connected to a low-noise, DC-coupled TIA or FEE, all encased within a mechanical housing.

LISA orbits in an Earth-like heliocentric trajectory at 1 Astronomical Units (AU) from the Sun, located at an angle of  $20^\circ$  behind the Earth, exposing LISA to various types of radiation, predominantly from the Sun, such as solar flares and solar wind. Energetic particles from these sources can

penetrate the spacecraft walls and interact with matter through the atomic electron cloud or nuclei. The former interaction can ionize atoms, creating electron-hole pairs and resulting in a cumulative effect known as Total Ionizing Dose (TID), measured by Linear Energy Transfer (LET). The latter interaction can eject nuclei, causing vacancies and interstitials in the semiconductor lattice, a process known as atomic displacement damage. This process is quantified by the NIEL and Displacement Damage Dose (DDD). The crystal defects resulting from ionizing or displacement damage introduce parasitic levels in the semiconductor bandgap, leading to electron-hole pair generation, recombination, carrier trapping, dopant compensation, and tunnelling effects. These phenomena impact the semiconductor properties and, by extension, the QPD electro-optical characteristics, such as the dark current.

In the context of LISA, given the extremely weak nature of GW signals to be detected, even minor degradations in the electro-optical characteristics of the QPDs, driven by environmental radiation exposure, can significantly impair system performance. Thus, understanding the impact of space radiation on such detectors is essential for predicting its specific effects on the performance of the LISA instrument.

## 1.6 Research goals and thesis structure

In this context, this thesis is structured around two primary goals:

1. **Evaluate the impact of LISA space radiation environment on its InGaAs QPDs.** This goal is divided into two sub-objectives. The first is to evaluate and predict the space environment’s impact on the LISA QPDs performance concerning dark current, capacitance, and QE. This evaluation is crucial to ensure that the QPDs not only withstand the harsh conditions of space but also consistently meet the strict LISA requirements throughout its entire mission duration. The second sub-objective aims to enhance our understanding of the irradiation damage mechanisms affecting InGaAs QPDs and to correlate these mechanisms with the observed degradation of QPDs performance. In our case, the specific devices and operating mode result in degradation primarily due to displacement damage. Therefore, the research focuses specifically on displacement damage and less on ionizing damage. Given that these new InGaAs QPDs have not been previously irradiated, this research will also contribute to expanding the knowledge on InGaAs detectors.
2. **Evaluate the impact of the irradiated QPD on LISA’s QPR performance and measurements.** This second goal takes a more global view, examining irradiation effects at the system level. This goal is also divided into two sub-objectives. The first sub-objective focuses on assessing how irradiated QPDs influence the QPR’s performance, principally regarding the EICN. Similar to the first goal, this includes verifying that the QPR continues to meet LISA’s noise requirements throughout the mission’s duration. The second sub-objective shifts focus towards evaluating how these irradiation-induced changes in the QPDs, impact LISA’s detection capabilities by measuring the phase and amplitude response of the QPR within a LISA like system.

The manuscript is organized into six main chapters as follows:

- **Chapter 1 - Introduction** corresponding to this chapter outlines the thesis’s context, goals, and structure.
- **Chapter 2 - Theoretical and technical background on GWs detectors** delves into the physics of GWs and the fundamental principles of optical interferometry, the primary physical method used for the detection of GWs. This chapter also discusses ground-based GW detectors, focusing on LIGO, then shifts to space-based detectors, with LISA, outlining its detection principles and onboard instruments. The final section delves into photodetection and detectors, detailing the operational principles and key characteristics of the QPR, with a focused discussion on its two critical components: the QPD and the FEE.

- **Chapter 3 - The LISA space radiation environment** develops into LISA’s orbit and the demanding space conditions it faces. This chapter reminds the interactions between radiation and matter and the implications of these interactions on the integrity and performance of the QPD. Special attention is given to displacement damage effects, which cause permanent degradation on the QPD, and looks into different models notably using the NIEL scaling approach. Lastly, the chapter outlines the radiation resilience requirements for LISA.
- **Chapter 4 - Experimental Setup** describes the experimental setups designed for the characterization of LISA QPDs, including assessments of dark current, capacitance, and QE. It also details the procedures for QPR characterization, featuring one setup for measuring the EICN and another for evaluating the QPR’s phase and amplitude response to LISA-like interferometric signals. Additionally, the text presents the three irradiation campaigns (protons, electrons and gamma-ray) conditions and protocols.
- **Chapter 5 - Results and Analysis** This chapter fulfils the thesis’s primary objectives by analyzing the experimental results from the setups described in Chapter 4. It is organized into two main sections, each dedicated to one of the thesis goals. The first section focuses on the resilience of two new InGaAs QPDs to the space radiation conditions anticipated for the LISA mission. It offers a comparative analysis of the QPDs’s performance before and after irradiation, discussing their durability against radiation and contributing to the broader knowledge base of InGaAs QPDs. The analysis integrates existing literature, evaluates discrepancies using damage factors and NIEL scaling, and delves into the impact of intrinsic QPD characteristics like doping levels and bias voltage on radiation resistance. The second section addresses how irradiated QPDs influence the performance and measurements of LISA’s QPR. This part of the chapter presents a detailed comparison of QPR functionality before and after irradiation, highlighting the system’s robustness and the observed impacts of radiation. It further correlates the degradation observed in QPR performance with the fundamental electro-optic characteristics degradation in the QPD
- **Chapter 6 - Conclusion** effectively summarizes and synthesizes the five chapters of the thesis, with a special emphasis on the experimental achievements highlighted in Chapter 4 and the core results and analyses detailed in Chapter 6. This chapter outlines the conclusions related to the two thesis’s primary objectives, addresses the research limitations encountered, and identifies emerging questions. Finally, it proposes directions for future research.

## Chapter 2

# Theoretical and technical background on GWs detectors

### 2.1 Detection of Gravitational Waves

#### 2.1.1 Introduction to Gravitational Waves

As mentioned in the introduction, GWs are the result of cataclysmic cosmic events. Analogous to how accelerating charges emit electromagnetic waves, the acceleration of masses generates GWs, travelling at the speed of light ( $c$ ). By employing the weak field approximation and considering the lowest order, the propagation of GWs is governed by the wave equation noted Equation 2.1 [19], [20].

$$\nabla^2 h_{\mu\nu} = \frac{\partial^2 h_{\mu\nu}}{c^2 \partial t^2}. \quad (2.1)$$

$h_{\mu\nu}$  represents the GWs's spatial and temporal dependence.  $\nabla^2$  is the Laplacian operator and represents a second-order differential operator that measures the rate of change of a quantity with respect to its spatial variation around a specific point. The solution to this equation is a transverse plane wave given by Equation 2.2, which links the infinitesimal interval between two events in spacetime ( $ds^2$ ) to  $g_{ij}$ , where  $g_{ij}$  is a metric tensor that allows the conversion of coordinates  $dx^i$  and  $dx^j$  into "true" coordinates represented in 4 dimensions (spatial and temporal).

$$ds^2 = g_{ij} dx^i dx^j. \quad (2.2)$$

The metric tensor  $g_{ij}$  is divided into two parts, as shown by Equation 2.3. The first part is the Minkowski tensor  $\eta_{ij}$ , plus a second tensor  $h_{ij}$  corresponding to the deformation of space and time induced by the GW.

$$g_{ij} = \eta_{ij} + h_{ij}. \quad (2.3)$$

Considering a GW propagating along the z-axis, the GW tensor, as shown by Equation 2.4,  $h_{ij}$  predominantly exhibits non-zero components in directions perpendicular to its motion.

$$h_{ij} = \begin{pmatrix} 0 & 0 & 0 & 0 \\ 0 & h_{xx} & h_{xy} & 0 \\ 0 & h_{yx} & h_{yy} & 0 \\ 0 & 0 & 0 & 0 \end{pmatrix}. \quad (2.4)$$

From  $h_{ij}$ , a first fundamental characteristic of GWs can be derived: their polarization. According to General Relativity, GWs cannot exhibit monopolar or dipolar radiation, unlike sound or electromagnetic waves. Instead, they are quadrupolar, and hence have two independent polarizations: [20]:

- The '+' polarization, defined when  $h_{xx} = -h_{yy}$ , illustrates spacetime compression and dilation along the  $x$  and  $y$  axes, as shown on the left side of Figure 2.1.
- The 'x' polarization, indicated when  $h_{xy} = h_{yx}$ , acts similarly to the '+' polarization except that it squeezes and stretches along a set of axes that are rotated with respect to the  $x$  and  $y$  axes by 45 deg, as shown on the right side of Figure 2.1.

Figure 2.1 visualizes these polarizations, highlighting how GWs can cause spacetime to stretch and compress. Consequently, if two objects are separated by a distance  $L$ , the passage of a GW will induce a change in their separation distance ( $\Delta L$ ), proportional to the wave's amplitude ( $h$ ).

$$\frac{\Delta L}{L} = \frac{h}{2}. \quad (2.5)$$

The term  $h$  denotes the time-varying deformation, commonly referred to as the 'strain,' a fundamental characteristic of GWs. This quantity is measurable and is used to detect GWs. Unfortunately, strains from GWs are extremely tiny, posing significant challenges for detection. For example, the strain from GW150914, arising from the merger of two black holes with masses around 36 and 29 solar masses and located approximately 1.3 billion light-years away, had a strain of roughly  $10^{-21}$  [21]. For instance, if two points are separated by a distance of 1000 km, detecting a GW would require measuring a change in separation of approximately  $10^{-15}$  meters between those two points, which is on the order of the size of an atom. Such precise measurements are achieved using optical interferometry, detailed in the following section.

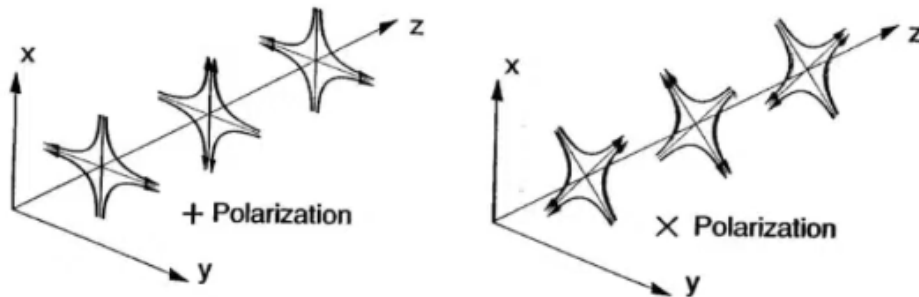


Figure 2.1: Illustration of a GW propagating in the  $z$ -axis with a '+' polarization (left), and with a 'x' polarization (right) [19], [20].

### 2.1.2 Introduction to interferometry

Light behaves as an electromagnetic wave, allowing different rays to interact or interfere with one another. Interference can occur between multiple beams. For interference to occur, the two beams must be coherent. If the beams are not coherent, the resulting interference pattern will fluctuate at rates significantly greater than  $1 \times 10^8$  Hz, making it impossible to observe with standard techniques. Two beams are considered coherent if they meet the following conditions:

- Temporal coherence: refers to the correlation between the value of a wave and itself delayed by a time  $\tau$  at a single point in space. A light source with high temporal coherence is highly monochromatic.
- Spatial coherence: refers to the uniformity or correlation of the phase of a light wave across different points in a wavefront at a given instant. A light source with high spatial coherence has wavefronts where the phase of the wave is consistent across different points in space.

An easy way to ensure these conditions is to generate the two beams from a single source. There are two fundamental methods for generating such beams:

- Division of wavefront: this method is used in Young’s double-slit experiment illustrated in Figure 2.2.
- Division of amplitude: this method is used in the Michelson interferometer illustrated in Figure 2.3.

### Young’s double-slit experiment

The results of interference using light can be seen using Young’s double-slit experiment [22]. Conducted by Thomas Young in 1801, this experiment is a pivotal demonstration of the wave-like behaviour of light, laying the foundation for the wave theory of light. Represented in Figure 2.2, Young’s setup involved a light source that emitted light towards a screen behind two closely spaced slits. As the light passed through these slits, it was observed to produce a pattern on the screen of bright and dark fringes refers as constructive and destructive interference.

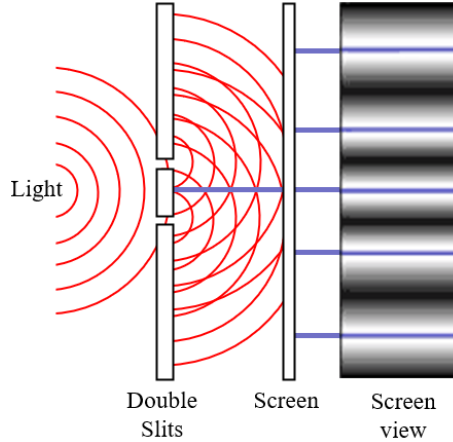


Figure 2.2: Diagram of Young’s double-slit experiment.

### Michelson Interferometer

The Michelson interferometer, developed by Albert A. Michelson in 1887, is a common and fundamental interferometer. As illustrated in Figure 2.3, the device splits a laser beam into two paths using a beam splitter. One path directs the beam towards a measurement mirror and the other towards a reference mirror. Upon reflection, the beams recombine at the beam splitter, generating an interference pattern captured by an optical detector such as a PD.

For simplicity, let’s consider that the two beams interacting at our detector are two perfectly monochromatic laser beams. Such beams are often described by a simple harmonic wave function with a sinusoidal electric field  $E_i(z, t)$ . The two beams are propagated along the Michelson light path and note  $z$  the position along this path. Based on these hypotheses,  $E_i(z, t)$  can be written as:

$$E_i(z, t) = E_i \cos(\omega t + kz + \phi_i). \quad (2.6)$$

$k = \frac{2\pi}{\lambda}$  is the wave number of the light with  $\lambda$  being the wavelength of the light in vacuum.  $\omega = 2\pi f$  is the angular frequency of the beam, with  $f$  being its frequency.  $\phi_i$  is the initial phase of the beam. Finally,  $t$  is the time variable.

At the point of interference, the interference results in the combination of their electric fields  $E_T(z, t) = E_1(z, t) + E_2(z, t)$ . The detector measures the intensity of the resulting total electric field

$E_T(z, t)$ . The intensity  $I_i$  is defined as the square of the total electric field, therefore the resulting intensity  $I_T$  of the total signal measured by the detector is:

$$I_T = \epsilon_0 c \langle E_T(z, t)^2 \rangle = \epsilon_0 c \langle (E_1(z, t) + E_2(z, t))^2 \rangle. \quad (2.7)$$

Where  $\epsilon_0$  is the vacuum permittivity. Expanding and simplifying Equation 2.7 allows us to express the total intensity  $I_T$  as [23, p.64]:

$$I_T = I_1 + I_2 + 2\sqrt{I_1 I_2} \cos(\delta). \quad (2.8)$$

$I_1$  and  $I_2$  represent the respective intensities of each of the beams.  $\delta$  is the phase difference defined by:

$$\delta = 2\omega t + k(z_2 - z_1) + (\phi_2 - \phi_1). \quad (2.9)$$

Hence, Equation 2.8 reveals that the total intensity consists of a constant (DC) component  $I_1 + I_2$  and a variable (AC) component dependent on  $\delta$ . In  $\delta$ , the term  $\omega t$  is not seen by the detector since light oscillates in the hundreds and even thousands of terahertz. Since the beams originate from the same source and no elements in the setup induce a phase difference, it is assumed that  $\phi_2 - \phi_1 = 0$ . Consequently,  $\delta \propto z_2 - z_1$  which represent the path length difference ( $\Delta L$  in Figure 2.3) and therefore is expressed as:

$$\delta = \frac{2\pi}{\lambda} \cdot (2\Delta L). \quad (2.10)$$

The factor of two accounts for the round-trip travel of the laser beam.

In summary, the movement of the measurement mirror alters  $\delta$ , significantly influencing the interference pattern. Specifically, transitioning from a minimum to a maximum in the interference pattern corresponds to a path length change of  $\Delta L = \lambda/4$ . For example, using laser beams operating at 1064 nm allows for the detection of distance variations smaller than 266 nm. Such precise sensitivity to path length adjustments is the fundamental principle behind applications such as high-resolution microscopy, seismic wave detection, atmospheric research, and spectrometry.

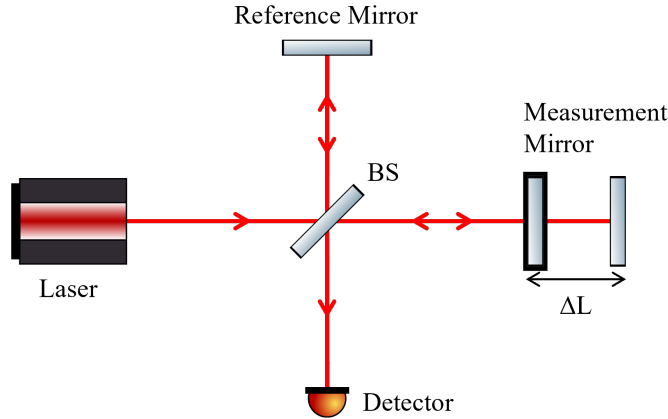


Figure 2.3: Schematic of the Michelson Interferometer.

## 2.1.3 Gravitational Waves detectors

### Ground based detectors

The Michelson interferometer's ability to detect minute distance variations is particularly suited for GWs detection. This capability is utilized in the U.S. by the LIGO GW detectors, located in Hanford, Washington, and Livingston, Louisiana, as well as in Europe by the Virgo GW detector in Pisa, Italy. Figure 2.4 presents a simplified diagram of LIGO, which employs fixed mirrors, in

contrast to the Michelson design shown in Figure 2.3. For simplicity, the arms of the interferometer, each of length  $L$  are perfectly aligned with the  $x$  and  $y$  axes and the GW detected has a '+' polarized, therefore aligned with the detector arms. This alignment results in differential length changes, represented as  $\Delta L = \delta L_x - \delta L_y$ , where one arm lengthens while the other shortens. Using Equation 2.5, this effect is quantified by:

$$\frac{\delta L_x}{L} = \frac{h_+}{2}, \quad \frac{\delta L_y}{L} = -\frac{h_+}{2}, \quad (2.11)$$

In reality, GWs are not perfectly aligned with the detector's arms. The actual change in path length ( $\Delta L$ ) depends on the GW's polarization and angle of incidence relative to the interferometer. Since GWs can have two polarization states, the detected signal, a combination of these states, is weighted by their alignment with the detector's arms. This result implies a directional sensitivity for the detector.

As previously mentioned, the strains of GW are extremely subtle ( $h \leq 1 \times 10^{-21}$ ). Hence, to detect them, the Michelson interferometers need exceptionally long arms. Notably, TAMA300, GEO600 [24], Virgo [10], and LIGO detectors [8] have arm's length of respectively 300, 600, 3000, and 4000 m which are by far the largest Michelson ever built. However, even these substantial lengths are insufficient and a Fabry Perot cavity is employed to oscillate the light back and forth, effectively magnifying the arm's length. In LIGO's case, this technique extends the effective arm length by a factor of 300, equivalent to a linear arm length of 1200 km.

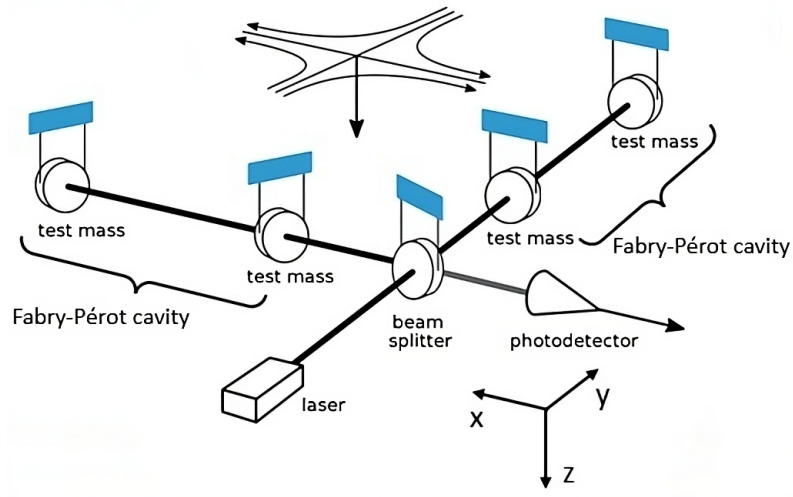


Figure 2.4: Simplified diagram of the LIGO detector [20].

### Space-based detectors

However, as outlined in the introduction (Section 1.2), ground-based detectors encounter constraints from Earth's gravitational barrier, also referred to as the 'seismic wall,' which limits the detection of GWs under 10 Hz [11]. The LISA mission is designed to overcome this limitation by operating in space, thereby accessing an unprecedented frequency range from 0.1 mHz to 1 Hz. Nevertheless, the transition to space poses some challenges such as:

- **Long arm length:** space-based detectors allows for substantial arm lengths, with LISA planning for arms extending up to  $2.5 \times 10^6$  km. However, this vast distance means the laser signal becomes extremely faint when it reaches another end's arm and significantly diverges despite precise optics aiming to minimize this effect. Hence, using mirrors to reflect light across millions of kilometres for a traditional optical path (division, reflection, and recombination) is impractical. Instead, LISA uses passive reflection (similar to transponders) where each LISA

spacecraft receives laser signals and generates a new laser signal based on the received signal to send back. The end arm mirrors of the Michelson are substituted with free-falling test mass 'mirrors' housed within each spacecraft.

- **Doppler shift:** the relative motion between spacecraft ( $v_d$ ) leads to frequency variations ( $f_D$ ) in the received light equals to [25]:

$$\Delta f_D = \frac{v_d}{c} f_0. \quad (2.12)$$

$f_0$  is the original frequency.  $c$  is the speed of light. To address this frequency shift, measurements utilize polarized, heterodyne detection techniques.

- **Radiation damage:** the radiation from the spacial environment can create defects in semi-conductors, adversely affecting detector performance. This issue is further explored in the subsequent chapter 3.

## 2.2 LISA mission

### 2.2.1 Spacecraft Constellation

Figure 2.5 is a simplified diagram of the LISA constellation, composed of three spacecraft, referred to as sciencecraft, arranged in an equilateral triangle with sides of 2.5 million km, referred to as an 'arm'. Each arm consists of bidirectional laser links between two spacecraft, equivalent to an arm of a Michelson interferometer. Unlike traditional Michelson interferometer, the endpoints of each link are two free-falling TMs instead of mirrors [26], [27].

In principle, a single arm is sufficient to detect GWs as the setup would be able to detect the variations in distance caused by GWs passing. However, this setup cannot adequately suppress frequency noise via common-mode rejection and requires two clocks with sufficient stability. Additionally, it cannot detect both GW polarizations [15]. Adopting a two-arm configuration, akin to an equal-arm Michelson interferometer with a 60 deg angle, enables common-mode noise rejection and the detection of both GW polarizations, enhancing sensitivity and allowing source direction detection. Expanding to a three-arm configuration further broadens the mission's capabilities. This configuration not only retains the benefits of the two-arm setup but also improves sky coverage, resolution, and most important, mission robustness against the failure of a single arm. Although adding more than three arms could improve performance, it would also increase cost and complexity unnecessarily [25]–[27]. A three-dimensional, linearly independent configuration of arms at 90 deg (or other angles) is avoided due to the requirement for at least four spacecraft, which would unnecessarily elevate costs and complexity [27].

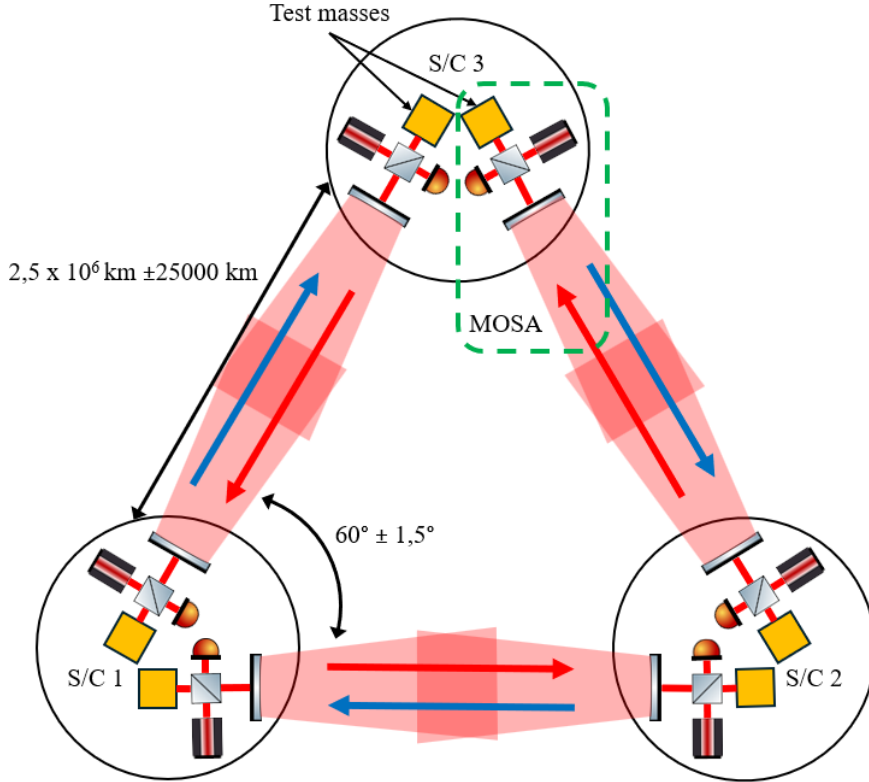


Figure 2.5: LISA’s equilateral triangle configuration.

## 2.2.2 Instrument description

Each spacecraft houses the advanced instruments essential for GWs observation, along with the necessary support systems. For example, each spacecraft hosts solar panels, batteries, and the Power Management and Distribution System (PMAD) to supply, store, and control the electrical power necessary for the optimal functioning of all subsystems. Part of the power management strategy includes managing the spacecraft’s thermal environment. Furthermore, each spacecraft has data storage, processing, and communication systems. Given the vast distances between the spacecraft and the limited communication windows, data is typically stored in onboard memory before being transmitted in batches during communication sessions with ground stations. Each spacecraft hosts also a high-gain antenna, optimized for long-distance communication with Earth [15], [25], [26].

The following subsections focus on the subsystems necessary for the interferometric measurements, including the MOSA, laser modules, and the phase measurement system [15], [25], [26].

### Drag-Free Attitude Control System (MOSA)

Each spacecraft contains two MOSA (Figure 2.5), each acting as an interferometric transponder at the end of each arm, simultaneously transmitting a high-power laser beam, refer as Transmit (TX) beam, toward the distant MOSA while receiving a small portion of the beam transmitted from that MOSA, refer as RX beam. Each MOSA contains three elements that support the optical measurement [15], [25]:

- **The telescope:** serves dual functions. It operates as a focal beam expander and facilitates both transmission and reception. In transmission mode, the telescope converts a collimated beam from the Optical Bench (OB), initially around 5 mm in diameter, into a larger collimated beam of approximately 400 mm in diameter. Conversely, in reception mode, it narrows the

light collected from the central beam portion of the distant spacecraft back to a size suitable for the OB. Different light polarizations allow the distinct separation of transmitted and received beams on the bench.

- **Optical Bench (OB)** houses all critical optical components, such as lenses, waveplates, and beamsplitters, enabling the operation of three distinct laser beam interferometers [15], [25]. The Inter-Satellite interferometer, known as the long-arm or Science Interferometer (SCI-IFO), measures the relative motion between the OB on one spacecraft and a corresponding OB on a distant spacecraft using the RX beam from the far spacecraft and a LO beam. This interferometer carries the GW information. The Test Mass Interferometer (TM-IFO) is used to monitor the relative motion of the local free-falling TM relative to the local OB using the LO beam with the TX beam after bouncing on the TM. Finally, the Reference Interferometer (Ref-IFO) is essential in measuring and mitigating common-mode noise from the local lasers and associated system elements. The output optical signals from this interferometer are detected and processed by electro-optical components known as Photoreceivers (PR), located on the OB. A Photoreceiver (PR) converts the optical signal from its corresponding interferometer into an electrical signal. The signal is then amplified before being sent to the phase measurement system. As illustrated in Figure 2.7, each optical signal is detected simultaneously by two nominal PRs using a method called balanced detection, which significantly reduces the impact of relative intensity noise on the signal’s phase noise. Each Interferometer (IFO) is equipped with two additional redundant PRs, intended for use if the nominal PRs becomes non-functional, thus ensuring continuous optical signal detection. Further details on the principles and characteristics of LISA’s PRs are discussed in Section 2.3.
- **Gravitational Reference System (GRS)** houses the TMs that function as the end mirrors of each arm. Its primary objective is to shield the free-falling TMs from external influences by maintaining a near-perfect vacuum and an electrostatically neutral setting. The GRS effectively isolates the TMs from all external disturbances, ranging from solar radiation pressure and solar wind particles to micro-meteoroids. It aims to establish the most ‘silent’ region within the solar system, creating an internal cavity devoid of electrical, magnetic, and thermal forces to the greatest extent possible. This isolation is critical, ensuring that the TMs remain in pure free-fall and are influenced solely by gravitational forces.

### Phase Measurement System

According to Equation 2.8, distance variation translates into phase variation. Thus, the GW information comes as phase fluctuations of the weak beam from the distant spacecraft. These fluctuations are converted by the PR on the OB, into phase fluctuations of the beatnote photocurrent, ranging from 6–25 MHz due to Doppler shifts and the laser RIN spectrum.

The Phase Measurement Subsystem (PMS) role is to read and analyze these phase fluctuations from the PR. Each PR channel requires a corresponding phasemeter channel to measure fringe arrival rate variations. The phasemeter also extracts ranging, clock, and telemetry information from laser sidebands and performs high-fidelity measurements of the relative angular and longitudinal motions of the spacecraft and free-falling TMs, as well as the reference laser.

Additionally, the phasemeter records auxiliary beatnotes with high fidelity and manages inter-spacecraft absolute ranging and data transfer. It tracks delays in Pseudo-Random Noise (PRN) code sidebands for precise pseudorange measurements for calculating arm length and synchronizing clocks. It decodes and encodes PRN signals for inter-spacecraft communication, supports heterodyne interferometry for precise constellation alignment, processes data through integration, reduction, and filtering across different transmission rates, and generates control signals for laser-locking to maintain a coherent and synchronized heterodyne frequency strategy across the spacecraft constellation [15], [25], [26].

## Lasers System

LISA employs three bi-directional laser links between spacecraft within the constellation. Each spacecraft's laser system delivers highly phase-coherent, tunable, and intensity-stable laser light to the onboard OB, along with high phase modulation capabilities. Each laser system comprises two laser heads for redundancy with only one active. Each head consists of two separate units [15]:

- The Laser Optical Module (LOM) includes optics and electro-optical elements for generating and modulating the laser light. Additionally, it controls amplitude fluctuations to prevent interference with the measurements. The LOM features several key components: a main oscillator laser source, or 'seed,' based on a Nd: YAG non-planar ring oscillator, providing a laser beam at 1064 nm with an output of up to 2 W; a power amplifier, and a phase modulator. The phase modulator is for imprinting sidebands onto the laser light and stabilizing the laser frequency using the Pound-Drever-Hall locking technique.
- The Laser Electrical Module (LEM) contains all the electronics necessary to drive the laser head, and interfaces with the spacecraft for electrical power, command, data handling, and instrument control functions. It includes controls for laser frequency, optical power, and phase modulation control.

Each laser system in the LISA constellation can operate in two distinct modes: controller mode and transponder mode. In controller mode, the laser frequency is locked to a local stable frequency reference, typically an optical cavity. Conversely, in transponder mode, the laser frequency is offset phase-locked (with a tuneable frequency offset) to another optical signal through an interference generated on the OB [15]. This mode incorporates a tuneable frequency offset that allows for the individual adjustment of transponder laser frequencies, thus maintaining all beat notes within the interferometric detection bandwidth and accommodating constantly changing Doppler shifts.

The lock-on mechanism is achieved by a Main Frequency Stabilization (MFS). There is only one MFS per laser system to which one of the three laser systems aboard each spacecraft can be locked. The redundancy of the MFS is managed at the constellation level, ensuring double cold redundancy with only one active MFS needed at any time [15].

Lastly, residual laser frequency noise is eliminated by the Time Delay Interferometry (TDI) method. TDI creates a 'virtual' equal-arm interferometer via on-ground post-processing, leveraging time-shifted measurements from spacecraft links to filter out the noise and preserve the GW signal. This technique depends on accurate arm length measurements and controlled clock noise [28].

### 2.2.3 Measurement Principle

Briefly introduced in Section 2.2.2, LISA employs three high-precision interferometers: the Reference Interferometer (Ref-IFO), the Test Mass Interferometer (TM-IFO), and the Science Interferometer (SCI-IFO). This trio enable precisely measuring distance variations between two TMs at the ends of each spacecraft arm, utilizing heterodyne interferometry to manage frequency Doppler shifts. Figure 2.6 shows a detailed configuration of each of the three interferometers with:

- The SCI-IFO: an interaction between the TX beam from the laser system and the RX from the far spacecraft.
- The TM-IFO: an interaction between the LO oscillator beam and the TX beam after a go and back from the TM.
- The Ref-IFO is an interaction between the TX beam and the LO oscillator beam.

Here, the TX beam is the laser beam produced by the local laser head, and the LO oscillator is derived from light delivered through the backlink fibre from the optical bench on the other adjacent MOSA. Note that this configuration is independent of the spacecraft. To measure the distance between two TMs, the measurement process is divided into three stages depicted in Figure 2.6 and detailed below:

- Stage 1: From the TM in spacecraft 2 to the OB in the same spacecraft, using the TM-IFO.
- Stage 2: From the OB in spacecraft 2 to the OB in spacecraft 3 through telescopes, using the SCI-IFO.
- Stage 3: From the OB in spacecraft 3 to the TM in the same spacecraft, using the TM-IFO.

In essence, the third interferometer (Ref-IFO) is not about tracking external changes such as those induced by GWs but rather about ensuring the internal integrity and stability of the spacecraft’s measurement systems. It effectively uses the LO as a baseline to detect and adjust for internal variabilities or noise in the TX path, ensuring that other critical measurements taken by the spacecraft’s interferometers are accurate and reliable.

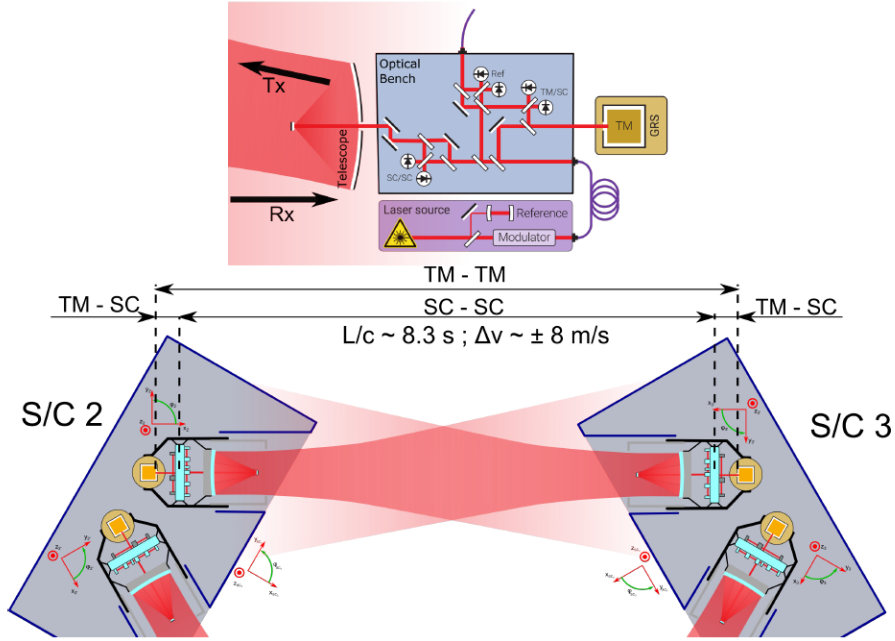


Figure 2.6: TM to TM measurement principle within a MOSA (top) and their combination to form a LISA link (bottom) [25].

### Optical Signals

This section aims to model each interferometric signal arriving at the PR, utilizing similar methodology detailed in previous works, which explains the equations governing the interference of two laser beams with differing optical powers. In the case of LISA, the minimum, average, and maximum optical power for each beam within each IFOs: Ref-IFO, TM-IFO, and SCI-IFO are resumed in Table 2.1.

Table 2.1: LISA Optical Power Ranges: Minimum, Average, and Maximum for each interfering beam in each IFO: Ref-IFO, the TM-IFO, and the SCI-IFO

	Minimum (W)	Mean (W)	Maximum (W)
$P_{RX}$ SCI	$3.020 \times 10^{-10}$	$7.069 \times 10^{-10}$	$1.112 \times 10^{-9}$
$P_{LO}$ TM	$7.810 \times 10^{-7}$	$2.691 \times 10^{-6}$	$4.601 \times 10^{-6}$
$P_{LO}$ Ref	$7.730 \times 10^{-7}$	$2.686 \times 10^{-6}$	$4.599 \times 10^{-6}$
$P_{TX}$ SCI	$6.820 \times 10^{-4}$	$1.223 \times 10^{-3}$	$1.764 \times 10^{-3}$
$P_{TX}$ TM	$1.940 \times 10^{-4}$	$4.010 \times 10^{-4}$	$6.080 \times 10^{-4}$
$P_{TX}$ Ref	$6.450 \times 10^{-4}$	$1.173 \times 10^{-3}$	$1.701 \times 10^{-3}$

To be more concrete, let's use the case of the SCI-IFO, illustrated in Figure 2.7 where the measured signal is the result of the interference between the incoming laser RX beam and the TX beam. Similarly to Section 2.1.2, the TX signal will be modelled as a simple harmonic wave function:

$$E_{TX}(t) = E_{TX_0} \cos(\omega_{TX}t + \phi_{TX}). \quad (2.13)$$

$E_{TX_0}$  is the amplitude of the TX signal,  $\omega_{TX}$  its angular frequency, and  $\phi_{TX}$  its initial phase. Analogously, the RX is modelled as a simple harmonic wave. However, having travelled across LISA's arm, it exhibits a GW induced phase shift ( $\Delta\phi_{GW}$ ) and a Doppler frequency shift due to spacecraft motion ( $\Delta\omega_D$ ). Thus, the RX can be represented as follows:

$$E_{RX}(t) = E_{RX_0} \cos((\omega_{RX} + \Delta\omega_D)t + \phi_{RX} + \Delta\phi_{GW}). \quad (2.14)$$

$E_{RX_0}$  is the amplitude of the RX signal,  $\omega_{RX}$  its angular frequency,  $\phi_{RX}$  its initial phase, and  $\Delta\phi_{GW}$  is the phase shift induced by the GW.

Based on those two signals and on Equation 2.8, the resulting interference of the RX and TX laser beam is [29]–[31]:

$$I = I_{LO} + I_{RX} + \sqrt{2\eta I_{LO} I_{RX}} \cos((\omega_{LO} - (\omega_{RX} - \Delta\omega_D))t + \phi_{het}). \quad (2.15)$$

The phase term  $\phi_{het}$  encompasses the initial phase difference, the GW induced phase shift, and the Doppler shift and is equal to :

$$\phi_{het} = \phi_{LO} - \phi_{RX} - \Delta\phi_{GW}. \quad (2.16)$$

However as mention before as depicted in Figure 2.7 and discussed in Section 2.2.2, the optical signal is read by four PRs, meaning each PR receives a signal equal to:

$$I = \frac{I_{LO} + I_{RX}}{4} + \sqrt{\frac{\eta I_{LO} I_{RX}}{2}} \cos((\omega_{LO} - (\omega_{RX} - \Delta\omega_D))t + \phi_{het}). \quad (2.17)$$

The optical signal from the other optical interferometers follows a similar formula but incorporates a different phase term and utilizes the optical power of their beam, as summarized in Table 2.1.

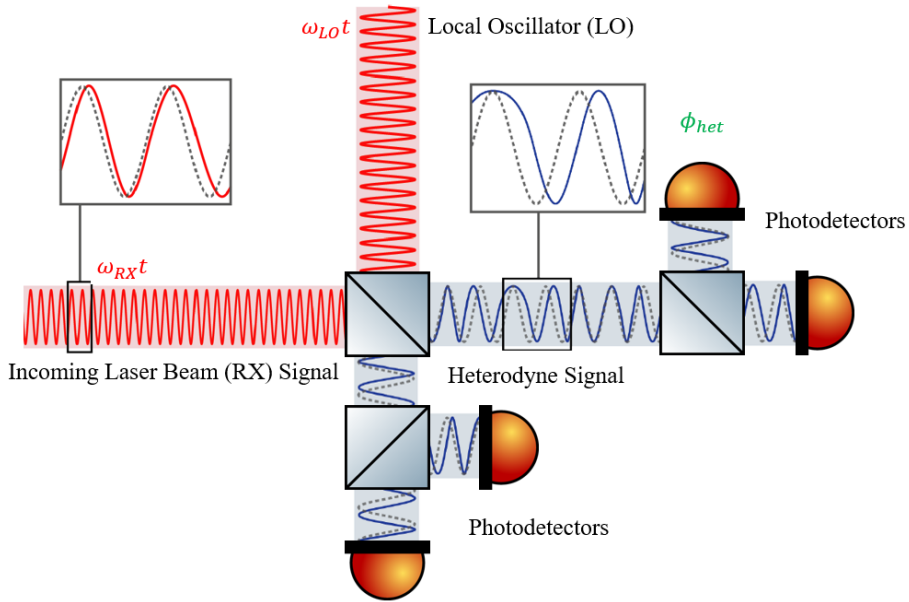


Figure 2.7: Interaction between LISA the incoming (RX) laser beam with the local (LO) laser beam.

## 2.3 Photoreceivers

### 2.3.1 General introduction

In the LISA mission, the PRs are key components for detecting heterodyne interferometric signals and converting them into a voltage delivered to the PMS for subsequent phase measurement and auxiliary functions. Illustrated on Figure 2.8, each PR is a sophisticated assembly comprising three components [15]:

1. The PD is a semiconductor element (InGaAs) in charge of converting the optical signal ( $P_{opt}$ ) into a current called photo-current ( $I_{ph}$ ). In LISA, the PDs used are Quadrant Photodiode (QPD), meaning it features four active segments. The use of four segments enables the application of differential wavefront sensing methods to estimate the tilt and misalignment of the laser beam [30]. Due to the presence of segment, the PRs of LISA are now referred to as Quadrant Photoreceiver (QPR) and Quadrant Photodiode (QPD).
2. The FEE amplifies and converts the photocurrent generated by each segment of the QPDs into a voltage (V) using a TIA.
3. The mechanical housing houses the QPD and FEE in a compact volume on the OB. It provides precise and stable positioning of each QPD to the optical beam and ensures the electromagnetic compatibility of the QPRs.

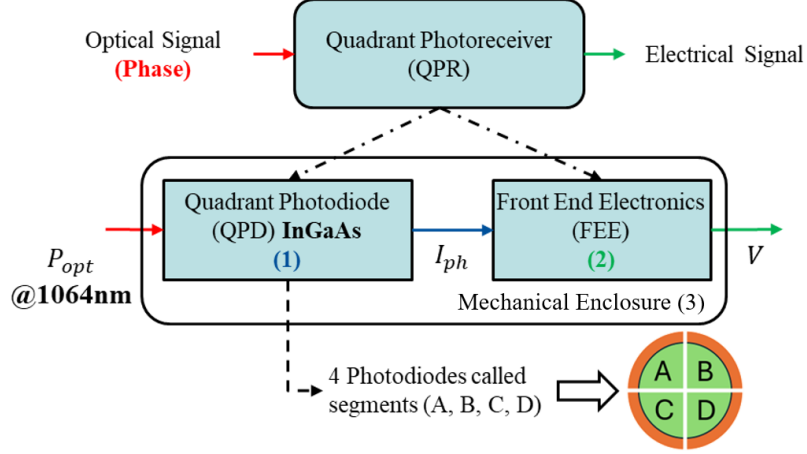


Figure 2.8: Schematic diagram of LISA QPR system with (1) the QPD, (2) the FEE, and (3) the mechanical enclosure.

Each segment functions as an independent PD. The upcoming sections delve into the fundamentals of a PD, examining characteristics crucial to meeting LISA’s requirements, including dark current, capacitance, and QE. Additionally, the main parameter regarding the QPR, which is the EICN model, will be discussed.

## 2.3.2 Photodiodes technologies

### The PN junction in photodiode mode

The band theory explains the electrical properties of materials by describing the evolution of discrete atomic energy states into continuous energy bands as the number of atoms increases. Two crucial bands are the Valence Band, filled with electrons at absolute zero, and the Conduction Band, where delocalized electrons enable material conductivity. Based on the characteristics of these bands, materials are categorized as conductors (with overlapping bands), insulators (with large band gaps preventing electron flow), and semiconductors (with narrower gaps allowing conditional conductivity). A band diagram of a semiconductor is represented at the bottom of Figure 2.9. Semiconductor electrical properties can be tuned through doping by introducing impurities into the material. N-type doping adds atoms with excess valence electrons, creating free electrons, while p-type doping introduces atoms with fewer valence electrons, leaving behind positively charged holes.

A PN junction is two contacting p-type and n-type semiconductors. Initially, electrons from the n-type region diffuse into the p-type region and recombine with holes, and vice versa. This diffusion leads to a build-up of immobile ions: positively charged donor ions in the n-type region and negatively charged acceptor ions in the p-type region. These fixed charges create an electric field that opposes further diffusion of charge carriers, acting as a recombination barrier. This region called the depletion zone, creates an internal electric field, influencing charge carrier movement (see Figure 2.9).

The output current flow ( $I$ ) generated by a PN junction depends on the applied voltage, known as the bias voltage ( $V_{\text{bias}}$ ), and the temperature ( $T$ ). This relationship is described by the Shockley equation (see Equation 2.18), represented in Figure 2.10

$$I = I_S \left( \exp\left(\frac{qV_{\text{bias}}}{nk_bT}\right) - 1 \right), \quad (2.18)$$

where  $I_S$  is the reverse saturation current,  $k$  is the Boltzmann constant, and  $q$  is the elementary charge. The PN junction operates in two primary modes (shown in Figure 2.10): forward bias and reverse bias.

- In forward bias mode, a PN junction reduces the barrier at the junction, facilitating the diffusion of majority carriers across the junction and creating an electric current. In this mode, the junction behaves as a solar cell, where light generates charge carriers that are separated by the junction's internal electric field, producing electricity without the need for an external voltage.
- In reverse bias mode, a PN junction increases the barrier, widening the depletion zone and minimizing the flow of charge carriers, corresponding to the behaviour of a PD. Hence, the bias voltage applied to a PD is always reverse bias. Therefore, throughout this manuscript, the voltage applied to the PD (or QPD) is by default a reverse bias, and thus  $V_{bias}$  represents the reverse bias voltage. When incident photons strike the PN junction, they are absorbed, exciting electrons from the valence band to the conduction band and creating electron-hole pairs. The internal electric field separates these charges, generating an electrical current proportional to the light intensity, thus converting light into an electrical signal (see Figure 2.9 for an illustration of this process).

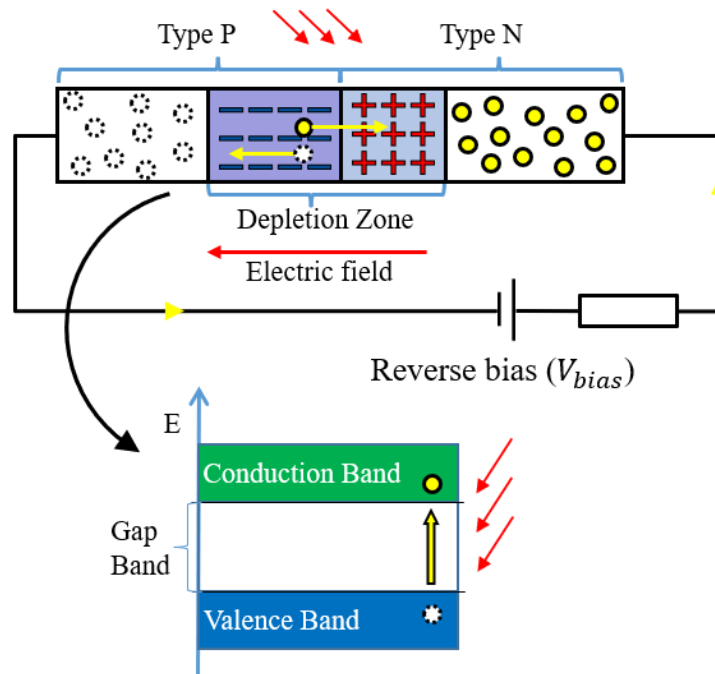


Figure 2.9: Light to electrical signal conversion in PD: energy diagram (bottom) and PN junction dynamics under a bias voltage.

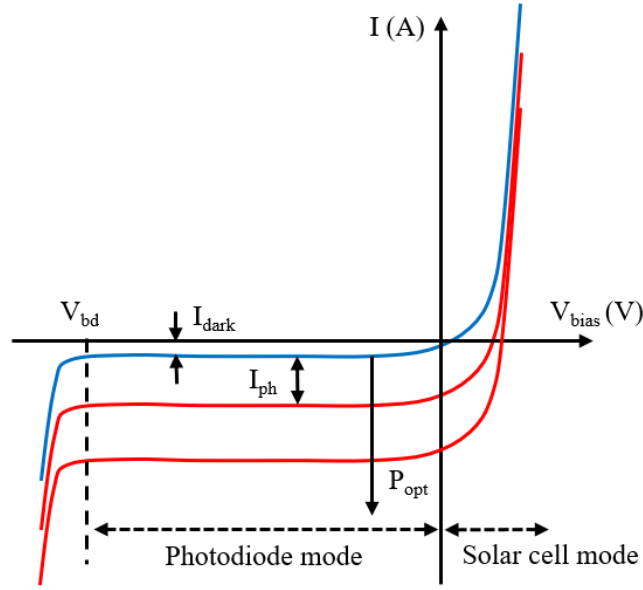


Figure 2.10: Output current of the PN junction in function of the  $V_{bias}$  applied. In blue correspond of the current with no incoming light ( $P_{opt} = 0$ ) and in red with  $P_{opt} > 0$  and increasing.

### PIN Photodiodes

Figure 2.11 illustrates a PIN photodiode. They incorporate an intrinsic layer between the p-type and n-type semiconductor regions. This intrinsic layer is essentially an undoped, pure semiconductor material that widens the depletion zone beyond what is typical in a simple PN junction [32], [33]. The intrinsic layer in PIN PD extends the depletion zone, allowing photon absorption across a larger volume of semiconductor material. This extension not only enhances the probability of photon absorption and the generation of electron-hole pairs, beneficial for detecting low light levels and photons with energies just above the band gap, but also reduces the diode's capacitance. The reduced capacitance leads to improved response times, enabling PIN photodiodes to operate at higher frequencies than standard PN photodiodes.

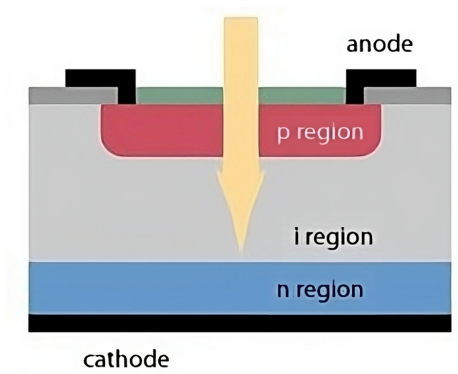


Figure 2.11: Cross-sectional view of a PIN PD.

### DDR Photodiodes

DDR photodiodes introduce an additional drift layer, as depicted in Figure 2.12, that extends the depletion region. Due to the extended electric field across the drift layer, DDR photodiodes enhance

the speed and efficiency of charge carriers, such as electrons and holes. This field accelerates carrier transit and shortens collection time [34]–[37]. This acceleration allows DDR photodiodes to mitigate the capacitance-transit time trade-off inherent in standard PIN photodiodes, improving bandwidth. For instance, Joshi (2006) [34] demonstrated an InGaAs DDR photodiode achieving a bandwidth of 10 GHz. The energy band diagrams in Figures 2.13 and 2.14 depict the operational dynamics of a DDR photodiode under unbiased and biased conditions. Initially, the band structure for the InGaAs/InP heterojunction shows an energy wall for electrons, aiding in their separation as holes do not encounter a similar barrier. Upon applying a reverse bias, the p+ and n+ regions are depleted, enhancing the electric field across the junction, and the energy bands develop a negative slope (as shown by the dashed Fermi line). This setup directs electrons to flow downwards from the InGaAs to the n+ InP region and propels holes towards the p+ InP region. Potential energy barriers in regions 1 and 2 may impede carrier movement. Applying a reverse bias to achieve full depletion enhances carrier flow, promoting rapid device response and excellent current handling while reducing transit times and maintaining linearity [34]. Further studies [36], [37] have shown that the DDR photodiodes structure, including the drift layer, can be optimized to reduce radiation damage effects, making them useful for the harsh radiation conditions of space missions like LISA.

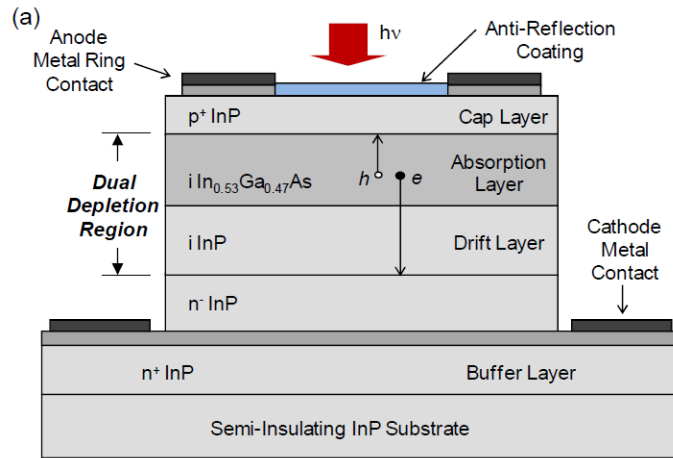


Figure 2.12: Ultra-fast InGaAs DDR PD structure [37].

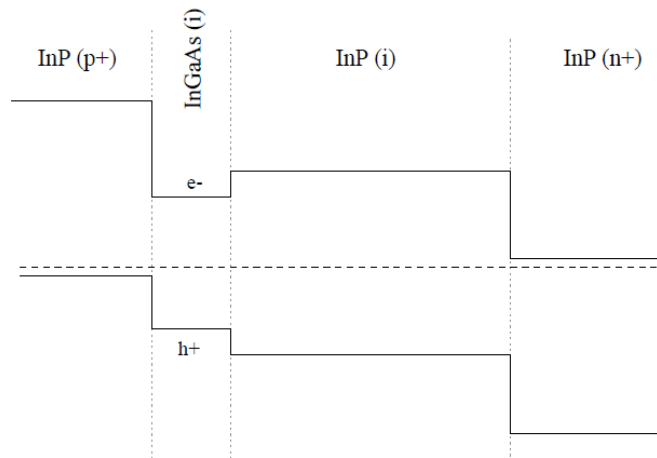


Figure 2.13: The basic InGaAs/InP heterojunction dual-depletion photodiode at zero bias [34].

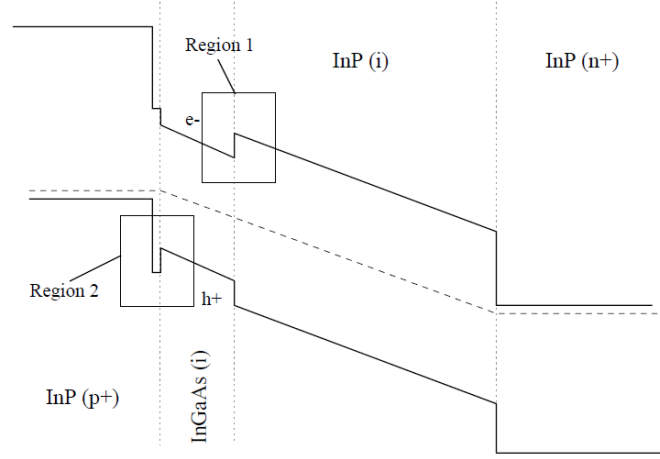


Figure 2.14: The basic dual-depletion diode under strong reverse bias voltage. Both the electrons and the holes have a barrier to overcome in order to reach the p+ and n+ electrodes [34].

### 2.3.3 Photodiodes optoelectronic characteristic

#### Electrical Equivalent Circuit

Figure 2.15 illustrates the various components that model the electrical behaviour of a PD, both in the absence of light (dark conditions) and when illuminated. The key elements of this model include:

- **Current Source ( $I_{ph}$ ):** This component represents the photocurrent generated by the PD. At a fixed  $V_{bias}$ , the photocurrent is directly proportional to the intensity of the incident light and the QE of the PD (discussed in more detail in Section 2.3.3).
- **Series Resistance ( $R_s$ ):** This resistance arises from the photodiode's contacts, wire bonds, and semiconductor material. Although  $R_s$  is typically low, it can affect the linearity and design of the detection circuit due to voltage drops that may forward bias the PD in zero-bias configurations.
- **Shunt Resistance ( $R_{sh}$ ):** This resistance accounts for the leakage current paths within the PD that do not pass through the p-n junction. A high shunt resistance is preferable as it indicates minimal leakage currents, thereby improving the PD's performance.
- **Capacitance ( $C$ ):** This capacitance is due to the depletion region formed at the p-n junction, where separated charge carriers create a region capable of storing electric charge. High capacitance can adversely affect the noise characteristics and bandwidth of the PD. The capacitance is influenced by the thickness of the depletion region ( $d$ ) and the photosensitive surface area ( $A = \pi r^2$ ) as described by Equation 2.19. The depletion region's thickness varies with the applied bias voltage.

$$C = \frac{\epsilon A}{d}, \quad (2.19)$$

where  $\epsilon = \epsilon_0 \epsilon_r$  is the relative permittivity of the material.

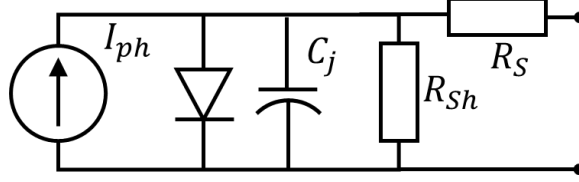


Figure 2.15: Equivalent circuit model of a PD.

### Dark current

As seen in Figure 2.10, at fixed  $V_{\text{bias}}$ , even without light arriving on the PD, meaning the PD is in complete darkness, a current, called: the dark current ( $I_{\text{dark}}$ ) is still generated. The origin of  $I_{\text{dark}}$  is attributed to defects within the semiconductor material, which introduce parasitic energy levels within the bandgap. These defect states, often resulting from imperfections during the fabrication process or from inherent material impurities, act as intermediate energy levels that facilitate the thermal generation-recombination process, even without incident light. Specifically, these parasitic levels can trap and release carriers, thereby contributing to a steady-state leakage current  $I_{\text{dark}}$ .

The magnitude of dark current is temperature-dependent because increased temperatures enhance the thermal generation of carriers, which populate the defect states and facilitate the generation-recombination process within the semiconductor material. According to the Arrhenius law (see Equation 2.20), the dark current dependency on temperature can be described by an exponential relation, where  $I_{\text{dark}}$  increases exponentially with temperature ( $T$ ). This relation is governed by the activation energy ( $E_a$ ) associated with the defect states and the thermal energy available.

$$I_{\text{dark}}(T) = I_0 \exp\left(\frac{-E_a}{kT}\right). \quad (2.20)$$

$k$  is the Boltzmann constant and  $I_0$  a pre-exponential factor.

The dark current adversely impacts PD performance by reducing sensitivity and accuracy, as it elevates the noise floor and diminishes the signal-to-noise ratio, critical for precise low-light measurements.

### Quantum efficiency

The QE of a PD is defined as the ratio of the number of charge carriers generated and collected by the PD to the number of incident photons. It serves as a crucial metric for assessing the PD's effectiveness in converting incoming light into an electrical signal. If the QE is too low, it results in reduced sensitivity, decreased signal-to-noise ratio, and limited dynamic range. These issues lead to poor light detection performance, compromising the accuracy and reliability of measurements with low light conditions like in LISA. QE can be expressed as a percentage and is represented by the following equation:

$$\text{QE} = \frac{N_e}{N_{ph}} = \frac{I}{\frac{P}{\frac{hc}{\lambda}}} = \frac{I}{P} \cdot \frac{hc}{\lambda e} = R_\lambda \cdot \frac{hc}{\lambda e}, \quad (2.21)$$

where  $N_e$  and  $N_{ph}$  denote the number of photoelectrons and incident photons, respectively,  $I$  represents the photocurrent,  $e$  is the elementary charge,  $P$  signifies the incident optical power,  $\lambda$  is the wavelength of the incident light,  $h$  is Planck's constant, and  $c$  is the speed of light. The term  $R_\lambda$  corresponds to the responsivity, defined as the ratio of the output photocurrent ( $I_{\text{ph}}$ ) to the incident optical power ( $P_{\text{opt}}$ ), measured in A/W. Responsivity is dependent on the wavelength of the incident light and is the quantity experimentally measured.

### 2.3.4 Photoreceivers noise model

This section outlines a noise model for the QPR used in the LISA mission, detailing the contributions of various noise sources to the overall noise profile. Specifically, it evaluates the noise of the QPR

using the concept of Equivalent Input Current Noise (EICN), a metric that consolidates all noise sources into a single current equivalent at the QPR’s input. This approach facilitates a direct comparison of noise levels with signal levels, expressed in the same units (A). Importantly, while EICN aligns with signal measurements by being presented in current units, its quantification adopts the unit  $\text{A}/\sqrt{\text{Hz}}$ . This provides insight into the noise power density over frequency and enables the evaluation of how noise varies across the operational bandwidth.

### The shot noise

The shot noise, or Poisson noise, is intrinsic to the photodetection process. It arises when photons arrive on the detector, creating electron-hole pairs in a process proportional to the incident photon count. However, due to the discrete nature of photons, their arrival is random. Governed by the Poisson distribution, this phenomenon illustrates that the probability of observing a certain number of events (electron-hole pair generation) within a fixed time interval depends on the average rate of photon arrivals. Due to its random nature, shot noise represents a fundamental limit to the accuracy of measurements in detection systems, such as LISA and others. The expression for shot noise ( $i_{\text{sn}}$ ) is related to the photocurrent ( $I_{\text{ph}}$ ) and dark current ( $I_{\text{dark}}$ ), as shown in Equation 2.22 [31], [38], [39]:

$$i_{\text{sn}} = \sqrt{2e [I_{\text{dark}} + I_{\text{ph}}]} \quad (\text{A}/\sqrt{\text{Hz}}), \quad (2.22)$$

where  $e$  denotes the elementary charge ( $1.6 \times 10^{-19}$  coulombs).

### The thermal noise

Thermal noise, also known as Johnson noise, arises due to the random thermal motion of charge carriers (electrons and holes) within a conductor, resistor, or any other electrical component at finite temperatures. This motion leads to fluctuations in the voltage or current of the component, independent of any external signals or stimuli. According to Nyquist’s theorem, the magnitude of thermal noise is directly proportional to the temperature ( $T$ ) of the component, its resistance ( $R$ ), and the Boltzmann constant ( $k_b$ ), as seen in Equation 2.23 [40].

$$i_{\text{jn}} = \sqrt{\frac{4k_b T}{R}} \quad (2.23)$$

Thermal noise is a fundamental limit to the sensitivity of electronic systems, affecting various devices such as amplifiers, resistors, and semiconductor components. Since both the QPD and FEE possess resistive elements, both contribute to the overall thermal noise. However, we can hypothesize that the Johnson noise from the QPD is significantly lower than the thermal noise from the FEE and can therefore be neglected. This is valid since active and resistive components in the FEE inherently have higher thermal noise, and the QPDs in LISA are designed to have very low intrinsic noise. To model the thermal noise of the FEE, a few considerations are made:

- **Feedback Resistor Dominance:** The thermal noise is primarily due to the feedback resistor, with other sources being secondary.
- **Linear Operation:** The TIA operates in a linear regime where its components (like the heterojunction bipolar transistors) do not introduce significant non-linear noise components.
- **Stable Temperature:** The temperature ( $T$ ) is stable and uniform across the TIA.

Following these hypotheses, we applied the Norton equivalent version of Johnson noise modelled by a current source in parallel to the resistor. In our case, the parallel resistor is the feedback resistor  $R_f$  [31], [39].

## Operational amplifier noise

Operational Amplifier (op amps) noise contribute to the total TIA input current noise. It refers to the inherent electrical noise generated within the op amps itself, distinct from external sources. This noise originates from various internal mechanisms such as semiconductor junctions, resistors, and amplification stages within the op amps circuitry. Common types of noise in op amps include [39]:

- Voltage Noise ( $i_{vn}$ ): represents fluctuations in the output voltage of the op amps due to internal sources, including thermal noise from resistors, shot noise from semiconductor junctions, and electronic noise from the amplification stages. Voltage noise is typically characterized by its spectral density ( $i_{in}$ ), measured in  $V/\sqrt{\text{Hz}}$ . It contributes to the overall noise level of the QPR's output. The op amps voltage noise ( $e_n$ ) translates to current noise at the FEE input ( $i_{vn}(f)$ ) over the input and feedback impedance ( $R_f$ ) as:

$$i_{vn}(f) = e_n \frac{\sqrt{1 + (2\pi f R_f C_T)^2}}{R_f}, \quad (2.24)$$

where  $C_T = C_d + C_f + C_{op} + C_s$  represents the total capacitance of the circuit, including the capacitance arising from the QPD capacitance  $C_d$ , feedback impedance  $C_f$ , op amps common-mode input capacitance  $C_{op}$ , and stray capacitance  $C_s$  from the board, components, and packaging.

- Current Noise ( $i_{in}$ ): reflects fluctuations in the output current. This type of noise arises due to the random movement of charge carriers within the amplifier's internal components, such as transistors and resistors. Current noise is also characterized by its spectral density measured in  $A/\sqrt{\text{Hz}}$ . While voltage noise predominantly affects the voltage output of the op amps, current noise influences the current output.
- Flicker Noise ( $1/f$  Noise): also known as  $1/f$  noise, is characterized by its dependence on frequency, with higher noise levels observed at lower frequencies. This type of noise arises from various mechanisms within the op amps, including fluctuations in carrier mobility and random trapping-detrapping processes in semiconductor materials. Flicker noise is often more pronounced at lower frequencies and can significantly impact the low-frequency performance ( $< 10\text{kHz}$ ) of the QPR. However, in our case, the bandwidth of LISA is from 3 to 30 MHz; at such frequencies, flicker noise is dominated by other noise sources and therefore neglected.

## Global noise model

The EICN in each quadrant of the QPR arises from a combination of each previously presented noise: the shot noise ( $i_{sn}$ ) due to the QPD dark current and photocurrent, the thermal noise ( $i_{jn}$ ) from the feedback resistance, the op amps voltage noise ( $i_{vn}$ ), and op amps current noise ( $i_{in}$ ). These noise sources are statistically independent and combine in quadrature to yield:

$$i_{en}(f) = \sqrt{i_{sn}^2 + i_{jn}^2 + i_{vn}^2 + i_{in}^2}. \quad (2.25)$$

Using Equation 2.22, 2.23, and 2.24, Equation 2.25, becomes:

$$i_{en}(f) = \sqrt{(2e [I_{\text{dark}} + I_{\text{ph}}]) + \left(\frac{4k_b T}{R}\right) + i_{in}^2 + e_n^2 \left(\frac{1}{R_f^2} + (4\pi^2 f^2 C_T^2)\right)}. \quad (2.26)$$

## Chapter 3

# Space Environment and Radiation Effects

### 3.1 LISA Space Environment

#### 3.1.1 Orbit

As depicted in Figure 3.1, LISA occupies a heliocentric orbit, forming a 'cartwheel' constellation that trails the Earth by approximately 20 degrees, at a distance of  $1 \pm 0.01$  AU from the Sun. The constellation's design, featuring three identical satellites arranged into an equilateral triangle with 2.5 million kilometres on each side, rotates around its centre annually, preserving a nearly invariant geometric configuration. Inclined at  $60^\circ$  to the ecliptic plane, the constellation's orbital dynamics are engineered to maximize rigidity, limiting inter-satellite distance variations to approximately 1%. This rigidity allows minimal angular fluctuations in the constellation's shape, thus maintaining a fixed orientation towards the Sun. This orientation guarantees a stable thermal environment and ensures a continuous supply of solar power to the satellites' onboard batteries [13]–[15], [25], [41].

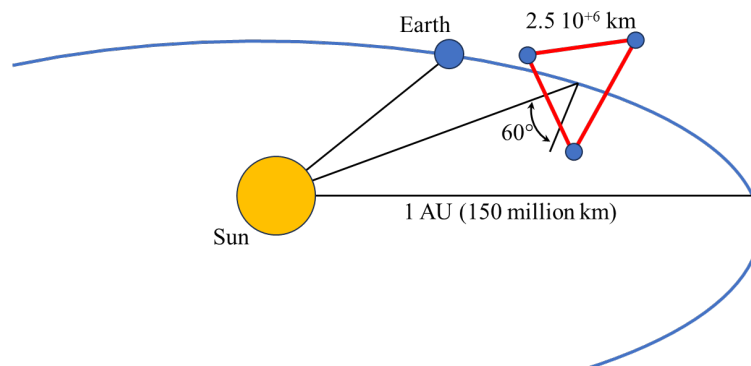


Figure 3.1: Orbital configuration of the LISA mission [14].

#### 3.1.2 Solar Radiation and Cosmic Radiation

LISA, like any other spacecraft, will encounter a harsh space environment and face exposure to radiation from various sources. Specifically, due to its orbit, the Sun stands out as a predominant contributor. The Sun, primarily composed of hydrogen (71%) and helium (27%), exhibits activity cycles approximately every 11 years, alternating between roughly 7 years of heightened activity and 4 years of quieter periods. This variability is driven by the Sun's magnetic field, leading to particle ejections via solar winds and solar eruptions.

Solar winds, originating from the Sun's corona, expel a plasma that carries the solar magnetic field outward. Starting as a hot, dense plasma near the Sun, it accelerates and cools down, becoming supersonic as it moves further away. The velocity of solar winds varies between 300 and 1200 km/s, often reaching speeds of about 700 km/s during solar minimum. Composed primarily of protons (95%), alpha particles (4%), and minor ions (1%), the solar wind exhibits significant variability, influencing surface charging and radiation effects in space. [42].

Solar eruptions as shown in Figure 3.2, driven by the Sun's intense magnetic activity, release substantial fluxes of solar energetic particles, known as solar particle events. During periods of solar maximum, these events, especially prominent, release a combination of protons, heavy ions, and electrons with varying compositions. The most intense eruptions (Class X flares) can emit particles energetic enough to penetrate satellite shielding, posing a significant risk to satellite components due to their high penetration capability. The environment of solar particle events in interplanetary space is typically isotropic due to scattering, although directed streaming can occur at higher energies, increasing the risk to missions like LISA [41]–[43].

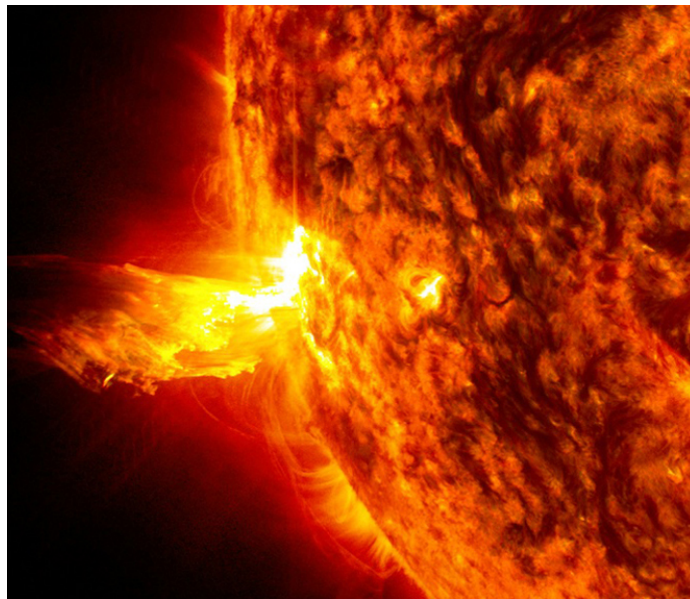


Figure 3.2: Prominence eruption on the Sun captured on June 20, 2013, at 11:15 p.m. EDT by NASA [44].

### 3.1.3 Cosmic Rays

Cosmic rays, originating from beyond our solar system, primarily from supernova (see Figure 3.3) and distant galaxies, pose another radiation source for LISA. These high-energy particles, mainly protons (87%) and helium ions (12%), with a small fraction of heavier ions, can cause damage to electronic components due to their high kinetic energy. Galactic cosmic rays, including energetic heavy ions, can lead to single event effects in electronics, traversing the solar system with a wide range of energies and capable of depositing significant energy in sensitive volumes [41], [43], [45].

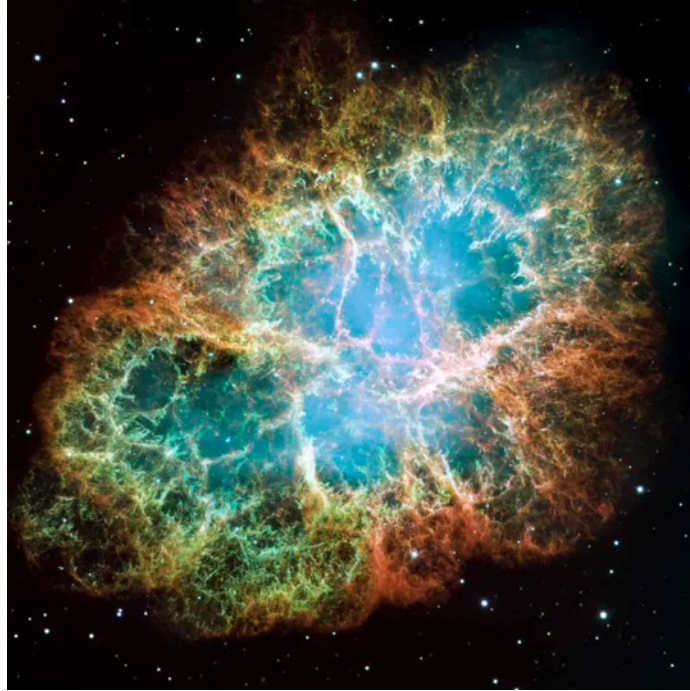


Figure 3.3: A vast mosaic image by NASA’s Hubble Space Telescope of the Crab Nebula, a six-light-year-wide supernova remnant [46].

### 3.1.4 Others

Among other radiation sources is the Van Allen belt, comprising two layers of charged particles orbiting Earth, held by the planet’s magnetic field. The inner radiation belt consists mainly of high-energy protons and electrons, from 640 to 12,000 kilometres above Earth’s surface, originating from cosmic ray-produced neutron decay. The outer belt, from 13,500 to 58,000 kilometres, consists of electrons and high-energy ions from the solar wind, changing in composition and intensity with solar activity [42], [43]. These layers can present challenges for spacecraft. However, because LISA is in a solar orbit, its exposure to the Van Allen belts is relatively minimal, posing little concern for the mission. Same for the influence of planetary electromagnetic and secondary radiations, primarily triggered by solar and cosmic rays, are considered negligible [41].

## 3.2 Radiation-Matter Interactions

Consequently, the LISA mission faces exposure to various radiation types. The high-energy particles originating from these sources can penetrate the spacecraft’s shielding and interact with the onboard materials, either through the atomic electron clouds or directly with the nuclei.

### 3.2.1 Interactions with the Electronic Cloud

The electronic cloud denotes the ensemble of electrons bound to an atom. The electrons orbit around the nucleus in distinct layers, organized into various orbitals. Each orbital represents a specific, discrete energy level with a limited capacity of electrons. Incident-charged particles from space, including protons, electrons, and ions, will interact with the electronic clouds of the target atom via electronic Coulomb forces. These forces can induce changes through attraction or repulsion, depending on the charge of the particles, without necessitating a direct collision. These forces decelerate and redirect the incident particle, impacting the valence electrons of the target atom in two principal manners, as illustrated in Figure 3.4. An electron may be either moved to a higher,

less tightly bound orbital (Figure 3.4a) or, if the energy transfer is substantial, it may be expelled from its orbit entirely, resulting in the ionization of the target atom (Figure 3.4b). This process of ionization leads to the formation of an electron-hole pair. [47]–[49].

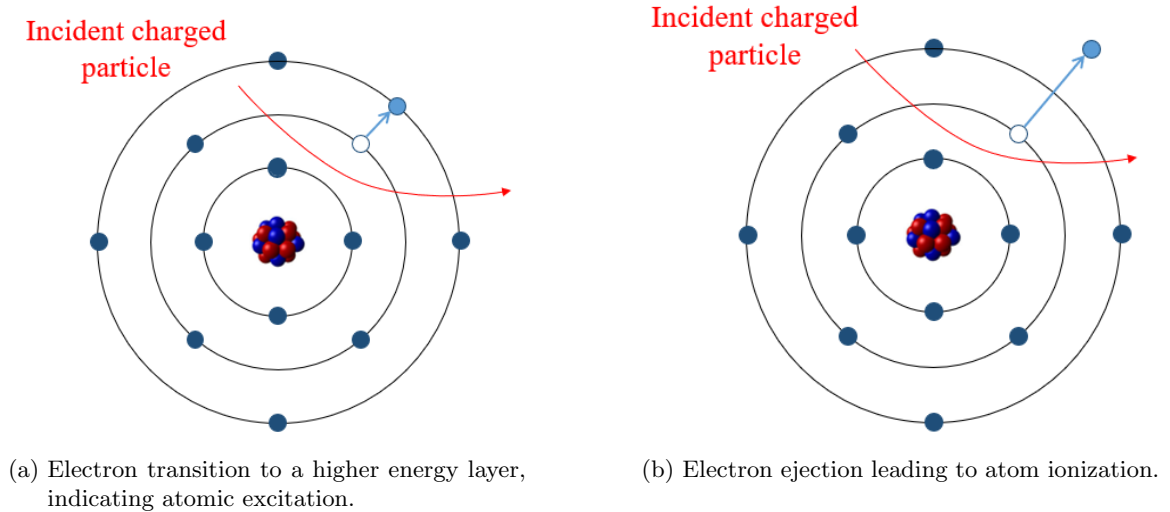
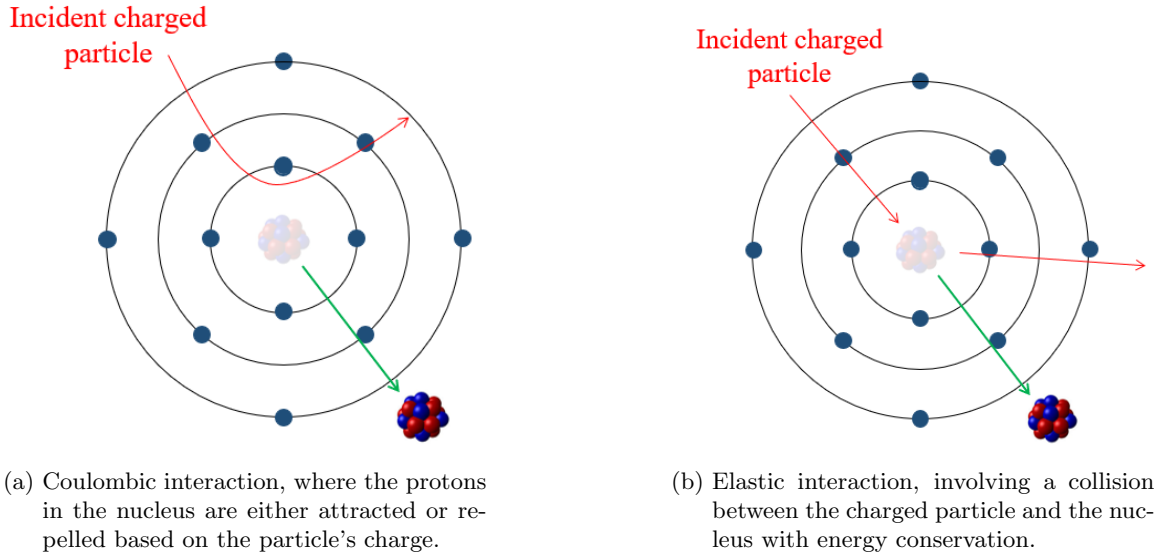


Figure 3.4: Illustration of Coulomb interactions between an electron and a charged particle in either atomic excitation (a) or ionization (b).

### 3.2.2 Interactions with the Atomic Nucleus

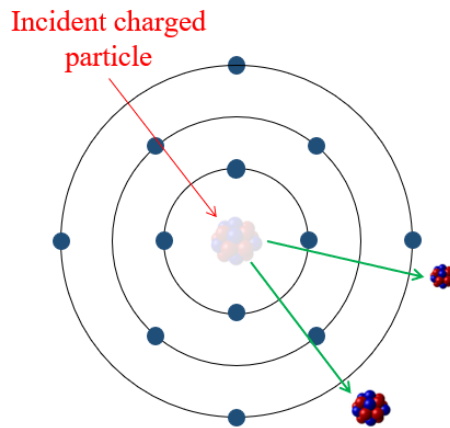
The interactions between incident charged particles and the atomic nuclei of target materials can be categorized into three primary types: Coulombic, elastic nuclear, and inelastic nuclear interactions [47]–[49]. All three are illustrated in Figure 3.5 and described as follows:

- **Coulombic interactions** (Figure 3.5a) are the most probable of the three interactions. Similar to electronic Coulomb interactions, the Coulomb force governs this process, which can either attract or repel incident particles based on the interplay between the nucleus's positive charges and the charges of these particles.
- **Elastic nuclear interactions** (Figure 3.5b) occur when a charged particle collides directly with a nucleus. This type of interaction is less common, as the incident particle must overcome the atom's potential barrier without being diverted by Coulomb forces. In this scenario, the particle may be absorbed if it transfers all its energy to the nucleus, or it may be deflected and continue its path with reduced energy.
- **Inelastic nuclear interactions** (Figure 3.5c) happen when a high-energy particle breaches the atomic potential barrier and strikes the nucleus, potentially causing the atom to fission. The nucleus then transitions to an unstable state, emitting particles such as neutrons, gamma rays, or light nuclei to return to stability. The resulting nucleus may be an isotope of the original or a different element altogether. The emitted particles are energetic enough to further interact with the surrounding material. This reaction is the least probable, requiring the incident particle to possess several MeV of energy, but is not uncommon for protons or electrons.



(a) Coulombic interaction, where the protons in the nucleus are either attracted or repelled based on the particle's charge.

(b) Elastic interaction, involving a collision between the charged particle and the nucleus with energy conservation.



(c) Inelastic interaction, where the charged particle penetrates the nucleus, resulting in its division into lighter elements.

Figure 3.5: Schematic representation of the Coulombic (a), elastic (b), and inelastic(c) interaction between a charged particle and an atomic nucleus.

### 3.2.3 Bremsstrahlung Radiation

Bremsstrahlung radiation is a type of secondary radiation that occurs when an energetic particle interacts with the electronic cloud or atomic nucleus, causing the charged particle to deflect and slow down, emitting energetic photons such as X-rays or gamma rays. It creates a nearly continuous energy spectrum and ionizes matter by interacting with electrons. This radiation is directly proportional to the charge density of the nucleus and electrons, and inversely proportional to the particle's mass. Bremsstrahlung radiation is considered a significant secondary source for engineering purposes and can be highly penetrating. In space, the most common source of Bremsstrahlung is electron scattering. When evaluating radiation background effects in detector systems, secondary radiation plays a crucial role due to factors such as heavy shielding, veto systems, and prompt and induced radioactivity [41], [49].

## 3.3 Displacement Deflects

### 3.3.1 Crystal Defects

The three interactions Coulombic, elastic nuclear, and inelastic nuclear interactions described in the previous section 3.2 share a common outcome: the ejection of an atom if the energy transferred from the incident particle exceeds a specific threshold called the Threshold Displacement Energy noted  $E_d$  (TDE). This leads to the displacement of an atom, referred to as the PKA, creating a vacancy in the crystal lattice. The PKA due to the collision received an amount of kinetic energy from the incident particle referred to as the recoil energy. The PKA moves and interacts with neighbouring atoms until its kinetic energy is fully depleted. When the PKA eventually occupies an interstitial position, not aligned with the lattice, it forms a vacancy-interstitial pair known as a Frenkel pair as shown in Figure 3.6 [50]–[53].

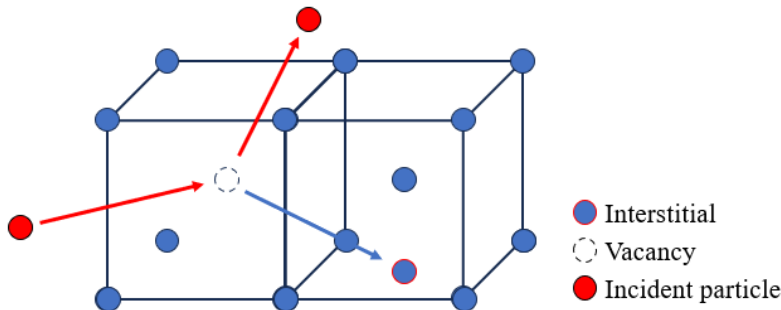


Figure 3.6: Illustration of Frenkel Pair Formation: showing the generation of an interstitial atom and a corresponding vacancy in the crystal lattice.

During its interactions, if the PKA possesses energy exceeding the  $E_d$  of a target atom, it can generate additional PKAs, called Secondary Knock-on Atomss (SKAs), hence initiating a displacement cascade as illustrated on Figure 3.7. The greater the PKA’s energy, the larger the number of SKAs produced. Similar to PKAs, SKAs with sufficient energy may also trigger further sub-cascades. This relationship between the PKA energy and the resulting number of SKAs, is depicted in Figure 3.7, which shows a logarithmic increase in the number of interactions with rising incident proton energy. These atomic displacements create distinct patterns along their recoil paths, leading to the categorization of defects into different types of defects as a function of the energy of the PKA in the case of Si [50], [54], [55]:

- Point Defects from PKA with low energy between 25 eV and 1 keV in Si. These defects, such as a single vacancy-dopant pair, are identified by an affected area with a diameter not exceeding 3 nm.
- Single Cascade Clusters are large clusters resulting directly from PKAs interactions. They contain a very high density of defects, locally reaching up to  $1 \times 10^{18} \text{ cm}^{-3}$ . In silicon, this occurs when PKA energies range from 1 keV to 20 keV.
- Sub-Cascade Clusters are formed by secondary cascades initiated by PKAs. These clusters cover broad areas, approximately 1000 Å, and feature a diluted defect density. This scenario arises in silicon for PKA energies greater than 20 keV.

The detailed characteristics of these clusters, such as their shape and size, are influenced by the particle’s energy, mass, and type. For example, at high energies, the probability of causing displacement and generating additional recoil atoms is low, leading the PKA to traverse long distances with minimal interactions, resulting in sparsely distributed point defects. However, as the PKA and any secondary recoils produced in the cascade decelerate, the spacing between vacancies decreases significantly, culminating in densely packed damage clusters towards the end of a recoil

### Displacement Damage Processes in Si

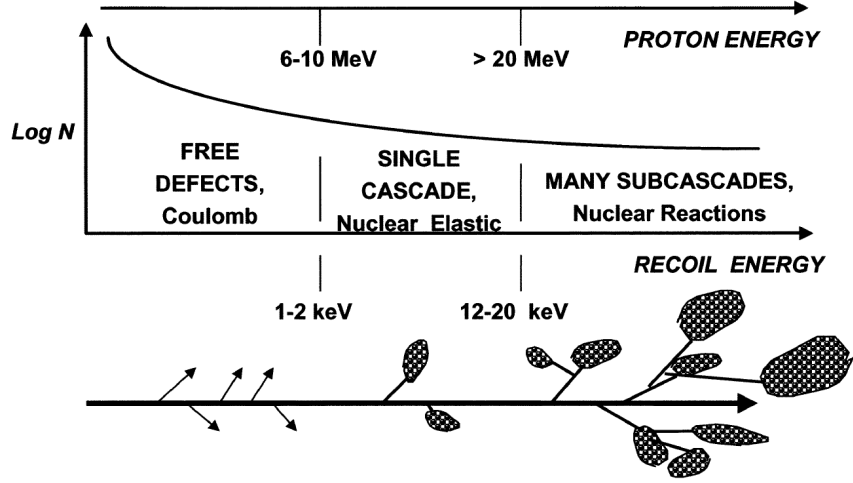


Figure 3.7: Schematic representation of defect and subcascade formation as a function of PKA energy [56].

track, known as 'terminal clusters.' This damage pattern manifests as a distinctive tree-like structure depicted in Figure 3.8. Research using molecular modelling, which demonstrates how these factors dictate the quantity, dimensions, and spatial distribution of the clusters, are depicted in Figure 3.9 [52], [57]–[59]. Additionally, in Figure 3.10, GEANT4 simulations reveal varied behaviours among particles: protons and heavy ions form intense, straight ionization tracks with high-density pairs (Figure 3.10a), in contrast to electrons or X-rays, which produce more curved paths, resulting in less linear tracks (Figure 3.10b) [49].

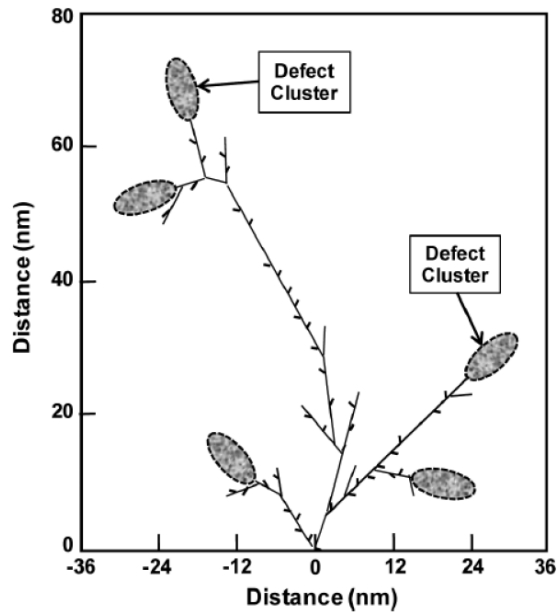


Figure 3.8: Conceptual illustration of the damage produced in Si by a 50-keV primary recoil atom with isolated defects and amorphous defect clusters shown [59].

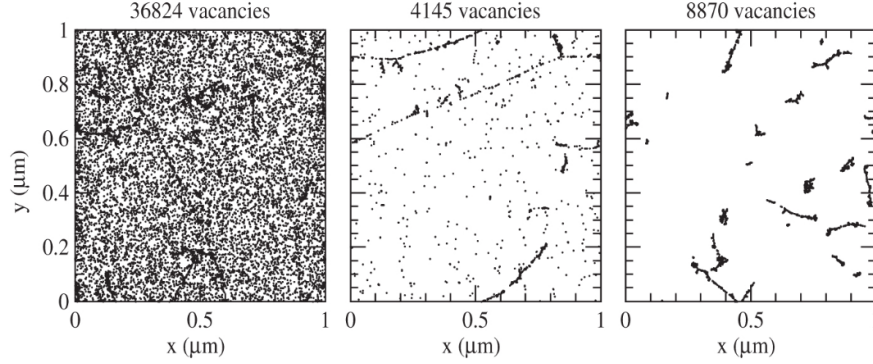


Figure 3.9: Initial distribution of vacancies produced by 10 MeV protons (left), 24 GeV protons (middle) and 1 MeV neutrons (right). The plots are projections over 1  $\mu\text{m}$  of depth ( $z$ ) and correspond to a fluence of  $1 \times 10^{14} \text{ cm}^{-2}$  [58].

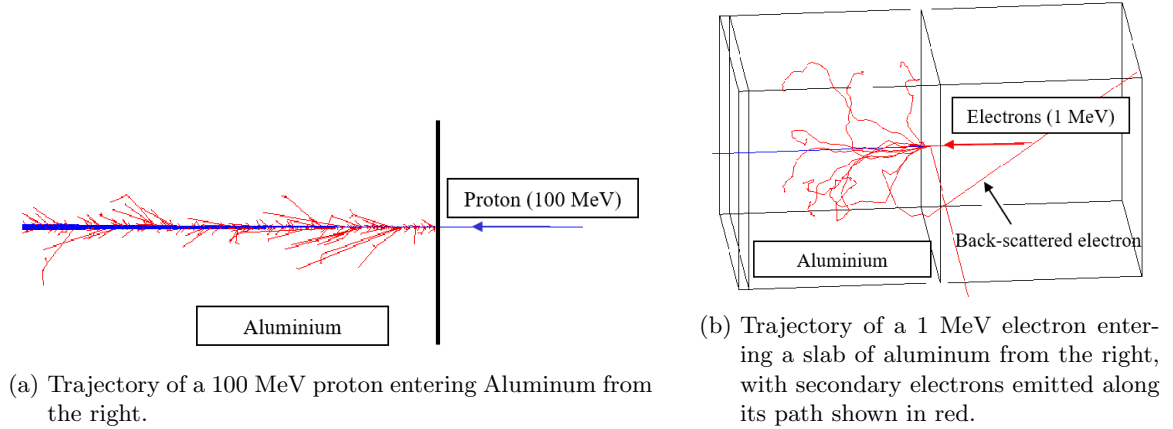


Figure 3.10: GEANT4 simulation results showcasing trajectories in Aluminum for a) a proton and b) a electron.

### 3.3.2 Formation of defect

The overall physical process, which allows the creation of stable defects since the passage of the particle, can be broken down into three stages described below and schematized in Figure 3.11 [51], [55], [57], [60]:

1. The first stage is the creation of displacement defects as explained in the previous section. Energetic particles incident on a solid can create displaced atoms (displacement damage) leading to the formation of Frenkel pairs, either localized on a single point or a local region of disorders. In general, incident energetic particles produce a mixture of isolated and clustered defects as described in Figure 3.8 and 3.9.
2. Following the initial displacement cascade, the second phase is known as the thermal spike. This event occurs on a very short timescale in the order of picoseconds, comparable to the time duration of the defect formation. This stage is characterized by a local temperature increase (hence the term "thermal spike") around the particle's path due to the energy not used for displacement but rather converted into vibrational energy. During this phase, the PKA can transfer its energy to the atoms within a small volume, leading to significantly high local energy densities. This can cause the material to reach its melting temperature, forming amorphous pockets. These pockets recrystallize quickly, within  $10^{-15}$  to  $10^{-12}$  seconds.

Experimental observations have confirmed the presence of such amorphous pockets following intense irradiation. The accumulation and coalescence of defects within these zones can cause them to grow to sizes that are observable with electron microscopy [60].

- Following the dissipation of energy characterized by the "thermal peak" and the formation of amorphous pockets ( $t = 10^{-13}$  to  $10^{-12}$  seconds), the defects undergoes an annealing stage with the creation of permanent and stable defect. The atomic lattice undergoes reorganization to minimize its potential energy, thereby reducing the crystalline disorder caused by the incident particle. This process involves the recombination of most initial vacancy-interstitial pairs with other defects from displacement damage or manufacturing processes. However, some defects (vacancies or interstitials) that do not recombine become mobile within the lattice through the thermal effect in the atomic network until they encounter another entity that stabilizes them. These entities are vacancies, interstitials, dopants, and impurities such as carbon or oxygen introduced during manufacturing processes or displacement damage. In Silicon, Frenkel pairs can remain stable when separated by about 1 nm. Given the mobility of vacancies even at liquid nitrogen temperatures, preventing the formation of these defects is impractical. The transition from initial vacancy-interstitial pairs to stable room temperature defects marks the "short-term annealing effects", a process typically concluding within seconds. The final pattern of damage remains concentrated in clusters areas, that were "hot" during the cascade. It's important to note that stable damage induced in space conditions tends to be very sparse. Long-term room temperature annealing may occur over days or weeks, but its impact is usually minor, rendering displacement damage a "permanent effect" in space-exposed devices.

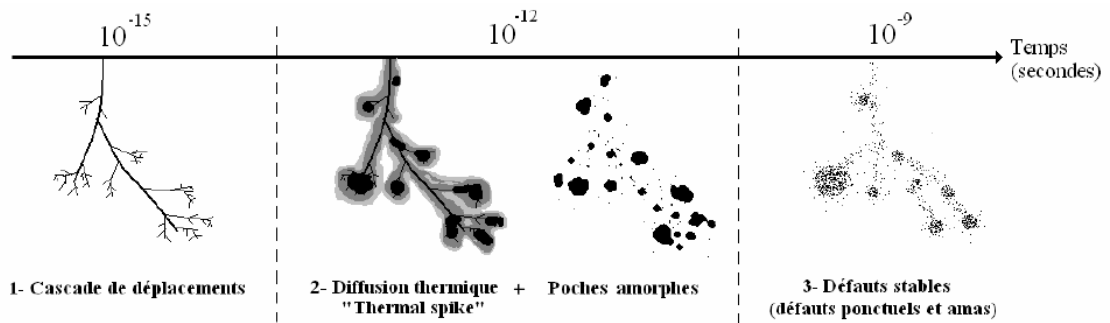


Figure 3.11: Stages of stable defect formation in irradiated materials: 1. Displacement cascades, 2. Thermal spike diffusion with amorphous pockets, and 3. Stable defect accumulation over time.

### 3.4 Effects of displacement damage in semi-conductors

Whether crystal defects arise from ionizing or displacement damage, they affect the electrical properties of semiconductors by introducing parasitic levels in the energy bandgap. These parasitic centres trigger physical mechanisms that degrade semiconductor characteristics, such as carrier lifetime and mobility. The effects of displacement damage manifest in the five ways depicted in Figure 3.13 [52], [53], [55], [61]:

- In the device depletion regions, where carrier density is low, **thermal generation of electron-hole pairs** is facilitated by the spontaneous transition of electrons to the conduction band or holes to the valence band. This process is further enhanced by intermediary levels, which assist in the transition of electrons from the valence band to the conduction band. Such mechanisms significantly increase the probability of electron-hole pair generation, leading to a rise in dark current. Energy levels located midgap within these depletion regions are highly effective in this generation mechanism.

- **Electron-hole recombination** occurs when a charge carrier is captured by a defect and stays unreleased until a carrier of the opposite charge is also captured. For instance, an electron held at a parasitic centre can combine with a captured hole, leading to either light emission, known as "radiative recombination," or the creation of vibrations in the lattice, termed "non-radiative recombination". The process of recombination is influenced by two main factors: the magnitude of the electric field, which can separate the pairs and the initial density of pairs produced by the incident particle. Notably, at a given electric field, the closer these pairs are initially, given a consistent electric field, the higher the chance of them recombining early on. As illustrated in Figure 3.12, the efficiency of this process varies with the type of particle involved, since each particle follows a distinct path behaviour through the material (Figure 3.10), influencing the spatial distribution of the electron-hole pairs it generates. The process of recombination reduces the minority carrier's lifetime.
- **Carrier trapping** happens when parasitic energy levels within the bandgap temporarily capture carriers. This process involves a carrier being seized by a defect and then released back to its original band. Such trapping results in a decrease in the concentration of majority carriers, as well as reductions in conductivity and mobility. In the context of a Charge-Coupled Device and, by extension, a PD, this phenomenon means that the signal charge might be trapped and only released after the signal packet has moved on, leading to a degradation in the charge transfer efficiency of the device.
- **Dopant compensation**, which leads to carrier removal, occurs when radiation-induced defects in p-type semiconductors introduce deep levels within the bandgap. These levels neutralize the effects of acceptor dopants by filling their levels, and the electrons from shallow donor levels are offset by these deep acceptor levels, effectively reducing the net carrier concentration.
- **Tunnelling effect** allows carriers to move from the conduction band to the valence band assisted by trap levels. In a p-n junction, the conduction band in the n-region may align with a defect-induced level in the p-region. Similarly, the valence band in the p-region may align with a defect-induced level in the n-region. This alignment allows carriers to move between regions at a constant energy level, which increases the number of collected charges and leads to higher leakage current.

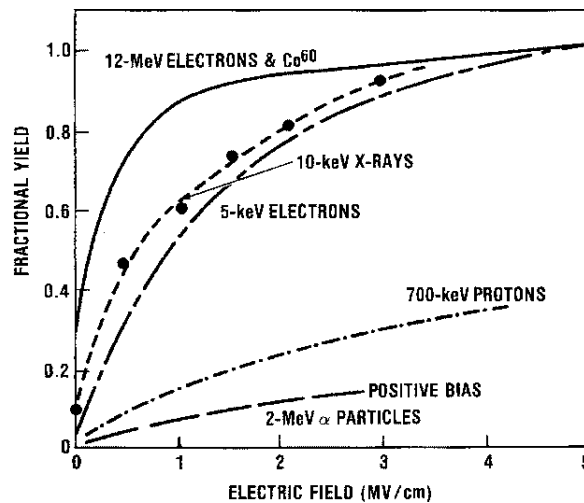


Figure 3.12: Experimental recombination yields for various incident particles as a function of the applied field [62].

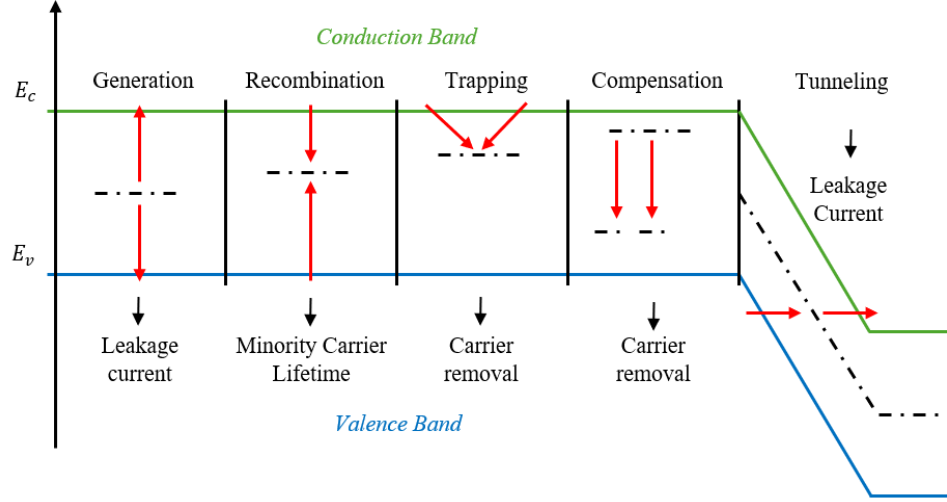


Figure 3.13: The five physical mechanisms created by crystal defects in the semi-conductor.

## 3.5 Modeling Radiation Damage in Semiconductors

The previous section offered a qualitative overview of radiation impacts on semiconductor devices. To thoroughly evaluate radiation effects and their implications, this section shifts our focus to quantitative assessment tools, introducing key concepts such as stopping power, NIEL, LET, and the damage factor.

### 3.5.1 Stopping power and cross section

As particles travel through a material, they lose energy due to mechanisms outlined in the previous section 3.2. The rate of energy loss per unit distance, known as stopping power, is typically measured in MeV/cm and is a key parameter in understanding particle-material interactions [49]. The stopping power quantifies the energy loss  $dE$  of an incoming particle with total energy  $E$ , over a distance  $dx$  in the material. This is mathematically expressed as the mean energy loss per unit length, as follows [49]:

$$-\frac{dE}{dx} = \frac{1}{dx} \int \frac{dP}{dQ} \cdot Q \cdot dQ \quad (3.1)$$

$dP$  denotes the probability of depositing energy  $Q$  within the interval  $[Q, Q + dQ]$ . In practice, the interaction probability is defined as a cross-sectional area equivalent,  $d\sigma$ , known as the cross-section. This metric quantifies the probability of a specific interaction between an incident particle and a target, resembling an area and measured in square centimetres or barns ( $1 \text{ barn} = 10^{-24} \text{ cm}^2$ ), defined as:

$$d\sigma = \frac{dP}{\rho \cdot dx} \quad (3.2)$$

By integrating equations 3.1 and 3.2, the energy loss can be expressed in function of the cross-section:

$$-\frac{dE}{dx} = \rho \int \frac{d\sigma}{dQ} \cdot Q \cdot dQ \quad (3.3)$$

It is reasonable to expect different probabilities and cross-sections based on the type of particle and the interaction nature. As such, the cross-section for a specific material changes based on the type of target particle and the interaction mechanism defined in section 3.2. Hence, each type of interaction is associated with a specific stopping power. [49], [63]:

- Electronic stopping power for interactions with electrons:  $\left. \frac{-dE}{dx} \right|_{\text{electronic}}$
- Nuclear stopping power for interactions with nuclei:  $\left. \frac{-dE}{dx} \right|_{\text{nuclear}}$
- Radiative stopping power for Bremsstrahlung emission:  $\left. \frac{-dE}{dx} \right|_{\text{radiative}}$

The total stopping power is the sum of the individual stopping powers for these interaction types:

$$\left. \frac{dE}{dx} \right|_{\text{total}} = \left. \frac{dE}{dx} \right|_{\text{electronic}} + \left. \frac{dE}{dx} \right|_{\text{nuclear}} + \left. \frac{dE}{dx} \right|_{\text{radiative}} \quad (3.4)$$

### 3.5.2 Linear Energy Transfer and Non-Ionizing Energy Loss

These stopping powers enable us to introduce two physical quantities: Linear Energy Transfer (LET) and Non-Ionising Energy Loss (NIEL). They measure energy deposition from interactions in materials, influenced by the material's properties, particle type, and energy  $E$  [49].

LET, measured in MeV/cm, quantifies energy loss primarily through ionization. This includes direct ionization from electronic interactions and energy loss from Bremsstrahlung emissions. X-rays and gamma rays from this process can also ionize other atoms. Thus, LET combines the stopping power from electronic interactions and radiative losses:

$$LET(E) \approx \left. \frac{-dE}{dx} \right|_{\text{electronic}} + \left. \frac{-dE}{dx} \right|_{\text{radiative}} \quad (3.5)$$

Similarly, NIEL, measured in MeV/g.cm, represents the energy lost to the nuclei of the target material per unit length, which causes atomic displacements and not ionization. NIEL is related to the nuclear-stopping power, which measures the energy loss per unit length due to nuclear collisions [49], [51]–[53]:

$$NIEL \approx \left. \frac{-dE}{dx} \right|_{\text{nuclear}} \quad (3.6)$$

Defined by the equation of stopping power, NIEL is expressed as follows:

$$NIEL = \left. \frac{dE}{dx} \right|_{\text{nuclear}} = \rho \int_{Q_{\min}}^{Q_{\max}} \frac{d\sigma}{dQ} \cdot Q dQ, \quad (3.7)$$

where,  $Q_{\min}$  and  $Q_{\max}$  denote the minimum and maximum energy levels that incident particles can transfer to the target's nuclei. Not all energy transferred to target nuclei directly leads to displacement damage; a part of this energy ionizes the medium, and only a specific segment contributes to defect creation. The Lindhard function provides a fraction of energy that results in atomic displacements rather than ionization [64]. The Kinchin-Pease model proposes a simplified approach to estimate radiation damage in materials. As an incident ion decelerates within the material, the primary damage mechanism involves elastic collisions with nuclei, leading to atomic displacements. Initially, electronic stopping can be significant for high-energy ions, but as the ion loses energy nuclear stopping becomes dominant. The model primarily focuses on the energy transferred to the lattice, known as the nuclear-deposited energy. The energy deposited by nuclear interactions refers to the amount of energy transferred from the incident particle to the target nuclei, causing atoms to be displaced from their lattice positions. This displacement occurs when the transferred recoil energy ( $Q$ ) exceeds the displacement damage threshold ( $E_d$ ), which is the minimum energy required to dislodge an atom from its lattice site, creating a defect [63], [65]. The displacement damage threshold and mechanism of this process will be developed in the next section 3.3. It's crucial to emphasize the significance of the displacement damage threshold in NIEL calculation, as it dictates the portion of nuclear-deposited energy that plays a role in defect formation. Software tools like NEMO [66] or SR-NIEL [67] use this threshold to compute NIEL values. By integrating over the energy transfer cross-section and incorporating the displacement damage threshold, these tools provide predictions of radiation damage in materials based on the NIEL scaling approach, developed in the next section.

### 3.5.3 Displacement damage threshold

From the energy loss ( $E_d$ ) to non-ionizing energy, creating displacement damage in the materials exposed to radiation requires the recoil atom to possess energy exceeding the Threshold Displacement Energy noted  $E_d$ . This threshold demarcates a binary condition where displacements are improbable below the TDE and almost certain above it.

$$P_n(E) = \begin{cases} 0 & \text{for } T_d < E_d \\ 1 & \text{for } T_d > E_d \end{cases} \quad (3.8)$$

The Kinchin-Pease model [65], one of the simplest and earliest approaches, provides a fundamental estimation of radiation damage by examining kinetic energy transfers that surpass a material's specific TDE. According to this model, the energy required to generate a stable defect must be higher than  $2E_d$ . This stipulation arises because a PKA displaced by radiation needs sufficient energy to not only surpass its displacement energy but also to confer additional energy onto another atom to create two defects, hence forming a Frenkel pair. This cascade effect is crucial for forming stable defects, leading to a straightforward damage calculation formula:  $\frac{T_d}{2E_d}$ , where  $T_d$  is the energy imparted by nuclear interactions, and  $E_d$  is the TDE.

However, even at cryogenic temperatures, spontaneous recombination of vacancies and interstitials can occur within several lattice spacings during the annealing process described in Section 3.3. The NRT Model [68] developed by Norgett, Robinson, and Torrens, addresses this by introducing a prefactor of 0.8. This adjustment accounts for the probability that around 20% of displaced atom sites might be refilled.

More sophisticated models have been developed, such as the Athermal Recombination Corrected (arc)-dpa Model. Stemming from molecular dynamics simulations, this contemporary model provides a detailed perspective on defect production both during and after the displacement cascade phase. It acknowledges the higher likelihood of Frenkel defect recombination as atomic velocities diminish and incorporates a refined displacement calculation formula. This formula takes into account the energy-dependent cascade radius and the distances over which spontaneous recombination occurs, offering a more nuanced understanding of defect formation processes [69], [70].

### 3.5.4 Radiation Dose

Radiation degradation materials are quantitatively assessed through the concept of dose, which represents the average energy deposited via ionization per unit mass of irradiated material. This absorbed dose is measured in Grays (Gy), with one gray equivalent to one joule of energy absorbed per kilogram of material. Alternatively, the dose can be expressed in rads (rd), where one rad equals an energy density of 100 ergs per gram (1 rad = 1 Gy) [49].

Consider a material of mass  $m$  irradiated by  $N_{part}$  particles, each depositing energy  $dE$ . The dose is defined in equation 3.9.

$$Dose = N_{part} \cdot \frac{dE}{m}, \quad (3.9)$$

where  $N_{part}$  represents the number of incident particles equivalent to the product of fluence  $\phi$  and the exposed section  $S$  of the sample.  $m$ , the mass of the sample is the product of the volume of the sample  $Sdx$  with the material's density  $\rho$ . Therefore, Equation 3.9 can be rewritten as:

$$Dose = \Phi \cdot S \frac{dE}{S \cdot dx \cdot \rho} = \Phi \cdot \left( \frac{1}{\rho} \frac{dE}{dx} \right). \quad (3.10)$$

In Equation 3.10, the stopping power concept appears. Two variations of dose can be distinguished, each corresponding to a specific type of damage. The ionizing dose, associated with ionizing damage, is formulated in terms of the LET as:

$$Dose = \Phi \cdot LET. \quad (3.11)$$

Similarly, the DDD measured in MeV/g, quantifies the energy deposited due to non-ionizing interactions caused by atomic displacements in the material. The DDD, analogue to ionizing dose is derived from the product of particle fluence and the NIEL, as shown in Equation 3.12 [49], [59].

$$DDD = \Phi \cdot NIEL. \quad (3.12)$$

These dose expressions are valid under the assumption that particle trajectories are nearly straight and that NIEL and LET do not significantly vary as the particle travels through the material.

## 3.6 From experimental damage factor to the NIEL

### 3.6.1 Experimental damage factor

Predicting irradiation damage on devices, such as the new LISA InGaAs QPRs, relies on understanding the material's response to radiation. Hence, let's introduce a theoretical parameter ( $k$ ) representing the material's response to radiation. As explored in section 3.3, the spacial environment, detailed in section 3.1, can impact the performance of optoelectronic devices by introducing displacement defects (interstitial and vacancies) into the material. Thus,  $k$  is defined as the number of defects created by the incident particle along its path, with the unit being the number of defects per meter. Due to the principles outlined in section 3.3, this parameter has to be contingent upon the energy ( $E$ ) and the type of the incident particle involved. Additionally, in section 2.3.3, dark current results from natural defects in the semiconductor material inherent to the fabrication process, meaning that dark current is proportional to the number of defects in the semiconductor. Therefore, when the semiconductor is irradiated, this introduces a new set of defects, denoted as  $N_{\text{defects, Irr}}$ , leading to an increase in the dark current proportionate to  $N_{\text{defects, Irr}}$ . The resulting increase in  $\Delta I_{\text{dark}}$  is defined by Equation 3.13.

$$\Delta I_{\text{dark}} \propto N_{\text{defects, Irr}} = k_{\text{InGaAs}}(E, \text{particle}) \cdot \Phi \cdot V \quad (3.13)$$

The volume is given by  $V = W \cdot S$  with  $S$  as the surface area of the PD, and  $W$  representing its depletion thickness. By rearranging Equation 3.13, we introduce the experimental damage factor for dark current ( $K_{\text{Idark}}$ ), defined as follows:

$$K_{\text{Idark}} = \frac{\Delta I_{\text{dark}}}{\Phi \cdot W \cdot S} \propto k(E, \text{particle}) \quad (3.14)$$

The use of a damage factor to quantify radiation-induced damage is not new. Early models expressed radiation-induced dark current density using a damage factor, as shown in the equation below [71]:

$$\Delta J_{\text{dark}} = \frac{q \cdot n_i \cdot \Phi \cdot W}{K_g}, \quad (3.15)$$

where  $q$  is the electronic charge,  $n_i$  the intrinsic carrier concentration,  $\Phi$  the particle fluence,  $W$  the width of the depletion region, and  $K_g$  the damage factor, which in this case, represents the generation lifetime coefficient for given particle types and energies. Throughout history, the damage coefficient has taken multiple forms, with  $K_p$  the damage factor by particle type [72],  $\alpha$  the damage coefficient for high energies [73], and  $K_{de}$  the mean radiation-induced increase in dark current density per unit amount of damage energy deposited in the depletion region [74]. However, these coefficients are all derived by fitting simulation data to experimental data, rendering them valid within certain energy ranges, fluences, or particle types, depending on the experimental data employed.

To overcome these limitations, Srour introduced a universal damage factor, established experimentally across a diverse number of devices, types, and fluences [75]. This universal damage coefficient, denoted as  $K_{\text{dark}}$ , quantifies the number of carriers thermally generated per unit volume per unit time in a depletion region per unit non-ionizing dose deposited in that volume [75].

$$\Delta J_{\text{dark}} = qc\dot{W} \cdot K_{\text{dark}} \cdot DDD \quad (3.16)$$

The concept of the universal damage factor  $K_{\text{dark}}$ , introduced by [75], corresponds to our experimental damage factor  $K_{\text{Idark}}$ . Both parameters serve to quantify the increase in dark current caused by radiation-induced defects. The main distinction is that  $K_{\text{dark}}$  is directly linked to a theoretical parameter, the NIEL, through the DDD (see section 3.5.4,  $DDD = NIEL \cdot \Phi$ ), while  $K_{\text{Idark}}$  is only proportional to a theoretical parameter  $k$  which according to section 3.5.3,  $k$  can be linked to NIEL using  $E_d$  and the mass density  $\rho$  based on the following equation:

$$k(E, \text{particle}) = NIEL \cdot \frac{1}{2E_d \cdot \rho} \quad (3.17)$$

### 3.6.2 NIEL scaling approach

The linear relationship between the experimental damage factor and the NIEL is primordial. Indeed, as early as the 1960s, researchers aimed to link semiconductor device damage with various particle types and their energies, driven by the potential ability to predict device responses to radiation exposure. Yet, converting fundamental defect data into practical guidelines for device design poses significant challenges. For instance, predicting the lifespan of minority carriers in a material post-radiation exposure demands a comprehensive understanding of the induced defects, including their energy levels, concentrations, and probabilities of capturing or releasing electrons and holes [51]. In 1980, Van Lint et al. compiled insights into and constraints on displacement damage correlation, underscoring the difficulties encountered with the cluster interpretation of neutron damage and its implications for correlational studies [76].

In 1987, research conducted by Summers and Marshall [77], [78] demonstrated that the damage factor for various particles is directly proportional to the initial number of defects produced, unaffected by subsequent defect cascades. They established a linear relationship between the non-ionizing energy deposition in the silicon lattice and the observed device degradation, enabling precise predictions of irradiation effects. From there subsequent research confirmed that, to first order, a linear relationship exists between particle-induced displacement damage and across various electrical parameters, incident particles, and device materials [51], [79]–[82].

This foundational understanding of the linear correlation between displacement damage and NIEL has laid the groundwork for the development of the 'NIEL scaling approach'. This approach allows to scale of the damage factor  $K_{\text{dark}}$  with the NIEL, facilitating a relative comparison of damage across different environments. This method enables extrapolating the experimental damage factor to various energy levels and particle types, significantly reducing the number of irradiation campaigns and tests required. Consequently, this approach allows the reduction of specifications to a fluence equivalent, also known as the DDEF, streamlining the evaluation process and improving efficiency in radiation testing and mission planning. Moreover, it aids in predicting the response of devices during missions with greater accuracy.

### 3.6.3 NIEL limitation

The NIEL scaling approach has limitations that must be considered for accurate predictions of device radiation tolerance, including some deviation with energy, particles types, and materials, such as [51], [60], [79], [81], [83]–[87]:

- NIEL calculations may deviate at very low particle energies for proton and electrons (<keV), approaching displacement energy thresholds. While not a major concern for applications in space due to minimal contribution to total displacement damage, it's an inherent limitation [51].
- Deviation is often observed between electron results and NIEL calculations [60], [83], [86].
- III-V materials deviation can be found for medium to high energy protons with some device's experimental data aligning closer to theoretical inelastic and others to the elastic NIEL curves [51], [88], [89].

- For silicon solar cells, a linear correlation with NIEL is observed for n-type material, whereas p-type material exhibits a quadratic dependence on NIEL, indicating material-dependent limitations in NIEL’s predictive accuracy [51], [53].

The observed deviations stem from multiple factors. These include variations in operating conditions, complex relationships between electrical parameters and damage levels, technological variances, and measurement inaccuracies. Additionally, discrepancies may arise from the theoretical NIEL curves, which rely on simulations that have their limitations. The effectiveness and applicability of simulation codes like MARLOWE in calculating recombination efficiency highlight limitations in static models and the need for dynamic modelling to capture the complexities of displacement damage accurately [51], [53]. The selection of a damage function, determining energy dependence through either calculated NIEL or experimental damage factors, has proven also to play a significant role in those discrepancies. For example, experimental data can be used to obtain an ‘effective’ value of the NIEL and reduce these deviations [70], [90], [91]. For low energy electrons, the use of a threshold distribution with the  $E_d$  values listed by Konobeiev [70] helps correct the deviation at low energies [92]. Hence, the choice between calculated NIEL and experimental damage factors as the damage function significantly influences the predicted on-orbit degradation, indicating the importance of selecting an appropriate damage model for accurate predictions.

## 3.7 Radiation resilience requirements for LISA

### 3.7.1 Non-ionizing Dose

The LISA mission, adhering to the ECSS standard, utilizes the NASA GSFC ESP model [93] for its environment model, incorporating data of solar particle events from three solar cycles to predict proton fluences and the presence of heavier ions up to uranium at 1 AU. The model’s approach is both statistical and analytical, offering predictions with user-defined confidence levels, typically at or below 95%. For the LISA mission, a confidence level of 90% has been selected. The model’s assumptions include a maximum time during solar maximum within an 11-year cycle, with a 4-year minimum, and a negligible impact from solar minimum periods. This impacts LISA’s 12.5-year mission by equating to 8.5 years of fluence exposure, considering these assumptions and conditions [41]. Figure 3.14 presents the model’s predictions for the average cumulative fluence over the mission’s nominal duration, both in integral and differential terms.

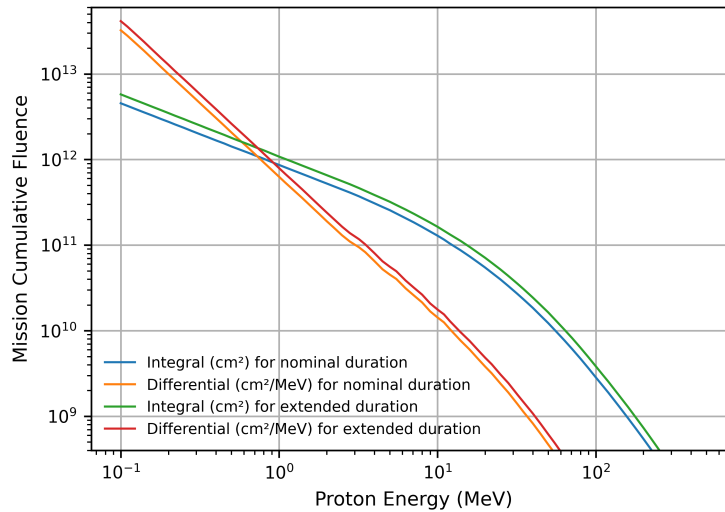


Figure 3.14: Mean cumulative solar proton flux spectra for the nominal LISA mission duration [41].

Based on this model, ESA has established the requirements for the InGaAs QPD, summarized

in Table 3.1. These specifications are defined for both extended and nominal mission durations, considering a 3 mm aluminium shielding for the InGaAs DDD.

Table 3.1: Radiation requirements from ESA for LISA QPR

Requirements	Energy (MeV)	DDD (MeV/g) (InGaAs)	DDEF (p/cm <sup>2</sup> )
Nominal duration	10	$5.10 \times 10^8$	$7.74 \times 10^{10}$
	20	$5.10 \times 10^8$	$1.09 \times 10^{11}$
	60	$5.10 \times 10^8$	$1.38 \times 10^{11}$
Extended	10	$6.62 \times 10^8$	$1.01 \times 10^{11}$
	20	$6.62 \times 10^8$	$1.41 \times 10^{11}$
	60	$6.62 \times 10^8$	$1.80 \times 10^{11}$

### 3.7.2 Ionizing Dose

For the ionizing dose, the reference [41] use the SHIELDOSE [94] for calculating the ionizing dose-depth curve. This approach relies on pre-calculated doses from electrons, electron-induced Bremsstrahlung, and protons based on Monte-Carlo simulations, related to material shielding thickness, with a solid aluminium sphere as the reference configuration. For a shielding of 3 mm the TID in Silicon is 15 krad for the nominal duration and 20 krad for an extended duration with a design margin factor of two the requirements are set to 40 krad for the all mission duration [15, p.100], [41]. In the report [95], the requirement was also set at 40 krad, but it is unclear whether a margin factor of 2 was included in this specification.

### 3.7.3 LISA requirements using OMERE Software

The main objective of this section is to find the ESA requirements and validate the experimental conditions that will be utilized during the irradiation campaigns (see section 4.2) using a second source OMERE. OMERE, an advanced software developed by TRAD with the support of Centre national d'études spatiales (CNES), is specifically designed for the analysis of space environments and the evaluation of radiation effects on electronic components. It can evaluate the impact of the space environment on electronics, including dose, atomic displacement, single-event effects, and degradation of solar cells. For this simulation, the assumptions are:

- The NASA GSFC ESP model [93] for the values of the cumulative fluence over the mission duration, similar to [41].
- The NIEL values for In<sub>0.53</sub>Ga<sub>0.47</sub>As presented on Figure 3.15 and obtained from NEMO [66]. The energy thresholds ( $E_d$ ) used for NEMO's calculation are 15 eV for In, 10 eV for Ga, and 10 eV for As, as adopted by [96].
- An assumed 3 mm aluminium shield for the optical bench, consistent with [95], and mirroring the 2.5 mm shielding for the laser reported in [25], given its similar position on the bench.

The DDEF results from OMERE for proton energies of 10 MeV, 20 MeV, and 60 MeV are presented in Figure 3.16 and resume in Table 3.2. The inclusion of 20 and 60 MeV aligns with the proton irradiation energies applied during the irradiation campaign, as detailed in section 4.2.

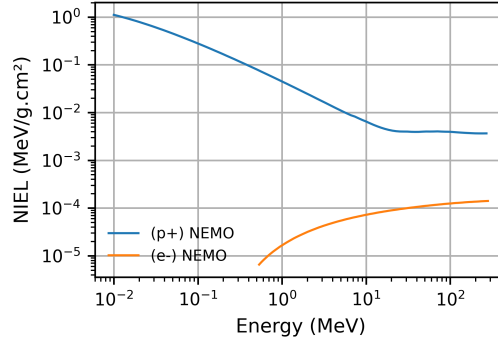
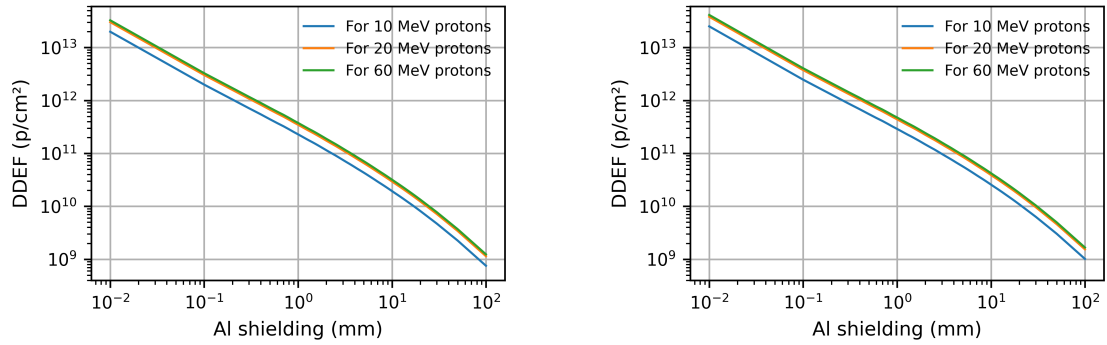


Figure 3.15: NIEL curve from NEMO for InGaAs both proton and electron



(a) DDEF for nominal mission duration

(b) DDEF for extended mission duration

Figure 3.16: The DDEF of 10 MeV, 20 MeV, and 60 MeV proton fluence as a function of shielding thickness for (a) nominal and (b) extended mission durations.

Table 3.2: Radiation requirement from ESA for LISA QPD

Requierements	Energy (MeV)	DDEF (p/cm <sup>2</sup> ) (OMERE)	DDEF (p/cm <sup>2</sup> ) (ESA)
Nominal duration	10	$7.52 \times 10^{10}$	$7.74 \times 10^{10}$
	20	$1.14 \times 10^{11}$	$1.09 \times 10^{11}$
	60	$1.24 \times 10^{11}$	$1.38 \times 10^{11}$
Extended	10	$9.75 \times 10^{10}$	$1.01 \times 10^{11}$
	20	$1.48 \times 10^{11}$	$1.41 \times 10^{11}$
	60	$1.60 \times 10^{11}$	$1.80 \times 10^{11}$

In conclusion, the DDEF requirements exhibit a high degree of similarity, validating the criteria for LISA and enabling the selection of relevant experimental fluences for the irradiation campaign discussed in Section 4.2. The observed discrepancies are likely attributable to variations in NIEL values between ESA and our analyses. Regarding dose assessment, OMERE's application of the NASA GSFC ESP model indicates a TID of 30 krad for the nominal mission duration and 40 krad for the extended duration. This results in a factor of two difference between LISA's requirements and OMERE's results, which can be explained by the use of different models (SHIELDOSE and NASA GSFC ESP).

## Chapter 4

# Irradiation Campaigns and LISA QPD and QPR tests

LISA will be the first space-based GW detector. As discussed in Chapter 2, GWs detection necessitates high-precision laser interferometers. A critical component is the QPR, which consists of a QPD and FEE, as illustrated in Figure 2.8. LISA's stringent requirements for its QPD and QPR include:

- A dark current per QPD segment of less than  $1 \mu\text{A}$  within LISA's operational temperature range of  $10$  to  $30^\circ\text{C}$ .
- A QE per QPD segment greater than  $80\%$  at  $1064 \text{ nm}$ .
- A noise level per QPR channel below  $2 \text{ pA}/\sqrt{\text{Hz}}$  across the operational bandwidth of  $3$  to  $30 \text{ MHz}$ .

However, as seen in Chapter 3, LISA will encounter various types of radiation that could affect the electrical properties of its QPDs and QPRs. The LISA radiation requirements are reiterated here:

- TID of  $40 \text{ krad}$
- DDD of  $6.62 \times 10^8 \text{ MeV g}^{-1}$

To ensure LISA's optimal performance throughout its mission, it is imperative to assess the radiation effects. This chapter outlines the LISA QPR, the methodology for evaluating QPDs and FEEs and the irradiation protocol. It details the approach to quantify the space environment's radiation impact on the performance of QPDs and QPRs, with a focus on dark current, QE, and EICN levels, in alignment with the previously stated LISA requirements. Additionally, it examines the impact on LISA's measurement capabilities.

## 4.1 Overview of LISA Photoreceivers

### 4.1.1 InGaAs Quadrant Photodiode (QPD)

The first element of the QPR is the QPD, responsible for converting the interference signal between optical beams of disparate powers ( $700 \text{ pW}$  and  $1 \text{ mW}$ ) at a wavelength of  $1064 \text{ nm}$  into a photocurrent ( $I_{\text{ph}}$ ).

The QPDs tested in this thesis are custom-made devices produced by JP (Hamamatsu industry), referred to now as JP QPDs and NL (Bright Photonics & SMART Photonics industries), referred to as NL QPDs. They were specifically designed for the LISA mission and thus optimised to have

low capacitance, and low noise while having a large photosensitive surface. The chosen absorber material for both QPDs is Indium Gallium Arsenide for optimum QE at LISA wavelength of 1064 nm. The molar proportions of indium (In), gallium (Ga), and Arsenic in both device types are  $\text{In}_{0.53}\text{Ga}_{0.47}\text{As}$ , note from now and the rest of the manuscript as InGaAs. To enhance further light detection and minimize stray light, the QPD surface is equipped with an anti-reflecting coating, aiming for a power reflectivity of less than 0.2%. As mentioned before, both JP and NL QPDs are Quadrant Photodiode (QPD), which means they have four quadrants, with each quadrant separated by a cross gap of 20  $\mu\text{m}$ . Each quadrant is referred to as a segment and is labelled A, B, C, or D according to Figure 4.1.

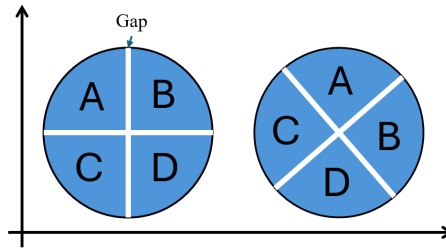


Figure 4.1: Labeling scheme of JP and NL QPDs (the QPDs are facing the LASER beam).

### JP QPDs

Figure 4.2 is a picture of the received QPDs for tests from JP. In total 15 QPDs were given in three different diameters (1.0, 1.5, and 2.0 mm) for the photosensitive area and five QPD samples for each size, in a TO5 packaging. For each set of QPDs size, a number from 1 to 5 is attributed to each QPDs. For each set, the QPD n°1 is not irradiated and is kept as the reference.

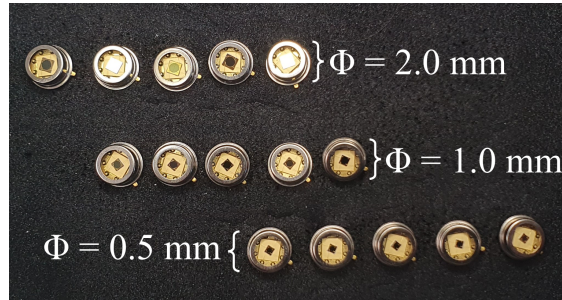


Figure 4.2: JP QPDs of 1.0, 1.5, and 2.0 mm diameter and labelled 1, 2, 3, 4, and 5 from left to right.

### NL QPDs

Figure 4.3 is a picture of the NL QPDs. In total, four QPDs of a unique size of 1.5 mm were given, in a TO5 packaging. Similar to the JP QPDs, each QPD is given a number (here from 1 to 4), number 1 being the reference QPDs.



Figure 4.3: NL QPDs of 1.5 mm diameter labelled 1, 2, 3, and 4 from left to right.

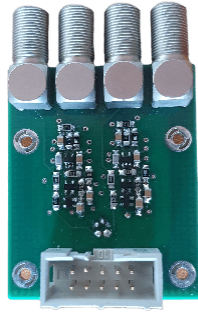
Table 4.1 sum up the information of the different QPD used for the thesis regarding their key parameters such as the diameters of photosensitive surface, numbers, origin, cross gaps (corresponding to the 'gap' separating each segment see Figures ), doping levels, standard reverse bias voltages ( $V_{\text{bias}}$ ), and full depletion voltages for each QPDs. Note that the information on those components is relatively limited as they are new non-commercial devices.

Table 4.1: Key Parameters of JP and NL QPDs.

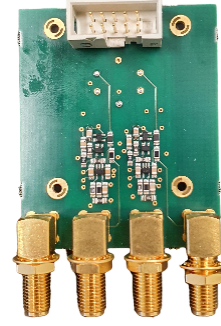
Origin	JP			NL
Diameter (mm)	1.0	1.5	2.0	1.5
Cross gap ( $\mu\text{m}$ )	20	20	20	20
Numbers	5	5	5	4
Doping level ( $\text{cm}^{-3}$ )				$< 1 \times 10^{14}$
Standard $V_{\text{bias}}$ (V)	5	5	5	20
Full depletion voltage (V)	$\approx 3.5$	$\approx 3.5$	$\approx 3.5$	$\approx 15$

#### 4.1.2 Front Ends Electronics

The second element of the QPR is the FEE, in charge of amplifying the photocurrent generated by the QPD and converting it into a voltage so the interferometric signal can be processed and the GW information extracted. The FEE is also a custom design made for the LISA mission by DE (Albert Einstein Institute (AEI)) to be ultra-low EICN. References [97]–[99] give more detailed information on the FEE electronics. The FEE is composed of four independent channels for each QPD segment. Each channel used a traditional op amps TIA for conversation and amplification of the photocurrent, combined with a heterojunction bipolar transistor for noise reduction. The FEE is powered by three DC voltages:  $\pm 5\text{V}$  for the TIA, and a specific reverse bias voltage for the QPDs, set at 5V for JP QPD and 30V for NL QPD. To face the difference between the two types of packaging (TO5 and TO8), two types of FEE cards were made. On Figure 4.4, is on the left a picture of the FEE for NL QPDs and on the right a picture of the FEE for JP QPDs. Both FEE cards have the same design except for two points. First, their size is adapted to the QPD packaging. Secondly, when the QPDs is coupled with the FEE its orientation is imposed leaving a distinct configuration for JP and NL QPDs. As represented in Figure 4.1, the cross gap axis for JP QPDs (right of the Figure) are rotated by 45 deg compared to NL QPDs (left of the Figure).



(a) FEE card adapt to TO5 packaging



(b) FEE card adapt to TO8 packaging

Figure 4.4: Picture of LISA’s FEE card provided by DE.

## 4.2 Irradiation Campaigns

### 4.2.1 Irradiation Facilities

#### Protons irradiation facility: Centre Antoine Lacassagne (CAL)

Located in Nice, France, the Mediterranean Institute of Proton Therapy at the CAL hosts the MEDICYC facility. Equipped with a 65 MeV isochronous cyclotron, MEDICYC primarily serves ocular proton therapy. Besides clinical use, it hosts an R&D beamline for irradiation hardness tests on electrical and optical components. In early 2022, the CNES officially validated this R&D beamline, affirming its suitability for irradiation tests. This approval was based on a thorough comparison of beam characteristics at CAL and the UCL facility in Belgium, as highlighted in the referenced study [100]. The proton fluence received by each device under test is measured in real-time using a large surface transmission ionization chamber. The chamber spans the entire beam field and amplifies the beam current approximately 100 times. Before each irradiation session, the following beam characteristics are measured [95], [100]:

- **Beam Field Homogeneity:** is measured using gafchromic film. A homogeneity of better than 5% over the total beam-field is required, although typically a value of 3% is achieved. Inhomogeneities are mainly due to a small drop-off at the edge of the beam field. On small scales ( $\approx$ cm), the homogeneity is better than 1%.
- **Proton Energy:** is measured within 0.1 MeV of the nominal value.
- **Ionization Chamber Gain:** is measured with a Faraday cup for each planned beam energy and for each decade in flux. However, being a destructive measurement technique, it’s not applicable during the irradiation process.

Figure 4.5 contains (from the right) the final bending magnet (M4), the beam nozzle and the irradiation table. The beam field diameter at the position of the devices is 100mm. Detailed information about the installation can be found in [101].

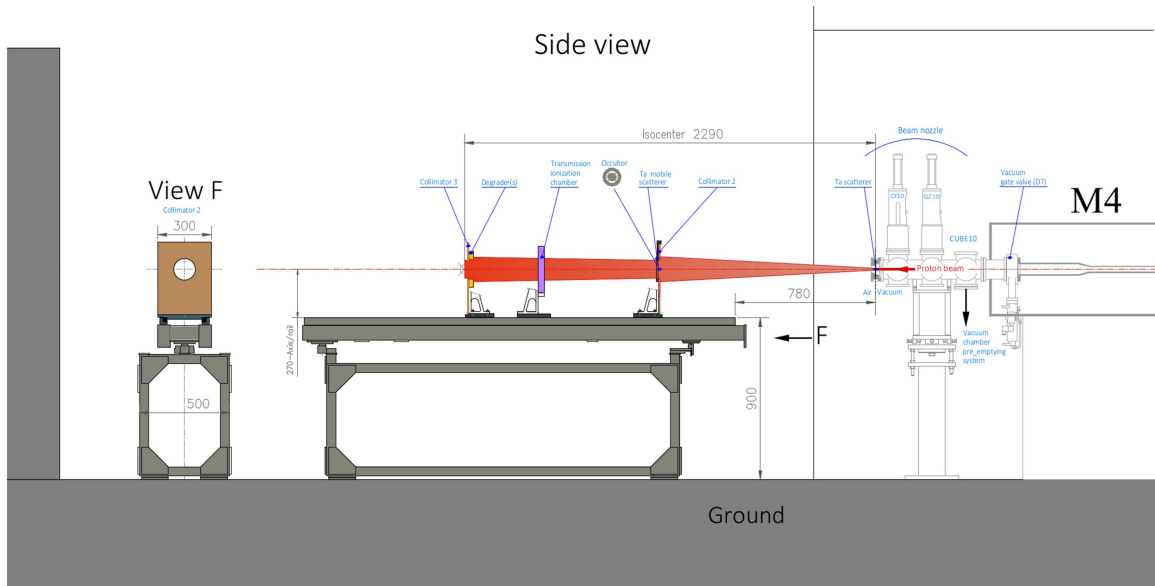


Figure 4.5: Side view of R&D irradiation room at CAL proton facility.

For the irradiation campaigns, a custom mechanical structure was designed to hold on the irradiation bench, two custom Printed Circuit Boards (PCB) measuring approximately 44 mm in length and 36 mm in height (see Figure 4.6, left). Each PCB is specifically designed to hold QPDs of either TO5 (JP QPDs) or TO8 (NL QPDs) packages and provide a bias voltage of 5 V for JP QPD and 30 V for NL QPD. Figure 4.6 shows the QPDs mounting support with the top PCB hosting one NL QPD, while the bottom PCB hosts three JP QPDs of sizes 1.0, 1.5, and 2.0 mm in TO5 packaging, along with two US QPDs of 0.5 and 1.0 mm not presented in this study.

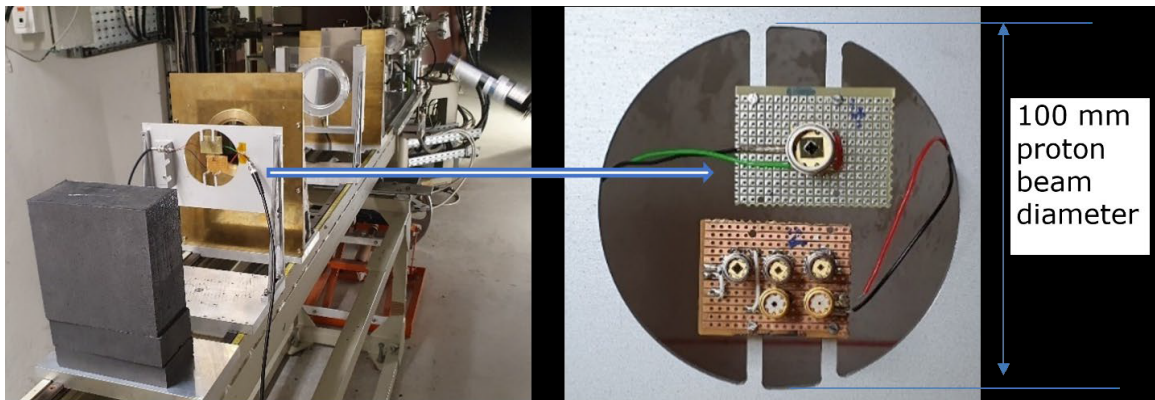


Figure 4.6: Left) CAL Proton beamline, including the QPD mounting. Right) Zoom on QPD mounting.

### Electrons Irradiation Facility: ONERA

Electron irradiation took place at the AXEL facility, at ONERA Toulouse centre in France, as depicted in Figure 4.7. This facility is equipped with two Van de Graaff accelerators, specifically made for the testing of materials and components. These accelerators are connected to the MIRAGE target chamber, allowing for electron and proton irradiation tests on devices within the same infrastructure. MIRAGE was originally developed to assess the durability of devices against various dose effects,

including both ionizing and non-ionizing radiation. The standard beam specifications include [102], [103]:

- Continuous beams : (scattered) electrons and (swept)protons
- Maximum energy outputs of 2 MeV for protons and 1.3 MeV for electrons
- Beam homogeneity of 10% across a 140 mm by 140 mm area.
- Stability and energy accuracy below 1%
- Beam current ranging from 1 to 80 nA on target, with a flux ranging from  $6 \times 10^9$  to  $5 \times 10^{11}$  part./cm s<sup>2</sup>
- Temperature monitoring from -150°C to +400°C.

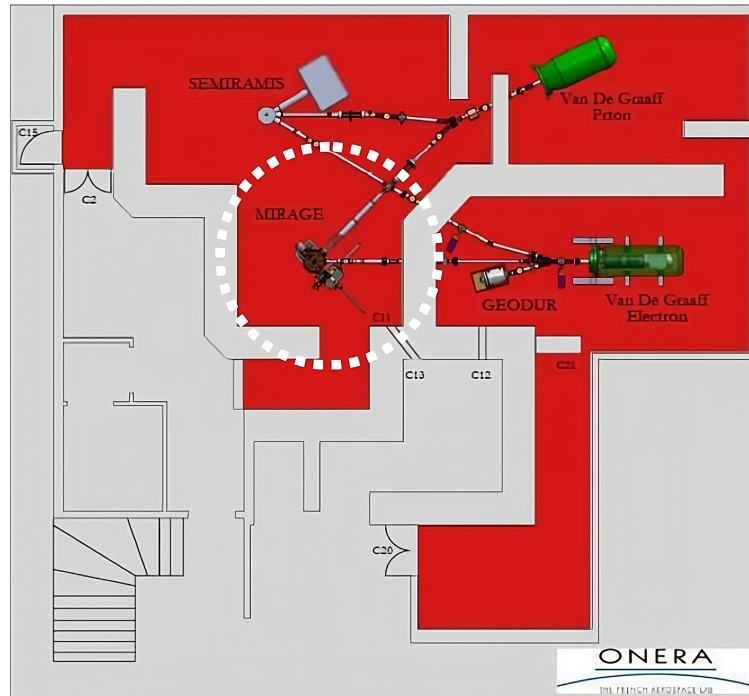


Figure 4.7: The accelerators and beam lines at ONERA (Mirage is highlighted with broken white line).

Samples were placed under a vacuum of  $1 \times 10^{-6}$  to  $1 \times 10^{-7}$  mbar. The QPDs were mounted on a small copper support, and integrated into a water cooling system to prevent overheating during irradiation, as illustrated in Figure 4.8.



Figure 4.8: Picture of the QPD copper support in the void chamber.

#### Gamma rays Irradiation Facility: ONERA

The gamma irradiation campaign was conducted at the MEGA facility, located at the ONERA Toulouse Centre. An image of the facility is shown in Figure 4.9, highlighting the  $\text{Co}^{60}$  gamma source (1), mounted on an automated mechanical Z-axis translation system. This setup allows precise control of the source's position relative to the devices tested, including (2) NL QPDs and (3) JP QPDs. The source-to-QPD distance is 19 cm which gives a dose rate of 60 Gy/hour. The overall accuracy is  $\pm 10\%$  and dosimetry was conducted using ionization chambers.

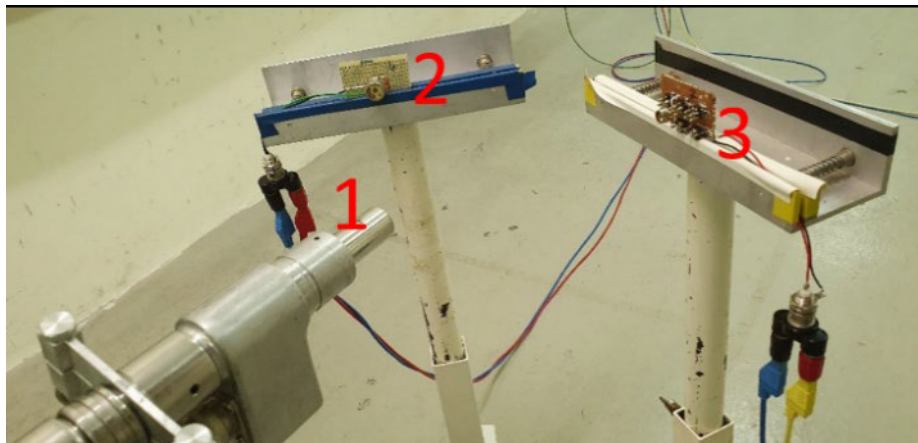


Figure 4.9: Picture of the QPD copper support in the void chamber.

#### 4.2.2 Irradiation conditions

The QPDs underwent three distinct irradiation campaigns: proton, electron, and gamma-ray at the ONERA and CAL facilities, as detailed in the previous section. Table 4.2 specifies how NL and JP

QPDs were allocated across these irradiation types. Each QPD set, encompassing 1.0 mm JP, 1.5 mm JP, 2.0 mm JP, and 1.5 mm NL QPDs, was numerically labelled from 1 to 5, as explained in Section 4.1. Non-irradiated QPDs (number 1 or reference QPD) served as controls for comparison. In total, 15 QPDs were subjected to irradiation. However, due to limited availability, only one QPD from each type was exposed to each radiation type.

Table 4.2: Irradiation QPDs Organisation.

Particle Type	Energy	JP QPDs			NL QPDs
		1.0 mm	1.5 mm	2.0 mm	1.5 mm
Reference		n°1	n°1	n°1	n°1
Protons	20	n°2	n°2	n°2	n°2
	60	n°3	n°3	n°3	n°3
Electrons	0.5	n°4	n°4	n°4	✗
	1.0	n°5	✗	n°5	✗
Gamma		✗	n°5	✗	n°4

Table 4.3 outlines the final exposure conditions for all irradiation campaigns. The TID is simply the product of the applied fluence by the electronic stopping power of the particles provided by SRIM [104] for protons and ESTAR [105] for electrons. Similarly, the DDD is the product of the applied fluence by the NIEL calculated with NEMO [66]. For proton irradiation at 20 MeV and 60 MeV, a fluence of  $1.0 \times 10^{12}$  p/cm<sup>2</sup> was achieved, resulting in a TID of 237 krad and 104 krad, and a DDD in InGaAs of  $4.8 \times 10^9$  MeV/g and  $3.6 \times 10^9$  MeV/g, respectively. Electron irradiation, at energies of 0.5 and 1.0 MeV and a fluence of  $5.0 \times 10^{12}$  e/cm<sup>2</sup>, led to TID of 105 and 100 krad, with DDD of  $3.4 \times 10^9$  MeV/g and  $9.7 \times 10^9$  MeV/g. Gamma irradiation at 1.25 MeV resulted in a TID of 237 krad and a DDD of approximately  $7.6 \times 10^7$  MeV/g. These applied TID and DDD correspond to approximately five times the LISA requirements specified in Section 3.7.

Table 4.3: TID and DDD applied on QPDs for all Irradiation Campaigns.

Particle type	Energy (MeV)	Fluence (p/cm <sup>2</sup> )	TID (krad)	DDD (MeV/g)
Proton (CAL)	20	$1.0 \times 10^{12}$	237	$4.8 \times 10^9$
	60	$1.0 \times 10^{12}$	104	$3.6 \times 10^9$
Electron (ONERA)	0.5	$5.0 \times 10^{12}$	105	$3.4 \times 10^7$
	1.0	$5.0 \times 10^{12}$	100	$9.7 \times 10^7$
Gamma (ONERA)	1.25		237	$\sim 1 \times 10^7$

Achieving the final fluence was a multi-step process, detailed in Table 4.4. For proton irradiation, the fluences cover a large range from  $2.0 \times 10^9$  p/cm<sup>2</sup> to  $1.0 \times 10^{12}$  p/cm<sup>2</sup>. At every irradiation step, in-situ measurements were conducted, including capacitance at 25 °C, dark current at temperatures of 20 °C, 35 °C, and 50 °C, and the EICN of the QPR. Due to the complexity of relocating the setup, optical measurements could not be performed in situ or on-site.

Table 4.4: Cumulative fluence and dose applied for protons, electrons, and gamma-ray at each irradiation step

Proton Cumulative Fluence (p/cm <sup>2</sup> )		Electron Cumulative Fluence (e/cm <sup>2</sup> )	Gamma Cumulative Dose (krad)
60 MeV	20 MeV	0.5 and 1.0 MeV	1.25 MeV
$2.0 \times 10^9$	$2.0 \times 10^9$	$0.5 \times 10^{12}$	1
$4.0 \times 10^9$	$4.0 \times 10^9$	$1.0 \times 10^{12}$	2
$8.4 \times 10^9$	$8.4 \times 10^9$	$2.0 \times 10^{12}$	22
$4.2 \times 10^{10}$			36
$2.1 \times 10^{11}$	$2.1 \times 10^{11}$	$4.0 \times 10^{12}$	108
$1.0 \times 10^{12}$	$1.0 \times 10^{12}$	$5.0 \times 10^{12}$	150
			237

## 4.3 QPD Dark current and capacitance measurement

### 4.3.1 Experimental bench and instruments description

The dark current and capacitance of the QPD are measured using the setup depicted in Figure 4.10. The QPD is housed within a metallic enclosure (1) to ensure total darkness and connected to a KEITHLEY 4200 Semiconductor Characterization System (2). The system's temperature is regulated using (3) an LTR-1200 temperature control unit. Figure 4.11 offers a closer look at the interior of the metallic enclosure, highlighting (1) the enclosure itself, (2) a copper support for thermal conduction, (3) the cathode output, and (4) outputs for the four anodes. A 4x4 cm Peltier cell located beneath the copper support heats and cools the copper support. A probe is centrally placed in the copper support for temperature monitoring, while a fan coupled with a heatsink placed under the Peltier cell manages the excess heat generated. Note that the copper support, designed for thermal conduction, is custom-made for each QPD type to ensure optimal thermal contact. Therefore, two enclosures exist, one for TO5 JP QPD and the other for TO8 NL QPD.



Figure 4.10: Images of the experimental setup for QPD dark current and capacitance measurements: (1) Metallic enclosure housing the QPD, (2) KEITHLEY measurement system, and (3) LTR-1200 temperature control unit.



Figure 4.11: Interior view of the QPD metallic enclosure: (1) Metallic enclosure, (2) Copper support for the QPDs, (3) Cathode output, and (4) Anode outputs.

The QPD pins are connected to KEITHLEY outputs via simple wires to female BNC connectors. Two configurations are used, depending on the measurement type.

- For dark current measurements, each QPD segment is connected to an SMU using triaxial cables as illustrated by Figure 4.12.
- For capacitance measurements, a four-point characterization setup illustrated in Figure 4.13 with SubMiniature version A connectors (SMA) cables is utilized. This method employs four contacts to separately manage the current drive and voltage measurement, significantly reducing errors from parasitic voltage drops. This approach enhances the accuracy and reliability of the capacitance measurements.

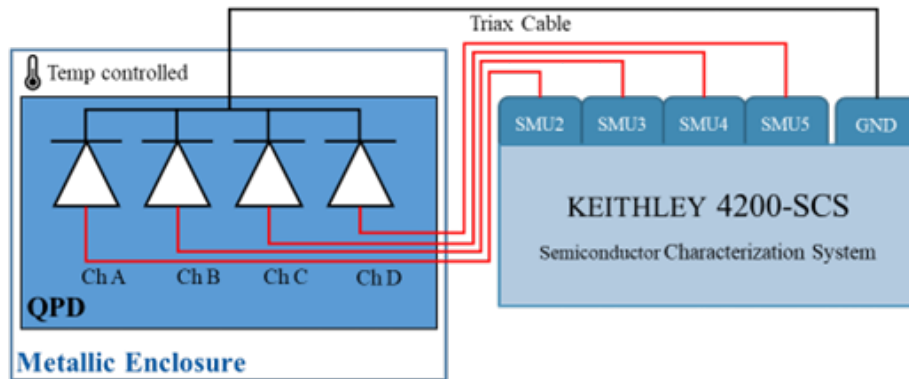


Figure 4.12: Diagram of the experimental setup for QPD dark current measurement.

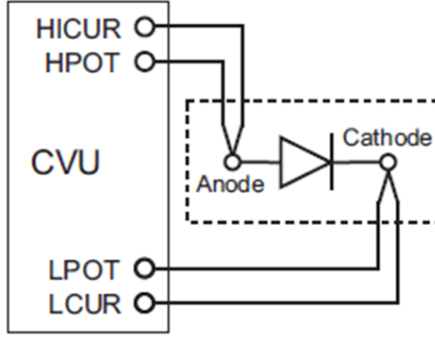


Figure 4.13: Four-point capacitance measurement configuration [106].

### 4.3.2 Measurement protocols

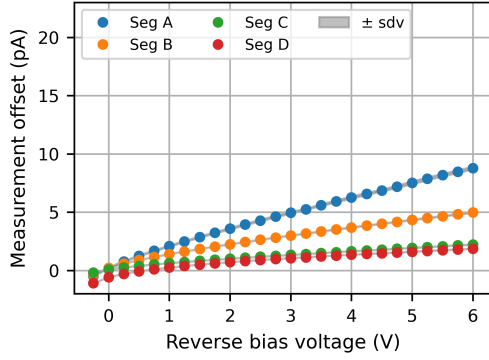
Before conducting dark current or capacitance measurements, the QPD’s temperature is set to the target value. Since the temperature probe measures the copper support’s temperature and not the QPD directly, a delay in heat transfer can cause discrepancies, affecting dark current accuracy. To counter this, the dependency of dark current on temperature is utilized. During the temperature stabilization phase, the QPD’s dark current is measured every 5 seconds at a constant reverse bias voltage (5 V for JP QPD and 20 V for NL QPD). The QPD is then considered to have reached the target temperature when its dark current levels are stabilized. The chosen temperatures for dark current measurement overlay LISA’s operational spectrum of 10 °C to 30 °C [107]. Despite the setup’s ability to operate near 0 °C, humidity at low temperatures caused condensation on the copper support and QPD, risking damage as seen with the NL QPD’s channel D. To protect the QPDs, temperatures under 20 °C were avoided. Therefore, the temperature range for measurements, both pre- and post-irradiation, was set between 20 °C to 50 °C, incrementing by 5 °C. Unlike dark current measurements, temperature has a minimal impact on capacitance. Initial tests assessing temperature effects from 15 °C to 50 °C showed that capacitance increases depending on less than 10%. Therefore capacitance measurements are performed at a unique temperature of 25 °C. Due to the lengthy nature of the test process and time constraint during irradiation campaigns, dark current measurements were only taken at 20, 35, and 50 °C and capacitance measurements at 25 °C.

Following temperature stabilization, dark current measurements are taken simultaneously across all segments, applying the same reverse bias voltage sweep to each segment. NL QPDs are subjected to a voltage sweep from 0 to 30 V in 1 V steps, while JP QPDs range from -0.25 to 6 V in 0.25 V steps. For capacitance, each segment is individually tested with NL QPDs experiencing a voltage sweep from 0 to 30 V in 1 V steps, and JP QPDs from 0 to 6 V in 0.5 V steps, along with a frequency sweep from 1 to 10 MHz in 1 MHz step. The stray capacitance and current introduced by the setup (measured in open circuit), including cables and instruments (see subsection 4.3.3) are subtracted from the raw measurements.

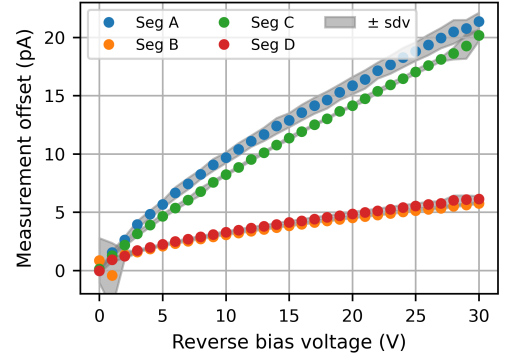
### 4.3.3 Evaluation setup performances

Offset currents induced by the setup are determined by conducting standard measurements with the QPD disconnected, following the voltage sweep protocol defined in Section 4.3.2. Figure 4.14 presents the average stray currents for four SMU channels in both TO5 and TO8 configurations, based on five sets of measurements with the grey area indicating the standard deviation. The highest stray current is recorded at 21 pA for 30 V. The same procedure is applied for capacitance measurements, detailed in Figure 4.15, revealing a maximum offset of 2.6 pF for the JP QPD configuration.

Eight rounds of dark current and capacitance measurements were conducted over one week to assess the precision of the setup. Between each round, the setup was rebooted. Measurements were performed on reference QPDs of each type: 1.0 mm, 1.5 mm, and 2.0 mm JP QPDs, as well as the 1.5 mm NL QPD. Table 4.5 displays the average dark current ( $I_{\text{dark}}$ ) and sdv from the

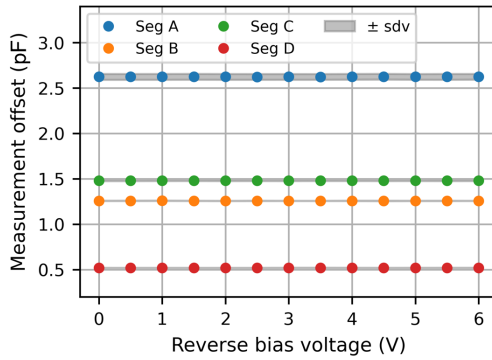


(a) TO5 JP QPD configuration

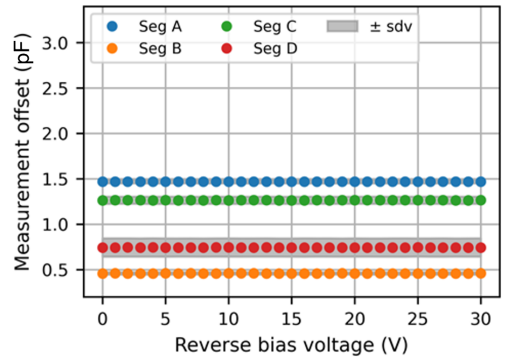


(b) TO8 NL QPD configuration

Figure 4.14: Measured stray currents for each SMU channel under JP (a) and NL (b) QPD configurations, highlighting the setup’s maximum stray current of 21 pA at 30V.



(a) TO5 JP QPD configuration



(b) TO8 NL QPD configuration

Figure 4.15: Measured stray capacitance for each channel under JP (a) and NL (b) QPD configurations, highlighting the setup’s maximum stray capacitance at 2.63 pF at 6V.

eight measurement sets at each QPD’s operational bias voltage (5 V for JP QPD and 20 V for NL QPD). The ”max ratio” is the highest ratio of mean to sdv across all bias voltages, indicating the channel’s measurement precision. Segment D of the NL QPD showed a significant deviation, likely due to a permanent degradation due to condensation during early low-temperature tests mentioned previously. It is confirmed by its dark current value, nearly 200 times higher than other channels, suggesting a defect in the QPD rather than a setup error. Excluding this anomaly, the maximum observed deviation was 8.09% for segment B of NL reference QPD. Considering a worst-case scenario, the setup’s estimated precision for dark current measurement is  $\pm 4.1\%$ . Table 4.6 presents the capacitance measurement results, following the same format as Table 4.5. The setup’s estimated precision for capacitance measurements is  $\pm 4.4\%$ .

The dark current of our reference QPDs varied from several dozen to hundreds of pA for dark current and a few pF for the capacitance as seen from Table 4.6 and 4.5. For this range of current, the datasheet [106] indicates a maximum error of  $\pm(0.5\% + 15 \text{ fA})$  for dark current measurements and  $\pm 0.36\%$  to  $\pm 0.92\%$  for capacitance at 10 MHz. Comparing those to the observed  $\pm 4.1\%$  for dark current and  $\pm 4.4\%$  error for capacitance are notably higher. Parasitic errors introduced by the wiring between the QPD pins and BNC connectors could explain these discrepancies. An improved setup could include a custom electrical board designed to connect SMA and triaxial cables directly to the QPD pin, limiting or suppressing completely the use of classic wires to limit their impact.

Table 4.5: Summary of dark current precision measurement for JP and NL QPDs.

QPD	QPD JP 1.0 mm				QPD JP 1.5 mm			
Segment	Seg A	Seg B	Seg C	Seg D	Seg A	Seg B	Seg C	Seg D
Mean (pA)	1541,41	1553,00	1476,87	1530,18	316,05	302,07	297,88	296,15
Sdv (pA)	7,16	13,67	8,54	5,47	2,64	4,70	2,61	2,50
Ratio max (mean/sdv) (%)	0,61%	0,94%	0,64%	0,49%	0,89%	1,55%	0,93%	0,84%
QPD	QPD JP 2.0 mm				QPD NL 1.5 mm			
Mean (pA)	366,85	364,30	378,43	381,87	177,03	160,61	162,41	35207,78
Sdv (pA)	3,25	4,67	2,30	1,77	4,88	12,57	5,08	3588,97
Ratio max (mean/sdv) (%)	0,92%	1,28%	0,63%	0,48%	6,79%	8,09%	6,65%	15,47%

Table 4.6: Summary of capacitance precision measurement for JP and NL QPDs.

QPD	QPD JP 1.0 mm				QPD JP 1.5 mm			
Segment	Seg A	Seg B	Seg C	Seg D	Seg A	Seg B	Seg C	Seg D
Mean (pF)	5,67	5,75	5,35	5,45	9,78	9,86	9,51	9,55
Sdv (pF)	0,064	0,016	0,036	0,027	0,073	0,039	0,072	0,032
Ratio max (mean/sdv) (%)	8,76%	4,08%	6,70%	3,74%	3,71%	2,38%	3,44%	3,41%
QPD	QPD JP 2.0 mm				QPD NL 1.5 mm			
Mean (pF)	14,53	14,51	14,28	14,34	5,74	6,08	5,92	5,90
Sdv (pF)	0,060	0,040	0,050	0,065	0,245	0,264	0,100	0,345
Ratio max (mean/sdv) (%)	2,00%	2,31%	2,63%	2,55%	4,81%	4,57%	2,14%	6,14%

## 4.4 QPD Quantum efficiency measurement

### 4.4.1 Experimental bench and instruments description

The QE measurement setup, shown in Figure 4.16, includes: (1) a Rio Planex fibre laser source emitting a continuous 1064 nm wavelength beam with power up to 600  $\mu$ W, adjustable from 0 to 600  $\mu$ W via (2) a variable optical fibre attenuator. (3) A 50%/50% beam splitter divides the beam into two paths, OUT3 and OUT4. Path OUT3 is directed to (4) a NIST-calibrated InGaAs PD (Newport 818-IG, 3 mm diameter, 0.677 A/W at 1064 nm), connected to (5) a USB Power Monitor for monitoring the power. The OUT4 beam is channelled through (6) an optical fibre collimator and focuses on (7) the QPD's segment inside a metallic enclosure, with alignment facilitated by (8) XYZ translation stages. Photocurrent and dark current for each QPD segment are measured using (9) a Keithley 2635B SMU. The configuration is detailed in Figure 4.17.

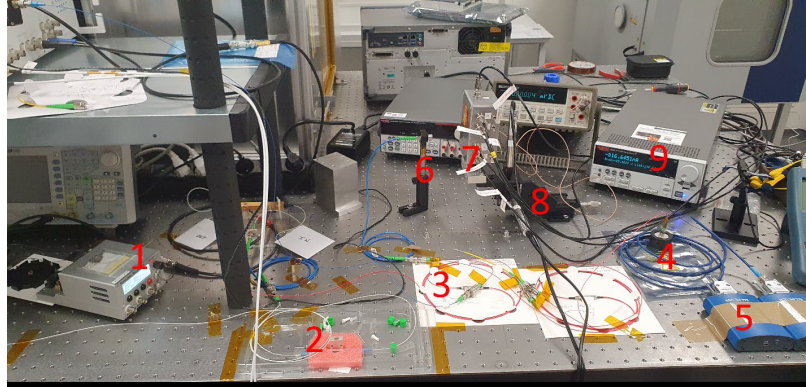


Figure 4.16: Image of the QPD QE setup, featuring: (1) 1064 nm fiber laser source, (2) variable optical fiber attenuator, (3) 50%/50% beam splitter, (4) NIST-calibrated InGaAs PD, (5) USB power monitor, (6) optical fiber collimator, (7) metallic enclosure housing the QPD, (8) XYZ translation stages, and (9) Keithley 2635B SMU.

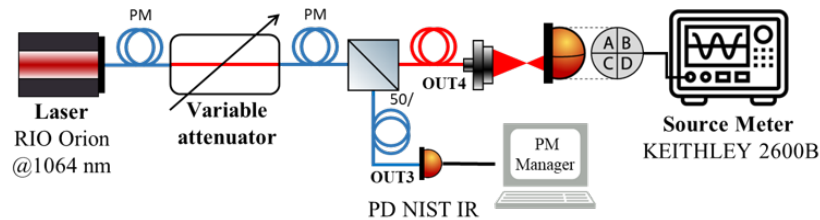


Figure 4.17: Diagram of the QPD QE set-up.

Figure 4.18 illustrates the electrical connection between the Keithley 2635B SMU and the QPD via triaxial cables. The Hi and Lo outputs of the SMU are connected to the anode of the segment being tested and the common cathode of the QPD, respectively, while the anodes of the non-tested segments are grounded. Switches are incorporated to facilitate the selection of different segments with minimal manipulation. Although temperature control is not integrated into the setup, it is situated in a clean room at the Observatoire de la Côte d'Azur (OCA), ensuring controlled humidity and a stable temperature of 20 °C. A temperature probe inside the enclosure monitors any significant temperature variations, with data recorded using a Hewlett Packard 34401A multimeter.

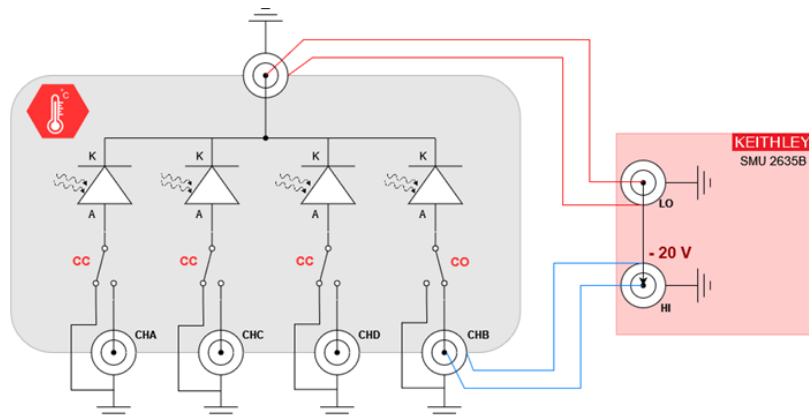


Figure 4.18: Electrical schematic of the QPD connection to the Keithley 2635B SMU.

#### 4.4.2 Measurement principle

As mentioned in section 2.3.3, the QE of each QPD segment is measured via the responsivity defined as the ratio of the incident optical power ( $P_{\text{opt}}$ ) to the generated photocurrent ( $I_{\text{ph}}$ ). This calculation starts with determining  $P_{\text{opt}}$  by multiplying the NIST-calibrated photodiode's ( $P_{\text{opt, NIST IR}}$ ) reading with the optical power ratio ( $R_{\text{out4,3}}$ ) between outputs 3 and 4, defined in Figure 4.17. The total current ( $I_{\text{Keithley}}$ ), recorded by the Keithley SMU, includes both the photocurrent ( $I_{\text{ph}}$ ) and the dark current ( $I_{\text{dark}}$ ).  $I_{\text{dark}}$  is subtracted from  $I_{\text{Keithley}}$  to isolate  $I_{\text{ph}}$ . Based on Equation 4.1, the QE is calculated as follows:

$$QE = R_{\text{QPD, seg}} \cdot \frac{hc}{\lambda} = \left( \frac{I_{\text{Keithley}} - I_{\text{dark}}}{P_{\text{opt, NIST IR}} \cdot R_{\text{out3, 4}}} \right) \cdot \frac{hc}{\lambda} \quad (4.1)$$

#### 4.4.3 Instruments and calibration methods

Three critical experimental parameters influence the accuracy and precision in the QE measurements:

- Ratio between outputs (OUT3 and OUT4): incorrect ratios can lead to errors in the calculated optical power incident on the QPD segment.
- Laser beam's shape and size: an oversized laser beam may result in light loss, leading to an underestimation of the QE.
- Alignment of the Laser Beam with the QPD: poor alignment can similarly cause an underestimation of the QE.

To limit these factors and precise measurements, three specific calibration steps are performed before each set of measurements:

- Optical ratio calibration
- Beam profile calibration
- Beam and QPD alignment control

#### Measurement of the optical power ratio $R_{\text{out4,3}}$

To accurately assess the optical power ratio between the OUT3 and OUT4 fibre outputs, as depicted in Figure 4.19, a second NIST-calibrated photodiode (e.g., 818 IR, Germanium, 3 mm diameter, 0.474 A/W at 1064 nm) is used in place of the QPD, as shown in Figure 4.19. Photocurrent from the PD NIST IG and IR are simultaneously taken at different optical laser beam powers from 0 to 200  $\mu\text{m}$ . The average and standard deviation of these ratio measurements over a year is displayed in Figure 4.20, revealing a 10% variation in this parameter. The ratio between the two outputs is equal to an average of 0.85, deviating from the expected 1.0 ratio suggested by a 50%/50% beam splitter. This 15% deviation from theoretical predictions is attributed to losses at fibre connectors, beam splitter transmission, and propagation through free space from output of the fibre to the QPD.

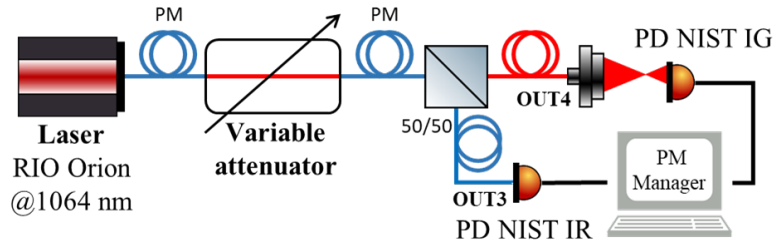


Figure 4.19: Diagram of the optical power ratio measurement.

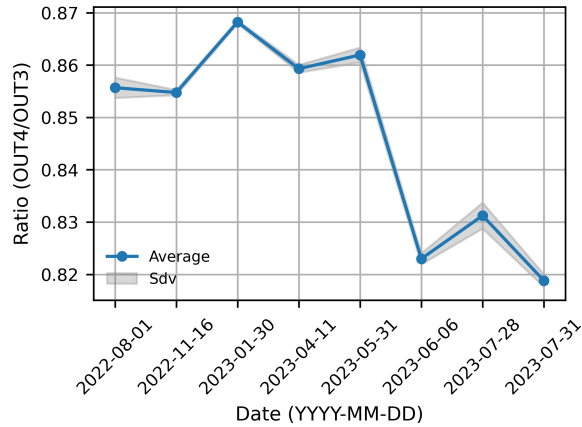


Figure 4.20: Evolution of the beam ratio between OUT4 and OUT3 over one year.

### Beam profile calibration

The beam profile calibration uses the setup detailed in Figure 4.17 with the QPD substituted by a Thorlabs BC106N-VIS/M Camera Beam Profiler. This profiler is connected to a computer via USB, facilitating real-time monitoring of the beam shape through dedicated software. A detailed view of the calibration setup is depicted in Figure 4.21, showcasing (2) the camera beam profiler connected to (3) the XYZ translation table to adjust the camera's position relative to the laser beam. To achieve a beam size that fits within a QPD segment, the (1) collimator is deliberately misadjusted, resulting in a non-collimated beam and making the QPD position crucial. A ruler is used to ensure both the camera and QPD are accurately positioned along the beam axis with a precision of 1 mm.

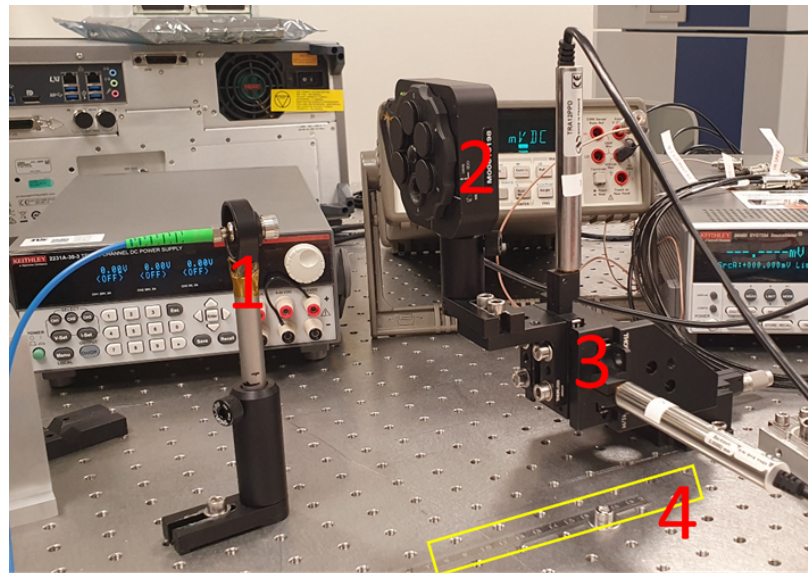


Figure 4.21: Picture on the optical beam profile calibration set-up with (1) the collimator, (2) the Thorlabs BC106N-VIS/M Camera Beam Profiler, and (3) the XYZ translation table.

After optimization, the final beam shape and size are shown in Figure 4.22. The beam diameter is slightly asymmetric, measuring  $160\ \mu\text{m}$  along the x-axis and  $180\ \mu\text{m}$  along the y-axis. However, this asymmetry is acceptable as long as the beam fits within the QPD segment. To fit within the segment of the smallest QPD ( $1.0\ \text{mm}$ ), the beam diameter must be less than  $353\ \mu\text{m}$ . The maximum

beam size is  $192\ \mu\text{m}$  along the y-axis. Considering a positioning error of  $\pm 1\ \text{mm}$ , the beam diameter does not exceed  $225\ \mu\text{m}$ , which is 64% of the maximum allowable diameter for the 1.0 mm QPD and less than 30% for the 2.0 mm QPD. Hence, even if over time small variation of the beam diameters was observed, the beam is entirely contained within the QPD segment with a correct alignment.

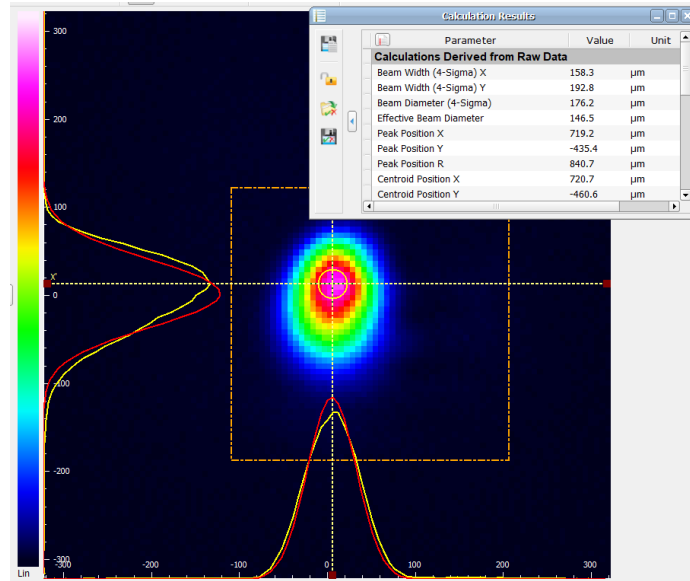


Figure 4.22: Image of beam profile.

### Beam alignment with the QPD

Alignment with the QPD is achieved through adjustments using XYZ translation tables. The Z-axis positioning, parallel to the beam's direction, is manually adjusted with a micrometric screw. In contrast, the XY axes adjustments are made through actuators with a precision of  $0.1\ \mu\text{m}$ . A MATLAB program controls and monitors the movements across the X and Y axes. To identify the center of each segment, the X and Y positions of the laser are varied while monitoring changes in photocurrent. During this process, the laser optical output is maintained constant. The centre position (X, Y) is found for a maximum photocurrent observed. The relative positioning of the laser beam across each segment, as determined by the coordinates provided by the MATLAB program, is depicted in Figure 4.23.

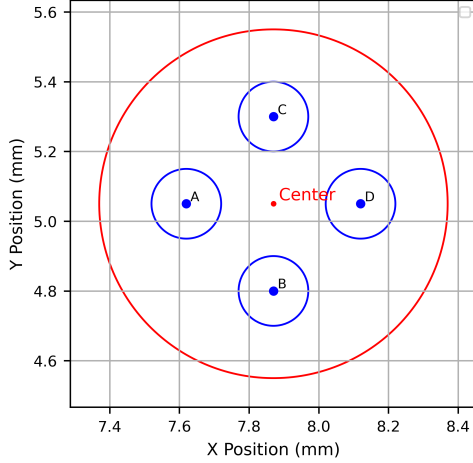


Figure 4.23: Illustration of the laser beam’s relative alignment across the QPD’s segments, using XYZ translation tables.

#### 4.4.4 Measurement Protocol

After adjusting the beam to the desired diameter and alignment, the procedure begins by measuring the QPD segment’s dark current, followed by simultaneous measurements of the photocurrent with the Keithley 2635B, the optical power using the NIST PD, and the temperature. Those measurements are conducted at a consistent optical power of approximately  $80 \mu\text{W}$ . This specific power setting minimizes the effects of ambient light and is low enough to prevent saturation of the QPD. Over one minute, it’s a total of 30 acquisitions taken. The final QE result is the average of each QE measurement obtained using Equation 4.1 and then repeated for each segment. Given the high sensitivity of the setup to any movement, relocating it is not an option. As such, in-situ measurements during irradiation cannot be conducted. Instead, measurements are strictly performed before and after the irradiation phase to maintain the integrity of the results.

#### 4.4.5 Evaluation of Setup Performance

##### Evaluation of the measurement error

Based on the equation 4.1, the error in measuring the QE of the QPD originates from three primary sources: the Keithley with  $I_{\text{ph}}$ , the PD NIST IR with  $P_{\text{opt}}$ , and the power ratio with  $R_{\text{out4,3}}$ . The total uncertainty in QE, denoted as  $\Delta QE$ , is computed using Equation 4.2 obtained by applying the principle of uncertainty propagation formula to our case.

$$\Delta QE = |QE| \sqrt{\left(\frac{\Delta I_{\text{ph}}}{I_{\text{ph}}}\right)^2 + \left(\frac{\Delta P_{\text{opt}}}{P_{\text{opt}}}\right)^2 + \left(\frac{\Delta R_{\text{out4,3}}}{R_{\text{out4,3}}}\right)^2}, \quad (4.2)$$

where  $\Delta x$  represents the error in each parameter. According to their respective datasheets:

- PD NIST 818-IG has an accuracy of  $\pm 2\%$  at 1064 nm [108].
- Keithley 2635B has an accuracy of  $0.02\% + 25 \text{ nA}$  (1-year accuracy at  $23^\circ\text{C} \pm 5^\circ\text{C}$ ) in the  $100\mu\text{A}$  range [109].
- The power ratio  $R_{\text{out4,3}}$  from the output is estimated to be  $\pm 2.43\% \approx 2.4\%$  using the formula for propagation of uncertainties.

The results for reference QPDs of each type, indicating a theoretical error ( $\Delta QE$ ) of less than  $\pm 3\%$ .

Following the methodology used for dark current and capacitance to gauge the setup’s precision, five sets of QE measurements were conducted on each type of QPD across a one week period. The analysis revealed a standard deviation of less than 1.5% across all measurements and segments for each QPD type. This result aligns with the prior estimation of  $\pm 3\%$ , demonstrating a good precision of our measurement setup. It’s important to note that this lower value primarily reflects the precision of the setup without its accuracy, distinguishing it from the  $\pm 3\%$  error derived from the uncertainty propagation formula, which considers both precision and accuracy.

## 4.5 QPR Input equivalent current noise measurement

The experimental benches detailed in Sections 4.3 and 4.4 are to test intrinsic characteristics of the QPDs (dark current, capacitance, responsivity). This section describes the experimental set-up developed principally to measure QPR EICN measured in  $A/\sqrt{Hz}$  and TIA transfer function using a method called ‘white light method’. Hence, the QPDs have been connected to a FEE board and placed in their respective enclosure, as shown in Section 4.1.

### 4.5.1 Principle behind the ‘White Light’ method

The ‘white light’ method is a technique for characterizing PRs, particularly useful for measuring their noise and TIA gain. It uses a shot-noise-limited white light source, which has a broad amplitude spectrum, to introduce a predictable and measurable amount of noise into the PR. By analyzing the total noise with and without this introduced shot noise, the intrinsic electronic noise of the PR can be derived. This method exploits that the shot noise, dependent on the light intensity, can be precisely controlled and quantified. The following demonstration can also be found in [31, p.79] and [39].

The TIA gain is defined as the ratio of the voltage output of the QPR ( $V_{QPR}$ ) to the input, which is the photocurrent ( $I_{ph}$ ) as demonstrated by Equation 4.3.

$$G_{TIA} = \frac{\text{Output}}{\text{Input}} = \frac{V_{QPR}}{I_{ph}}. \quad (4.3)$$

Based on Equation 4.3, the voltage noise at the QPR output  $v_{dark}(f)$  without any illumination is:

$$v_{dark}(f) = G_{TIA} \cdot i_{en}(f), \quad (4.4)$$

where  $i_{en}(f)$  is the EICN. When the QPR is illuminated the total voltage noise  $v_{light}(f)$  becomes:

$$v_{light}(f) = G_{TIA} \sqrt{i_{sn}^2 + i_{en}(f)^2}, \quad (4.5)$$

with  $i_{sn}$  the shot-noise introduced by the limited light source dependent on the DC photocurrent  $I_{DC}$  generated by the light source:  $i_{sn} = \sqrt{2qI_{DC}}$  where  $q$  is the charge of an electron. By comparing the noise measurements with and without the shot noise, the electronic noise can be isolated and calculated by dividing Equation 4.4 and 4.5. This comparison leads to the Equation:

$$i_{en}(f)^2 = \frac{2qI_{DC}}{\left(\frac{v_{light}(f)}{v_{dark}(f)}\right)^2 - 1}. \quad (4.6)$$

Once  $i_{en}$  is known, the TIA gain ( $G_{TIA}$ ) can be calculated directly from the EICN measurements:

$$G_{TIA} = \frac{e_n}{i_{en}}. \quad (4.7)$$

### 4.5.2 Experimental setup and instrument description

Figure 4.24 is a picture of our experimental bench, and Figure 4.25 provides its electrical schematic. The components displayed in the photograph include:

1. QPR with QPD and FEE: the QPR is housed within a mechanical enclosure to minimize electromagnetic interference. The enclosure features a front opening to allow for experiments under both dark and light conditions. The tested channel is connected to the oscillator via an SMA cable.
2. RS Pro E10 Filament (Reference 655-9312): this lamp is positioned in front of the QPR to provide controlled illumination.
3. WaveRunner 9054 LECROY Oscilloscope: utilized for measuring the DC output voltage of the QPR under dark and light conditions.
4. Thorlabs EF500 DC Block: this device filters out the DC component from the QPR's output, ensuring that only the AC signal is sent to the amplifier and spectrum analyzer.
5. Stanford Research Systems SR445A Preamplifier: amplifies the QPR's weak output signal, particularly noticeable in dark conditions where the signal falls below the spectrum analyzer noise floor. Amplifying the signal by a factor of 25 allows the QPR signal in darkness to surpass the noise level of the Rohde & Schwarz spectrum analyzer by a factor of  $\approx 4$  within the frequency range of 1.0 to 40 MHz.
6. Rohde and Schwartz FSP13 Spectrum Analyzer: the final instrument in our chain, used to measure the QPR's noise voltage in both dark ( $v_{\text{dark}}(f)$ ) and light ( $v_{\text{light}}(f)$ ) conditions. The analyzer possesses a large band from 9 kHz to 12.6 GHz, covering LISA bandwidth from 3 to 30 MHz.

The experimental setup is not temperature-controlled. However, for pre-and post-irradiation measurements, the setup is placed in a clean room with regulated temperature and humidity, similar to the QE setup.

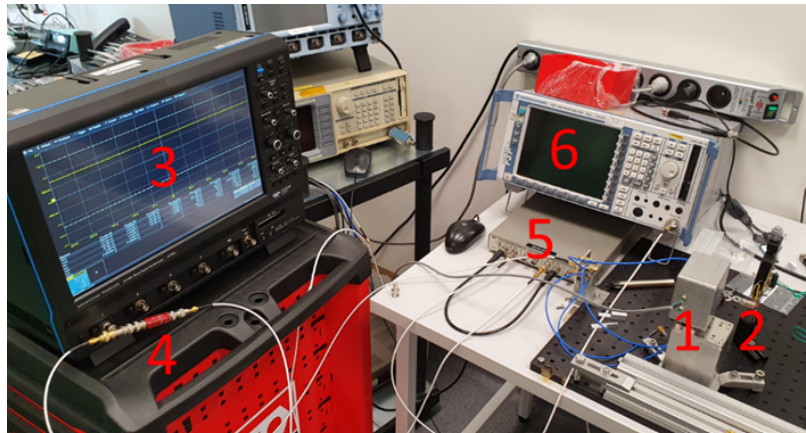


Figure 4.24: Picture of the QPR EICN measurement set-up: 1. QPR in a mechanical enclosure, 2. White light source, 3. LECROY Oscilloscope, 4. Thorlabs EF500 DC Block, 5. Preamplifier, and Rohde and Schwartz Spectrum Analyzer.

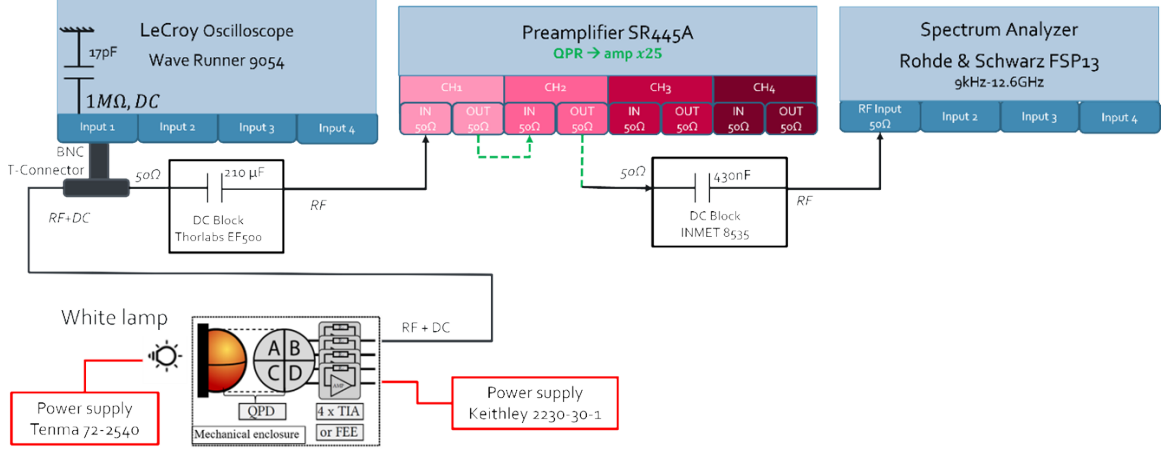


Figure 4.25: Electrical diagram of the QPR noise and TF experimental bench.

### 4.5.3 Experimental protocol description

As outlined in the section 4.5.1 and references [31], [97], [98], [110], to measure the EICN characteristics and TIA Gain of the QPR, two distinct measurements are needed.

#### Dark Condition Measurement

Initially, the QPR is assessed under dark conditions, with its DC output voltage measured using the Lecroy oscilloscope, typically registering approximately +750 mV across all channels. The noise voltage ( $v_{\text{dark}}(f)$ ) is measured using a spectrum analyzer, with a frequency sweep from 1 to 100 MHz in 30 kHz increments over a 110 ms timeframe. The final recorded spectrum is an average of over 20 individual sweeps. Due to the detection of significant parasitic electromagnetic interference from various sources, including instruments, radio, Wi-Fi, and cellular phones, the spectrum analyzer's measurement duration and the number of sweeps are finely tuned based on the setup location. This adjustment ensures maximal reduction of external noise impact on the data.

#### Light condition measurement

The second measurement is conducted under illuminated conditions. Unlike some devices where the output voltage increases with light intensity, in this case, the output voltage decreases, reaching saturation at  $\approx -4$  V. The light intensity is adjusted to achieve a DC output of  $\approx 0$  V consistent for all measurements. Subsequent noise voltage measurements ( $v_{\text{dark}}(f)$ ) are performed under identical conditions to those used in dark environments.

#### Setup floor measurement

Due to the high-performance noise level of the QPRs, the noise level from the spectrum analyzer itself can influence the results. Consequently, diverging from the methodologies outlined in references [31], [97], [98], [110], an additional third measurement is incorporated to determine the 'floor' noise of the setup. This noise floor measurement involves an open circuit configuration where the input of the Lecroy is disconnected from the QPR and instead connected to a 50-ohm DC block. As a result, the value of  $v_{\text{dark}}(f)$  is adjusted using the following Equation 4.8 to account for the setup's floor noise ( $v_{\text{floor}}(f)$ ):

$$v_{\text{dark corrected}}(f) = \sqrt{v_{\text{dark}}(f)^2 - v_{\text{floor}}(f)^2}. \quad (4.8)$$

This adjustment accounts for the additional noise introduced by the experimental setup, thereby enhancing the accuracy of the measurements by approximately 2%. This estimated improvement is determined by comparing noise values with and without the correction for the noise floor. Figure

4.26 presents typical results of the noise voltage spectral density and impact of the consideration of the 'floor' noise from the three measurements: dark, light, and floor, done with a 2.0 mm JP QPD.

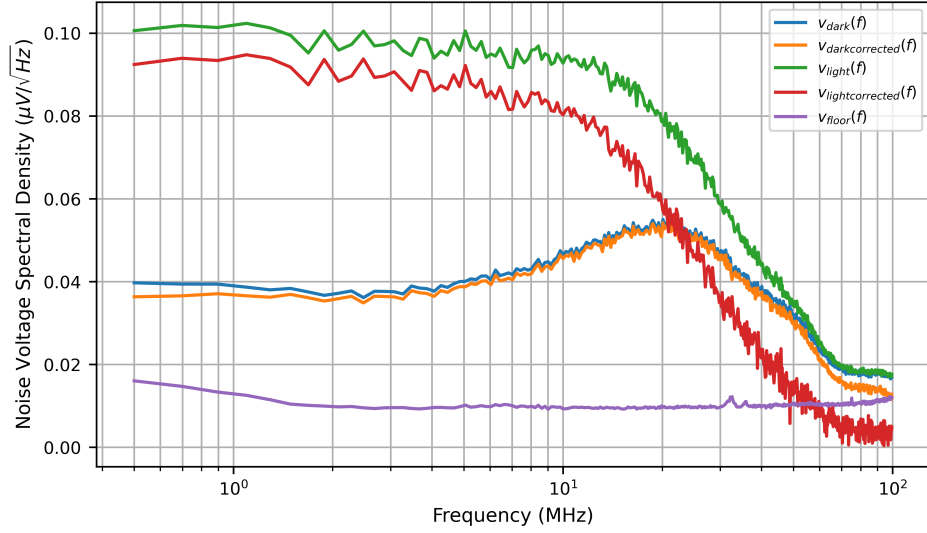


Figure 4.26: Noise voltage spectral density of the QPR as a function of frequency under dark and light conditions, including the noise voltage floor of the setup.

### Data Processing

Finally, the TIA gain and EICN are obtained by employing respectively Equation 4.7 and Equation 4.6, utilizing the adjusted value of  $v_{\text{dark}}(f)$  and with  $I_{\text{DC}} = (V_{\text{DC,dark}} - V_{\text{DC,light}})/Z_t$ , where  $V_{\text{DC,dark}}$  and  $V_{\text{DC,light}}$  represents the DC output voltage recorded by the Lecroy oscilloscope during measurement in dark and light, and  $Z_t$  the DC gain of the TIA set by the feedback transistor. The QPR's DC gain is  $42.2 \text{ k}\Omega$ , based on the TIA design specifications provided by DE [98].

Despite the system's precision, its extreme sensitivity to ambient electromagnetic fields significantly affects high-frequency noise ( $<20 \text{ MHz}$ ), as illustrated in Figure 4.27. This sensitivity is due to the experimental setup functioning similarly to an antenna, causing noise levels to vary based on the measurement location. Our data processing Python program integrates a smoothing function to enhance high-frequency data interpretation and filter out additional noise from the ambient environment rather than the QPR. For the smoothing function, four methods were considered:

- **The moving average method:** a simple technique involving averaging data points within a sliding window. Its effectiveness is limited and highly dependent on the chosen window size, which can cause considerable variation in results across different datasets. While a larger window size can smooth the data more effectively, it often introduces mid-frequency deviations (10 to 30 MHz).
- **Exponential smoothing:** applies diminishing weights to past observations, showed slightly better performance and robustness than the moving average method. However, it faces similar challenges in balancing smoothness against fidelity to the original data.
- **Polynomial fitting:** models data using polynomial equations. While polynomial fitting can effectively smooth data, its robustness is contingent upon the degree of the polynomial, which may require optimization based on the quality of measurements. This method tends to exhibit notable deviations at the extreme frequencies when improperly calibrated.
- **LOESS:** stands out for its adaptability and lack of reliance on a predefined functional form, making it particularly suited for complex, nonlinear patterns. Its main drawback is the compu-

tational demand for large datasets, which was not a concern in our context. Given its flexibility and balance between smoothness and adherence to the data. Ultimately, LOESS was selected to smooth our data, utilizing an optimized smoothing parameter of 0.1. The same methods and comparisons were applied to the TIA gain results, yielding similar conclusions.

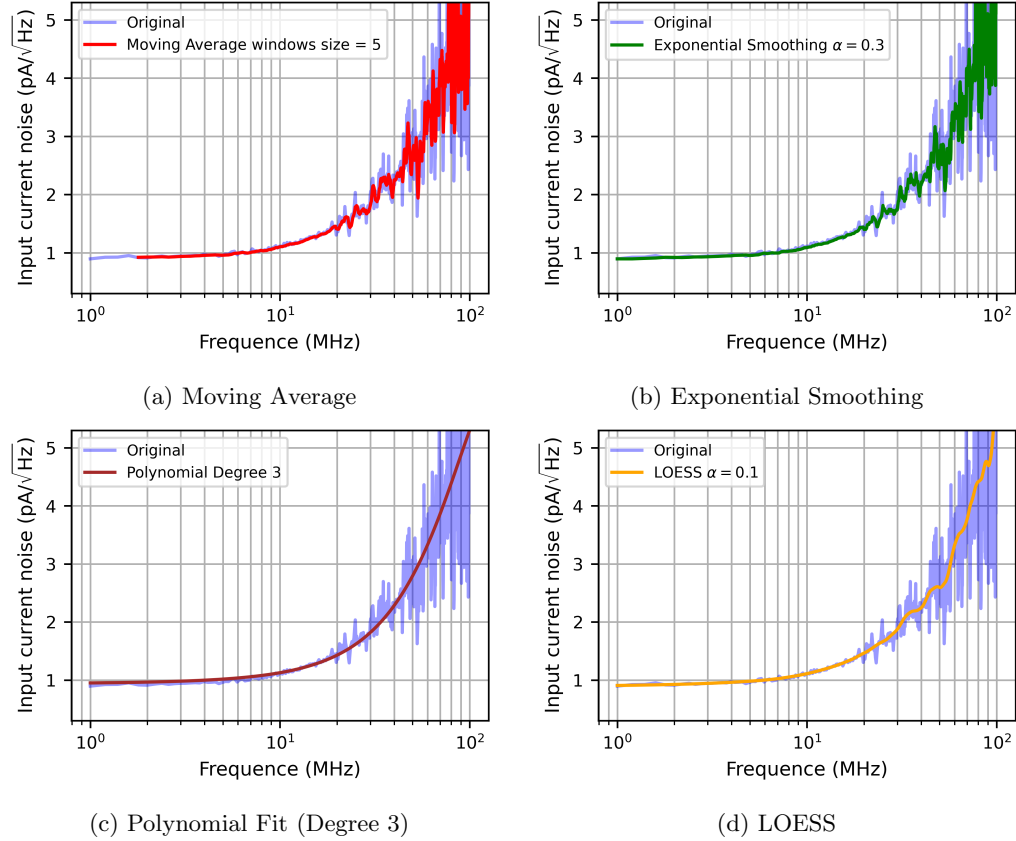


Figure 4.27: Comparative analysis of EICN data smoothing techniques for channel A of the QPR using JP 1001 QPD. Techniques include a) Moving Average, b) Exponential Smoothing, c) Polynomial Fit (Degree 3), and d) LOESS.

#### 4.5.4 Instruments and calibration methods

The internal gain of the setup, particularly the amplifier and spectrum analyzer represents the principal source of measurement error. Hence, accurate determination of the TIA gain of the QPR requires measuring the frequency-dependent gains of setup including the pre-amplifier, spectrum analyzer, and cables.

Figure 4.28 displays the configuration of the experimental setup, with the significant alteration from Figure 4.25 being the substitution of the QPR with a wave generator, the RIGOL DG4162, which has a bandwidth extending to 160 MHz. The gain of the arrangement is evaluated by the ratio of  $V_1(t)$  to  $V_2(t)$ , where  $V_2(t)$  is the sinusoidal voltage output generated by the Rigol and monitored via the Lecroy oscilloscope, and  $V_2(t)$  is the voltage measured by the Rohde & Schwarz analyzer. The evaluation uses sinusoids with amplitudes varying from 100 mV to 1000 mV at frequencies ranging from 1 MHz to 100 MHz.

The results of the setup gain shown in Figure 4.28 highlight two observations. First, there is a noticeable frequency dependence of the setup's gain, with an increase of 11.6% between 1.0 and 100

MHz. Second, while the expected amplification factor from the amplifier is 25, the voltage division effect due to the output impedance of the QPR and the 50-ohm input impedance of the analyzer leads to an additional factor of 0.5, resulting in an anticipated setup gain of 12.5. Experimentally, the observed average gain is approximately 10.6, representing a deviation of about 15% from the theoretical value. This discrepancy is primarily due to the amplifier exhibiting a gain of slightly less than 25 and the spectrum analyzer showing a gain that varies with frequency.

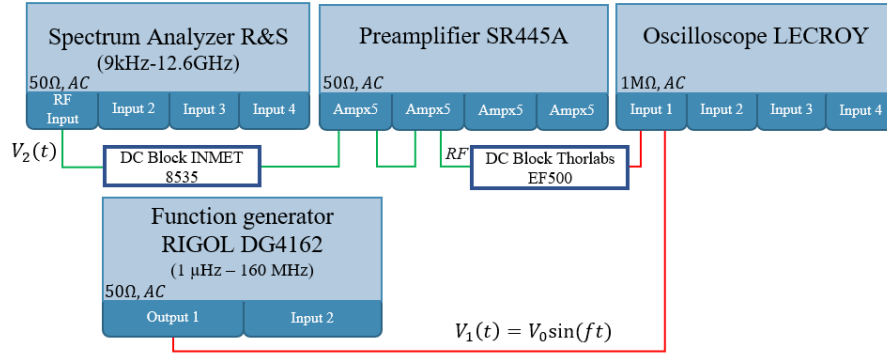


Figure 4.28: Electrical diagram of the EICN setup with QPR replaced by a wave generator.

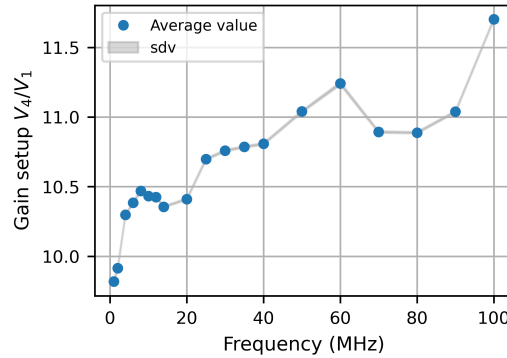
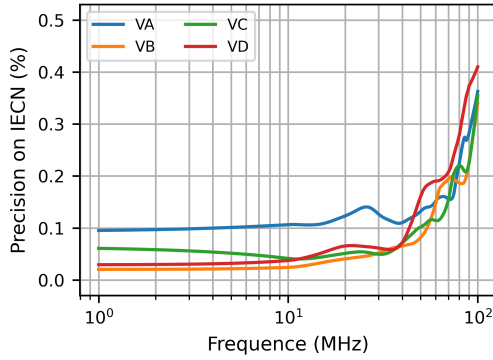


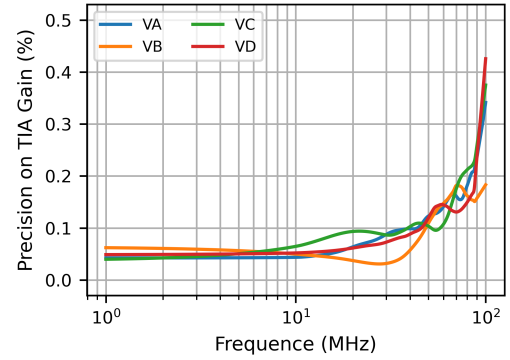
Figure 4.29: Estimation of the experimental setup gain in function of the frequency.

#### 4.5.5 Evaluation of setup performance

Precision estimation for the EICN setup mirrored the approach used for dark current and capacitance, involving five measurement sets per QPD type performed over an extended period, with reboots between each acquisition. Mean and sdv were calculated from these sets, as shown in Figure 4.30a, which highlights the maximum mean-to-standard deviation ratio for precision assessment across all QPDs types and for each channel. Frequencies under 40 MHz (which includes the LISA bandwidth), the frequency-dependent precision stays under 10% but rises to a maximum of 40% at higher frequencies. Compared to other channels, a lower precision by a factor of two at low frequencies is observed for channel A. Given the uniformity of the measurement chain from the QPR output to the R&S analyzer, this discrepancy is possibly due to potential asymmetry in the FEE. However, further investigation is necessary to confirm this hypothesis. The same methodology was applied to assess the precision of the TIA Gain. As depicted in Figure 4.30b, the findings align closely with those from the noise measurement, exhibiting similar behaviour patterns across frequencies. Notably, in this instance, Channel A does not show a higher error rate compared to the other channels.



(a) Precision on the EICN measurement function of the frequency.



(b) Precision on the TIA Gain measurement function of the frequency

Figure 4.30: Precision estimation for QPD a)EICN measurement and b)TIA gain for all channels VA, VB,VC, and VD

## 4.6 QPR Phase and amplitude response to LISA interferometric equivalent signal

At the beginning of 2022, an initial version of the setup was developed with the Artemis team at OCA for the optical characterization of QPRs designed for the SCI-IFO, a heterodyne interferometer intended for assessing LISA’s performance during its assembly phase [111]. The version discussed here is a modified version of this experimental bench.

### 4.6.1 Detailed Experimental Setup and Instrumentation

Figure 4.31 is a diagram of the experimental setup used to assess the phase and amplitude responses of the QPR to a LISA-like a signal. This setup, called the interferometric setup, consists of three main blocks:

- **LISA interferometric signal generation (Red):** mimics each one of the different LISA interferometric signal.
- **Signal Monitoring and test module (Green):** Keeps track of the signal’s fidelity and stability.
- **Control and acquisition system (Blue):** Manages data collection and oversees the experiment’s operational parameters.

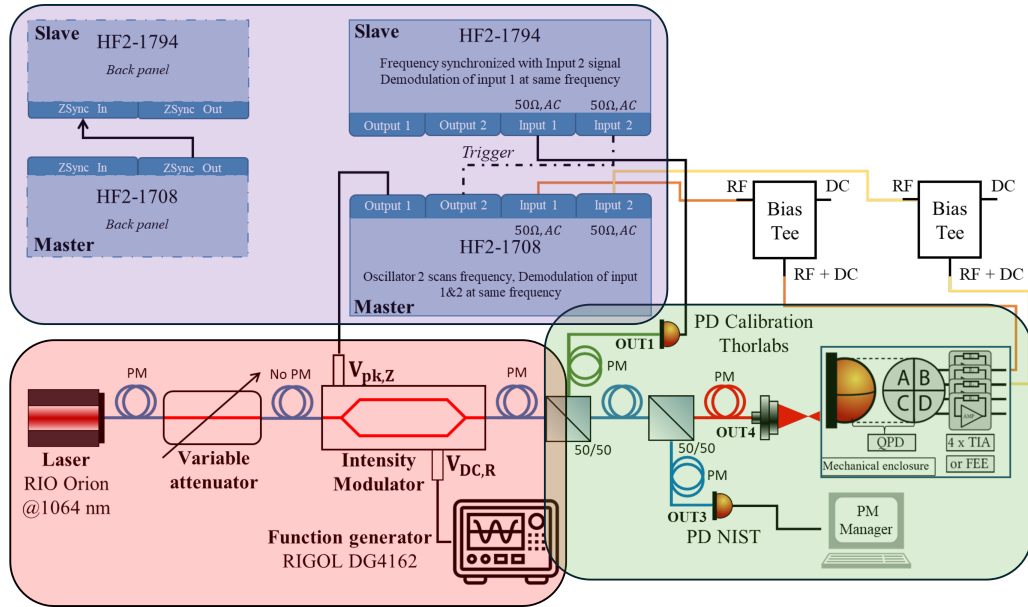


Figure 4.31: Diagram of the interferometric setup with red: LISA interferometric signal generation block, green: Signal monitoring and test module block, and blue: Control and acquisition block.

Each of these three blocks of the setup is described in detail below, using elements shown in the picture in Figure 4.32:

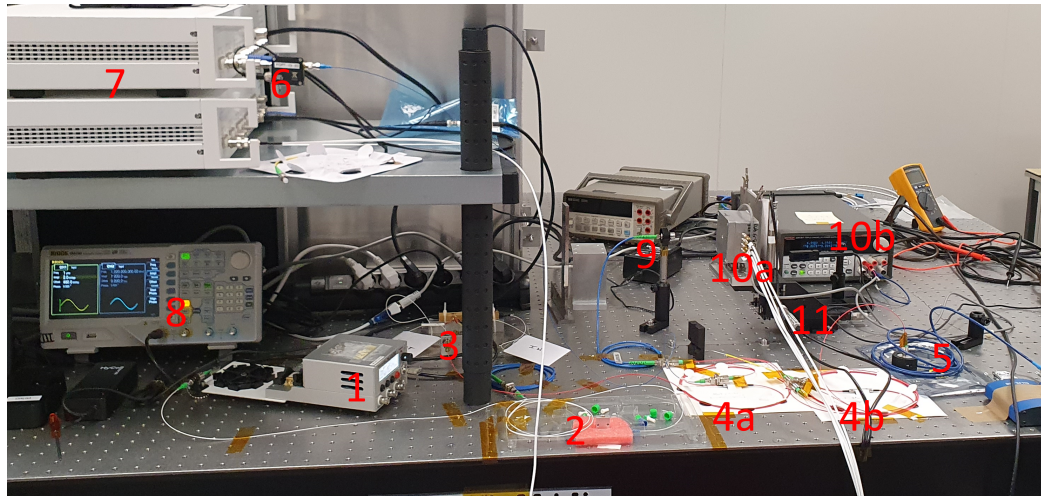


Figure 4.32: Picture of the interferometric setup.

### LISA interferometric signal generation

This block uses the same components from the QE measurement setup, with a modulator to replicate LISA-like signals under various conditions. The setup features (1) the RIO Planex laser source for signal generation, (2) a variable optical fibre attenuator for optical beam power, and (3) an Optilab Mach-Zehnder IM-1060-10-PM FIM for signal modulation, as depicted in Figure 4.31.

A FIM was chosen to replicate LISA’s heterodyne signal, despite its inherent challenges:

- **Non-linearity:** FIMs can distort the signal, influenced by environmental conditions, necessitating periodic re-calibration. The setup is located in a controlled clean room environment, reducing the impact of these effects.
- **Limited Functionality:** FIMs mainly provide intensity modulation, without the ability to directly adjust signal phase. As a result, the system can only simulate the amplitude modulation seen in the LISA interferometer, not the phase shifts induced by GW.

Despite these challenges, the primary advantage of using the FIM is its capability to test QPRs across the entire LISA frequency range of 1 to 30 MHz, which provides significant benefits over traditional bulk optics. Additionally, the seamless integration of fibres in the FIM setup offers substantial improvements. This integration not only makes the setup more compact but also facilitates smoother incorporation with the other fibre-based components, enhancing overall system cohesion. The design simplifies the experimental arrangement, reducing alignment errors and losses typically associated with coupling light between different mediums. Moreover, FIMs' inherent design reduces susceptibility to external light interference, an essential factor for accurately replicating the LISA long-arm interferometer's conditions, where the optical power is exceptionally low (on the order of nanowatts).

The FIMs design and functional principle are shown in Figure 4.33. An input waveguide divides the input optical signal into two pathways, forming each of two interferometer's arms. Modulation of the optical index in one of these paths results in intensity modulation at the device's output. The modulated output signal, denoted as  $S^{\text{MOD}}(t)$ , at the time ( $t$ ) is influenced by two electrical inputs: the modulation voltage  $V(t)$  (RF voltage) and the bias voltage  $V_{R,\text{mod}}$  (DC voltage), described by:

$$S^{\text{MOD}}(t) = P_0 \left[ 1 + \cos \left( \pi \frac{V(t)}{V_\pi} - \phi_{\text{mod}} \right) \right]. \quad (4.9)$$

( $P_0$ ) is the initial optical power, adjusted to account for the insertion loss,  $V_\pi$  represents the modulator's half-wave voltage indicating the voltage required to induce a phase shift of  $\pi$  radians in the light passing through one arm of the modulator relative to the other.

The RF voltage ( $V(t)$ ) acts as the primary modulation input, dynamically adjusting the light's intensity via the modulator by altering the phase difference between its two arms. This voltage simulates signals analogous to those anticipated in LISA.

The DC bias voltage,  $V_{R,\text{mod}}$ , sets the initial phase offset ( $\phi_{\text{mod}}$ ) between the two arms. By adjusting  $V_{R,\text{mod}}$ , the modulator is ensured to operate within its linear range, maximizing the fidelity of signal reproduction and minimizing distortion. The voltage is generated and controlled using a (8) RIGOL function generator.

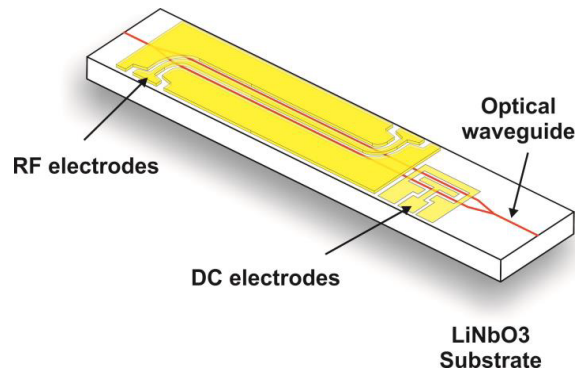


Figure 4.33: FIM principle schematics.

### Signal monitoring and test module

Upon its generation, the beam is divided into three distinct paths by two 50%/50% beam splitters, labelled 4a and 4b in Figure 4.32. These paths lead to outputs OUT1, OUT3, and OUT4.

OUT1 and OUT3 are directed towards a dual photodiode monitoring system, comprising a NIST-calibrated PD, designated as (5), to monitor the DC component of the signal and a Thorlabs PD (6), with a bandwidth exceeding 1 GHz for AC signal monitoring. This setup ensures precise signal characterization of continuous DC and dynamic AC components.

OUT 4 replicates the configuration from the QE setup, directing the laser beam through a collimator (9) and focusing it onto a single segment of the QPD. The QPDs are integrated with the same FEE (detailed in 4.1) used for noise measurement. Both the QPD and FEE are housed within a mechanical enclosure (10a). The system is powered by a Keithley multi-channel DC power supply (10b).

### Control and acquisition system

Measurement of the phase and amplitude of the QPR and control of FIM are realized by two HF2 lock-in Zurich detectors (7), configured in a master-slave configuration (see Figures 4.31 and 4.32). The Zurich 1794 (slave) is responsible for the acquisition of the AC signal part of the output signal generated by the FIM and monitored by the Thorlabs PD. The Zurich detector 1708 (master), generates the modulating voltage ( $V(t)$ ) sent to the FIM. The modulation voltage is defined as:

$$V(t) = \frac{V_{\text{pk}, Z}}{2} \sin(2\pi f_0 t), \quad (4.10)$$

where ( $V_{\text{pk}, Z}$ ) denotes the peak modulation amplitude from Zurich's output adjusted by a factor 0.5 for the  $50 \Omega$  impedance at the modulator's RF input, and  $f_0$  the modulation frequency. The sinusoidal form of  $V(t)$  creates a phase modulation in one arm of the interferometer. The Zurich master is also responsible for measuring the phase and amplitude of each QPR channel output using the Lock-In Detection method.

The principle of Lock-In Detection involves a process known as phase-sensitive detection to isolate a specific signal from a noisy environment. This method depends on the lock-in amplifier's ability to discern the amplitude and phase of a signal at a specific frequency (named the reference frequency) effectively filtering out noise and unrelated signals, thus significantly enhancing the signal-to-noise ratio. This process is highly efficient for extracting signals within a defined frequency band around the reference. The core of lock-in detection illustrated in Figure 4.34 involves multiplying (mixing) the input signal with a reference signal. This reference is typically a sine wave at a known frequency, closely related to the frequency of the signal of interest. The mixed signal is then subjected to phase-sensitive detection, also known as dual-phase demodulation achieved by the master Zurich. By performing dual-phase demodulation, it splits the input signal and multiplies each part by the reference signal and its 90 deg phase-shifted version. After demodulation, the signal passes through an adjustable low-pass filter. This filtering further eliminates high-frequency noise, leaving only the desired signal component. After the low-pass filters, the final step involves analyzing the filtered signal to determine its amplitude and phase the outputs, known as the in-phase (X) and quadrature (Y) components, are obtained. The amplitude ( $R = \sqrt{X^2 + Y^2}$ ) and phase ( $\Phi = \arctan 2(X, Y)$ ) of the signal relative to the reference can then be accurately determined [112].

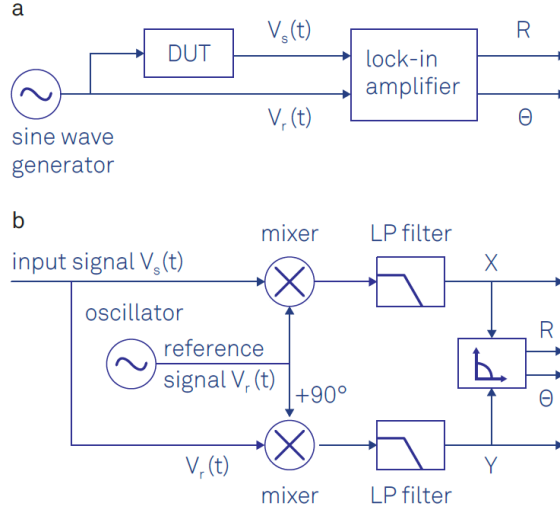


Figure 4.34: Lock-In Detection Process: (a) Lock-in measurement setup with a sinusoidal reference signal stimulating the DUT, and its response analyzed for amplitude and phase. (b) Lock-in amplification process, where the input signal is mixed with the reference signal and its 90 deg phase-shifted version, followed by low-pass filtering to isolate the signal from noise, with results presented in polar coordinates [112].

## 4.6.2 Measurement principle

### LISA Heterodyne Signal

The interaction between two laser beams with optical powers  $P_1$  and  $P_2$ , characterized by a heterodyne efficiency  $\rho$ , was previously defined in Equation 2.17 from Chapter 2. This equation is reformulated to introduce the modulator factor ( $m$ ) as shown in Equation 4.11.

$$S^{\text{HET}}(t) = K \cdot P_{\text{DC}} [1 + m \cdot \sin(2\pi ft - \phi_{\text{het}})]. \quad (4.11)$$

In this expression,  $K$  is to take into account the sequential division of optical power by two at the first beam splitter and further by four for each QPD segment.  $m$  is the modulator factor,  $f$  the heterodyne frequency, and  $S^{\text{HET}}(t)$  denotes the optical signal detected by each channel of the QPR. The modulator factor  $m$  is a parameter used for the characterization of our interferometric signal and is defined as follows:

$$m = \frac{P_{\text{DC}}}{P_{\text{AC}}(t)}, \quad (4.12)$$

where ( $P_{\text{DC}} = P_1 + P_2$ ) represents the continuous DC part of the interferometric signal, while ( $P_{\text{AC}}(t) = \sqrt{2\rho P_1 P_2}$ ) represents the dynamic RF component of the signal.

### Modulator Output Signal

To sum up the modulator behaviour, the output signal of the modulator  $S^{\text{MOD}}(t)(t)$  is controlled by two electrical voltage inputs:

- The modulation voltage  $V(t)$  (RF voltage) a sinusoidal (defined by Equation 4.10) fixed by the Zurich.
- The bias voltage  $V_{\text{R,mod}}$  (DC voltage).

The optical output signal of the FIM ( $S^{\text{MOD}}(t)(t)$ ) is described by Equation 4.13, a developed version of previous Equation 4.9.

$$S^{\text{MOD}}(t) = P_0 [1 + \cos(\pi\Phi_m \cdot \sin(2\pi f_0 t) - \phi_{\text{mod}})]. \quad (4.13)$$

In this formula,  $(P_0)$  denotes the input optical power,  $(f_0)$  the modulation frequency,  $(\phi_{mod})$  the phase term, set by the bias voltage  $(V_{R,mod})$  and in our case equals to  $\pi/2$  to ensure the modulator operates within its linear functioning range. Finally,  $(\Phi_m)$  is the modulation depth defined as follows:

$$\Phi_m = \frac{V_{pk, Z}}{2V_\pi} \quad (4.14)$$

### Matching the two signals

In order, for our modulator output signal to match a LISA heterodyne signal, the two signals need to respect the three following conditions:

- Frequency matching: both the heterodyne and modulator frequencies need to be identical. The frequency matching is done using the master Zurich 1708 to fix the modulator frequency  $f_0$  to match with our LISA interferometer frequency  $f$ .
- Phase conformity: the phases of the two signals must be equal. Unfortunately, as explained in the modulation section FIM mainly does not allow for a direct phase adjustment without impacting the modulation depth. Hence, a second element would be needed to change the phase.
- Power level equality: continuous (DC) component of our signal must match in magnitude. The DC power matching is done using the variable attenuator so  $P_0 = P_{DC}$ .
- Modulation depth parity: the dynamic (RF) components of the output signals from our LISA interferometer and FIM must match in scale. This aspect more complex is further elaborated in the subsequent paragraph.

The modulation depth parity is obtained if the following equation is valid:

$$\langle S^{\text{HET}}(t) \rangle = \langle S^{\text{MOD}}(t) \rangle. \quad (4.15)$$

$\langle S^{\text{HET}}(t) \rangle$  can be calculated for each modulator factor  $(m)$  at fixed frequency  $f$  as the result is not dependent on it.  $\langle S^{\text{HET}}(t) \rangle$  is obtained by averaging from  $t = 0$  to  $t = 1/f$  Equation 4.11.  $\langle S^{\text{HET}}(t) \rangle$  must then equal to the each value found of  $\langle S^{\text{MOD}}(t) \rangle$  for each modulator factors.

An important note is that  $\langle S^{\text{MOD}}(t) \rangle$  depends on  $\Phi_m$ , which is also calculable. The relationship is illustrated in Figure 4.35, which plots  $\langle S^{\text{MOD}}(t) \rangle$  as a function of  $\Phi_m$ , showing a direct and linear relationship for  $\Phi_m$  values lower than 0.25. This linear relationship is significant as  $\Phi_m$  is directly linked to the Zurich input parameter  $(V_{pk, Z})$ , as detailed in Equation 4.14. Hence, this direct relationship enables the calculation of  $V_{pk, Z}$  to validate the modulation depth parity.

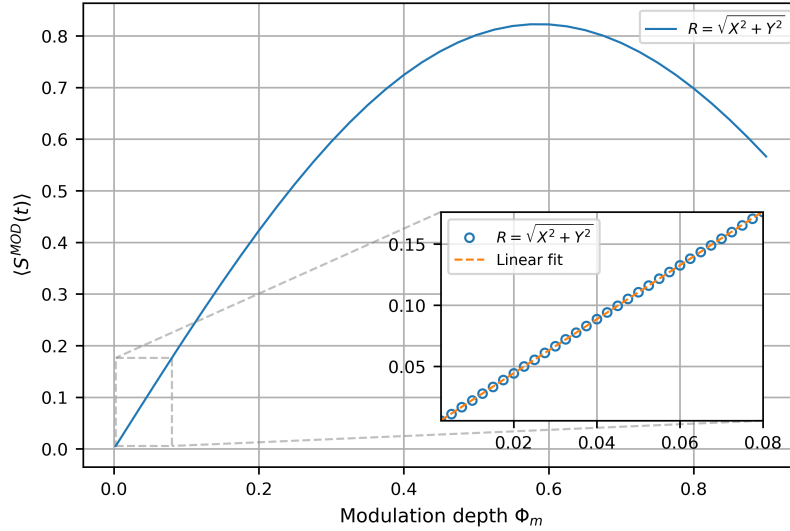


Figure 4.35: Modulation depth ( $\Phi_m$ ) function average modulated signal ( $\langle S^{\text{MOD}}(t) \rangle$ ).

### 4.6.3 Instruments and calibration methods

Similar to the QE setup, the interferometric setup is sensitive to the optical power ratio between different outputs (OUT1, OUT3, and OUT4), the laser beam's shape and size, and the alignment of the laser beam with the QPD's segment under test. The protocols are the same as those presented in Section 4.4, except for the calibration of the optical ratio.

Figure 4.36 illustrates the setup schematic used for beam ratio calibration. During QPR characterization measurements, the ratio OUT4/OUT3 is utilized to obtain the DC component of the interferometric signal arriving at the QPD segment. The ratio is obtained from ratio between the measured outputs from PD NIST IR and PD NIST IG, similar to the same method applied in the QE setup calibration.

During measurement QPR characterization measurements, the ratio OUT4/OUT1 evaluates the RF component of the interferometric signal. For simplicity, instead of measuring only the ratio OUT4/OUT1 using the PD NIST, it is more effective to measure directly the ratio OUT4/OUT1 with the responsivity of the PD Thorlabs. This is done by connecting a multimeter to the Thorlabs PD output to measure its produced photocurrent corresponding to an optical power arriving on the PD NIST IR.

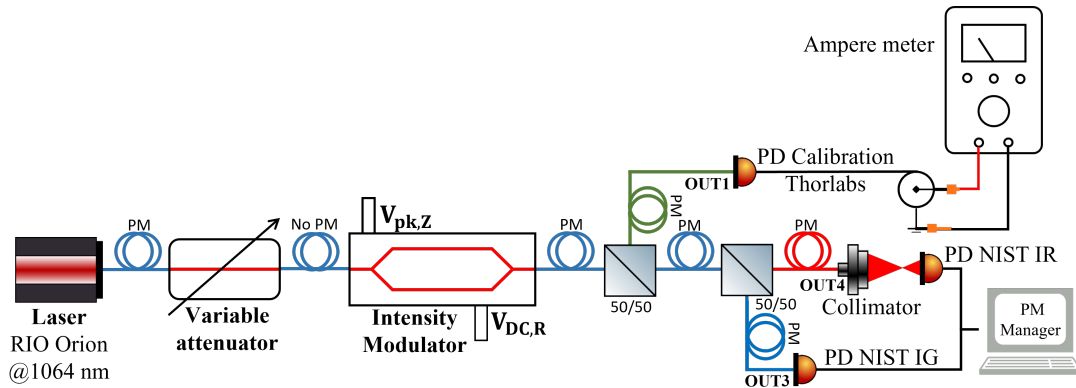


Figure 4.36: Detailed schematic of the experimental setup for measuring beam intensity ratios across OUT1, OUT3, and OUT4 outputs.

#### 4.6.4 Measurement Protocols

Transitioning to the experimental methodology, this procedure involves directing a laser beam onto a single QPD segment to evaluate the amplitude and phase response to the modulated signal using Zurich phasemeters. The optical laser is controlled across three parameters: optical power,  $V_{pk, z}$  (which sets the modulator factor  $m$ ), and frequency  $f$ .

Initially, the modulation depth is fixed using  $V_{pk, z}$  to match one of the LISA interferometers, following the methodology outlined in Section 4.6.2.

Table 4.7 summarizes the modulator factor ( $m$ ) calculated for each interferometer using Equation 4.11 and the optical power values of each laser beam in the LISA interferometers. The minimum, average, and maximum values are derived from the respective optical power values of each LISA laser beam. These values were initially calculated at the beginning of the thesis and have evolved over time as the LISA project has progressed. Therefore, the factors presented in the table are not directly derived from the values shown in Table 4.7 from Chapter 2.

Table 4.7: Modulation factor for each interferometer (SCI-IFO, TM-IFO, Ref-IFO).

$m$	Min	Ave	Max
$m_{LARM}$	$1.375 \times 10^{-3}$	$1.317 \times 10^{-3}$	$1.153 \times 10^{-3}$
$m_{TM}$	$1.564 \times 10^{-1}$	$1.474 \times 10^{-1}$	$1.145 \times 10^{-1}$
$m_{REF}$	$9.392 \times 10^{-2}$	$8.647 \times 10^{-2}$	$6.262 \times 10^{-2}$

To limit the duration of the tests not all configurations are tested and three modulation factors  $m = [0.0007177, 0.08644, 0.2132]$ , were selected. These factors still to this date span the range of all current LISA modulator factors, making them still relevant and representative of various operational scenarios, from the SCI-IFO to the TM-IFO.

For each modulation factor, a test referred to as the plotter test is conducted at a fixed frequency  $f$ . This test involves sweeping the optical power of the laser beam from 0 to 110  $\mu$ W and back to 0 using the manual attenuator, to obtain conditions where  $P_0 = P_{DC}$ . This test is performed for  $f$  at various frequencies in the LISA bandwidth between 3 to 28 MHz with 5 MHz step.

For  $m = 0.3132$ , a second type of test called the sweeper test, is conducted. This test maintains a constant optical power of about 110  $\mu$ W and sweeps the frequency from 100 kHz to 45 MHz. The sweeper test is specific to this modulation factor, as conducting it for others would be redundant with the plotter tests (given that plotter tests are already performed across various frequencies) and excessively time-consuming. It should be noted that this test facilitated the measurement of crosstalk between the QPR channels, the results of which have been presented to the LISA QPR consortium but are not included in this document.

#### 4.6.5 Evaluation of Setup Performance

Unlike the previous experimental benches for dark current, capacitance, QE, and EICN, the interferometric setup does not currently have estimated precision or error margins due to its complexity. However, two parameters can be experimentally measured and compared to their theoretical predictions: the modulation factor ( $m$ ) and the TIA gain. Additionally, the TIA gain measured in the interferometric setup can also be compared with the TIA gain obtained from the EICN measurements.

##### Modulator factor

$m$  is defined by Equation 4.12 as the ratio of the DC to AC components of the optical signal, which are monitored using the PD NIST IR and Thorlabs PD, respectively. Figure 4.37 displays the experimental modulation factors for the target values  $m = [0.0007177, 0.08644, 0.2132]$  during plotter measurements, plotted against the optical power measured by the Thorlabs PD.

At low optical powers, the Thorlabs PD measures insufficient power, making accurate modulation factor determinations challenging. However, at optical powers above  $1 \mu\text{W}$ , the experimental values of  $m$  are within  $\pm 10\%$  of the target  $m$  values. For the smallest target  $m$  value, the experimental value can differ by up to a factor of two. Indeed, the amplitude of  $V_{\text{pk}, z}$  required to achieve such low modulation factors is very small (1.1 mV), challenging Zurich's ability to generate an accurate sinusoidal waveform. To mitigate this, the Zurich output is initially set to 20 times the desired  $V_{\text{pk}, z}$  and then reduced to the target value of 1.1 mV using an attenuator. Despite this adjustment, an offset remains visible.

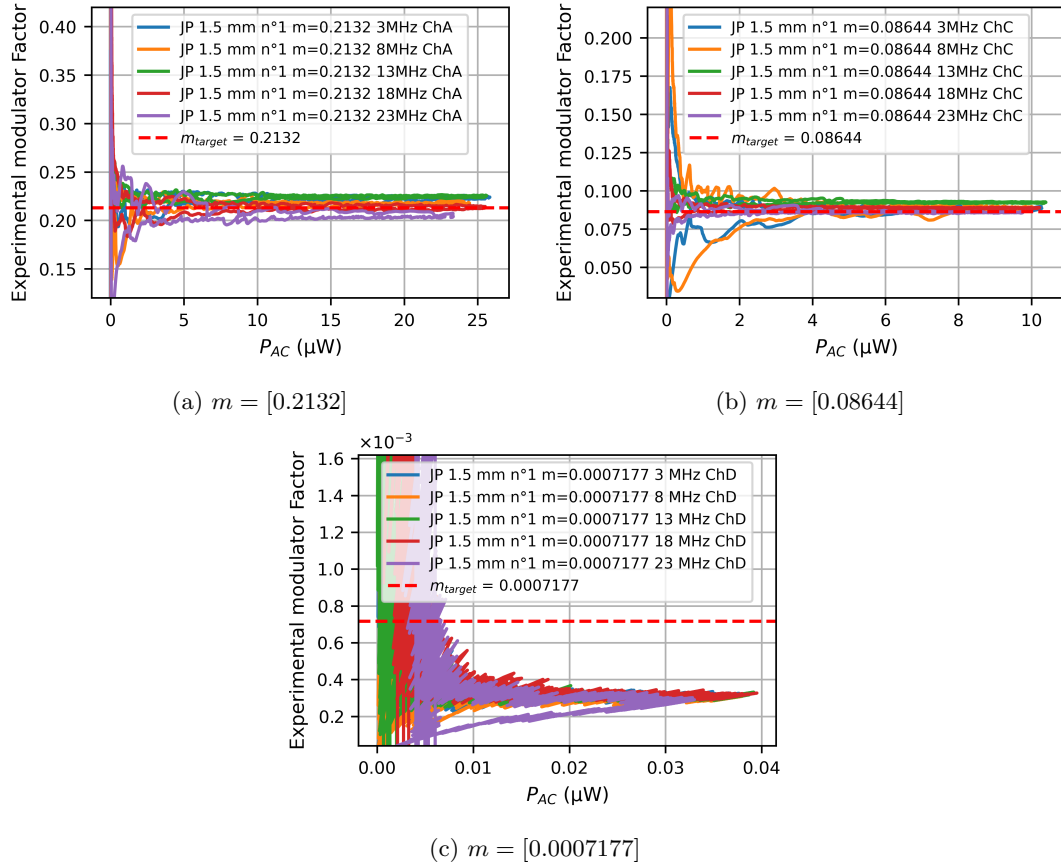


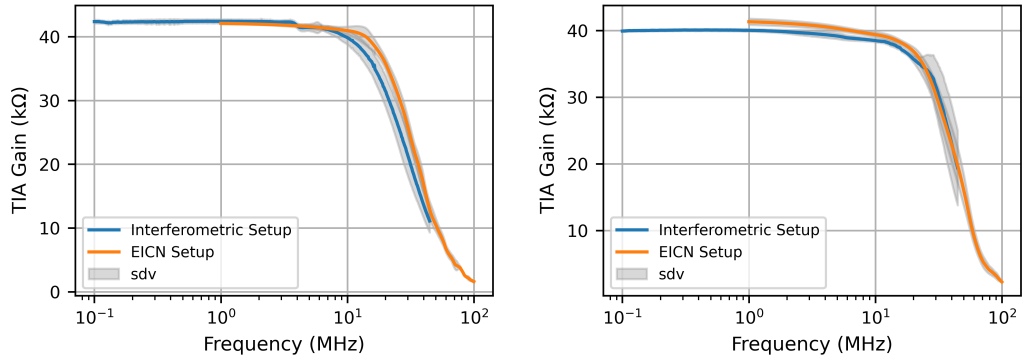
Figure 4.37: Experimental modulation factors for target values a)  $m = [0.0007177]$ , b)  $m = [0.08644]$ , and c)  $m = [0.2132]$  plotted against optical power measured by Thorlabs PD.

### TIA Gain

The TIA gain is the ratio of the output to the input. In our case, the output corresponds to the voltage output from the QPR channel, measured by the Zurich instrument. The input corresponds to the photocurrent from the QPD. The photocurrent is calculated by multiplying the QPD's responsivity, obtained from the QE setup, by the incident optical power arriving on the QPD, measured by PD NIST IR.

Figure 4.38 displays TIA gain results versus frequency for the 1.5 mm JP reference QPD and 1.5 mm NL reference QPD, using both EICN and interferometric setups. The results demonstrate a strong correlation, validating both the methods and the measurements from the QE and interferometric setup. However, minor discrepancies around 20 MHz suggest a potential unknown intrinsic

gain within one or both experimental setups. It is important to note that the calculation of the TIA gain presented in Figure 4.38 includes the impact from the transfer functions of both the Zurich instrument and the cables (bias-T and SMA cables) connecting the QPR output to the Zurich Master 1708.



(a) 1.5 mm JP QPD n°1 (reference)

(b) 1.5 mm NL QPD n°1 (reference)

Figure 4.38: TIA gain results versus frequency, using a) 1.5 mm JP reference QPD, and b) 1.5 mm NL reference QPD, for both EICN and interferometric setups.

# Chapter 5

## Results and Analysis

This chapter unfolds in two main sections, each addressing a specific objective outlined in the introduction 1.6:

- The first section investigates how irradiation affects the internal parameters of QPDs, specifically dark current, capacitance, and QE. It also evaluates whether the QPDs meet LISA’s requirements following irradiation. Additionally, this analysis involves characterizing the degradation through damage factors and comparing these findings with existing literature. The last part concerns a study using the NIEL scaling approach applied to our experimental damage factors.
- The second section explores how irradiation affects the performance of the QPR, focusing on noise levels and optical performance metrics like amplitude and phase of AC signals within a simulated LISA interferometer setup. This part also checks whether the QPR meets LISA’s noise requirements post-irradiation.

As detailed in Section 4.2, both JP and NL QPDs were subjected to irradiation tests involving 20 and 60 MeV protons, 0.5 and 1.0 MeV electrons, and gamma rays, with exposure levels up to five times the requirements set for the LISA mission. The specific irradiation conditions are detailed in Table 4.3. Each QPD was assigned a unique identifier, organized and outlined in Table 4.2, which also details the allocation to different irradiation types. During this chapter, references to QPDs are based on the numbering system established in Table 4.2. Relevant requirements are provided throughout the analysis, with a comprehensive list available in the Chapter 4 introduction.

### 5.1 Impact of Irradiation on QPD Performance

#### 5.1.1 Pre-Irradiation test results

##### Dark Current

Figure 5.1 presents pre-irradiation dark current results at 25 °C for all JP and NL QPDs, plotted against reverse bias voltage ( $V_{\text{bias}}$ ). Data points show the average dark current over the four QPD segments, and the grey-shaded area shows the standard deviation between segments. Error bars represent the measurement precision. The data demonstrate that the dark current varies from 80 pA to 2.5 nA at 25 °C. Although the JP 1.5 mm, JP 2.0 mm, and NL 1.5 mm QPDs exhibit consistent results across QPDs and channels, the JP 1.0 mm QPDs show disparities. Additionally, the NL QPDs show a significant exponential increase in dark current at bias voltages above 25 V, reaching up to 2.5 nA, with considerable variability among channels and QPDs, indicating that at that bias voltage, the NL QPDs reached their critical breakdown zone.

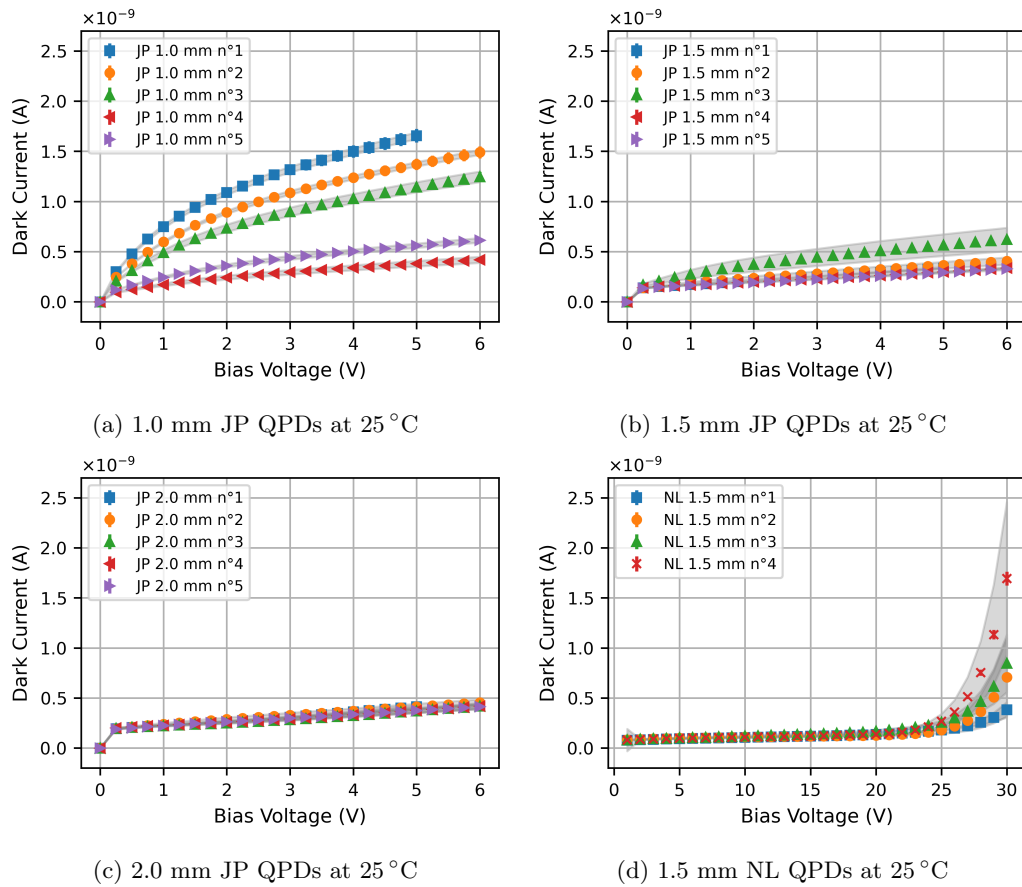


Figure 5.1: Dark Current versus bias voltage ( $V_{\text{bias}}$ ) for a) 1.0 mm JP QPDs, b) 1.5 mm JP QPDs, c) 2.0 mm JP QPDs, and d) 1.5 mm NL QPDs at 25 °C before irradiation. Data points show the average dark current over the four QPD segments, and the grey-shaded area shows the standard deviation. Error bars represent the measurement precision.

Figure 5.2 illustrates the temperature dependence of dark current for all QPDs, confirming the exponential increase with temperature, as explained in Section 2.3.3. This behaviour aligns with the Arrhenius law (Equation 2.20). The data reveal a dark current reaching 7.2 nA at 50 °C. Despite this increase, the QPDs remains well below the 1  $\mu$ A requirement for the LISA mission.

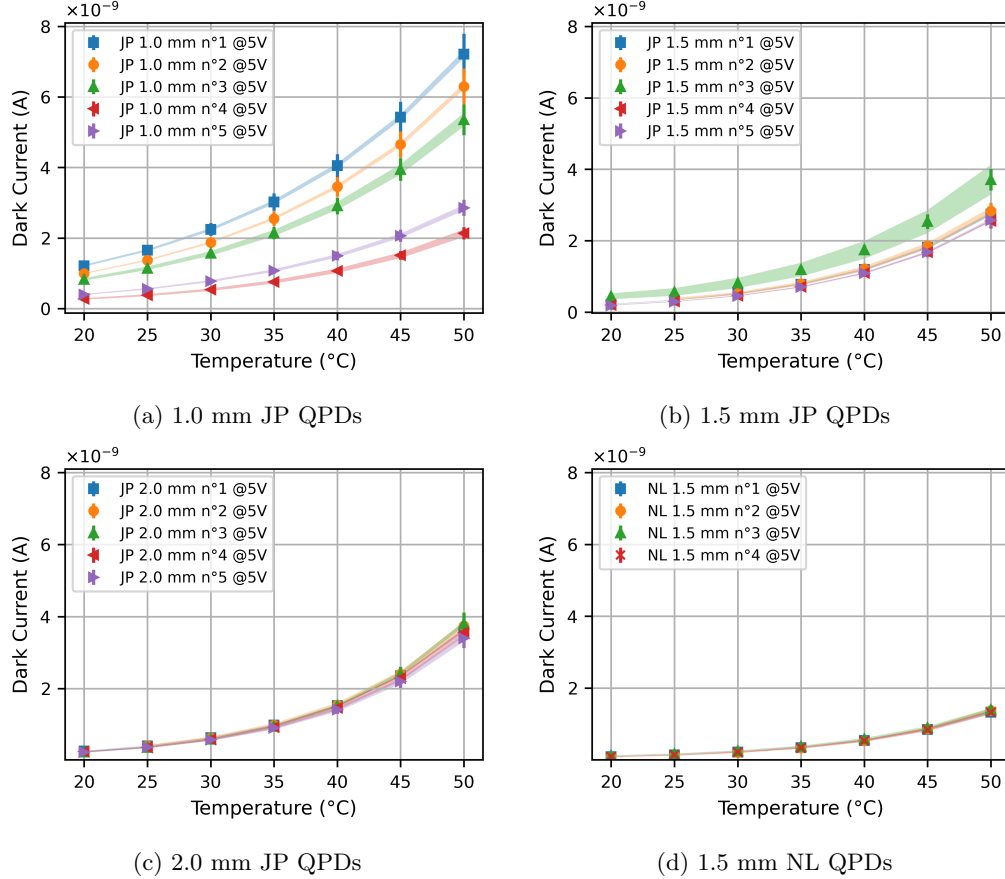


Figure 5.2: Dark Current versus temperature for a) 1.0 mm JP QPDs, b) 1.5 mm JP QPDs, c) 2.0 mm JP QPDs, and d) 1.5 mm NL QPDs at 5 V for JP QPDs and 20 V for NL QPDs. Data points show the average dark current over the four QPD segments, and the shaded area shows the standard deviation between segments. Error bars represent the measurement precision.

### Capacitance

Figure 5.3 presents pre-irradiation capacitance at 25 °C and 1 MHz for all JP and NL QPDs, plotted against reverse bias voltage ( $V_{bias}$ ). Data points show the average capacitance over the four QPD segments, and the grey-shaded area shows the standard deviation between segments. Error bars represent the measurement precision. The capacitance measurements at a 5 V bias voltage show 5.5 pF for 1.0 mm JP QPDs, 9.7 pF for 1.5 mm JP QPDs, 14.5 pF for 2.0 mm JP QPDs, and 5.6 pF for 1.5 mm NL QPDs. These results confirm a linear increase in capacitance with QPD size, predicted by Equation 2.19. Dispersion between segments is small, at less than 2% for JP QPDs and 6% for NL QPDs, indicating good consistency across all segments. The NL QPDs also show a dispersion of less than 5% at 20 V, just below the breakdown bias voltage. Capacitance measurements across varying frequencies reveal a stable, modest reduction of approximately 5% as the frequency increases from 1.0 to 10.0 MHz, indicating stable capacitance characteristics within the operational range.

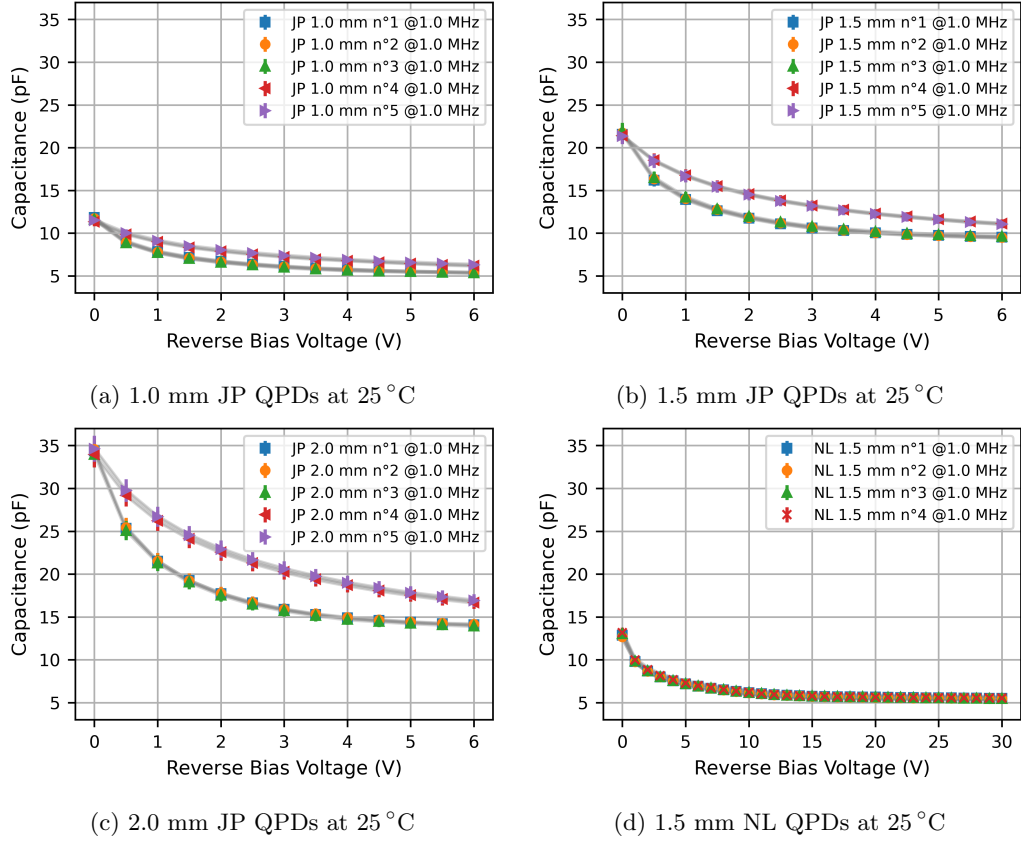


Figure 5.3: Capacitance versus bias voltage ( $V_{\text{bias}}$ ) for a) 1.0 mm JP QPDs, b) 1.5 mm JP QPDs, c) 2.0 mm JP QPDs, and d) 1.5 mm NL QPDs at 25 °C and 1 MHz. Data points show the average dark current over the four QPD segments, and the grey-shaded area shows the standard deviation between segments. Error bars represent the measurement precision.

## Quantum Efficiency

Due to the late arrival of the Keithley equipment after the proton irradiation campaign, QPDs exposed to proton irradiation could not be tested before their exposure. Consequently, Figure 5.4 presents QE at room temperature only for the non-irradiated QPDs (numbers 4, 5, and reference QPD number 1) across all QPD types, excluding those subjected to proton irradiation. Data points show the average QE over the four QPD segments, and the grey-shaded area shows the standard deviation between segments. Error bars represent the measurement precision.

For the 1.0 mm JP QPDs, an average QE of 92.4% was recorded, with a 0.3% standard deviation across segments. The 1.5 mm JP QPDs had a slightly higher QE of 92.7%, with 0.1% standard deviation, while the 2.0 mm JP QPDs showed a QE of 92.9%, also with 0.1% standard deviation. The slight increase in QE with QPD size is mainly due to alignment challenges; smaller QPDs are more difficult to align, resulting in more light loss from beam dispersion, accounting for the subtle rise in efficiency and variance. The 1.5 mm NL QPDs exhibited a QE of 95.4%, with 0.2% standard deviation. All tested QPDs exceed the LISA mission's 80% QE requirement.

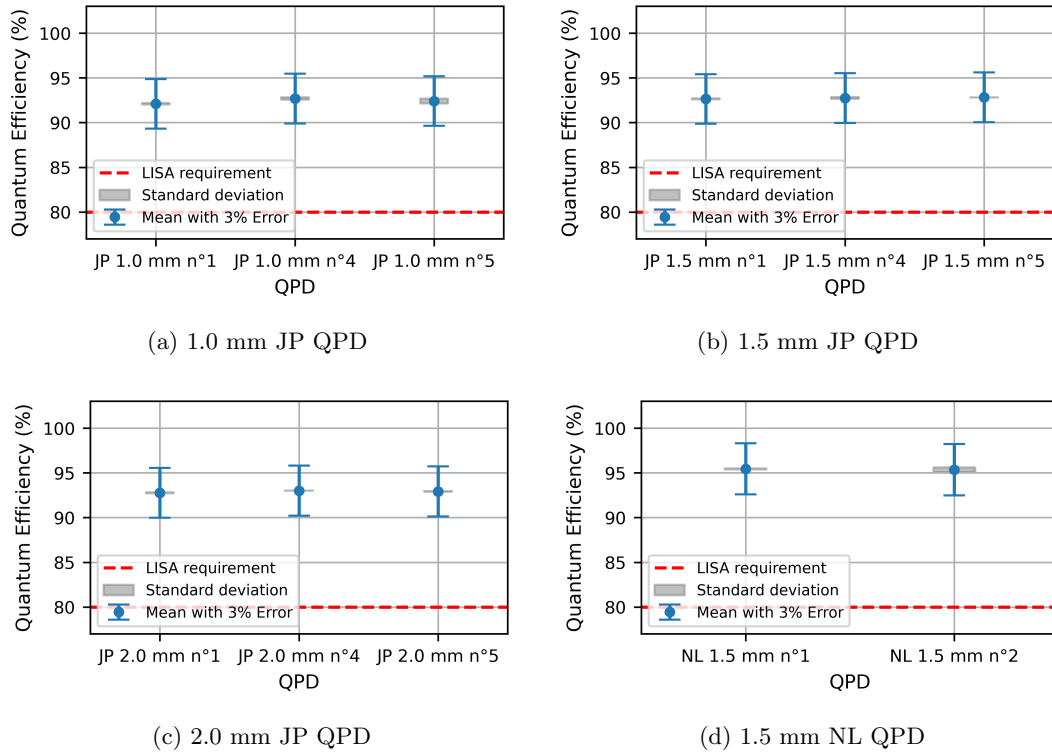


Figure 5.4: QE for a) 1.0 mm JP QPDs, b) 1.5 mm JP QPDs, c) 2.0 mm JP QPDs, and d) 1.5 mm NL QPDs. Data points show the average dark current over the four QPD segments, and the grey-shaded area shows the standard deviation between segments. Error bars represent the measurement precision. Measurements were performed in a clean room at a temperature of approximately  $25 \pm 1$  °C.

### 5.1.2 In-situ and post-irradiation test results

Chapter 3 discussed how radiation damage introduces parasitic energy levels, which trigger five mechanisms: generation, recombination, trapping, compensation, and tunnelling, all of which impact the optoelectronic characteristics of the QPD. Hence, this section presents the raw data. It examines the direct impact of proton, electron, and gamma irradiation on QPD performance, specifically in dark current, capacitance, and QE. None of the QPDs experienced a breakdown throughout the

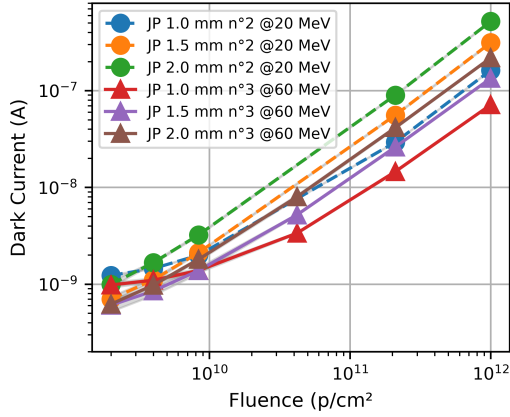
irradiation campaigns. However, the 1.5 mm NL QPD (number 3) suffered a pin breakage under 60 MeV proton irradiation, likely due to excessive mechanical stress during handling. Consequently, for this specific QPD, all subsequent analyses and calculations are based solely on segments A, B, and C, excluding segment D.

### **Dark Current versus irradiation conditions**

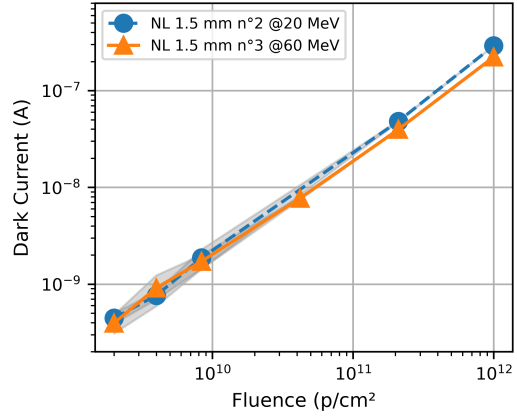
Figure 5.1 presents insitu dark current measurements taken on-site after each irradiation step at 20 °C for all JP and NL QPDs, plotted against the applied fluence. Specifically, Figures 5.5a, 5.5b, 5.5c, and 5.5d detail the effects of proton irradiation on JP and NL QPDs, as well as the effects of electron and gamma-ray exposure, respectively.

Consistent with predictions, an increase in dark current is observed across all QPDs. The observed degradation depends on irradiation particle, energy, QPD type, and size. Proton irradiation at 20 MeV caused the most significant dark current rise. For electrons, the highest degradation occurred at 1.0 MeV. These findings align with NIEL predictions, discussed later in Section 5.1.4. The QPD type influenced radiation results susceptibility, with NL and JP QPDs showing different responses. Within JP QPDs, larger sizes exhibited higher dark current increases, consistent with Equation 3.13, which predicts more defects in larger volumes.

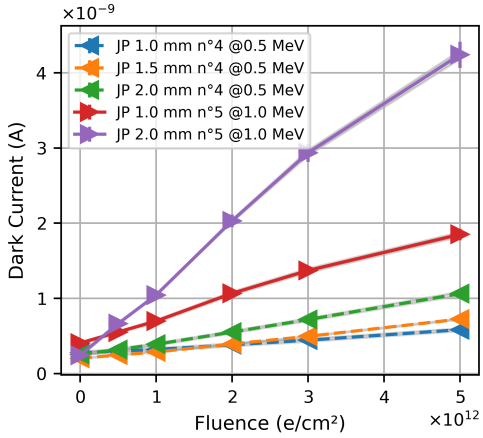
The most significant dark current increase was in the 2.0 mm JP QPD under 20 MeV proton irradiation, reaching 0.5  $\mu\text{A}$  at 20 °C and up to 4.4  $\mu\text{A}$  at 50 °C. Nevertheless, under LISA's specific fluence requirement for proton irradiation ( $1.41 \times 10^{11}$  p/cm<sup>2</sup> at 20 MeV and temperatures up to 30 °C), all QPDs maintained dark current levels beneath the LISA maximum of 1  $\mu\text{A}$ .



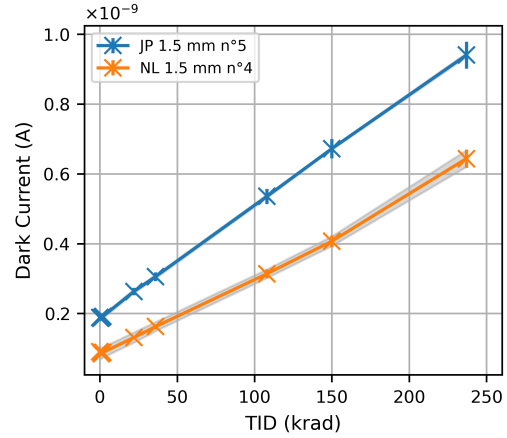
(a) JP QPDs under 20 and 60 MeV protons



(b) NL QPDs under 20 and 60 MeV protons



(c) JP QPDs under 0.5 and 1.0 MeV electrons



(d) 1.5 mm NL and JP QPDs under gamma-rays

Figure 5.5: Dark current versus applied fluence for each irradiation step at 20 °C and 5 V for JP QPDs and 20 V for NL QPDs. The subfigures show (a) JP QPDs under 20 and 60 MeV protons, (b) NL QPDs under 20 and 60 MeV protons, (c) JP QPDs under 0.5 and 1.0 MeV electrons, and (d) 1.5 mm NL and JP QPDs under gamma-rays. Data points show the average dark current over the four QPD segments, and the grey-shaded area shows the standard deviation between segments. Error bars represent the measurement precision.

## Capacitance versus irradiation conditions

Figure 5.6, 5.7, and 5.8 presents the capacitance measurements taken on-site after each irradiation step at 25 °C for all JP and NL QPDs, plotted against the applied fluence. Specifically, Figures 5.6, 5.7, and 5.8 detail the effects of proton, electron, and gamma-ray exposure, respectively.

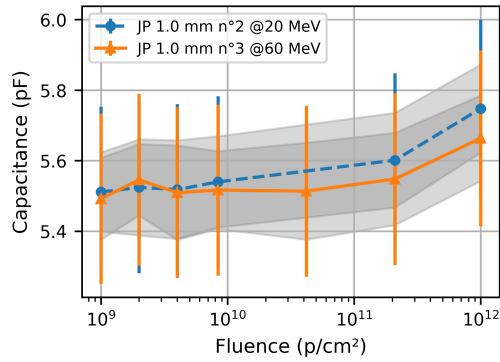
Gamma and electron irradiation had minimal impact on capacitance, as shown in Figure 5.7 and 5.8. For protons, NL QPD number 3 exhibited an unusual decrease in capacitance at the third irradiation step, followed by an increase. This anomaly is likely due to the broken pin, which may have also affected other segments, making it unrelated to radiation damage. NL QPD number 2, exposed to 20 MeV protons, showed no significant irradiation effects.

In contrast, the JP QPDs capacitance seems to increase with fluence:

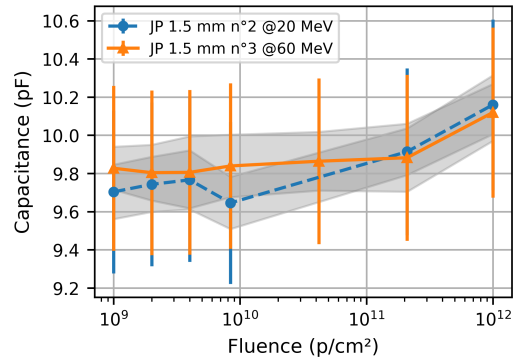
- 1.0 mm QPD: +0.24 pF (4.4%) at 20 MeV, +0.17 pF (3.1%) at 60 MeV
- 1.5 mm QPD: +0.46 pF (4.7%) at 20 MeV, +0.29 pF (3.0%) at 60 MeV
- 2.0 mm QPD: +0.80 pF (5.5%) at 20 MeV, +0.48 pF (3.4%) at 60 MeV

However, these increases are within the measurement precision (except for 1.5 mm and 2.0 mm QPD under 20 MeV protons) and should be interpreted cautiously. Nevertheless, similar to dark current, the capacitance increase depends on irradiation particle, energy, QPD type, and size.

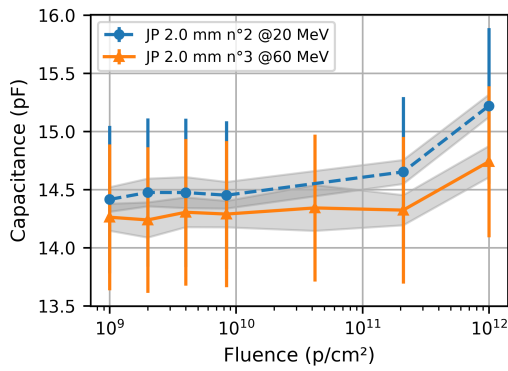
While LISA has no specific capacitance requirements, capacitance directly influences noise levels, a critical parameter for LISA.



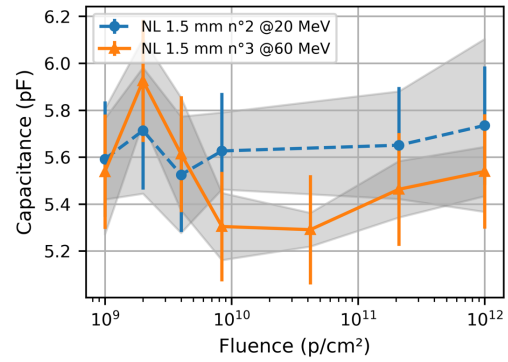
(a) JP 1.0 mm QPDs



(b) JP 1.5 mm QPDs

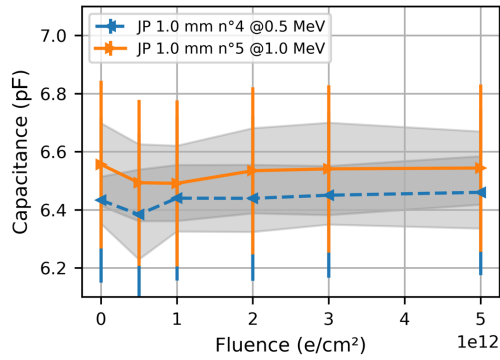


(c) JP 2.0 mm QPDs

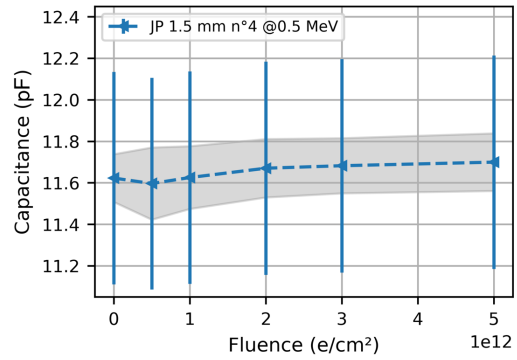


(d) NL 1.5 mm QPDs

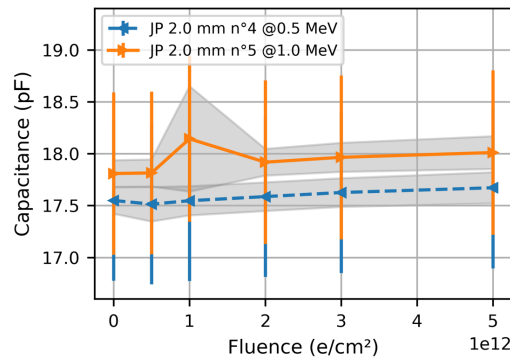
Figure 5.6: Capacitance versus applied fluence for each irradiation step under 20 and 60 MeV protons for a) 1.0 mm JP QPDs, b) 1.5 mm JP QPDs, c) 2.0 mm JP QPDs, and d) 1.5 mm NL QPDs at 25 °C and 5 V for JP QPDs and 20 V for NL QPDs. Data points show the average dark current over the four QPD segments, and the grey-shaded area shows the standard deviation between segments. Error bars represent the measurement precision. For clarity in the graph, the data point at  $1 \times 10^9$  p/cm represents the pre-irradiation results and does not correspond to an actual irradiation step.



(a) JP 1.0 mm QPDs



(b) JP 1.5 mm QPDs



(c) JP 2.0 mm QPDs

Figure 5.7: Capacitance versus applied fluence for each irradiation step under 0.5 and 1.0 MeV electrons for a) 1.0 mm JP QPDs, b) 1.5 mm JP QPDs, and c) 2.0 mm JP QPDs at 25 °C and 5 V. Data points show the average dark current over the four QPD segments, and the grey-shaded area shows the standard deviation between segments. Error bars represent the measurement precision. For clarity in the graph, the data point at  $1 \times 10^9$  p/cm represents the pre-irradiation results and does not correspond to an actual irradiation step.

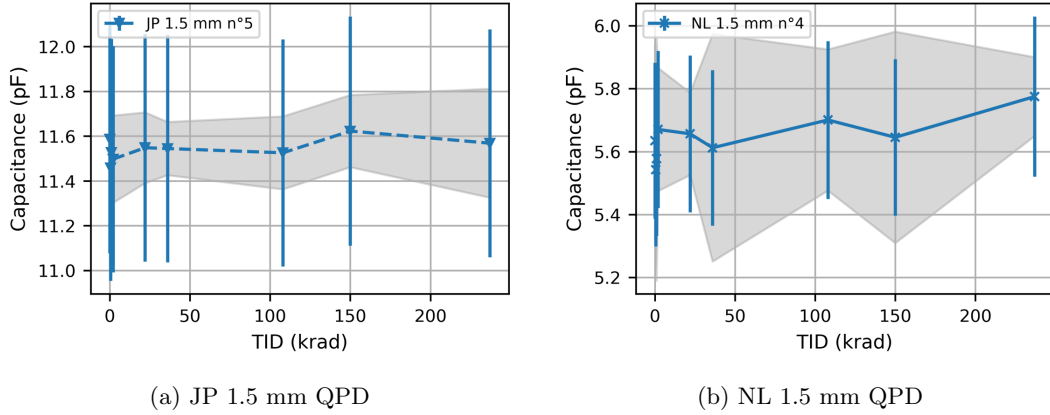


Figure 5.8: Capacitance versus applied fluence for each irradiation step under gamma-rays for a) 1.5 mm JP QPD and b) 1.5 mm NL QPD at 25 °C and 5 V for JP QPD and 20 V for NL QPD. Data points show the average dark current over the four QPD segments, and the grey-shaded area shows the standard deviation between segments. Error bars represent the measurement precision.

In a study by Gilard [96], researchers conducted capacitance measurements on four PDs: PM1R, 1931SGM, GAP394, and G8195—following proton irradiation across energies ranging from 5 to 60 MeV, with fluences reaching up to  $1 \times 10^{12}$  p/cm<sup>2</sup>. Among these, only the G8195 PD showed a significant increase in capacitance, rising from 1.76 pF to 6.11 pF. In contrast, the PM1R, 1931SGM, and GAP394 PD exhibited a reduction in capacitance. A subsequent study by Li [113] also observed a decrease in capacitance when exposing devices to 10 MeV protons at fluences of  $2.19 \times 10^{11}$  p/cm<sup>2</sup>,  $2.19 \times 10^{12}$  p/cm<sup>2</sup>, and  $4.37 \times 10^{12}$  p/cm<sup>2</sup>. Under a bias of -5 V, the capacitance gradually dropped from 1.75 nF to 1.26 nF.

These differences in capacitance behaviour likely result from the effects discussed in Section 3.4, which influence carrier lifetime, mobility, and concentration, directly affecting capacitance through changes in the depletion region’s width. The following points discuss several potential explanations:

- **Introduction of donor and acceptor levels:** According to Section 3.4, irradiation-induced defects can introduce shallow energy levels in semiconductors, releasing more charge carriers (electrons or holes). This surge in free carrier concentration leads to better shielding of the electric field caused by ionized impurities at the edges of the depletion region, effectively reducing its width. Because junction capacitance is inversely related to the width of the depletion region (see Equation 2.19), an increase in free carrier concentration results in a narrower depletion zone, thereby increasing capacitance.
- **Partial compensation of doping:** Irradiation-induced defects in semiconductors with high initial doping concentrations can introduce energy levels that act as dopants of the opposite type, such as acceptor levels in n-type material or donor levels in p-type material. These defects partially compensate for the existing doping, effectively reducing the net doping concentration. This reduction does not primarily increase the free carrier concentration as in the previous case but alters the balance of ionized dopant atoms. As the width of the depletion region is inversely proportional to the square root of the doping concentration, a decrease in net doping can lead to a narrower depletion region, leading to an increase in capacitance. Therefore, a reduced depletion region width leads to higher capacitance.
- **Introduction of deep-level traps:** Irradiation can create deep-level traps in semiconductors, which differ from shallow-level defects that introduce new free carriers. These deep traps capture free carriers, such as electrons or holes, effectively removing them from the conduction process. This increased recombination rate reduces the average lifetime of free carriers, thereby

diminishing the PD's effective charge storage capacity. Since the capacitance of PD is directly influenced by the availability of free carriers to store charge, a reduction in carrier lifetime due to increased recombination results in a decrease in capacitance. This effect contrasts with the potential capacitance increase caused by the introduction of shallow-level donors or acceptors and partial doping compensation.

### **Quantum efficiency versus irradiation conditions**

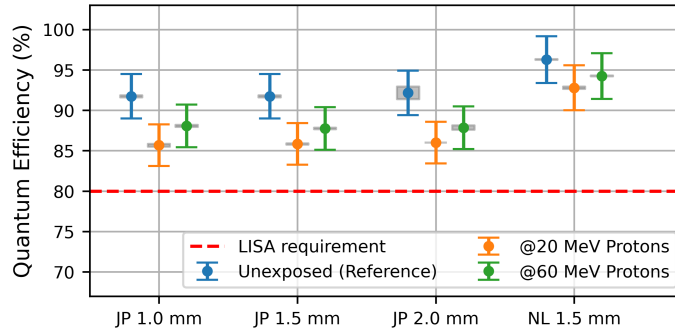
Figure 5.9 presents post-irradiation QE at room temperature for all JP and NL QPDs. Specifically, Figures 5.9a, 5.9b, and 5.9c detail the effects of proton, electron, and gamma-ray exposure, respectively. Due to the difficulty of moving the QE set up on-site, the measurements were performed after all irradiation campaigns and all at the same moment; so six months after the proton irradiation campaign, two months following the electron and one month after the gamma irradiation campaign.

Gamma and electron irradiation had minimal impact on capacitance, as shown in Figure 5.9b and 5.9c. For protons, the QE decreases after protons irradiation of:

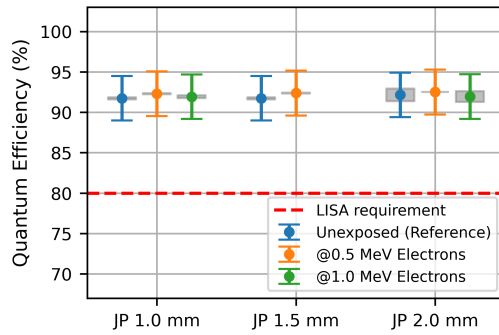
- 1.0 mm JP QPD: 7.0% at 20 MeV, 4.1% at 60 MeV
- 1.5 mm JP QPD: 6.9% at 20 MeV, 4.4% at 60 MeV
- 2.0 mm JP QPD: 7.1% at 20 MeV, 5.1% at 60 MeV
- 1.5 mm NL QPD: 3.8% at 20 MeV, 2.2% at 60 MeV

Similar to dark current, the results depend on energy and QPD type, but not on QPD size, as QE is not influenced by the size of the QPD.

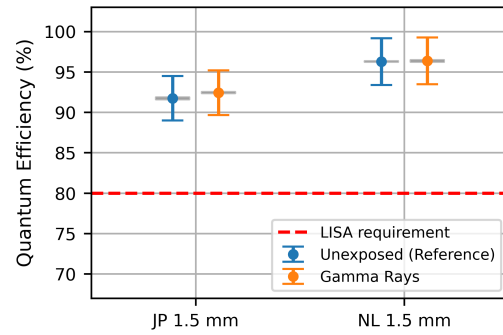
Despite these decreases, all JP and NL QPDs maintained a QE above the LISA mission's minimum requirement of 80%, even at a fluence level of  $1 \times 10^{12}$  p/cm<sup>2</sup>.



(a) Protons



(b) Electrons



(c) Gamma-rays

Figure 5.9: QE for a) JP and NL QPDs under 20 and 60 MeV, b) JP QPDs under 0.5 and 1.0 MeV electrons, and c) 1.5 mm JP and 1.5 mm NL QPD under gamma-rays performed at room temperature and 5 V for JP QPD and 20 V for NL QPD. Data points show the average dark current over the four QPD segments, and the grey-shaded area shows the standard deviation between segments. Error bars represent the measurement precision.

Compared to previous work, in Carrasco’s 2021 study [114], QE diminished by 3.8% after exposure to 63 MeV protons with a final fluence of  $6.1 \times 10^{11}$  p/cm<sup>2</sup>. This degradation aligns with the trends observed in both JP and NL QPDs. Conversely, Li (2023) [113] reported no significant changes in responsivity, even at a higher fluence of  $4.37 \times 10^{12}$  p/cm<sup>2</sup> from 10 MeV protons. These decreases in QE likely result from the effects discussed in Section 3.4, which influence carrier lifetime, mobility, and concentration. The following points discuss several potential explanations:

- **Creation of recombination centres:** Irradiation can introduce defects within the semiconductor that function as recombination centres, capturing both electrons and holes and causing their immediate recombination. This process diminishes the population of free carriers available for generating photocurrent, directly reducing QE by decreasing the overall charge carrier population.
- **Absorption by radiation defects:** Irradiation-induced defects can also act as unintended photon absorbers within the semiconductor. These defects capture photons that would otherwise generate electron-hole pairs in the semiconductor lattice. Instead of contributing to carrier generation, the energy from these absorbed photons is converted into vibrational energy. This absorption by defects reduces the number of photons available for effective carrier generation, thereby decreasing QE.
- **Increased carrier trapping:** Irradiation can introduce defects within the semiconductor’s bandgap that act as traps for charge carriers (electrons or holes) after their generation. Unlike recombination centres, these traps do not immediately cause carrier recombination but temporarily immobilize the carriers, inhibiting their contribution to the electrical current. This trapping effect reduces the effective number of free carriers available for photocurrent generation, leading to a decrease in QE.
- **Damage to the anti-reflective coating:** Although it does not directly affect carrier lifetime, irradiation can compromise the integrity of the QPD’s anti-reflective coating. Damage to this coating can reduce its effectiveness, leading to increased light reflection and decreased transmission into the semiconductor. Consequently, fewer photons reach the device’s active layer, diminishing the efficiency of photon-to-current conversion. This issue is relevant in our case, as these QPDs employ a specific coating optimized at 1064 nm. Carrasco [114] provides comparative data on devices with and without anti-reflective coatings, highlighting the significance of this effect.

### 5.1.3 Experimental damage factors applied to dark current

The concept of the damage factor, introduced in Section 3.6.1, is essential for assessing and predicting the radiation resilience of devices and semiconductors [51], [59], [60], [77], [79], [81], [90], [91], [115]–[117]. This factor applies to analyzing the dark current increase in response to radiation, as detailed by [75], [118], [119] and depicted in Figure 5.5. The damage factor for dark current ( $K_{\text{Idark}}$ ), defined by Equation 5.1, diverges slightly from Srour’s universal formula [75] and the one introduced in Section 3.6.1 due to the unknown width of the depletion region in the NL and JP QPDs. However, this deviation does not compromise the proportionality between NIEL and the damage factor, enabling us to apply the NIEL scaling approach to our data in the next section.

$$K_{\text{Idark}} = \frac{I_{\text{dark}}(\Phi) - I_{\text{dark}}(0)}{\Phi \cdot S}. \quad (5.1)$$

$I_{\text{dark}}(\Phi)$  is the dark current after irradiation at fluence  $\Phi$ ,  $I_{\text{dark}}(0)$  is the pre-irradiation dark current value, and  $S$  represents the photosensitive surface of the QPD.

Figure 5.10 presents the experimental damage factors from insitu dark current results at 20 °C of irradiated JP and NL QPD plotted against the applied fluence. Data points show the average dark current over the four QPD segments, and the grey-shaded area shows the standard deviation between segments. Figure 5.10a includes experimental damage factors for JP QPDs exposed to 20

MeV and 60 MeV protons, 5.10b) NL QPDs exposed to 20 MeV and 60 MeV protons, and 5.10c JP QPDs exposed to 0.5 MeV and 1.0 MeV electrons.

Damage factors due to electron irradiation showed no significant changes, indicating stability. Meanwhile, the damage factor increased by 19% under 60 MeV proton irradiation and 50% under 20 MeV proton. Ideally, such factors should remain consistent across fluences. Although statistical effects might explain some variability in the damage factors [120], [121], for large diameter PDs, this phenomena typically occur at much lower fluences, suggesting other causes. To be quantitative, the number of nuclear reaction  $n$  can estimated using the following Equation 5.2:

$$n = S \cdot W \cdot \sigma \cdot \Phi \cdot N, \quad (5.2)$$

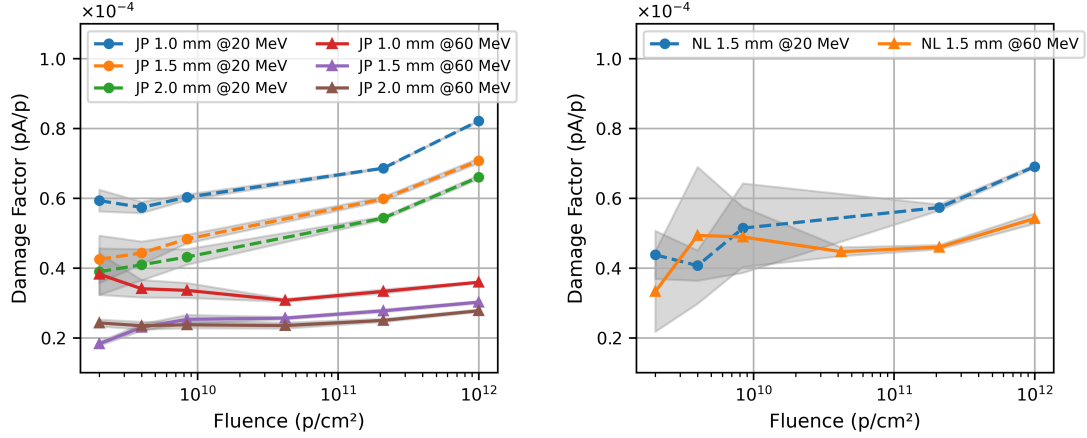
With  $S$  the QPDs surface area,  $W$  the depletion width,  $\Phi$  the applied fluence,  $N$  the number of atoms per  $\text{cm}^{-3}$  and  $\sigma$  the nuclear cross-section of the material. In our case, the QPDs are using a complex material ( $\text{In}_{0.47}\text{Ga}_{0.53}\text{As}$ ), therefore the total number of reactions will be the sum of the  $n_i$  for each material (In, Ga, and As).  $\sigma$  was evaluated for In, Ga, and As using Geant4 [122] software and are resumed in the Table 5.1. Table 5.2 resumes the number of nuclear reactions.

Table 5.1: Nuclear cross sections ( $\sigma$ ) for Indium, Gallium, and Arsenic for 20 MeV and 60 MeV protons, calculated using Geant4.

Energy	$\sigma_{In} \text{ cm}^2$	$\sigma_{Ga} \text{ cm}^2$	$\sigma_{As} \text{ cm}^2$
20 MeV	$6.25 \times 10^{-24}$	$7.0 \times 10^{-24}$	$67.2 \times 10^{-24}$
60 MeV	$7.5 \times 10^{-24}$	$6.3 \times 10^{-24}$	$6.8 \times 10^{-24}$

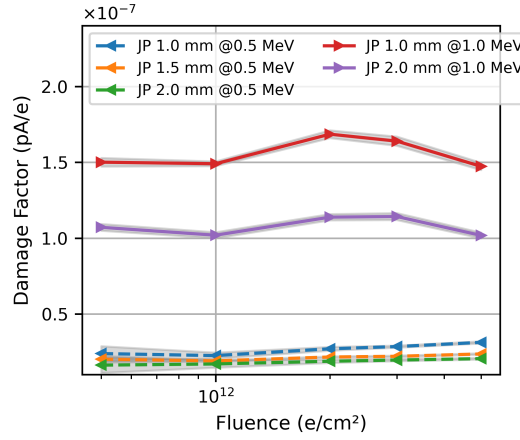
Table 5.2: Estimated number of nuclear reactions in  $\text{In}_{0.47}\text{Ga}_{0.53}\text{As}$  for various proton fluences at 20 MeV and 60 MeV, based on cross sections from Table 5.1.

Fluence	$2 \times 10^9$	$4 \times 10^9$	$8.4 \times 10^9$	$2.1 \times 10^{11}$	$1 \times 10^{12}$
20 MeV	11298	22596	47452	1186311	5649100
60 MeV	11536	23073	48454	1211352	5768344



(a) JP QPDs under 20 and 60 MeV proton

(b) NL QPDs under 20 and 60 MeV proton



(c) JP QPDs under 0.5 and 1.0 MeV electrons

Figure 5.10: Dark current experimental damage factors applied fluence for each irradiation step for a) JP QPDs under 20 and 60 MeV proton, b) NL QPDs under 20 and 60 MeV protons, and c) JP QPDs under 0.5 and 1.0 MeV electron. Data points show the average dark current over the four QPD segments, and the grey-shaded area shows the standard deviation between segments. Error bars represent the measurement precision.

The damage factors depicted in Figures 5.10 appear relatively low compared to existing literature. Table A.1 in Appendix I compiles damage factors for InGaAs detectors, summarizing findings from various studies [34], [37], [96], [113], [114], [118], [123]–[131] completing work done by Gilard 2018 [96]. These studies encompass over 30 In<sub>0.47</sub>Ga<sub>0.53</sub>As PD from different manufacturers, sizes ranging from 30  $\mu\text{m}$  to 2.0 mm, and subjected to 2 to 300 MeV protons and 0.5 to 6 MeV electrons. Table A.1 includes manufacturers, device references, sensitive surface areas, particle types, energy, fluence, and experimental damage factors calculated according to equation 5.1. Notably, the Excelitas Technologies C30618 device, examined in both Nuns 2020 [118] and Gilard [96], showed consistent damage factors, diverging by only 6.4%.

The average damage factor across studies for protons is  $6.93 \times 10^{-4}$  pA/p+, with a sdv of  $6.88 \times 10^{-4}$  pA/p+. Compared to existing literature, the damage factors for NL and JP QPDs (in average  $5.45 \times 10^{-5}$  pA/p+ with a sdv of  $5.45 \times 10^{-5}$  pA/p+) are substantially lower, averaging an order of magnitude smaller than those reported for other devices at the same energy. Only the devices studied by Joshi [34], [37] exhibit damage factors comparable to those of the NL and JP QPDs. Notably, the

2018 study utilized DDR PD technology, discussed in Section 4.1, known for its enhanced radiation tolerance over traditional PIN PDs. The foundational technology described by Joshi in 2006 [34] was further refined in the devices reported in Joshi 2018 [37], specifically adapted to meet the requirements of LISAs. The variation in damage factors could also relate to doping levels' influence, as indicated in [126]. The QPDs discussed here have relatively low doping levels, with NL QPDs doping being below  $1 \times 10^{14} /\text{cm}^3$ , which is 70 times lower than the levels in [126], highlighting the role of doping in radiation response.

#### 5.1.4 NIEL Scaling Approach applied to dark current

The NIEL scaling approach explained in section 3.6.2, is founded on the linear relationship between the NIEL and the damage factor and provides a framework for estimating and predicting radiation damage in semiconductor devices. Sections 3.4 demonstrated that displacement damage can increase the dark current by creating crystal defects. As non-ionizing damage, ionizing damage also participates in elevating dark current levels [118], [132]. As a result, the damage factor, which considers both ionizing and non-ionizing effects, may lead to inaccuracies when directly compared to NIEL values, which only account for displacement energy loss [118].

To estimate the contribution of ionizing damage to the experimental damage factor, gamma irradiation effects primarily attributed to ionizing doses serve as a benchmark for assessing the maximum potential impact of ionizing damage during proton and electron irradiations. This analysis selects gamma rays due to their higher likelihood of forming defects without immediate recombination [62], which suggests they have a higher potential for causing ionizing damage compared to electrons or protons. Here, we assume, as a worst-case scenario, that all observed increases in dark current from gamma irradiation are solely attributable to ionizing doses. Data from Figures 5.5 show that dark current spikes by approximately  $0.3 \mu\text{A}$  for protons at a TID of 237 krad, whereas gamma irradiation incurs a sub-1 nA increase under the same QPD and TID conditions. Hence, the ionizing damage contribution for protons is minimal ( $<1\%$ ) and can be neglected. Conversely, electron irradiation leads to a 550 pA rise in dark current for a 1.5 mm JP QPD at 104 krad TID, compared to a 350 pA increase due to gamma rays, suggesting that ionizing damage could constitute up to 60% of the total damage from electron irradiation in the most extreme cases. Hence, the impact of ionization damage could be significant and cannot be neglected as for proton, potentially resulting in an overestimation of displacement damage assessments when using the NIEL scaling approach. However, the LET curve for electrons in InGaAs decreases from 500 keV to 1.0 MeV and Figure 5.5c reveals a higher increase in dark current at 1.0 MeV compared to 0.5 MeV, suggesting displacement damage predominates over ionizing damage, and also questioning the validity of our hypothesis. Nevertheless, precisely quantifying displacement damage's exact contribution continues to pose a significant challenge. The unavailability of NL QPDs for electron irradiation limits the scope of conclusions regarding this aspect.

Figures 5.11 display the damage factors derived from dark current measurement, scaled to the NIEL values for protons and electrons. NIEL calculations utilized the NEMO [66] and SR-NIEL [67] software, adopting 'classical' displacement energy thresholds ( $E_d$ ) of 15 eV for Indium and 10 eV for Gallium and Arsenic, consistent with the value ( $E_d$ ) used in [96]. The scaling factor used for JP QPDs is the ratio of the NIEL value at 20 MeV from SR-NIEL to the damage factor for the 1.5 mm JP QPD at a bias voltage of -5 V after the final 20 MeV proton irradiation. For NL QPDs, it is the ratio of the NIEL value at 20 MeV from SR-NIEL to the damage factor for the 1.5 mm NL QPD at a bias voltage of -20 V after the final 20 MeV proton irradiation. Using the 1.5 mm JP QPD as a reference standard enables effective comparisons across JP QPD types, highlighting that in our case, radiation tolerance improves with increasing QPD size. Figures 5.12 display the damage factors derived from dark current measurement, scaled to the NIEL values for protons and electrons. But in contrast to Figures 5.11, the scaling factor is specific to each QPD type, suppressing the dependency on the size.

Overall, JP QPDs and NL QPDs demonstrate a consistent response to the NIEL scaling approach and exhibit uniform behaviour across types, as depicted in Figures 5.12a for proton exposure and 5.12b for electron exposure. NL QPDs align closely with the general NIEL trend. In contrast,

JP QPDs exhibit a deviation, aligning more with the predictions associated with Coulombic NIEL interactions. This divergence reflects the variability in literature, where detector outcomes oscillate between the total NIEL curve and the Coulombic NIEL curve. For example, the 1931SGN detectors, discussed in [125], demonstrate a damage factor ratio of approximately 2, closely resembling the behaviour seen in JP QPDs. Conversely, NL QPDs and detectors such as PD7006 and the Spot 4 MIR, cited in [96] and [118], present a lower damage ratio of 1.3 closer to the total NIEL, signifying a distinct pattern of damage.

Regarding electrons, Figure 5.11b reveals a clear deviation from NIEL values at low energy, aligning with findings in [60] and [118]. This deviation is not exclusive to this study or InGaAs detectors and is observed in various contexts as detailed in Section 3.6.3 [60], [83], [86], indicating a broader relevance of these observations.

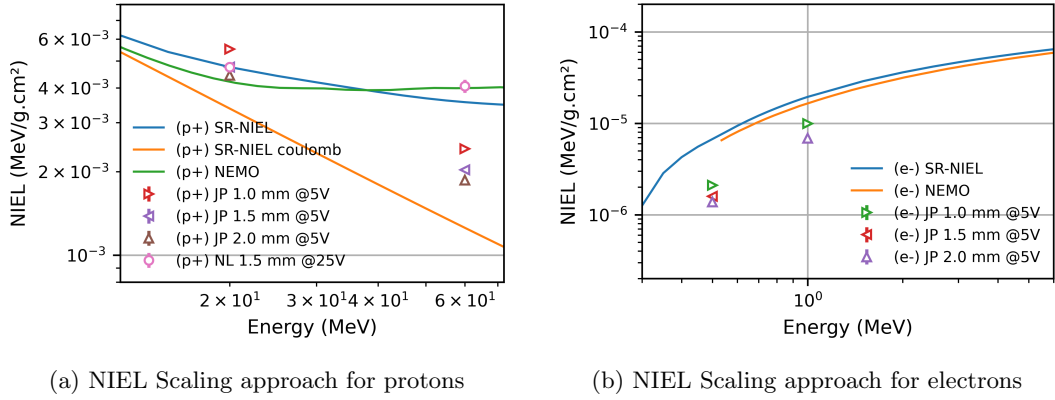


Figure 5.11: Relative comparison between the NIEL of InGaAs and the dark current experimental damage factors from a) JP and NL QPDs under 20 and 60 MeV protons and b) JP QPDs under 0.5 and 1.0 MeV electron. Data points show the average dark current over the four QPD segments.

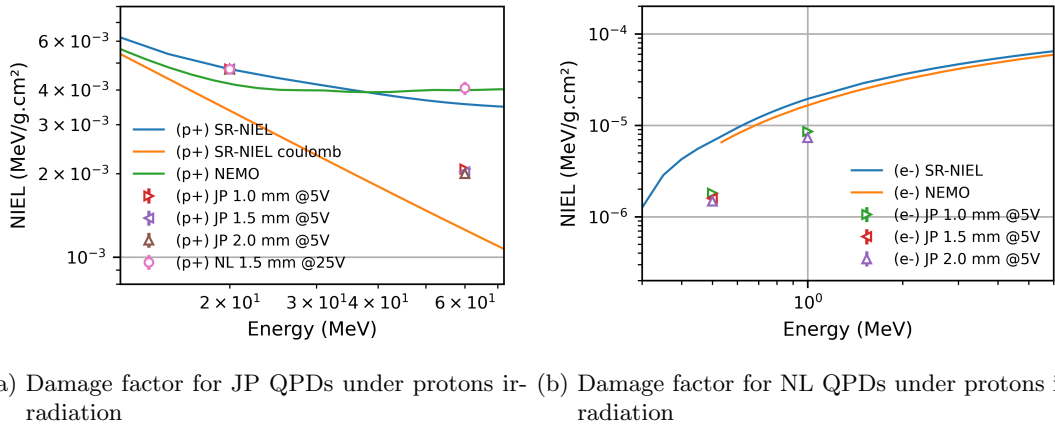


Figure 5.12: Relative comparison between the NIEL of InGaAs and the dark current experimental damage factors from a) JP and NL QPDs under 20 and 60 MeV protons and b) JP QPDs under 0.5 and 1.0 MeV electron. The scaling factor is specific to each QPD type and size. Data points show the average dark current over the four QPD segments.

## Refined Electron NIEL Calculations

As detailed in Section 3.6.3, threshold values are often derived from a range of experimental data to fit with the NIEL. For example, a recent publication from Konobeyev [70] proposes a compilation of new value of displacement threshold energy ( $E_{d_{av}}$ ) incorporating updated averaged displacement threshold energy ( $E_{d_{av}}$ ) and effective displacement energy ( $E_{d_{eff}}$ ) from different publications.

- $E_{d_{av}}$  is derived from experimental data and correlations with material properties like atomic number, density, and melting temperature.
- $E_{d_{eff}}$ , on the other hand, is estimated from reactor experiments at low temperatures.

In addition, the software SR-NIEL [67] proposed a default value for In, Ga, and As, derived from experimental data on irradiated solar cells [90], [91].

Figure 5.13 presents our data alongside the revised NIEL values using the SR-NIEL method, which incorporates the updated average displacement threshold energy ( $E_{d_{av}}$ ), the effective displacement energy ( $E_{d_{eff}}$ ) from Konobeyev’s study [70], and the ‘SR-NIEL default’ values. The exact value for each  $E_d$  can be found in Table 5.3. However, despite improved scaling with the revised NIEL values, a deviation persists for 0.5 MeV electrons.

Table 5.3: Displacement threshold energy value for In, Ga, and As.

$E_d$	Indium In (eV)	Gallium Ga (eV)	Asenide (eV)
$E_d$ Classic	15	10	10
$E_{d_{av}}$	12	23	31
$E_{d_{eff}}$	52	70	76
SR-NIEL default	43	21.5	21.5

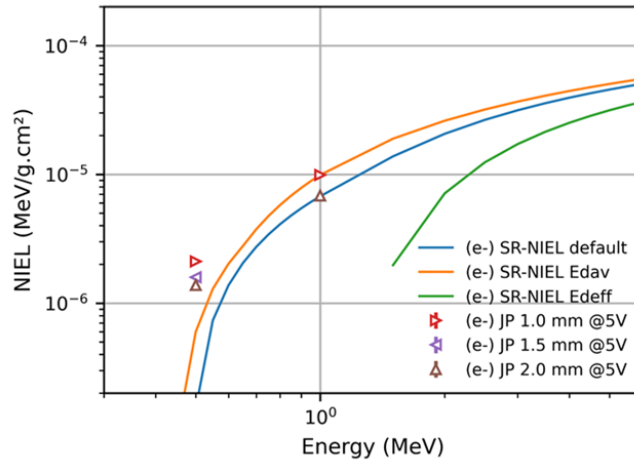


Figure 5.13: Relative comparison between new NIEL values for InGaAs and the dark current experimental damage factors from JP QPDs under 0.5 and 1.0 MeV electron. Data points show the average dark current over the four QPD segments.

References [86], [133] suggest that the traditional model, based on a sudden onset of atom ejection at a specific energy threshold, may not accurately capture low-energy interactions. For low-energy electrons that generate numerous low-energy PKAs, the classical model may significantly overestimate NIEL values. Therefore, the article describes two main approaches to improve the calculation of NIEL for materials subjected to radiation:

- **Distribution of Threshold Displacement Energies:** This approach introduces a distribution for  $E_d$ , incorporating the variability and anisotropy of displacement threshold energies in solids to more accurately represent the physical process of atom displacement due to irradiation. The distribution spans the minimum and maximum  $E_d$  values provided in [70], employing an appropriate model (such as a uniform distribution) to capture the range of possible displacement energies. This distribution is then utilized in NIEL calculations, with refinements made by comparing the results to experimental damage observations and molecular dynamics simulations, thereby ensuring that the selected range accurately models radiation damage effects.
- **Cross Interactions in Compound Materials:** For complex or compound materials such as InGaAs, the method acknowledges the presence of cross interactions between different types of atoms within the compound (e.g., In-Ga, In-As in InGaAs). This approach involves solving an integro-differential equation that describes the dynamics of damage cascades and explicitly includes these cross terms for a more detailed treatment considering all possible interactions within a compound.

Figure 5.13 represents our experimental data from electron irradiation compared to values of NIEL using the software NEMO and a uniform distribution for  $E_d$  from 10 eV to 52 eV centred in 31 eV for In, from 12 eV to 70 eV centred in 41 eV for Ge, and from 15 eV to 76 eV centred in 45 eV for As.

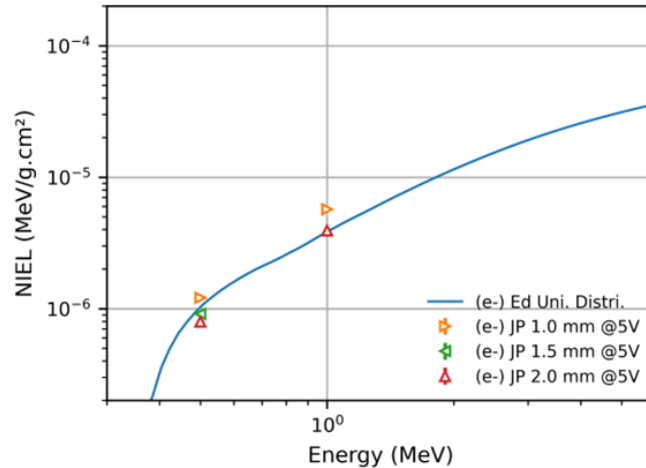


Figure 5.14: Relative comparison between NIEL values based on uniform distribution of  $E_d$  for InGaAs and the dark current experimental damage factors from JP QPDs under 0.5 and 1.0 MeV electron. Data points show the average dark current over the four QPD segments.

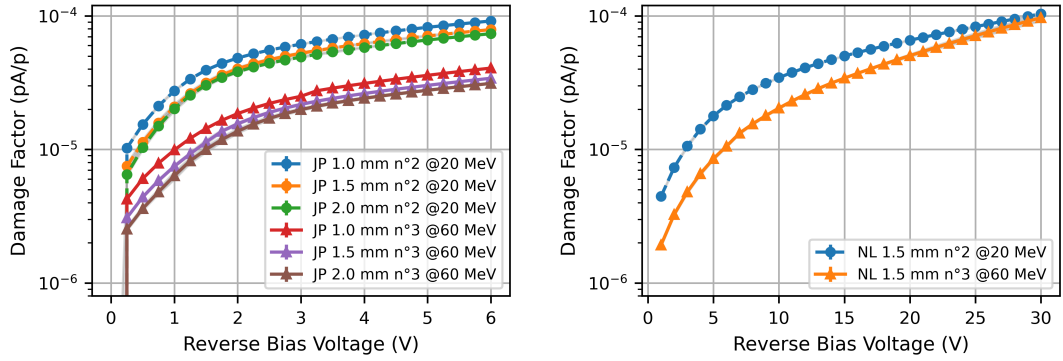
### Impact of the electric fields on the damage factor

Figure 5.1 presents the damage factor from the last irradiation step dark current measurement for all JP and NL QPDs, plotted against reverse bias voltage ( $V_{\text{bias}}$ ). Data points show the average damage factor value over the four QPD segments. The investigation into the impact of reverse bias voltage on the damage factor, as illustrated in our findings, draws significant parallels with the study by [125]. These figures suggest that the bias voltage influences the damage factor, aligning with the phenomena in [125] where the electric field intensifies thermal carrier generation in PDs due to Shockley-Read-Hall generation centres. Building upon this understanding, our analysis extends to quantify the effects of proton irradiation on activation energy ( $E_a$ ), providing a direct measure of the energy barrier that carriers must overcome in the presence of these electric fields. Specifically,

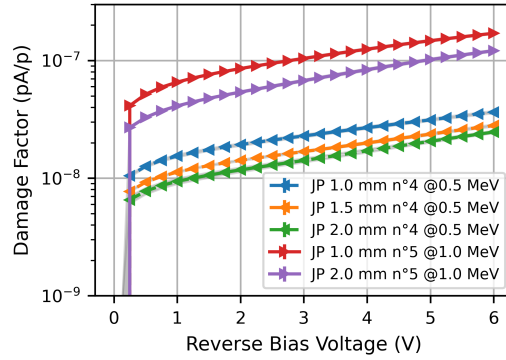
variation in  $E_a$  with bias voltage highlights a shift towards generation-recombination dominated dark current [125].

The activation energy ( $E_a$ ) was determined from dark current measurements for 1.5 mm JP and NL QPDs subjected to proton irradiation. The reported  $E_a$  values are averages across all four channels. Distinct behaviours were observed: JP QPDs irradiated with 20 MeV protons at a bias voltage of 5 V exhibited minimal changes in  $E_a$ , varying slightly from 0.63 eV to 0.58 eV post-irradiation, with similar trends observed for 60 MeV protons, suggesting a sustained generation-recombination mechanism. Conversely, NL QPDs irradiated with 20 MeV protons at a bias voltage of 20 V experienced a significant shift in  $E_a$  from 0.79 eV to 0.49 eV, indicating a transition from diffusion-limited to generation-recombination-dominated dark current. This shift is consistent with findings from [125], where electric field effects intensified carrier generation in irradiated InGaAs QPDs. Gilard [96] report similar behaviour with 1931SGM and G8195 detectors, where  $E_a$  decreases with increasing reverse bias. Pre-irradiation JP QPDs exhibited a variation in  $E_a$  from 0.7 eV at 1 V to 0.60 eV at 5 V, while NL QPDs showed a decrease from 0.85 eV at 1 V to 0.55 eV at 30 V, aligning with observations in [125], where  $E_a$  decreased from approximately 0.88 eV to 0.58 eV with increased reverse bias. However, it is important to acknowledge the limitations of this study, particularly the lack of detailed data on depletion thickness, exact doping levels, and electric field profiles, which precludes a comprehensive comparison with [96] and [125]. In addition to the factors discussed, the impact of electric fields on the activation energy ( $E_a$ ) in irradiated QPDs may also be influenced by other mechanisms like the Poole-Frenkel effect or phonon-assisted tunnelling. The Poole-Frenkel effect primarily reduces the thermal activation energy required for carriers to escape from traps, effectively lowering the  $E_a$  under strong electric fields. Phonon-assisted tunnelling, on the other hand, facilitates carrier tunnelling through potential barriers with the assistance of phonons, further increasing the generation rate under high electric fields.

It is also critical to consider the expected dependence of  $E_a$  on the bias voltage, given that the damage factor is not normalized by the depletion thickness ( $W$ ). Although the NIEL scaling approach cancels this dependence with  $W$ , differences are still observed. This is evident in both our results (see Figure 5.16 for protons and Figure 5.17 for electrons) and the findings presented in [134], where the NIEL scaling approach was applied across a range of voltages (in our case from 1 to 6 V for JP QPDs and from 1 to 30 V for NL QPDs). The variation in these factors spans from the Coulombic component at the lowest bias to the total NIEL at the highest, likely influenced by the magnitude of the electric field in the depleted region where irradiation-induced defects are located. However, a comprehensive explanation for this behaviour remains elusive. The NIEL scaling approach is based on several assumptions, including the uniformity of the electric field within the depletion zone and the consideration of only charges within this region. It also assumes that charge diffusion is negligible and that defects are confined to the depletion zone volume. However, the presence of defects at interfaces, the nature of these defects, and the fabrication process (including impurities and doping levels) can all impact the scaling results.

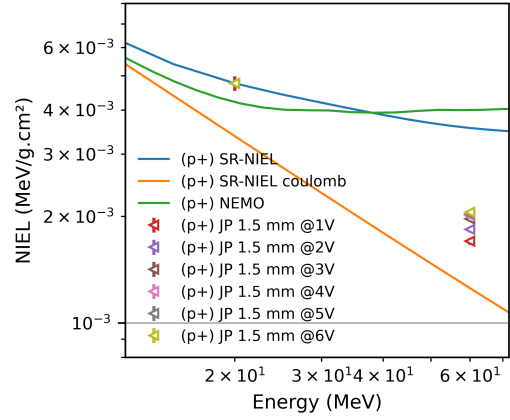
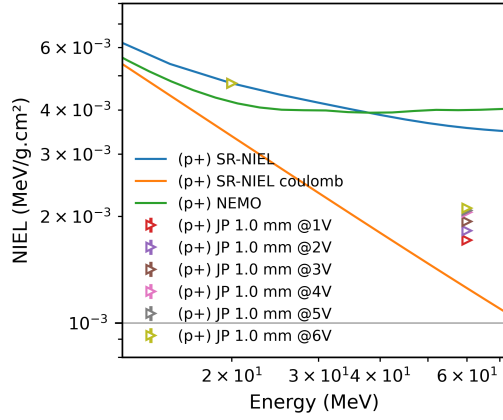


(a) Damage factor for JP QPDs under protons irradiation (b) Damage factor for NL QPDs under protons irradiation

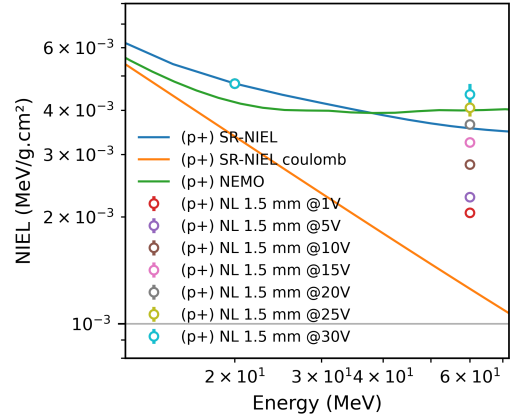
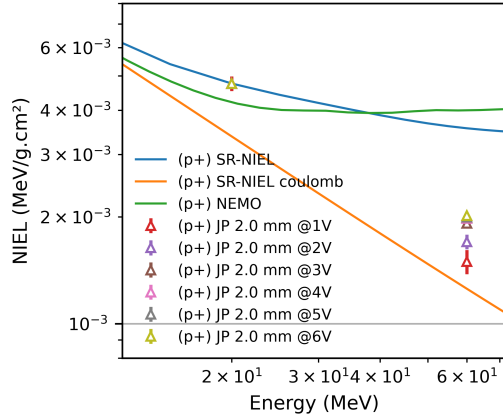


(c) Damage factor for JP QPDs under electrons irradiation

Figure 5.15: Experimental damage factor from dark current at last irradiation step for a) JP QPDs under protons, b) NL QPDs under protons, and c) JP QPDs under electrons at different  $V_{\text{bias}}$ . Each point is the average damage factor across the four QPD segments at each irradiation step at 25 °C.

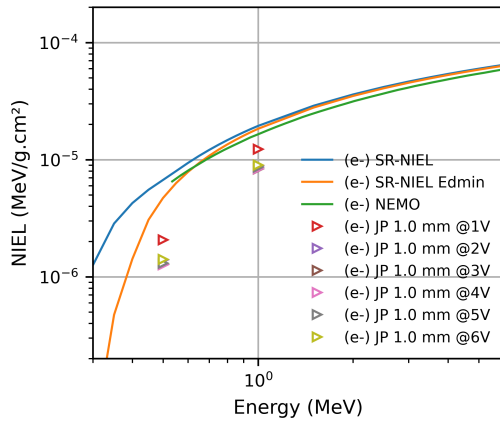


(a) Damage factor for JP QPDs under protons irradiation (b) Damage factor for 1.5 mm JP QPDs under protons irradiation

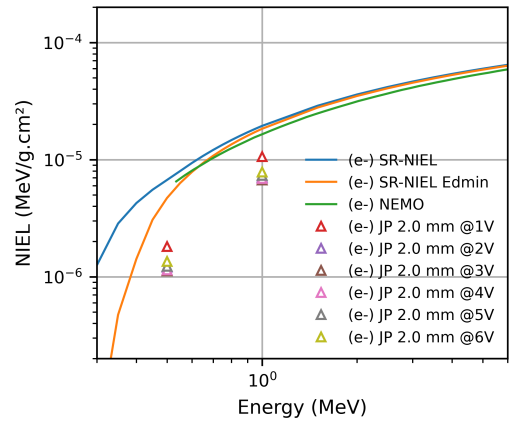


(c) Damage factor for JP QPDs under electrons irradiation (d) Damage factor for 1.5 mm NL QPDs under electrons irradiation

Figure 5.16: NIEL scaling approach for a) 1.0 mm JP QPDs, b) 1.5 mm JP QPDs, c) 2.0 mm JP QPDs, and d) 1.5 mm NL QPDs under protons at different  $V_{bias}$ . Data points show the average damage factor over the four QPD segments.



(a) Damage factor for JP QPDs under protons irradiation



(b) Damage factor for JP QPDs under electrons irradiation

Figure 5.17: NIEL scaling approach for a) 1.0 mm JP QPDs and b) 2.0 mm JP QPDs under electrons at different  $V_{\text{bias}}$ . Data points show the average damage factor over the four QPD segments.

### 5.1.5 NIEL Scaling Approach applied to the capacitance and quantum efficiency

As detailed in Chapter 3 and the analysis from section 5.1.2, the QE of the QPD, the ratio of charge carriers collected to photons absorbed, is affected by displacement damage. Similarly, capacitance, which reflects the device's charge storage capability, is affected by radiation-induced defects. Given that NIEL quantifies displacement damage, a correlation between NIEL and the damage factors for both QE and capacitance is expected. Consequently, the NIEL scaling approach is extended to analyze changes in capacitance and QE using methodologies similar to those applied to dark current. The capacitance damage factor utilizes the same formula as the dark current (Equation 5.1) but uses capacitance values. For QE, the damage factor ( $K_{QE}$ ) is introduced as follows:

$$K_{QE} = -\frac{QE(\Phi) - QE(0)}{\Phi}, \quad (5.3)$$

where  $QE(\Phi)$  and  $QE(0)$  represent post-irradiation and pre-irradiation QE, respectively. A negative sign precedes the formula to denote degradation, aligning with damage factor conventions for dark current and capacitance.

The NIEL scaling approach is applied to QE and capacitance under proton, mirroring methodology used for the dark current (see Section 5.1.4); with each QPD type 1.0 mm JP, 1.5 mm JP, and 2.0 mm JP, and 1.5 mm NL QPDs assigned a unique scaling damage factor. Electrons are excluded, as Section 5.1.2 noted their negligible effects on capacitance and QE.

Figure 5.18a illustrates the NIEL scaling approach for the capacitance results of JP QPDs under proton irradiation and Figure 5.18b, the NIEL scaling approach applied to the QE results for NL and JP QPDs under proton irradiation.

In the case of NL QPDs, the capacitance results of QPD number 3 irradiated under 60 MeV are attributed to mechanical loss from the pin break during the third proton irradiation step rather than radiation damage. This incident left us with data from only one energy level (20 MeV), making the NIEL scaling approach inapplicable for NL QPDs. Despite this limitation, the results demonstrate that the NIEL scaling approach remains valid and is applied to both the capacitance and QE, with data following the total NIEL from SR-NIEL.

Although the results show relative consistency across dark current, capacitance, and QE, some minor deviations were observed. Specifically, JP QPDs exhibited behaviour more closely aligned with the total NIEL, compared to the dark current results (closer to the coulomb NIEL curve), and greater variability was noted among different QPD sizes. These deviations may stem from measurement precision limitations, as the observed degradation in QE and capacitance was minimal compared to the significant increase in dark current, often nearing our precision measurement. The anti-reflective coating on the QPDs used in QE measurements may have also influenced the results. Additionally, the six-month gap between irradiation and post-irradiation measurements could have led to discrepancies due to differing annealing rates between NL and JP QPDs.

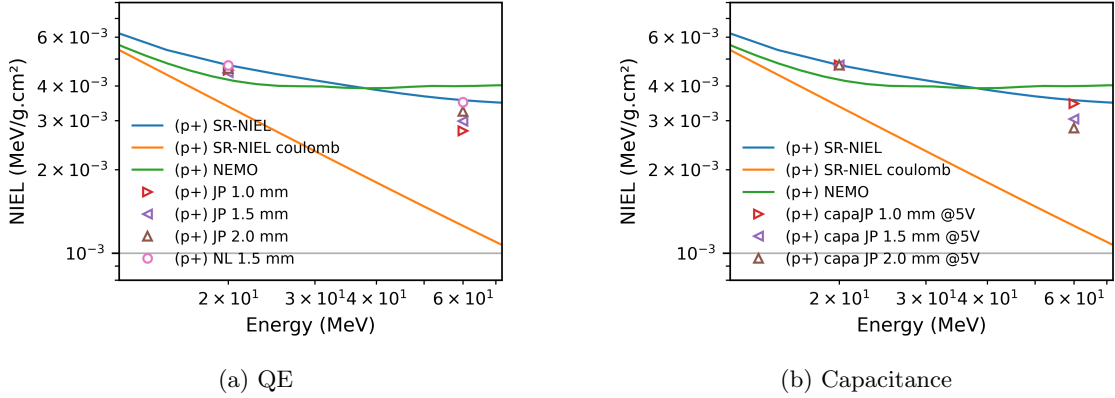


Figure 5.18: NIEL scaling approach applied to a) QE results for JP and NL QPDs, and b) Capacitance results from JP QPDs. Data points show the average damage factor over the four QPD segments.

## 5.2 Impact of irradiated QPD on QPR performances

This section focuses on the second key objective of this thesis: the impact of irradiated QPD on QPR performance, regarding noise levels and the amplitude and phase response to LISA-like optical signals. Each irradiated QPD was paired with its corresponding FEE card, developed by DE [98]. As outlined in Section 4.1, the JP and NL QPDs require distinct FEE designs due to differences in  $V_{\text{bias}}$  and packaging (TO5 and TO8). Despite these variations, the electrical design and components of the channels remain consistent across both FEE versions.

### 5.2.1 Pre-irradiation test results

#### Input Equivalent Current Noise

Figure 5.19 presents pre-irradiation EICN results for all JP and NL QPDs at room temperature with a bias voltage  $V_{\text{bias}} = 5$  V for JP QPDs and  $V_{\text{bias}} = 30$  V for NL QPDs, plotted against frequency. Detailed EICN values and capacitance for the reference QPD (number 1) are summarized in Table 5.4. From this Table 5.4 and Figure 5.19, two key observations emerge:

- **Frequency dependence:** Figure 5.19 indicate an increase in EICN as the frequency rises. This increase is detailed in the EICN model of the QPR presented in Section 2.3.4, Equation 2.26. Precisely, the frequency dependency comes from the op amps's voltage noise,  $i_{vn}$  described by Equation 2.24.
- **Capacitance dependency:** At a fixed frequency, an observed increase in EICN correlates with rising QPD capacitance, as evidenced by the values in Table 5.4, which show lower EICN levels at lower capacitance. This relationship is due to the voltage noise of the op amps, where the frequency-dependent term is also proportional to QPD capacitance. Furthermore, since capacitance increases with the surface area of the QPD as detailed in Equation 2.19, EICN levels also rise with increased surface area.

The LISA mission stipulates a EICN level below  $2.0 \text{ pA}/\sqrt{\text{Hz}}$  across a frequency range of 5 to 30 MHz. Within this criteria, NL QPDs with 1.5 mm diameters and JP QPDs with 1.0 mm diameters meet the specified noise threshold. However, JP QPDs with a 2.0 mm diameter exceed this limitation due to their higher capacitance value, linked to a larger photosensitive area unlike other QPDs. 1.5 mm JP QPDs do not also fulfill the requirement. However, 1.5 mm JP QPDs satisfy the EICN requirement up to 25 MHz, coinciding with the expected frequency variation of the LISA Heterodyne signal due to orbital dynamics of  $15 \pm 8$  MHz [15], therefore could be potential candidates.

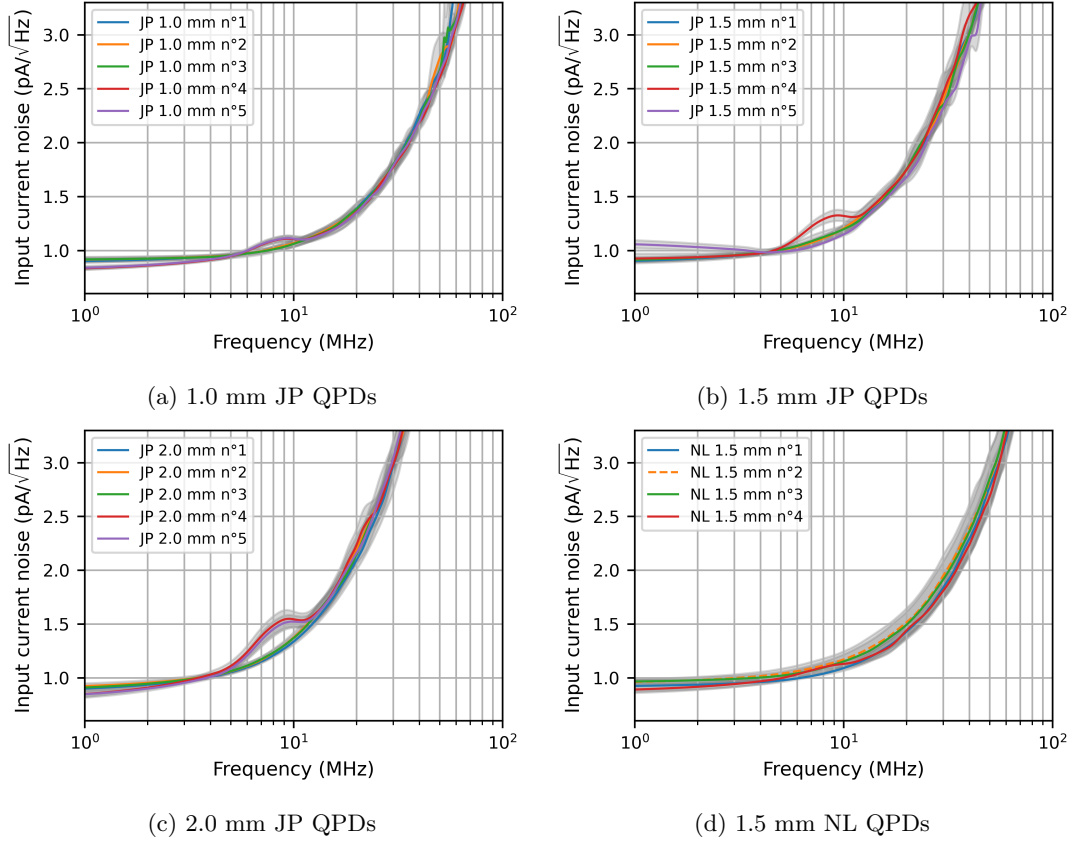


Figure 5.19: EICN versus frequency for a) 1.0 mm JP QPDs, b) 1.5 mm JP QPDs, c) 2.0 mm JP QPDs, and d) 1.5 mm NL QPDs, before irradiation performed at rooms temperature with  $V_{\text{bias}} = 5$  V for JP QPDs and  $V_{\text{bias}} = 30$  V for NL QPDs. Data points represent the average noise across four channels, processed via LOESS smoothing (detailed in Section 4.5). The grey-shaded area shows the standard deviation between segments.

Table 5.4: Capacitance and EICN at 25 MHz for JP and NL reference QPDs.

QPD Type	Capacitance (pF)				EICN pA/ $\sqrt{\text{Hz}}$ at 25 MHz			
	A	B	C	D	A	B	C	D
JP 1.0 mm ( $V_{\text{bias}}=5\text{V}$ )	5.50	5.69	5.44	5.45	1.85	1.73	1.73	1.79
JP 1.5 mm ( $V_{\text{bias}}=5\text{V}$ )	9.79	9.90	9.64	9.56	2.79	2.24	2.35	2.34
JP 2.0 mm ( $V_{\text{bias}}=5\text{V}$ )	14.27	14.49	14.41	14.36	3.25	2.88	2.61	3.11
NL 1.5 mm ( $V_{\text{bias}}=30\text{V}$ )	5.71	5.58	5.39	5.29	1.97	1.73	1.91	1.73

### Phase and Amplitude Output Signal

Figure 5.20 shows the output amplitude of channel A of the QPR using 1.5 mm JP or NL QPD at three different frequencies (3, 18, and 28 MHz) and  $m = 0.2132$  in function of the AC amplitude of the interferometric signal. The results indicate the amplitude QPR response increases linearly with the incident optical power. However, the QPR saturate for  $P_{\text{AC}}(t)$  values exceeding  $22 \mu\text{W}$  as seen at a frequency of  $f = 3$  MHz in Figure 5.20a.

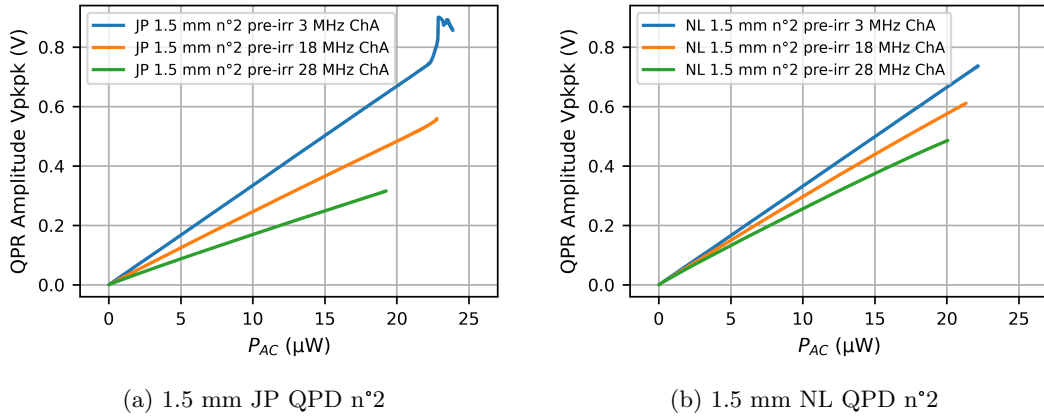


Figure 5.20: QPR output amplitude voltage at frequencies of  $f = 3, 18,$  and  $28$  MHz and  $m = 0.2132$  versus the AC signal amplitude arriving on the a) 1.5 mm JP QPD n<sup>2</sup>, and b) 1.5 mm NL QPD n<sup>2</sup>. Measurement performed at room temperature with  $V_{\text{bias}} = 5$  V for JP QPDs and  $V_{\text{bias}} = 30$  V for NL QPDs.

To efficiently present the results from both test protocols (plotter and sweeper) without generating excessive plots, Figure 5.21 integrates both measurements by utilizing the QPR gain as a common parameter. The QPR gain, defined as the ratio of the output voltage to the AC amplitude input, is determined differently for each measurement type. For plotter measurements, the QPR gain is calculated by obtaining the slope of the QPR output amplitude versus the AC amplitude input curve (see Figures 5.20) through linear regression, with saturation values excluded. For sweeper measurements, the QPR gain is obtained from the ratio of the QPR output voltage recorded by the Zurich instrument to the AC amplitude input specified by the PD NIST IG.

A strong consistency is observed between the two measurement methods (plotter and sweeper) for the 1.5 mm JP QPD No. 2, with only a minor deviation noted for the 1.5 mm NL QPD No. 2. However, at a slope of  $m = 0.000718$ , a significant discrepancy emerges between the plotter and sweeper results at high frequency ( $f = 28$  MHz) for both QPD types. This deviation is likely due to the very low AC amplitude of the signal at this frequency, which adversely affects the accuracy of the linear regression analysis.

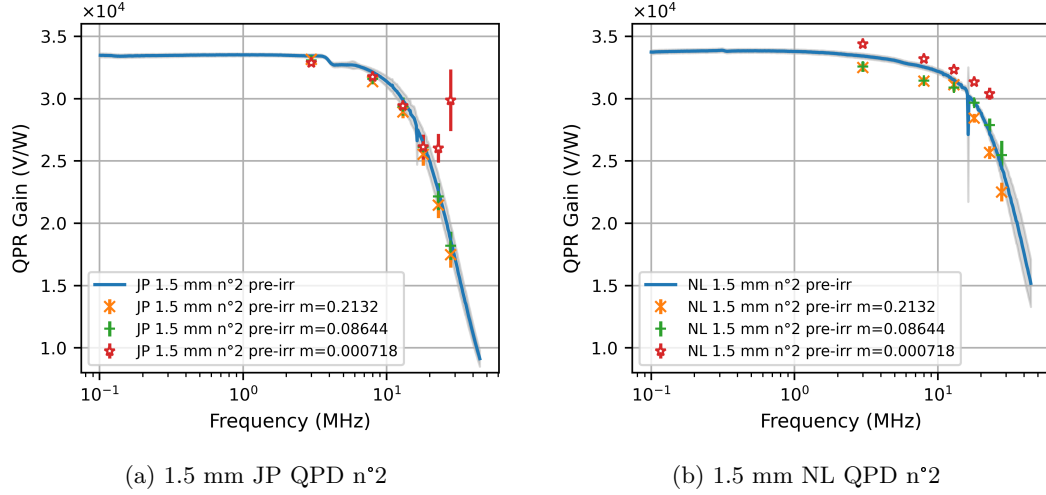


Figure 5.21: QPR gain from plotter and sweeper results versus the frequency for a) 1.5 mm JP QPD n<sup>2</sup> and b) 1.5 mm NL QPD n<sup>2</sup>. Measurement performed at room temperature with  $V_{\text{bias}} = 5$  V for JP QPDs and  $V_{\text{bias}} = 30$  V for NL QPDs. Data points show the average QPR gain over the four QPR channels, and the error bars area shows the standard deviation between channels.

The QPR's phase denoted as  $\phi_{Z,QPR}$  and read by the Zurich 1708, represents the cumulative phase shifts induced by each component of the experimental setup, mathematically expressed as:

$$\phi_{Z,QPR} = \phi_0 + \phi_{Z,1708} + \phi_{\text{cables}} + \phi_{QPR} + \phi_{\text{opt}}. \quad (5.4)$$

$\phi_0$  denotes the initial phase from the signal generation block of the interferometric setup,  $\phi_{Z,1708}$  the phase contribution from the Zurich 1708,  $\phi_{\text{cables}}$  the phase shifts from the SMA cables and the bias-T, and  $\phi_{\text{opt}}$  the phase shifts introduced by optical elements between the second beam splitter and the QPR, including the optical fibre and the small passage in free space at the collimator output.

Similarly, the phase of the PD Thorlabs, read by the slave Zurich 1794, denoted  $\phi_{Z,PDCalib}$  and is given by:

$$\phi_{Z,PDCalib} = \phi_0 + \phi_{Z,1794} + \phi_{PDCalib}. \quad (5.5)$$

$\phi_{Z,1794}$  is the phase contribution from the Zurich 1794 and  $\phi_{PDCalib}$  the phase of the Thorlabs PD. Given the Thorlabs PD's large bandwidth of 1.2 GHz, which far exceeds the study frequency band of 100 kHz to 45 MHz,  $\phi_{Z,1794}$  is approximated to zero. By combining Equations 5.4 and 5.5, the extracted QPR phase is defined as:

$$\phi_{QPR} = [\phi_{Z,QPR} - \phi_{Z,PDCalib}] - [\phi_{Z,1708} - \phi_{Z,1794}] - [\phi_{\text{cables}} + \phi_{\text{opt}}] \quad (5.6)$$

Using the same methodology as presented for the QPR amplitude results, Figure 5.21 compiles the QPR phase (derived using Equation 5.6) from both plotter and sweeper results. From this figure, two key observations can be made:

- **Frequency dependence:** The QPR phase exhibits frequency dependence, ranging from approximately -180 to -420 degrees. This variability may be attributed to either the QPR or the experimental setup, as phase precise evaluation is particularly challenging. Notably, due to uncertainties in  $\phi_{\text{opt}}$  evaluation, potential inaccuracies in the assumed phase characteristics of the Thorlabs PD, and unknown phase variation in one to the coupling elements.
- **Deviation between plotter and sweeper results:** Unlike the QPR amplitude results, where plotter and sweeper outcomes closely align, notable deviations are observed here. Since the discrepancy is consistent across all QPDs, it likely originates from a processing error in

either the sweeper or plotter data or a difference in the initial Zurich configuration parameters between the two test procedures.

Due to time constraints, the exact origins of these observations were not fully explored. Nevertheless, the findings are reproducible and consistent over time across different QPDs. Considering that the primary objective of this thesis is to assess changes between pre- and post-irradiation states, these observations do not pose a significant concern.

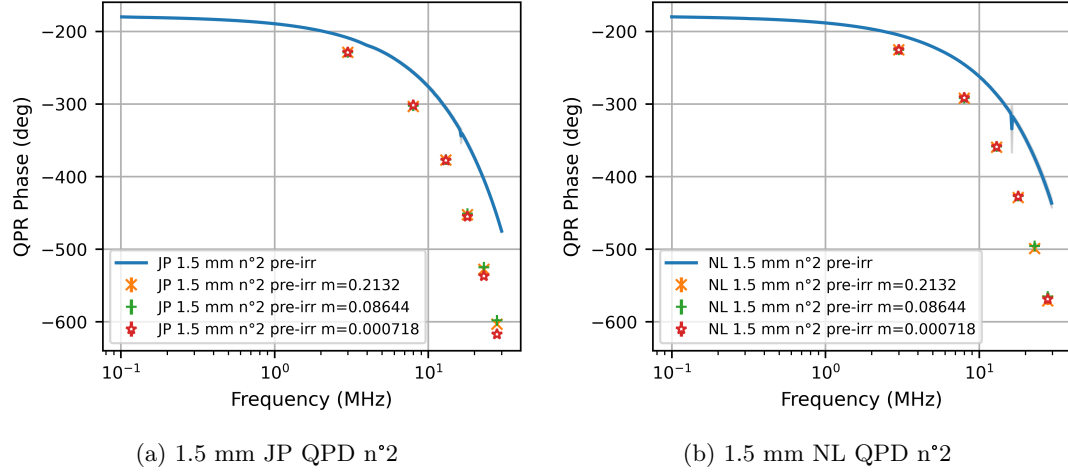


Figure 5.22: QPR phase response from plotter and sweeper results versus the frequency for a) 1.5 mm JP QPD n<sup>2</sup> and b) 1.5 mm NL QPD n<sup>2</sup>. Measurement performed at room temperature with  $V_{\text{bias}} = 5$  V for JP QPDs and  $V_{\text{bias}} = 30$  V for NL QPDs. Data points show the average QPR phase response over the four QPR channels, and the error bars area shows the standard deviation between channels.

## 5.2.2 In-situ and post-irradiation test results

### Input Equivalent Current Noise versus irradiation conditions

Figure 5.23 presents the in situ EICN measurement at three different frequencies: 3, 15, and 30 MHz for all JP and NL QPDs, plotted against applied fluence. Table 5.5 presents the exact value from Figure 5.23 and the increase between pre-irradiation and the last irradiation step. From Figure 5.23, two key observations emerge:

- **20 MeV protons irradiation:** All QPDs irradiated with 20 MeV protons exhibit a slight, frequency-dependent increase in noise, in contrast to those irradiated with 60 MeV protons, with no significant change. Table 5.5 gives exact noise values. However, for the 1.0 mm QPD, the observed increase in noise is below the measurement precision.
- **Gamma and Electrons irradiation:** overall results from gamma and electrons irradiation revealed no significant impact on the EICN.

The EICN and sdv of the 1.5 mm NL QPD No. 3 increase rapidly following the third irradiation step when the segment D's pin broke due to mechanical stress. Consequently, as with the capacitance results, the observed degradation is attributed not to irradiation but to the lack of polarization in segment D, which adversely affected the other segments of the QPD.

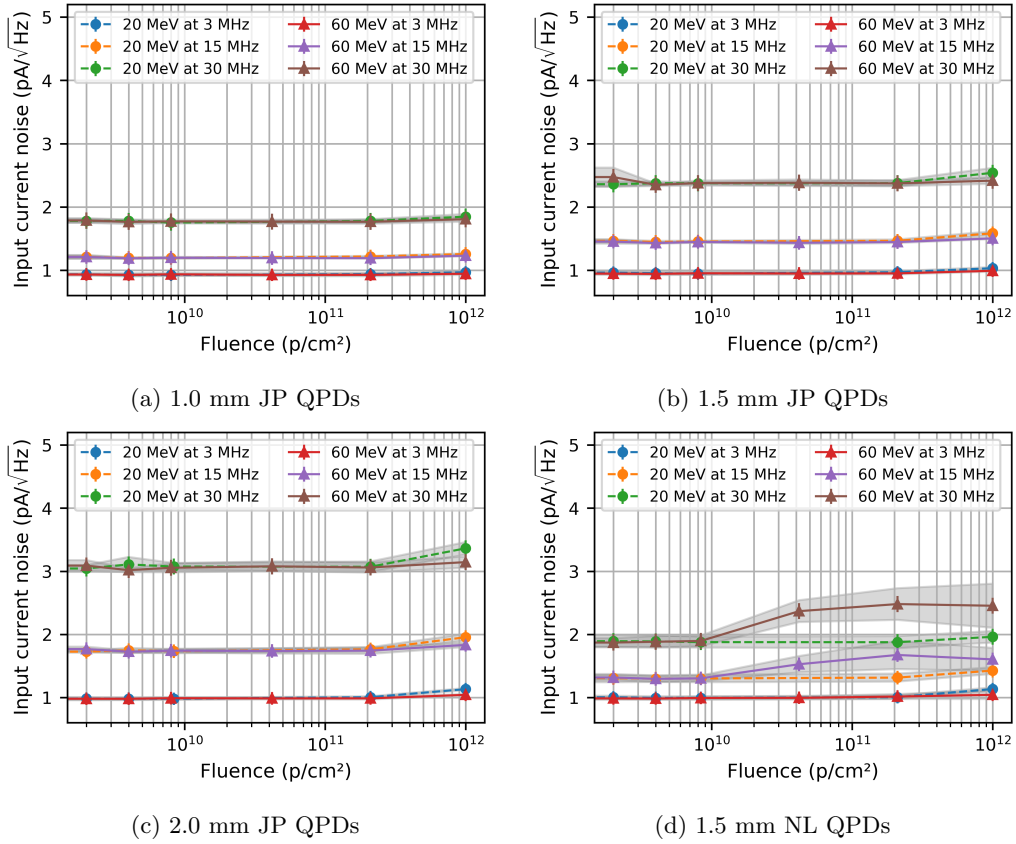


Figure 5.23: EICN versus applied fluence for each irradiation step at  $f = 3, 15,$  and  $30$  MHz and  $5$  V for JP QPDs and  $20$  V for NL QPDs. The subfigures show (a)  $1.0$  mm JP QPDs, (b)  $1.5$  mm JP QPDs, (c)  $2.0$  mm JP QPDs, and (d)  $1.5$  mm NL under  $20$  and  $60$  MeV protons. Data points show the average EICN over the four QPR channels, and the grey-shaded area shows the standard deviation between channels. Error bars represent the measurement precision.

Table 5.5: EICN results at 3, 15, and 30 MHz at each irradiation step

Fluence (p/cm <sup>2</sup> )	JP 1.0 mm n <sup>2</sup>			JP 1.5 mm n <sup>2</sup>			JP 2.0 mm n <sup>2</sup>		
Frequency (MHz)	3	15	30	3	15	30	3	15	30
0	0.93	1.21	1.78	0.95	1.47	2.41	0.98	1.76	3.03
$2 \times 10^9$	0.94	1.21	1.78	0.96	1.46	2.36	0.98	1.73	3.04
$4 \times 10^9$	0.93	1.20	1.78	0.95	1.45	2.373	0.98	1.75	3.11
$8.4 \times 10^9$	0.93	1.19	1.75	0.95	1.45	2.37	0.98	1.73	3.07
$2.1 \times 10^9$	0.94	1.22	1.78	0.97	1.46	2.38	1.01	1.76	3.07
$1 \times 10^{12}$	0.97	1.26	1.85	1.03	1.58	2.54	1.13	1.95	3.36
$i_{en}(1 \times 10^{12}) - i_{en}(f)(0)$	0.04	0.04	0.07	0.08	0.11	0.13	0.15	0.19	0.33

### Equivalent Input Current Noise versus model

The observed increase in EICN originates primarily from changes in the increased capacitance of the irradiated QPDs. Since the EICN variation is frequency-dependent, and the only frequency-dependent term in the EICN model is the op amps voltage noise—directly proportional to the capacitance (see Equation 2.24). However, this does not fully explain the EICN increase at low frequencies, where other noise sources overshadowed the op amps voltage noise. Post-irradiation results show a 500-fold increase in dark current, suggesting that the increase in shot noise, due to the significant rise in dark current, is also a contributing factor.

To validate our hypothesis, Figure 5.24 displays the pre- and post-irradiation results plotted against the frequency for the 1.5 and 2.0 mm QPDs n<sup>2</sup>, irradiated with 20 MeV protons. Additionally, the theoretical EICN, based on the model detailed in Section 2.3.4, incorporates values for  $I_{\text{dark}}$  and  $C$  from dark current and capacitance measurements. Most parameters are sourced from [98], with missing parameters adjusted to align the model with pre-irradiation results. For the post-irradiation model, only the dark current and capacitance values are modified to reflect the EICN changes observed in the QPDs post-irradiation.

Table 5.6 presents the Mean Squared Error (mse) between the noise model and experimental data for 1.5 and 2.0 mm QPDs No. 2, both before and after irradiation. The MSE values in Table 5.6 demonstrate a strong consistency between the modelled and observed EICN levels, supporting the hypothesis that the increase in dark current and capacitance is the primary contributor to the elevated EICN levels observed post-irradiation.

Table 5.6: MSE values for 1.5 and 2.0 mm JP QPD n<sup>2</sup> between noise model and experimental EICN results.

mse	pre-irradiation	post-irradiation
1.5 mm JP QPD n <sup>2</sup>	0.033	0.010
2.0 mm JP QPD n <sup>2</sup>	0.046	0.157

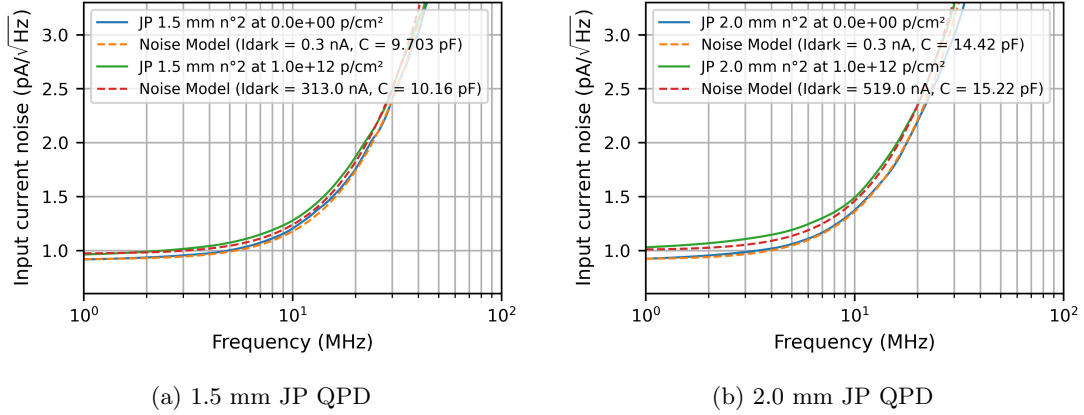


Figure 5.24: Experimental value and EICN model versus frequency for a) 1.5 mm JP QPD and b) 1.5 mm NL QPD, before and after irradiation performed at rooms temperature with  $V_{\text{bias}} = 5$  V for JP QPDs and  $V_{\text{bias}} = 30$  V for NL QPDs. Data points represent the average noise across four channels, processed via LOESS smoothing (detailed in Section 4.5).

### Phase and Amplitude QPR response versus irradiation conditions

Figure 5.25 presents the pre- and post-irradiation QPR gain results for the 1.5 mm JP QPD and 2.0 mm NL QPD, obtained from plotter and sweeper measurements. The results illustrate a decrease in QPR gain of 11.6% for the QPR with JP QPD and 5.3% for the QPR with NL QPD.

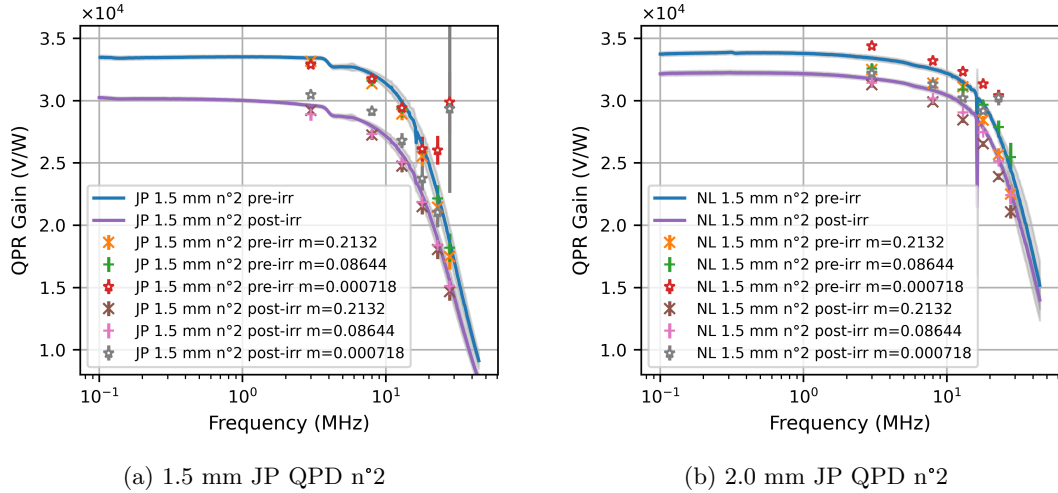


Figure 5.25: Pre and post 20 MeV protons irradiation results of the QPR gain versus frequency for a) JP 1.5 mm QPDs n<sup>2</sup> and b) JP 2.0 mm QPDs n<sup>2</sup>, regrouping data from sweeper and plotter tests. Data points represent the average noise across four channels while error bars denotes the sdv across four the four channels.

The QPR gain, defined as the ratio of the output voltage to the AC amplitude input, can be expressed as a function of the TIA gain and QE:

$$G_{\text{QPR}} = \text{QE} \frac{e}{h\nu} \cdot G_{\text{TIA}} \quad (5.7)$$

The observed decrease in gain is likely due to the degradation of the QPD's QE, which reduces photocurrent and, in turn, lowers the QPR amplitude. This hypothesis is tested by comparing

changes in QE and QPR gain from sweeper results before and after irradiation, as shown in Table 5.7. The QE values presented in Section 5.1.2 were performed five months after the QPR phase and amplitude measurements. Hence, the QE measurements for 1.5 mm JP QPD No. 2 and 2.0 mm NL QPD No. 2 were achieved just after phase and amplitude measurements to limit annealing effects. Consequently, they differ from those in Section 5.1.2. 5.7 confirms a strong correlation between QE degradation and the decrease in QPR gain, validating our hypothesis.

Table 5.7: Average reduction of QE and QPR gain (from sweeper measurements) over four the four segments for both 1.5 mm JP QPD and 1.5 mm NL QPD irradiated under 20 MeV protons.

	1.5 mm JP QPD n°2	1.5 mm NL QPD n°2
QE reduction	10.4 %	5.5 %
QPR gain reduction	11.6 %	5.3 %

Figure 5.25 illustrates the pre- and post-irradiation QPR phase results as a function of frequency for the 1.5 mm JP and NL QPDs obtained from both plotter and sweeper measurements. In contrast to the QPR amplitude, the phase remained largely unaffected by radiation, with less than a 1% difference between pre- and post-irradiation results for the 1.5 mm JP and NL QPDs.

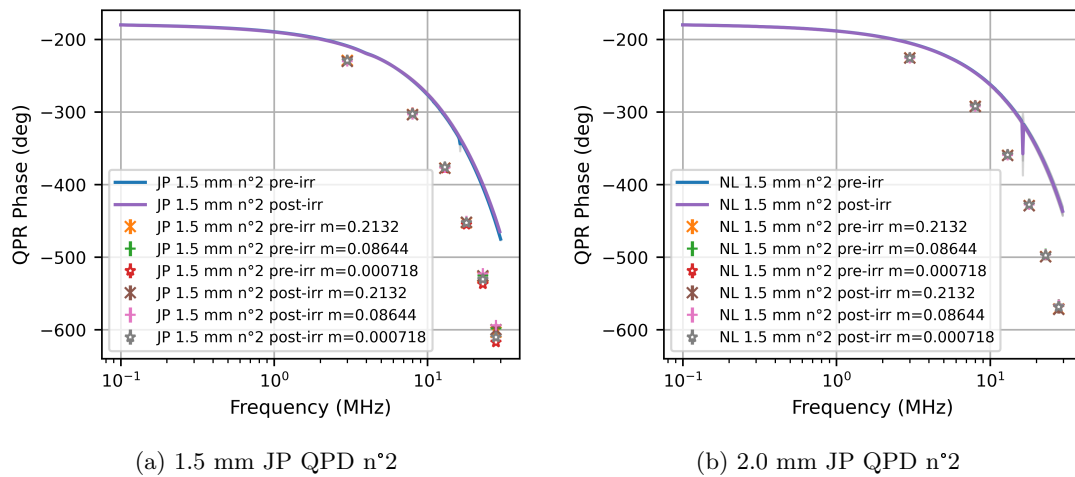


Figure 5.26: Pre and post 20 MeV protons irradiation results of the QPR phase versus frequency for a) JP 1.5 mm QPDs n°2 and b) JP 2.0 mm QPDs n°2, regrouping data from sweeper and plotter tests. Data points represent the average noise across four channels while error bars denotes the sdv across four the four channels.

## Chapter 6

# Conclusion

LISA mission, led by the ESA will be the first space-based GW detector, operating in the frequency range of  $1 \times 10^{-4}$  to 1 Hz. This low-frequency band, inaccessible to ground-based detectors, has the potential to open new frontiers in the study of the universe. The primary objective of this thesis was to investigate the performance of novel InGaAs QPDs within the context of the space radiation environment associated with LISA. The thesis is structured into six chapters, encompassing both the introduction, which outlines the context and objectives of the research, and the conclusion, which synthesizes the essential findings and implications of the study.

Chapter 2 presents the technical background describing the LISA mission and its interferometric and photodetection capabilities within the context of GWs detection and detectors. The LISA mission will consist of three spacecraft, arranged in an equilateral triangle with 2.5 million km arms, orbiting in the Earth-like heliocentric orbit at 1 AU from the Sun. The detection of GWs is achieved by measuring the distance variations between two free-fall test masses located in separate spacecraft, using three high-precision laser interferometers, referred to as TM-IFO, SCI-IFO, and Ref-IFO operating at a wavelength of 1064 nm. Interferometric signal detection in LISA is achieved with QPRs, the key subsystem for detecting, converting and amplifying the optical interference between optical signals of disparate powers  $\approx 700$  pW and 1 mW. Each QPR is composed of a new low noise and low capacitance QPD, connected to a low-noise DC-coupled TIA, assembled in a mechanical housing.

Chapter 3 presents the effects of space radiation environment on optoelectronics components on board of LISA. Throughout its 12.5-year mission, LISA will face exposure to various radiation types, such as solar wind, solar flares, and cosmic radiation. These energetic particles can penetrate spacecraft walls, causing two main types of damage to the materials. The first, known as TID, results from interactions with the atomic electron cloud, ionizing atoms and generating electron-hole pairs. The second, atomic displacement damage, arises from interactions with atomic nuclei, leading to semiconductor lattice defects quantified by NIEL and DDD, leading to electron-hole pair generation, recombination, carrier trapping, dopant compensation, and tunnelling effects. These phenomena degrade semiconductor properties and by extension, the QPD performances. For a 12.5-year mission with a 3 mm aluminium shield, ESA's worst-case scenario requirements for the optical bench components defined a TID of 40 krad (InGaAs) and a DDEF of  $1.01 \times 10^{11}$  p/cm<sup>2</sup> for 10 MeV protons, corresponding to a DDD of  $6.62 \times 10^8$  MeV g<sup>-1</sup> (InGaAs).

In this context, Chapter 4 presents the experimental methodology developed and used during the thesis to evaluate the LISA QPR in the space environment. The work focuses on two new InGaAs QPDs custom designed for the LISA mission: JP QPD (Hamamatsu industry) of three sizes (e.g. 1 mm, 1.5 mm and 2 mm diameter) and NL QPD (Bright Photonics & SMART Photonics industries) with one size (e.g. 1.5 mm diameter). The FEE, designed and produced by DE (AEI, Hannover), is also presented. For integration into the LISA mission, these QPDs and QPRs must meet ESA's requirements throughout the mission. Some critical requirements are: dark current per

segment should be less than  $1\ \mu\text{A}$  at operational temperature ranging from  $10\ ^\circ\text{C}$  to  $30\ ^\circ\text{C}$ ; QE at 1064 nm wavelength shall be  $\geq 80\%$ ; EICN per segment should not exceed  $2.0\ \text{pA}/\sqrt{\text{Hz}}$  within an operational bandwidth from 3 to 30 MHz. Therefore, to validate the suitability of those QPDs for the LISA mission, I developed four different experimental benches allowing for a complete electro-optical evaluation of the QPDs and QPRs:

- **QPD’s dark current and capacitance:** this setup utilizes a KEITHLEY 4200 for QPDs’ dark current and capacitance measurements. The QPD is placed in a metal enclosure to assure darkness and temperature control thanks to copper support connected to a Peltier cell, regulated by a Thermoelectric Controller (TEC). The dark current of each QPD segment is measured at different temperatures between 20 and  $50\ ^\circ\text{C}$  under constant reversed bias voltage: NL QPD voltage sweeps range from 0 to 30 V (1 V step) and JP QPD from -0.25 to 6 V (0.25 V step). The capacitance of each QPD segment is measured at  $25\ ^\circ\text{C}$ , applying a similar voltage as those mentioned previously, and over a frequency sweep range from 1 to 10 MHz. The precision of the experimental bench is estimated to be  $\pm 4.1\%$  for dark current and  $\pm 4.4\%$  for capacitance.
- **QPD’s QE:** the second bench measures the ratio between the photocurrent generated by a QPD segment (e.g. detected number of photons) and the incident optical power on the QPD segment (e.g. incident number of photons). The incident optical signal is generated using a 1064 nm continuous fibre laser source and monitored using a calibrated InGaAs PD NIST. The QPD resulting photocurrent is accurately measured using a Keithley 2600B source meter. The measurements were performed at a fixed optical power of  $\approx 80\ \mu\text{W}$  and bias voltage of 5 V for JP QPDs and 30 V for NL QPDs, and performed in a cleaned room with control environment. The system’s estimated error is  $\pm 3\%$ .
- **QPR’s EICN:** this setup is based on the "white light" method. It uses a filament white lamp of broad-spectrum (e.g. well-known shot noise). The DC and AC signals from each QPR channel are recorded in both dark and light (lamp on) illumination conditions by the Lecroy oscilloscope and by the R&S FSP13 spectrum analyzer over a frequency range from 1 to 100 MHz. In addition to assessing EICN, this setup also facilitates the evaluation of TIA gain. The QPDs are biased at a fixed voltage of 5 V for the JP QPD and 30 V for the NL QPD. All measurements are conducted in a clean room with a controlled environment. The experimental precision of the setup is estimated to be approximately  $\pm 5\%$  within the LISA bandwidth frequency range (3 to 30 MHz) and approximately  $\pm 20\%$  in the higher frequency range ( $> 40\ \text{MHz}$ ).
- **QPR’s amplitude and phase response to LISA-like signal:** is performed using an FIM controlled by a HF2LI Zurich lock-in amplifier to mimic a LISA-like heterodyne signal. The optical signal, produced by a 1064 nm continuous fibre laser, is monitored using a NIST-calibrated InGaAs PD for the DC component and a large bandwidth Thorlabs calibrated PD for the AC component of the signal. The phase and the amplitude of the AC QPR signals are read out by the Zurich lock-in amplifier. Two protocols of measurement were executed. The first utilized a sweep of optical laser power from 0 to  $110\ \mu\text{W}$ , with fixed modulation factors  $m$  between the following three values:  $[0.0007177, 0.08644, 0.2132]$ , representing various LISA operational scenarios from the Science OB where the AC optical beam amplitude is the lowest, to the Reference OB where the AC optical beam amplitude is the highest. For each  $m$  the measurement is performed at various fixed frequencies ( $f$ ) between 3 and 28 MHz. The second protocol was conducted for a frequency sweep from 1 to 45 MHz and at a fixed optical power of  $110\ \mu\text{W}$  close to saturation, targeting real OB conditions with  $m = 0.2132$ . Measurements were conducted under the same conditions as the QE tests (in a clean room and with the same bias voltage).

Following experimental characterisation of the parameters presented previously, LISA QPDs were irradiated with 20 and 60 MeV protons, 0.5 and 1 MeV electrons, and  $\text{Co}_{60}$  gamma rays. An exposure corresponding to a DDEF of  $1 \times 10^{12}\ \text{p}/\text{cm}^2$  for 20 and 60 MeV protons and a total ionising dose

of 237 krad were applied, exceeding the radiation requirements for the LISA mission by a factor five.

Chapter 5 presents the experimental results from pre-, in-situ, and post-irradiation and their analysis, concluding the thesis's two primary objectives reiterated here.

The first section of chapter 5 underscores the radiation effects on the QPD: a dark current increase across all irradiation conditions, reaching a maximum current of 0.5  $\mu\text{A}$  at 20°C; a maximum capacitance increase of 0.8 pF after proton irradiation and no significant changes after electron and gamma irradiations; a maximum QE reduction of 7.1% after proton irradiation while no significant changes were observed after electron and gamma irradiations. Nevertheless, all QPDs maintained functionality without critical failure and surpassed LISA's benchmarks. The degradation due to various types of irradiations was quantified using the universal damage factor defined by Srour [75] at each irradiation step based on pre-, in-situ, and post-irradiation dark current measurements. An unexpected rise in the damage factor was observed with increasing proton fluences, particularly at the two highest fluences of  $2.1 \times 10^{11}$  p/cm<sup>2</sup> and  $1 \times 10^{12}$  p/cm<sup>2</sup>. This increase was initially attributed to statistical effects. However, after calculating the expected number of nuclear reactions in InGaAs for NL QPDs at different fluences, this hypothesis was dismissed. Comparing the damage factors to literature, our QPDs showed relatively low values, at least ten times lower than those of references [123], [125], [126] and devices Excelitas C30618 in [96] and [118]. In contrast, Joshi's DDR-based InGaAs devices designed also for LISA show damage factors of the same order of magnitude as JP and NL QPDs, underscoring DDR technology's radiation tolerance. Lowering the doping concentration was proven to improve radiation tolerance according to [126], and therefore could also explain the low value of damage factor for our QPDs, since the doping level for NL QPDs is 70 times lower than in reference [126]. When applying the NIEL scaling approach to our experimental results under protons and electrons, we observed a correlation with NIEL curves for protons and a deviation for electrons. This deviation is corrected by using new NIEL curves based on a uniform distribution of displacement energy threshold to account for the variability and anisotropy of displacement threshold energies in solids as proposed by [133]. Additionally, the NIEL scaling approach was not limited to dark current measurements alone and was extended to capacitance and QE. Across these diverse measurements: dark current, capacitance, and QE, the data constantly aligned well with the predictions made by the NIEL, underscoring the robustness of this method in our analysis over different parameters.

The second section of chapter 5 underscores how irradiated QPDs affect the QPR and overall LISA performances: noting a frequency-dependent increase (less than 0.33 pA/ $\sqrt{\text{Hz}}$ ) of the EICN for the 1.5 and 2.0 mm JP QPDs irradiated under 20 MeV protons and degradation of the amplitude response for all QPR. In contrast, no significant variation in the phase was observed. Regarding LISA's EICN specifications, the 1.0 mm JP QPDs and 1.5 mm NL QPDs satisfied the requirements after irradiation. In comparison, the 1.5 and 2.0 mm JP QPD did not meet the specifications. We established that this degradation in EICN and amplitude are directly linked to observed changes in QPDs' electro-optical fundamental characteristics. Indeed, the EICN increase is correlated with dark current and capacitance augmentation. Similarly, the AC signal amplitude reduction is due to the decrease of the photocurrent (e.g. lower QE). This important observation highlights a direct relationship between the degradation of the QPD electro-optical characteristics under the LISA mission radiation conditions and the overall system performances (e.g. QPR or LISA instrument). Furthermore, future LISA QPD tests on capacitance, dark current, and QE are sufficient to fully model the space environment radiation impact on the overall QPR system.

In summary, this thesis achieved its primary objectives. Moreover, despite the observed degradation of the QPDs and QPR characteristics under the irradiation conditions applied during this thesis, the studies carried out allowed us to validate that the design and the technology of the DDR InGaAs photodiodes are suitable for the flight QPDs models of the LISA mission.

These results, however, are derived from tests and analyses conducted on a single QPD of each geometry and manufacturer for each irradiation condition, which limits the statistical robustness of the findings. Future studies should involve a larger sample of QPDs for each irradiation condition and, if possible, a broader range of irradiation conditions to validate these initial findings.

Additionally, the present research raised important questions for further study:

- Firstly, the observation of increased damage factor with the fluence.
- Secondly, different radiation responses between JP and NL QPDs under the NIEL scaling approach with NL QPDs closely matched the expected total NIEL. At the same time, JP QPDs leaned towards the Coulombian component of NIEL, and distinct patterns emerged when examining the impact of the electric fields on these responses.
- Lastly, the damage factor appears to depend on the QPD size.

While this thesis presents initial hypotheses and gives preliminary answers, a more complete response would need additional data about QPD characteristics like depletion thickness, doping levels, and field distribution within the junction— technological parameters that are not accessible.

Extending the perspectives to an experimental standpoint, while the developed setups met expectations and yielded relevant results, they suffered certain limitations. For example, for the capacitance and the dark current setup, the regular wires connecting the QPD pins to the SMA/BNC outputs of Keithley’s coaxial cables affect precision and resolution. Reducing their length or replacing them with coaxial cables would enhance measurement accuracy. Currently, the laser beam diameter in the QE setup is nearly the same as the QPD segment size. Reducing the beam diameter under the micrometres would enable segment scanning, leading to more precise QE analysis. The QPR characterization benches, even if the research showed that they are not mandatory for assessing the radiation’s impact, the noise characterization setup could be improved concerning the electromagnetic compatibility by adding filtering systems. Lastly, the optical interferometric setup designed to simulate a heterodyne LISA-like system uses an FIM and cannot replicate GW induced phase shifts. Integrating an Electro-Optic Modulator could solve or at least add perspective regarding the phase of response dynamic of the QPR.

# Bibliography

- [1] A. Einstein, ‘Approximative integration of the field equations of gravitation,’ *Sitzungsber. Preuss. Akad. Wiss. Berlin (Math. Phys. )*, vol. 1916, pp. 688–696, 1916.
- [2] S. Antier, *Multi-messenger studies of binary neutron stars*, Presented at the 2nd MaNiTou Summer School for PhD and Master Students, University of La Côte d’Azur, Nice, France, July 3-8, 2023.
- [3] S. Mastrogiovanni, *Gravitational waves and cosmology*, Presented at the 2nd MaNiTou Summer School for PhD and Master Students, University of La Côte d’Azur, Nice, France, July 3-8, 2023.
- [4] M. Sakellariadou, *Gravitational waves and fundamental physics*, Presented at the 2nd MaNiTou Summer School for PhD and Master Students, University of La Côte d’Azur, Nice, France, July 3-8, 2023.
- [5] J. Weber, ‘Observation of the thermal fluctuations of a gravitational-wave detector,’ *Phys. Rev. Lett.*, vol. 17, pp. 1228–1230, 24 Dec. 1966. DOI: 10.1103/PhysRevLett.17.1228. [Online]. Available: <https://link.aps.org/doi/10.1103/PhysRevLett.17.1228>.
- [6] R. A. Hulse and J. H. Taylor, ‘Discovery of a pulsar in a binary system.’, vol. 195, pp. L51–L53, Jan. 1975, Provided by the SAO/NASA Astrophysics Data System. DOI: 10.1086/181708. [Online]. Available: <https://ui.adsabs.harvard.edu/abs/1975ApJ...195L..51H>.
- [7] M. E. Gerstenshtein and V. I. Pustovoit, ‘On the detection of low frequency gravitational waves,’ *Soviet Physics - JETP*, vol. 16, no. 2, pp. 433–435, Jan. 1963, ISSN: 0038-5646.
- [8] B. P. and al., ‘Observation of gravitational waves from a binary black hole merger,’ *Phys. Rev. Lett.*, vol. 116, p. 061102, 6 Feb. 2016. DOI: 10.1103/PhysRevLett.116.061102. [Online]. Available: <https://link.aps.org/doi/10.1103/PhysRevLett.116.061102>.
- [9] G. M. Harry and the LIGO Scientific Collaboration, ‘Advanced ligo: The next generation of gravitational wave detectors,’ *Classical and Quantum Gravity*, vol. 27, no. 8, p. 084006, Apr. 2010. DOI: 10.1088/0264-9381/27/8/084006. [Online]. Available: <https://doi.org/10.1088/0264-9381/27/8/084006>.
- [10] F. Acernese and et al., ‘Advanced virgo: A second-generation interferometric gravitational wave detector,’ *Classical and Quantum Gravity*, vol. 32, no. 2, p. 024001, Dec. 2014. DOI: 10.1088/0264-9381/32/2/024001. [Online]. Available: <https://doi.org/10.1088/0264-9381/32/2/024001>.
- [11] K. S. Thorne, *Gravitational waves*, 1995. DOI: <https://doi.org/10.48550/arXiv.gr-qc/9506086>. arXiv: gr-qc/9506086 [gr-qc].
- [12] T. V. collaboration, *Aerial view of the virgo site*, Online; accessed: Feb. 02, 2024, 2015. [Online]. Available: [https://commons.wikimedia.org/wiki/File:Virgo\\_aerial\\_view\\_01.jpg](https://commons.wikimedia.org/wiki/File:Virgo_aerial_view_01.jpg).
- [13] P. Amaro-Seoane and al., *Laser interferometer space antenna*, 2017. DOI: <https://doi.org/10.48550/arXiv.1702.00786>. arXiv: 1702.00786 [astro-ph.IM].
- [14] J. Baker, J. Bellovary and al., *The laser interferometer space antenna: Unveiling the millihertz gravitational wave sky*, 2019. arXiv: 1907.06482 [astro-ph.IM].

- [15] European Space Agency (ESA), ‘LISA definition study report,’ European Space Agency, Technical Report ESA-SCI-DIR-RP-002, 2023, [Online]. Available: <https://www.esa.int/>.
- [16] T. eLISA Consortium and al., ‘The gravitational universe,’ 2013. DOI: <https://doi.org/10.48550/arXiv.1305.5720>. arXiv: 1305.5720 [astro-ph.CO]. [Online]. Available: <https://arxiv.org/abs/1305.5720>.
- [17] P. Amaro-Seoane and al., ‘Astrophysics with the laser interferometer space antenna,’ *Living Reviews in Relativity*, vol. 26, no. 1, Mar. 2023, ISSN: 1433-8351. DOI: 10.1007/s41114-022-00041-y. [Online]. Available: <http://dx.doi.org/10.1007/s41114-022-00041-y>.
- [18] NASA, *Nasa illustration of lisa*, Online; accessed Feb. 19, 2024, 2010. [Online]. Available: <http://lisa.jpl.nasa.gov/gallery/lisa-waves.html>.
- [19] É. É. Flanagan and S. A. Hughes, ‘The basics of gravitational wave theory,’ *New Journal of Physics*, vol. 7, p. 204, Sep. 2005. DOI: 10.1088/1367-2630/7/1/204. [Online]. Available: <http://www.njp.org/>.
- [20] R. Weiss, *Lecture 1: Gravitational wave detectors: Past and future*, YouTube video, Accessed: 14 June 2021, Jun. 2021. [Online]. Available: <https://www.youtube.com/watch?v=gNBHXYDBOY4>.
- [21] *GW150914: Fact Sheet*, Online, First direct detection of gravitational waves and first direct observation of a black hole binary. Observed by LIGO L1 H1., LIGO Scientific Collaboration and Virgo Collaboration, 2016. [Online]. Available: <https://www.ligo.org/detections/GW150914/fact-sheet.pdf>.
- [22] T. Young, *A Course of Lectures on Natural Philosophy and the Mechanical Arts*, English. London: Printed for J. Johnson, 1807. DOI: 10.5962/bhl.title.22458.
- [23] B. E. A. Saleh and M. C. Teich, *Fundamentals of Photonics*, 3rd ed. Canada: Wiley, 2019, ISBN: 9781119506874.
- [24] B. Willke, P. Aufmuth, C. Aulbert *et al.*, ‘The geo 600 gravitational wave detector,’ *Classical and Quantum Gravity*, vol. 19, no. 7, p. 1377, Mar. 2002. DOI: 10.1088/0264-9381/19/7/321.
- [25] Payload Coordination Team, ‘LISA Payload Description Document Input,’ European Space Agency (ESA), Keplerlaan 1, 2201 AZ Noordwijk, The Netherlands, Technical Report ESA-L3-EST-INST-DD-001, 18th Nov. 2017, Draft 7b061e7. [Online]. Available: <https://www.esa.int/>.
- [26] ESA and NASA, ‘Laser Interferometer Space Antenna (LISA) Mission Concept,’ European Space Agency (ESA) and National Aeronautics and Space Administration (NASA), Technical Report LISA-PRJ-RP-0001, Apr. 2009.
- [27] M. Gehler, ‘Lisa measurement concept justification document,’ ESA ESTEC, Keplerlaan 1, 2201 AZ Noordwijk, The Netherlands, Technical Note ESA-LISA-EST-MIS-TN-002, 2nd May 2022, Approved by LISA Study Manager, Martin Gehler, Date of Approval: 12/05/2022.
- [28] M. Otto, ‘Time-delay interferometry simulations for the laser interferometer space antenna,’ English, Advisors: Prof. Dr. Karsten Danzmann, Prof. Dr. Klemens Hammerer, Maître de Conférences Dr. Antoine Petiteau, Doctoral Thesis, Gottfried Wilhelm Leibniz Universität Hannover, Hannover, Feb. 2016. DOI: <https://doi.org/10.15488/8545>. [Online]. Available: <https://www.repo.uni-hannover.de/bitstream/handle/123456789/8598/866525041.pdf?sequence=1&isAllowed=y>.
- [29] S. Barke, ‘Inter-spacecraft frequency distribution for future gravitational wave observatories,’ PhD dissertation, QUEST-Leibniz Research School, Gottfried Wilhelm Leibniz Universität Hannover, Hannover, Germany, 2015.
- [30] O. Gerberding, ‘Phase readout for satellite interferometry,’ Ph.D. dissertation, Ph.D. dissertation, Albert Einstein Institute, Hannover, Germany, 2014. DOI: 10.15488/8255.
- [31] G. F. Barranco, ‘Photodetection in intersatellite laser OBs,’ Ph.D. dissertation, The Faculty of Electrical Engineering and Computer Science, University of Gottfried Wilhelm Leibniz, Hanover, Germany, 2018.

- [32] S. M. Sze and M.-K. Lee, *Semiconductor Devices: Physics and Technology*, 3rd ed. Hoboken, NJ: John Wiley & Sons, Inc., 2016, ISBN: 978-0-470-53794-7.
- [33] D. A. Neamen, *Semiconductor Physics and Devices: Basic Principles*, 4th ed. New York, NY: McGraw-Hill, 2012, Library of Congress Cataloging-in-Publication Data: QC611.N39 2011 537.6'22—dc22 2010045765, ISBN: 978-0-07-352958-5. [Online]. Available: [www.mhhe.com](http://www.mhhe.com).
- [34] A. M. Joshi, F. Heine and T. Feifel, 'Rad-hard ultrafast ingaas photodiodes for space applications,' in *Proc. SPIE 6220, Spaceborne Sensors III*, May 2006. DOI: 10.1117/12.666055.
- [35] A. Joshi, J. Rue and S. Datta, 'Low-noise large-area quad photoreceivers based on low-capacitance quad ingaas photodiodes,' *IEEE Photonics Technology Letters*, vol. 21, no. 21, pp. 1585–1587, Nov. 2009. DOI: 10.1109/LPT.2009.2030665.
- [36] A. Joshi, S. Datta, J. Rue, J. Livas, R. Silverberg and F. G. Cervantes, 'Ultra-low noise large-area ingaas quad photoreceiver with low crosstalk for laser interferometry space antenna,' in *High Energy, Optical, and Infrared Detectors for Astronomy V*, SPIE, Sep. 2012, pp. 711–720. DOI: 10.1117/12.918285.
- [37] A. M. Joshi and S. Datta, 'Space qualification of ingaas photodiodes and photoreceivers,' in *SPIE Defense + Security*, Orlando, FL, United States, May 2018. DOI: 10.1117/12.2304973. [Online]. Available: <https://doi.org/10.1117/12.2304973>.
- [38] R. Alabedra and D. Rigaud, 'Noise in photodiodes and photoreceiver systems,' in *Optoelectronic Sensors*, D. Decoster and J. Harari, Eds., London, UK: ISTE, 2009, pp. 223–268. DOI: 10.1002/9780470611630.ch7. [Online]. Available: <https://doi.org/10.1002/9780470611630.ch7>.
- [39] F. G. Cervantes, J. Livas, R. Silverberg, E. Buchanan and R. Stebbins, 'Characterization of photoreceivers for lisa,' *Classical and Quantum Gravity*, vol. 28, no. 9, p. 094010, May 2011. DOI: 10.1088/0264-9381/28/9/094010. [Online]. Available: <https://doi.org/10.1088/0264-9381/28/9/094010>.
- [40] J. B. Johnson, 'Thermal agitation of electricity in conductors,' *Physical Review*, vol. 32, no. 1, pp. 97–109, Jun. 1928. DOI: 10.1103/PhysRev.32.97. [Online]. Available: <https://doi.org/10.1103/PhysRev.32.97>.
- [41] M. Millinger and P. Jiggins, 'Lisa environment specification,' European Space Agency (ESA), Noordwijk, Netherlands, Tech. Rep. ESA-TEC-SP-006666, Jun. 2020.
- [42] P. Lantos, 'The sun, the solar wind and their effects on the earth's environment,' in *Space Radiation Environment and Its Effects on Spacecraft Components and Systems*. Toulouse, France: Cepadues-Editions, 2004, vol. 4, ch. I-01, pp. 29–40.
- [43] S. Bourdarie and D. Boscher, 'Space radiation environment,' in *Space Radiation Environment and Its Effects on Spacecraft Components and Systems*. Toulouse, France: Cepadues-Editions, 2004, vol. 4, ch. I-02, pp. 74–76.
- [44] NASA, *Nasa science image detail*, Online; accessed: Jan. 31, 2024, 2017. [Online]. Available: [https://science.nasa.gov/image-detail/amf-gsfc\\_20171208\\_archive\\_e001434/](https://science.nasa.gov/image-detail/amf-gsfc_20171208_archive_e001434/).
- [45] E. Stassinopoulos and J. Raymond, 'The space radiation environment for electronics,' *Proceedings of the IEEE*, vol. 76, no. 11, pp. 1423–1442, 1988. DOI: 10.1109/5.90113.
- [46] NASA, *Microscopic "timers" reveal likely source of galactic radiation - nasa*, Online; accessed: Jan. 31, 2024, 2016. [Online]. Available: <https://www.nasa.gov/news-release/microscopic-timers-reveal-likely-source-of-galactic-space-radiation/>.
- [47] D. Halliday, *Introduction à la Physique Nucléaire*. Dunod, 1957.
- [48] D. Blanc, *Physique Nucléaire*. PARIGI: Masson, 1980, pp. 25–28, ISBN: 2225672768.
- [49] C. Inguibert, 'Radiation-matter interaction,' in *Space Radiation Environment and Its Effects on Spacecraft Components and Systems*. Toulouse, France: Cepadues-Editions, 2004, vol. 4, ch. I-03, pp. 83–111.

- [50] S. Wood *et al.*, ‘Simulation of radiation damage in solids,’ *IEEE Transactions on Nuclear Science*, vol. 28, no. 6, pp. 4107–4112, Dec. 1981. DOI: 10.1109/TNS.1981.4335684.
- [51] J. R. Srour, C. J. Marshall and P. W. Marshall, ‘Review of displacement damage effects in silicon devices,’ *IEEE Transactions on Nuclear Science*, vol. 50, no. 3, pp. 653–670, Jun. 2003. DOI: 10.1109/TNS.2003.813197.
- [52] S. Dusseau, D. Boscher and J. Gasiot, ‘Basic mechanisms,’ in *Space Radiation Environment and Its Effects on Spacecraft Components and Systems*. Toulouse, France: Cepadues-Editions, 2004, vol. 4, ch. II-02, pp. 145–174.
- [53] G. Hopkinson, ‘Displacement damage: Analysis and characterisation of effects on devices,’ in *Space Radiation Environment and Its Effects on Spacecraft Components and Systems*. Toulouse, France: Cepadues-Editions, 2004, vol. 4, ch. II-03, pp. 175–198.
- [54] D. Bielle-Daspet, ‘Effects of high-energy protons on silicon and germanium electric properties,’ FRCEA-TH-9466, France, Tech. Rep., Mar. 1970, p. 20.
- [55] C. J. Marshall and P. W. Marshall, ‘Proton effects and test issues for satellite designers: Displacement effects,’ in *1999 NSREC Short Course*, NASA/Goddard Space Flight Center, 1999.
- [56] J. W. Walker and C. T. Sah, ‘Properties of 1.0 mev electron-irradiated defect centers in silicon,’ *Phys. Rev. B*, vol. 7, no. 10, pp. 4587–4605, 1973. DOI: 10.1103/PhysRevB.7.4587.
- [57] K. Nordlund, M. Ghaly, R. Averback, M. Caturla, T. Diaz de la Rubia and J. Tarus, ‘Defect production in collision cascades in elemental semiconductors and fcc metals,’ *Phys. Rev. B*, vol. 57, pp. 7556–7570, Apr. 1998. DOI: 10.1103/PhysRevB.57.7556.
- [58] M. Huhtinen, ‘Simulation of non-ionising energy loss and defect formation in silicon,’ *Nuclear Instruments and Methods in Physics Research Section A: Accelerators, Spectrometers, Detectors and Associated Equipment*, vol. 491, no. 1, pp. 194–215, 2002. DOI: 10.1016/S0168-9002(02)01227-5. [Online]. Available: [https://doi.org/10.1016/S0168-9002\(02\)01227-5](https://doi.org/10.1016/S0168-9002(02)01227-5).
- [59] J. R. Srour and J. W. Palko, ‘Displacement damage effects in irradiated semiconductor devices,’ *IEEE Transactions on Nuclear Science*, vol. 60, no. 3, pp. 1740–1766, Jun. 2013. DOI: 10.1109/TNS.2013.2261316.
- [60] P. Arnolda, C. Inguibert, T. Nuns and C. Boatella-Polo, ‘Niel scaling: Comparison with measured defect introduction rate in silicon,’ *IEEE Transactions on Nuclear Science*, vol. 58, pp. 756–763, Jun. 2011. DOI: 10.1109/TNS.2011.2131154.
- [61] G. Hopkinson, C. Dale and P. Marshall, ‘Proton effects in charge-coupled devices,’ *IEEE Transactions on Nuclear Science*, vol. 43, no. 2, pp. 614–627, 1996. DOI: 10.1109/23.490905.
- [62] T. R. Oldham and J. M. McGarrity, ‘Comparison of 60co response and 10 kev x-ray response in mos capacitors,’ *IEEE Transactions on Nuclear Science*, vol. 30, no. 6, pp. 4377–4381, 1983. DOI: 10.1109/TNS.1983.4333141.
- [63] K. Nordlund *et al.*, ‘Primary radiation damage: A review of current understanding and models,’ *Journal of Nuclear Materials*, vol. 512, pp. 450–479, Dec. 2018. DOI: 10.1016/j.jnucmat.2018.10.027. [Online]. Available: <https://doi.org/10.1016/j.jnucmat.2018.10.027>.
- [64] J. Lindhard, V. Nielsen, M. Scharff and P. Thomsen, ‘Integral equations governing radiation effects,’ *Mat. Fys. Medd. Dan. Vid. Selsk.*, vol. 33, 1963, Issue 33, No. 64.
- [65] G. H. Kinchin and R. S. Pease, ‘The displacement of atoms in solids by radiation,’ *Reports on Progress in Physics*, vol. 18, no. 1, pp. 1–51, 1955. DOI: 10.1088/0034-4885/18/1/301. [Online]. Available: <https://doi.org/10.1088/0034-4885/18/1/301>.
- [66] C. Inguibert and R. Gigante, ‘Nemo: A code to compute niel of protons, neutrons, electrons, and heavy ions,’ *IEEE Transactions on Nuclear Science*, vol. 53, no. 4, pp. 1967–1972, Aug. 2006. DOI: 10.1109/TNS.2006.880926.

- [67] M. J. Boschini, P. G. Rancoita and M. Tacconi, *Sr-niel-7 calculator: Screened relativistic (sr) treatment for calculating the displacement damage and nuclear stopping powers for electrons, protons, light- and heavy- ions in materials and electronic stopping power*, <https://www.sr-niel.org/>, [Online]. Available: <https://www.sr-niel.org/>, 2023.
- [68] M. J. Norgett, M. T. Robinson and I. M. Torrens, 'A proposed method of calculating displacement dose rates,' *Nuclear Engineering and Design*, vol. 33, no. 1, pp. 50–54, Aug. 1975. DOI: 10.1016/0029-5493(75)90035-7. [Online]. Available: [https://doi.org/10.1016/0029-5493\(75\)90035-7](https://doi.org/10.1016/0029-5493(75)90035-7).
- [69] K. e. a. Nordlund, 'Improving atomic displacement and replacement calculations with physically realistic damage models,' *Nature Communications*, vol. 9, no. 1, 2018. DOI: 10.1038/s41467-018-03415-5. [Online]. Available: <https://doi.org/10.1038/s41467-018-03415-5>.
- [70] A. Y. Konobeyev, U. Fischer, Y. A. Korovin and S. P. Simakov, 'Evaluation of effective threshold displacement energies and other data required for the calculation of advanced atomic displacement cross-sections,' *Nuclear Energy and Technology*, vol. 3, no. 3, pp. 169–175, Sep. 2017. DOI: 10.1016/j.nucet.2017.08.007. [Online]. Available: <https://doi.org/10.1016/j.nucet.2017.08.007>.
- [71] J. Srour, S. Chen, S. Othmer and R. Hartmann, 'Neutron damage mechanisms in charge transfer devices,' *IEEE Transactions on Nuclear Science*, pp. 1251–1260, Dec. 1978, 1, 50, 56, 57.
- [72] C. Dale, P. Marshall, E. Burke, G. Summers and G. Bender, 'The generation lifetime damage factor and its variance in silicon,' *IEEE Transactions on Nuclear Science*, vol. 36, no. 6, Not provided, Dec. 1989, 1, 50, 55, 56, 57, 67, 70, 72, 73.
- [73] H. Kraner, Z. Li and K. Posnecker, 'Fast neutron damage in silicon detectors,' *Nuclear Instruments and Methods in Physics Research*, vol. 279, pp. 266–271, 1989, 56.
- [74] P. Marshall, C. Dale and E. Burke, 'Proton-induced displacement damage distributions and extremes in silicon microvolumes,' *IEEE Transactions on Nuclear Science*, vol. 37, pp. 1776–1783, Dec. 1990, 40, 50, 56, 57, 67, 70, 72, 73.
- [75] J. R. Srour and D. H. Lo, 'Universal damage factor for radiation-induced dark current in silicon devices,' *IEEE Transactions on Nuclear Science*, vol. 47, no. 6, pp. 2451–2459, Dec. 2000. DOI: 10.1109/23.903792.
- [76] V. A. J. van Lint, T. M. Flanagan, R. E. Leadon, J. A. Naber and V. C. Rogers, *Mechanisms of Radiation Effects in Electronic Materials*. New York: John Wiley and Sons, 1980, vol. 1, pp. 316–320.
- [77] G. P. Summers, E. A. Burke, C. J. Dale, E. A. Wolicki, P. W. Marshall and M. A. Gehlhausen, 'Correlation of particle-induced displacement damage in silicon,' *IEEE Transactions on Nuclear Science*, vol. 34, no. 6, pp. 1133–1139, Dec. 1987. DOI: 10.1109/TNS.1987.4337442.
- [78] P. W. Marshall, C. J. Dale, G. P. Summers, E. A. Burke and E. A. Wolicki, 'Proton, neutron and electron-induced displacement damage in germanium,' *IEEE Transactions on Nuclear Science*, vol. 36, pp. 1882–1888, Dec. 1989.
- [79] G. P. Summers, E. A. Burke, S. R. Shapiro P. and and R. J. Walters, 'Damage correlations in semiconductors exposed to gamma, electron and proton radiations,' *IEEE Transactions on Nuclear Science*, vol. 40, no. 6, pp. 1372–1379, Dec. 1993. DOI: 10.1109/23.273529.
- [80] J. Warner, S. Messenger, R. Walters and G. Summers, 'Displacement damage correlation of proton and silicon ion radiation in gaas,' *IEEE Transactions on Nuclear Science*, vol. 52, no. 6, pp. 2678–2682, Dec. 2005. DOI: 10.1109/TNS.2005.860737.
- [81] J. H. Warner *et al.*, 'Correlation of electron radiation induced-damage in gaas solar cells,' *IEEE Transactions on Nuclear Science*, vol. 53, no. 4, pp. 1988–1994, Jun. 2006. DOI: 10.1109/TNS.2006.877877.

- [82] A. M. Tonigan, C. N. Arutt, E. J. Parma, P. J. Griffin, D. M. Fleetwood and R. D. Schrimpf, ‘Correlation of a bipolar-transistor-based neutron displacement damage sensor methodology with proton irradiations,’ *IEEE Transactions on Nuclear Science*, vol. 65, no. 1, pp. 495–501, Nov. 2018. DOI: 10.1109/TNS.2017.2774759.
- [83] P. G. Lucasson and R. M. Walker, ‘Production and recovery of electron-induced radiation damage in a number of metals,’ *Phys. Rev.*, vol. 127, no. 2, pp. 485–500, Jun. 1962. DOI: 10.1103/PhysRev.127.485.
- [84] S. R. Messenger *et al.*, ‘Nonionizing energy loss (niel) for heavy ions,’ *IEEE Transactions on Nuclear Science*, vol. 46, no. 6, pp. 1595–1602, Dec. 1999. DOI: 10.1109/23.819126.
- [85] S. R. Messenger, G. P. Summers, E. A. Burke, R. J. Walters and M. A. Xapsos, ‘Modeling solar cell degradation in space: A comparison of the nrl displacement damage dose and the jpl equivalent fluence approaches,’ *Progress in Photovoltaics: Research and Applications*, vol. 9, no. 2, pp. 103–121, Apr. 2001. DOI: 10.1002/pip.357.
- [86] C. Inguibert, P. Arnolda, T. Nuns and G. Rolland, ‘Effective niel’ in silicon: Calculation using molecular dynamics simulation results,’ *IEEE Transactions on Nuclear Science*, vol. 57, no. 4, pp. 1915–1923, Aug. 2010. DOI: 10.1109/TNS.2010.2049581.
- [87] C. Baur, M. Gervasi, P. Nieminen, S. Pensotti, P. G. Rancoita and M. Tacconi, ‘Niel dose dependence for solar cells irradiated with electrons and protons,’ pp. 692–707, Nov. 2013. DOI: 10.1142/9789814603164\_0111.
- [88] R. J. Walters *et al.*, ‘Correlation of proton radiation damage in ingaas-gaas quantum-well light-emitting diodes,’ *IEEE Transactions on Nuclear Science*, vol. 48, no. 6, pp. 1773–1777, Dec. 2001. DOI: 10.1109/23.983129.
- [89] E. E. Allam, C. Inguibert, S. Addarkaoui, A. Meulenberg, A. Jorio and I. Zorkani, ‘Niel calculations for estimating the displacement damage introduced in gaas irradiated with charged particles,’ *IOP Conference Series: Materials Science and Engineering*, vol. 186, p. 012005, Mar. 2017. DOI: 10.1088/1757-899X/186/1/012005.
- [90] R. Campesato, C. Baur, M. Casale *et al.*, ‘Effects of irradiation on triple and single junction ingap/gaas/ge solar cells,’ in *Proc. 35th Eur. PV Solar Energy Conf.*, Brussels, Belgium, Sep. 2018, pp. 959–964. DOI: 10.4229/35thEUPVSEC20182018-4C0.5.4. [Online]. Available: <http://arxiv.org/abs/1809.07157>.
- [91] R. Campesato, C. Baur, M. Carta *et al.*, ‘Niel dose analysis on triple and single junction ingap/gaas/ge solar cells irradiated with electrons, protons and neutrons,’ in *2019 IEEE 46th Photovoltaic Specialist Conference (PVSC)*, Chicago, IL, USA, Jun. 2019, pp. 2381–2384. DOI: 10.1109/PVSC40753.2019.8980581. [Online]. Available: <https://arxiv.org/abs/1911.08900>.
- [92] C. Inguibert, ‘Including a distribution of threshold displacement damage energy on the calculation of the damage function and electron’s non ionizing energy loss,’ *Journal of Nuclear Materials*, vol. 559, p. 153398, Nov. 2021. DOI: 10.1016/j.jnucmat.2021.153398.
- [93] M. A. Xapsos, G. P. Summers, J. L. Barth, E. G. Stassinopoulos and E. A. Burke, ‘Probability model for cumulative solar proton event fluences,’ *IEEE Transactions on Nuclear Science*, vol. 47, no. 3, pp. 486–490, 2000.
- [94] S. Seltzer, ‘Shieldose: A computer code for space shielding radiation dose calculations,’ National Bureau of Standards, Washington, D.C., Technical Note 1116, Apr. 1980.
- [95] N. Dinu-Jaeger and al., ‘Lisa qpd irradiation tests report for tra,’ Observatoire de la Côte d’Azur, Technical Report LISA-OCA-QPR-TR-001, 9th May 2023. [Online]. Available: <https://www.osti.gov/biblio/4788263>.
- [96] O. Gilard and al., ‘Damage factor for radiation-induced dark current in ingaas photodiodes,’ *IEEE Transactions on Nuclear Science*, vol. 65, no. 3, pp. 884–895, Mar. 2018. DOI: 10.1109/TNS.2018.2799742.

- [97] G. F. Barranco, B. S. Sheard, C. Dahl, W. Mathis and G. Heinzl, ‘A low-power, low-noise 37-mhz photoreceiver for intersatellite laser interferometers using discrete heterojunction bipolar transistors,’ *IEEE Sensors Journal*, vol. 18, no. 18, pp. 7414–7420, Sep. 2018. DOI: 10.1109/JSEN.2018.2857202.
- [98] G. Fernández Barranco and G. Heinzl, ‘A dc-coupled hbt-based transimpedance amplifier for the lisa quadrant photoreceivers,’ *IEEE Transactions on Aerospace and Electronic Systems*, 2021, Article accepted for publication but not fully edited. DOI: 10.1109/TAES.2021.3068437.
- [99] G. F. Barranco, G. Heinzl, R. Wanders and E. Fitzsimmons, ‘Qpr interface description document,’ LISA Consortium, Technical Report LISA-LCST-INST-IF-001, Feb. 2021.
- [100] P. Hofverberg, F. Bezerra, M. Ruffenach *et al.*, *Validation of a new 60 mev proton beam-line for radiation hardness testing*, 2023. arXiv: 2310.12744 [physics.acc-ph].
- [101] P. Hofverberg *et al.*, ‘A 60 mev proton beam-line dedicated to research and development programs,’ *Applied Radiation and Isotopes*, vol. 184, p. 110 190, Jun. 2022. DOI: 10.1016/j.apradiso.2022.110190.
- [102] S. Duzellier, G. Hubert, R. Rey and F. Bezerra, ‘Mirage: A new proton facility for the study of direct ionization in sub-100nm technologies,’ in *IEEE Radiation Effects Data Workshop*, vol. 2015, Jul. 2014. DOI: 10.1109/REDW.2014.7004578. [Online]. Available: <https://doi.org/10.1109/REDW.2014.7004578>.
- [103] S. Duzellier *et al.*, ‘Axel lab.: Representative ground simulation for investigating radiation effects in materials and electronics,’ in *2017 17th European Conference on Radiation and Its Effects on Components and Systems (RADECS)*, Geneva, Switzerland, 2017, pp. 1–7. DOI: 10.1109/RADECS.2017.8696228.
- [104] J. Ziegler, *Srim & trim*, <http://www.srim.org/>, Accessed: Feb. 10, 2024.
- [105] *Estar*, <https://physics.nist.gov/PhysRefData/Star/Text/ESTAR.html>, Accessed: Feb. 10, 2024.
- [106] Keithley Instruments, Inc., *Model 4200-scs semiconductor characterization system technical data*, Available from Keithley Instruments, Inc., 2009. [Online]. Available: <http://www.keithley.com>.
- [107] J. in ’t Zand, M. Adams, G. Aitink-Kroes *et al.*, ‘Lisa qpr trl6 design report,’ SRON Netherlands Institute for Space Research, Technical Report SRON-LISA-QPR-RP-001, May 2023, Issue 1.1.
- [108] I. MKS Instruments, *818 series calibrated photodiode sensors*, Datasheet for the 818 Series Calibrated Photodiode Sensors, Jun. 2020. [Online]. Available: [www.MKSINST.com](http://www.mksinst.com).
- [109] Keithley Instruments, *2600b system sourcemeter smu instruments datasheet*, Datasheet for the Series 2600B System SourceMeter SMU Instruments, 2023. [Online]. Available: <https://www.tek.com/>.
- [110] G. F. Barranco, ‘Characterization of lisa qpr fees prior to irradiation,’ Albert Einstein Institute, Hannover, Germany, Technical Report, Jun. 2021.
- [111] S. Bruhier, J.-P. Coulon, N. Dinu-Jaeger, D. Huet, M. Lintz *et al.*, *Design and characterization of quadrant photoreceivers for the aivt of the lisa space instrument*, Poster presented at Optique Nice 2022, HAL Id: hal-03772904, Nice, France, Jul. 2022. [Online]. Available: <https://hal.science/hal-03772904>.
- [112] Z. Instruments, *Principles of lock-in detection and the state of the art*, White Paper, Nov. 2016. [Online]. Available: <https://www.zhinst.com>.
- [113] R. Li, Y. Li, H. Maliya *et al.*, ‘Study of displacement damage effects in ingaas pin photodiode under 10 mev proton irradiation,’ *AIP Advances*, vol. 13, no. 11, p. 115 028, Nov. 2023. DOI: 10.1063/5.0172476. [Online]. Available: <https://doi.org/10.1063/5.0172476>.

- [114] R. A. Carrasco, J. George, D. Maestas *et al.*, ‘Proton irradiation effects on ingaas/inassb mid-wave barrier infrared detectors,’ *Journal of Applied Physics*, vol. 130, p. 114501, Sep. 2021. DOI: 10.1063/5.0064043. [Online]. Available: <https://doi.org/10.1063/5.0064043>.
- [115] S. R. Messenger, R. J. Walters, E. A. Burke, G. P. Summers and M. A. Xapsos, ‘Niel and damage correlations for high-energy protons in gallium arsenide devices,’ *IEEE Transactions on Nuclear Science*, vol. 48, no. 6, pp. 2121–2126, Dec. 2001. DOI: 10.1109/23.983182.
- [116] C. Inguibert, T. Nuns, J. Barbero *et al.*, ‘Displacement damage effects in ingaas photodiodes produced by electrons, protons and neutrons irradiations,’ in *Proceedings of the European Conference on Radiation and its Effects on Components and Systems (RADECS)*, Montpellier, France, Sep. 2019. DOI: 10.15488/8255.
- [117] T. Nuns, C. Inguibert, S. Soonckindt, B. Dryer, T. Bugey and C. Poivey, ‘Experimental study of the niel scaling for silicon devices,’ in *2018 18th European Conference on Radiation and Its Effects on Components and Systems (RADECS)*, Sep. 2018, pp. 1–8. DOI: 10.1109/RADECS45761.2018.9328677.
- [118] T. Nuns *et al.*, ‘Displacement damage effects in ingaas photodiodes due to electron, proton, and neutron irradiations,’ *IEEE Transactions on Nuclear Science*, vol. 67, no. 7, pp. 1263–1272, Jul. 2020. DOI: 10.1109/TNS.2020.2984133.
- [119] J. R. Srour and J. W. Palko, ‘A framework for understanding displacement damage mechanisms in irradiated silicon devices,’ *IEEE Transactions on Nuclear Science*, vol. 53, no. 6, pp. 3610–3620, Dec. 2006. DOI: 10.1109/TNS.2006.885796.
- [120] A. Jouni *et al.*, ‘Proton-induced displacement damages in 2-d and stacked cmos spads: Study of dark count rate degradation,’ *IEEE Transactions on Nuclear Science*, vol. 70, no. 4, pp. 515–522, Apr. 2023. DOI: 10.1109/TNS.2023.3248521.
- [121] C. Inguibert, A. Durand, T. Nuns and K. Lemièrre, ‘Statistical spread on the displacement damage degradation of irradiated semiconductors,’ *Nuclear Instruments and Methods in Physics Research Section B: Beam Interactions with Materials and Atoms*, vol. 490, pp. 7–17, Mar. 2021. DOI: 10.1016/j.nimb.2021.01.002. [Online]. Available: <https://doi.org/10.1016/j.nimb.2021.01.002>.
- [122] GEANT4 Collaboration, *Geant4 - a simulation toolkit*, <https://geant4.web.cern.ch/>, [Online]. Available: <https://geant4.web.cern.ch/>.
- [123] P. W. Marshall and C. J. Dale, ‘Space radiation effects on optoelectronic materials and components for 1300 nm fiber optic data bus,’ *IEEE Transactions on Nuclear Science*, vol. 39, no. 6, pp. 1982–1989, Dec. 1992. DOI: 10.1109/TNS.1992.XXXXXXX.
- [124] S. Barde, E. Ecoffet, J. Costeraste, A. Meygret and X. Hugon, ‘Displacement damage effects in ingaas detectors: Experimental results and semi-empirical model prediction,’ *IEEE Transactions on Nuclear Science*, vol. 47, no. 6, pp. 2466–2472, Dec. 2000. DOI: 10.1109/TNS.2000.XXXXXXX.
- [125] M. Benfante *et al.*, ‘Electric field-enhanced generation current in proton irradiated ingaas photodiodes,’ *IEEE Transactions on Nuclear Science*, vol. 70, no. 4, pp. 523–531, Apr. 2023. DOI: 10.1109/TNS.2023.3244416. [Online]. Available: <https://doi.org/10.1109/TNS.2023.3244416>.
- [126] M. Benfante, J. -. Reverchon, C. Virmontois, S. Demiguel and V. Goiffon, ‘Impact of irradiation temperature, doping and proton energy on ingaas photodiodes,’ *IEEE Transactions on Nuclear Science*, 2023. DOI: 10.1109/TNS.2023.3340625.
- [127] G. T. Nelson *et al.*, ‘In situ deep-level transient spectroscopy and dark current measurements of proton-irradiated ingaas photodiodes,’ *IEEE Transactions on Nuclear Science*, vol. 67, no. 9, pp. 2051–2061, Sep. 2020. DOI: 10.1109/TNS.2020.3011729.
- [128] G. Pedroza, M. Boutillier, L. S. How *et al.*, ‘Proton irradiation effects on ingaas/inp photodiodes for space applications,’ *Journal of Applied Physics*, vol. 130, no. 114501, Sep. 2012. DOI: 10.1063/5.0064043. [Online]. Available: <https://doi.org/10.1063/5.0064043>.

- [129] Kohiki, H. Sunaga and T. Hakata, ‘Degradation of ingaas pin photodiodes by neutron irradiation,’ *Semiconductor Science and Technology*, vol. 11, pp. 1461–1463, 1996.
- [130] G. Shaw, S. Messenger, R. Walters and G. Summers, ‘Radiation-induced reverse dark currents in in0.53ga0.47as photodiodes,’ *Journal of Applied Physics*, vol. 73, no. 11, pp. 7244–7249, Jun. 1993. DOI: 10.1063/1.353744.
- [131] R. Aniceto, R. Milanowski, S. Moro, K. Cahoy and G. Schlenvogt, ‘Proton radiation effects on hamamatsu ingaas pin photodiodes,’ in *Proceedings of the RADECS 2017*, 02–06 Oct. 2017, Geneva, Switzerland, Oct. 2017. [Online]. Available: <https://ieeexplore.ieee.org/document/8377405>.
- [132] J.-P. David, ‘Total dose effects on devices and circuits,’ in *Space Radiation Environment and Its Effects on Spacecraft Components and Systems*. Toulouse, France: Cepadues-Editions, 2004, vol. 4, ch. II-04, pp. 199–219.
- [133] C. Inguibert, ‘Damage energy threshold anisotropy in non ionizing energy loss calculation,’ *IEEE Transactions on Nuclear Science*, pp. 1–1, 2024. DOI: 10.1109/TNS.2024.3376966.
- [134] M. Benfante *et al.*, *Proton radiation-induced dark current increase in ingaas photodiodes*, Oral presentation at RADOPT, Toulouse, France, Nov. 2023.

# Scientific productions

Conferences attended during the thesis (in chronological order):

1. P. Colcombet, N. Dinu-Jaeger, C. Inguibert, T. Nuns, P. Hofverberg, N. Van Bakel, J. In't Zand, G. F. Barranco, K. Izumi, "Radiation-induced degradation of low noise quadrant photoreceivers for LISA," 2022 LISA Symposium XIV, [Online]. Available: [https://www.youtube.com/watch?v=Z\\_Z0GM6qe4o](https://www.youtube.com/watch?v=Z_Z0GM6qe4o).
2. P. Colcombet et al., "Radiation Tolerance of Low-Noise Photoreceivers for the LISA Space Mission," RADECS 2023 Oral Presentation with proceedings, Toulouse, France, Sept. 2023.
3. P. Colcombet, N. Dinu-Jaeger, C. Inguibert, T. Nuns, P. Hofverberg, N. Van Bakel, J. In't Zand, G. F. Barranco, K. Izumi, "Radiation Tolerance of Low Noise Photoreceivers for Laser Interferometric Space Applications," Oral Presentation, RADOPT 2023, Toulouse, France, Nov. 2023.
4. P. Colcombet et al., "Investigation of Radiation Effects on Low Noise Photoreceivers for Laser Interferometric Space Applications such as LISA," Oral Presentation with proceedings, OPTRO 2024, Bordeaux, France, Jan. 2024.
5. LISA QPR working group online meetings, monthly oral presentations over thesis periode 2021-2023 presentation (France, Netherlands, Japan, Germany, Belgium, UK).

Paper publication on the thesis results

5. P. Colcombet et al., "Radiation Tolerance of Low-Noise Photoreceivers for the LISA Space Mission," RADECS 2023, Manuscript ID: TNS-00006-2024, under review at IEEE TNS, 2023.
6. P. Colcombet et al., "Investigation of Radiation Effects on Low Noise Photoreceivers for Laser Interferometric Space Applications such as LISA," Proceedings of OPTRO 2024, Manuscript ID: OPTRO2024 53, Bordeaux, France, Jan. 2024.

## Appendix A

# Experimental damage factor from literature

REFS	Manufacturer	S ( $\mu\text{m}$ )	Particle Type	Energy (MeV)	Fluence (p/cm <sup>2</sup> )	KIdark (pA/p)	
This work	Hamamastu	1000/4	Protons	20	1,00E+12	8,22E-05	
				60	1,00E+12	3,59E-05	
		1500/4	Protons	20	1,00E+12	7,07E-05	
				60	1,00E+12	3,02E-05	
	2000/4	Protons	20	1,00E+12	6,60E-05		
			60	1,00E+12	2,77E-05		
	Nikhef	1500/4	Protons	20	1,00E+12	6,91E-05	
				60	1,00E+12	5,42E-05	
	Gilard 2018	Hamamatsu G8195	80	Protons	60	1,00E+10	3,21E-04
						1,00E+11	2,80E-04
1,00E+12						2,74E-04	
II-VI laser PM1R		320	Protons	60	1,00E+10	2,16E-04	
					1,00E+11	2,02E-04	
					1,00E+12	1,98E-04	
GPD Optoelectronic GAP394		300	Protons	60	1,00E+10	3,23E-04	
					1,00E+11	2,67E-04	
					1,00E+12	2,98E-04	
Lumentum EPM605LL		55	Protons	60	1,00E+10	5,78E-04	
					1,00E+11	8,37E-04	
					1,00E+12	6,76E-04	
					4,30E+10	5,21E-04	
					4,30E+10	4,35E-04	
					4,30E+10	3,42E-04	
					4,30E+10	3,79E-04	
					4,30E+10	3,79E-04	
					4,30E+10	3,19E-04	
					7,80E+10	4,82E-04	
7,80E+10		3,99E-04					
Lumentum HRS	300	Protons	60	7,80E+10	4,26E-04		
				7,80E+10	4,38E-04		
				7,80E+10	4,53E-04		
					7,80E+10	3,99E-04	

					1,30E+11	4,63E-04
					1,30E+11	3,69E-04
					1,30E+11	4,34E-04
					1,30E+11	3,94E-04
					1,30E+11	4,56E-04
					1,30E+11	3,95E-04
					5,00E+10	5,78E-04
					5,00E+10	5,72E-04
					1,00E+11	5,30E-04
				30	1,00E+11	5,46E-04
					5,00E+11	5,40E-04
					5,00E+11	5,76E-04
					1,00E+12	3,52E-04
					1,00E+12	3,44E-04
				80	5,00E+11	7,04E-04
					5,00E+11	2,18E-04
				190	5,00E+11	1,88E-03
					5,00E+11	1,66E-03
				60	3,00E+11	8,07E-04
					3,00E+11	7,73E-04
				170	5,00E+11	7,92E-04
					6,30E+11	7,86E-04
				5	5,00E+10	2,22E-03
				10	5,00E+10	1,29E-03
				15	5,00E+10	9,70E-04
				30	5,00E+10	7,90E-04
				60	5,00E+10	7,92E-04
				9,1	2,00E+09	4,78E-04
				10,55	3,00E+08	4,77E-04
					2,00E+09	5,55E-04
				17	2,00E+09	3,18E-04
					1,00E+10	3,98E-04
				35,8	2,00E+09	3,18E-04
				63,5	2,00E+09	2,55E-04
					1,00E+10	3,18E-04
				100	1,00E+10	1,43E-04
				200	1,00E+10	2,86E-04
				300	1,00E+10	1,67E-04
					5,00E+09	6,52E-04
				105	1,50E+10	8,00E-04
					3,30E+10	8,70E-04
					8,00E+10	1,01E-03
				60	3,00E+11	7,55E-04
				100	4,30E+11	6,70E-04
				170	6,30E+11	6,91E-04
				60	3,00E+11	3,62E-04
				100	4,30E+11	3,64E-04
				170	6,30E+11	3,28E-04
					1,00E+10	2,33E-03
				49,7	3,00E+10	1,72E-03
					1,00E+11	1,84E-03

					3,00E+11	1,70E-03		
Benfante 2023 (doping)	III-V Lab NIELSC2023	150	Protons	14,4	3,84E+10	1,80E-03		
				30,1	6,72E+10	2,00E-03		
				49,7	9,60E+10	2,80E-03		
				62	1,25E+11	2,75E-03		
	III-V Lab 200170	150	Protons	49,7	1,00E+10	9,00E-04		
				III-V Lab 200175	150	Protons	49,7	3,00E+10
III-V Lab 200303	150	Protons	49,7	1,00E+11	3,30E-03			
			III-V Lab 200329	150	Protons	49,7	3,00E+11	3,60E-03
Carrasco 2021	Air Force Laboratory	200		63	6,10E+11	9,02E-05		
Joshi 2006	Discovery DSC30	30	Protons	35	9,30E+10	1,20E-03		
					1,85E+11	6,65E-04		
	Discovery DSC30	30	Protons	35	2,78E+11	5,39E-04		
					1,06E+11	1,24E-03		
Joshi 2018	Discovery Semiconductors Inc.	500	30		6,89E+10	2,12E-05		
					1,38E+11	6,37E-05		
	Discovery Semiconductors Inc.	1000	30		2,30E+11	1,08E-04		
					6,89E+10	4,24E-05		
	Discovery Semiconductors Inc.	2000	30		1,38E+11	2,12E-05		
					2,30E+11	3,82E-05		
					6,89E+10	5,31E-06		
Nelson 2020	Air Force AEDC	500x500 square	Protons	2		1,10E+10	2,64E-04	
						1,00E+11	2,90E-04	
						1,00E+12	1,10E-04	
						1,00E+13	1,00E-04	
				3,5		1,10E+10	2,73E-04	
						1,00E+11	2,90E-04	
						1,00E+12	1,10E-04	
						1,00E+13	9,00E-05	
Li 2023	Xinjiang Technical Institute	3000	Protons	10		2,19E+11	1,25E-03	
						2,19E+12	1,44E-03	
						4,37E+12	1,02E-03	
Pedroza 2012	3SPHOTONICS		Protons	30	5,00E+11	4,60E-04		
This work	Hamamastu	1000/4	Electrons	0,5	5,00E+12	3,13E-08		
				1	5,00E+12	1,47E-07		
		1500/4	Electrons	0,5	5,00E+12	2,37E-08		
				0,5	5,00E+12	2,06E-08		
Gilard 2018	Excelitas C30618	350	Electrons		0,5	1,00E+12	9,85E-07	
						1,5	2,50E+12	9,00E-07
							5,00E+11	8,50E-06
							2,00E+12	7,95E-06

				6	1,18E+12	2,25E-05
				20	7,16E+11	4,97E-05
Kohiki 1996	IMEC	300	Electrons	1	1,00E+14	2,22E-07
					1,00E+15	2,22E-07
Shaw 1993	Epitaxx ETX-3000-T5	3000	Electrons	1	8,00E+13	7,06E-07
	Excelitas C30618	350	Electrons	0,5	2,50E+12	7,07E-07
				1,5	2,00E+12	6,50E-06
Nuns 2020	OSI Optoelectronics FCIQ1000	1000	Electrons	0,5	2,50E+12	2,65E-07
				1,5	2,00E+12	2,55E-06